Digital quantum simulation, Schrödinger cat state spectroscopy and setting up a linear ion trap

Thesis submitted to the
Faculty of Mathematics, Computer Science and Physics
of the Leopold-Franzens University of Innsbruck
in partial fulfillment
of the requirements for the degree of

Doctor of Philosophy
(Physics)

by

Cornelius Hempel

Innsbruck, August 2014

This work was carried out at the

Institute for Quantum Optics and Quantum Information (IQOQI)
of the Austrian Academy of Sciences
Technikerstr. 21a
6020 Innsbruck
Austria

under the supervision of

o. Univ.-Prof. Dr. Rainer Blatt and
PD Dr. Christian Roos.

NOTE

This version of the manuscript has been compiled after the work was submitted, reviewed and defended. While the content remains unchanged, a number of spelling, formatting and some grammatical errors have been fixed. A few cross-references and clarifying comments have been added. The original version of the text is available from the author and at `http://diglib.uibk.ac.at/ulbtirolhs/content/titleinfo/197952` via the digital publication repository of the university and regional library (ULB) of the University of Innsbruck.

Abstract

This PhD thesis reports on two experiments in the field of quantum information processing using trapped calcium ions. In addition, the text covers the setup and characterization of a new linear Paul trap accompanied by a novel implementation of single-ion addressing using an acousto-optic deflector.

The first of the two experiments is concerned with the proof-of-principle implementation of digital quantum simulations using up to 6 ions and 100 gate operations. It investigates the scaling behavior of simulations of elementary models of magnetism in terms of the number of involved spins and the complexity of their mutual interactions.

The second experiment introduces the application of a Schrödinger cat state in the indirect detection of photon scattering events on a broad electronic transition. The method is shown to have a sensitivity down to the single photon level in a proof-of-principle demonstration using a mixed-isotope crystal of $^{40}\mathrm{Ca}^{+}$ and $^{44}\mathrm{Ca}^{+}$.

A brief outlook towards future experiments and extensions of the experimental setup concludes the manuscript.

Zusammenfassung

In dieser Dissertationsschrift wird über zwei Experimente auf dem Gebiet der Quanteninformationsverarbeitung mit gespeicherten Kalzium-Ionen berichtet. Zusätzlich werden der Aufbau und die Charakterisierung einer neuen linearen Paul-Falle sowie die Implementierung einer neuartigen akustooptischen Adressierung einzelner Ionen vorgestellt.

Das erste der beiden Experimente beschäftigt sich mit dem Machbarkeitsnachweis von digitalen Quantensimulationen unter Verwendung von bis zu 6 Ionen und 100 Gatteroperationen. Es untersucht die Skalierbarkeit von Simulationen elementarer Modelle des Magnetismus im Hinblick auf die Anzahl der beteiligten Spins und die Komplexität ihrer gegenseitigen Wechselwirkungen.

Das zweite Experiment stellt die Anwendung eines Schrödinger-Katzen-Zustands zum indirekten Nachweis von Einzelphotonen-Streuvorgängen an einem breiten elektronischen Übergang vor. In einer Machbarkeitsstudie mit einem Ionenkristall unterschiedlicher Isotope aus $^{40}\mathrm{Ca}^{+}$ und $^{44}\mathrm{Ca}^{+}$ wird die Empfindlichkeit der Methode bis hin zum Niveau einzelner Photonen demonstriert.

Die Arbeit schließt mit einem kurzen Ausblick auf zukünftige Untersuchungen und Erweiterungen des experimentellen Aufbaus.

Contents

Acknowledgements

Joining a successful, well-staffed experiment is quite an adventure, very exciting and highly dynamic – setting up a new experiment... not so much, it mostly takes time. During my time in Innsbruck, I got to do both, which greatly enriched my experience and really made me understand what it means “to stand on the shoulders of giants”. As my PhD comes to its conclusion, I would like to take the opportunity to express my gratitude to the many people that made this work possible. As I can only mention a select few, I offer my apologies to those whose names do not appear.

First, I would like to thank Rainer Blatt for giving me the opportunity to carry out my PhD research in this wonderful scientific environment that he majorly helped to shape and sustain in Innsbruck. I am also thankful for granting me the luxury of time to write what I hope has become a text that is useful to other researchers starting in the field. Sharing this first address of gratitude is Christian Roos, who has been the close co-advisor of my thesis project. His deep understanding of physics combined with his endless patience at explaining even the most basic concepts really made all the difference in my learning process and greatly contributed to all that was achieved.

Ben Lanyon joined the experiment at IQOQI as a postdoc shortly after I did. He continually keeps pushing forward and has taught me the virtue of knowing exactly where you are on the fine line between “good enough” and “needs to be better” – one of the most valuable lessons in academic science. René Gerritsma was already a postdoc on the experiment when I joined the group. He not only shared an office with me but also his passion for physics which kept me going when I was getting frustrated with numerical simulations of the new trap.

I would like to thank my direct predecessors Gerhard Kirchmair and Florian Zähringer for the work they did during their PhDs. It provided a large part of the foundation on which I could build. Gladly I am now passing on the senior-PhD-student-torch to Petar Jurcevic, who has already made a number of valuable contributions. Christine Maier, who only recently joined the project as a PhD student, has been great fun to work with and showed me again, that the best way of learning really is teaching.

IQOQI is located in a separate building on the University of Innsbruck’s Technik campus. As most of the other members of the Blatt group work at the Institute for Experimental Physics, interactions were naturally limited to the weekly Monday morning meetings and the annual group retreat to Obergurgl. However, having such a number of experienced people in close proximity, and be it only over the phone, has always been

very helpful. I would like to mention two names representative of the whole group: Daniel Nigg, who has been my counterpart at our sister experiment “the linear trap” at the university (fiber-noise! ;) and Mike Chwalla, who has shown me that a “three-cornered hat” is not necessarily a type of headgear. Mike and I also got to team-up in the preparation of an ESA grant application - what an experience!

One name I feel, thus far, has not gotten the credit he deserves, so I am printing it in bold: **Stefan Haslwanter**. Stefan designed and built most of the linear blade traps in use throughout the group. He always came up with solutions for the impossible dreams of us physicists and has not only provided us with innovative designs, he also brought them into reality at IQOQI’s fine-mechanical workshop.

Work in an academic environment would not be possible without the invaluable administrative support provided behind the scenes by Doris Corona and Elisabeth Huck at IQOQI as well as Patricia Moser at the University of Innsbruck.

I am also very grateful to IQOQI’s administrative director Markus R. Knabl for running a tight ship since the institute’s opening day, which ensures that it still is smoothly sailing on its course “bound for the future”.

A number of weekends at the institute and Sunday morning brunches I shared with Simon Stellmer, who has became a good friend over the years. He has given me valuable feedback on this text and found an incredible number of mistakes even in the final drafts, which - I hope - are now fixed at least to some degree.

Last but by no means least, I would like to express my gratitude towards my parents Beate and Wolf, who have supported and encouraged me throughout my long journey that took me through four very different areas of study and three countries.

List of acronyms and abbreviations

AC	alternating current
AM	amplitude modulation
AOD	acousto-optic deflector
AOM	acousto-optic modulator
APC	angled physical contact (FC/APC)
BSB	blue sideband
CAR	carrier
CF	“ConFlat” (type of ultra-high vacuum flange)
COM	center of mass
CTE	coefficient of thermal expansion
DC	direct current
DDS	direct digital synthesizer
DP	double pass (AOM)
EMCCD	electron multiplying charged coupled device
FC	ferrule connector (fiber optics)
FEM	finite element method
FPGA	field-programmable gate array
FSR	free spectral range
FWHM	full width at half maximum
GND	ground (electrical)
IQOQI	Institut für Quantenoptik und Quanteninformation
MOPA	master oscillator power amplifier

MS	Mølmer Sørensen (gate operation)
NA	numerical aperture
NEG	non evaporable getter (type of passive vacuum pump)
NIST	National Institute of Standards and Technology
NTC	negative temperature coefficient (thermistor)
OEAW	Österreichische Akademie der Wissenschaften (Austrian Academy of Sciences)
OFHC	oxygen-free high conductivity (copper)
PC	physical contact (FC/PC)
PCB	printed circuit board
PDH	Pound–Drever–Hall (laser locking scheme)
PER	polarization extinction ratio
PID	proportional-integral-derivative (controller)
PM(F)	polarization maintaining (fiber)
PMT	photomultiplier tube
PT(1000)	positive temperature coefficient (resistance temperature detector, RTD)
QE	quantum efficiency
QLS	quantum logic spectroscopy
RF	radio frequency
RGA	residual gas analyzer
RMS	root mean square
RSA	public-key crypto-algorithm named after Rivest, Shamir and Adleman
RSB	red sideband

SHG	second harmonic generation
SNR	signal-to-noise ratio
SP	single pass (AOM)
TA	tapered amplifier
TEC	thermoelectric cooler (Peltier element)
TEM	transverse electromagnetic (mode)
TTL	transistor-transistor logic
ULE	ultra-low expansion glass (titania silicate glass, trademark by Corning, Inc.)
UV-A	ultraviolet A (light spectrum from 315 to 400 nm)

1. Introduction

The invention of traps for charged particles, namely the Penning and Paul trap [1, 2], has given us access to a domain that was previously thought to be out of our reach, as most famously put by Erwin Schrödinger in 1952: "[...] we never experiment with just one electron or atom or (small) molecule. In thought-experiments we sometimes assume that we do; this invariably entails ridiculous consequences [...]" [3].

With the ability to trap single electrons and atoms (in ionized form), it became possible in the 1980s to take a closer look at these "ridiculous consequences" such as instantaneous jumps between the quantized energy levels of an atom (more on that in Chapter 6). Early experimental research was spurred by interest in the improvement of atomic frequency standards [4]. In parallel, ideas were put forward that envisioned how the control of individual quantum systems could be put to use. As one of the first, Richard Feynman considered employing a well-controlled quantum system to simulate another quantum system which, by itself, would pose a computationally intractable problem [5] (more on this topic in Chapter 5).

Then, in 1994, Peter Shor discovered that a computer directly operating at the quantum level could find the prime-factors of an arbitrary large number in polynomial time compared to the exponential time scaling with problem size[1] exhibited by classical algorithms on ordinary computers [6]. A year later, Ignacio Cirac and Peter Zoller published an influential proposal [7] which suggested a way to a practical realization of such a *quantum computer* using trapped ions.

Motivated by these findings, quantum information science has grown enormously over the last 20 years and now encompasses not only well-isolated atomic but also solid-state and optical systems[2]. Each implementation has different strengths and weaknesses in terms of the available coherence time, their scalability and the overhead required for interfacing with "the classical world" and other quantum nodes[3]. In this light, the

---

[1] This very fact ensures the security of modern public-key encryption systems such as RSA.

[2] A review of currently pursued quantum computing architectures can be found in reference [8].

[3] See, e.g., reference [9] for a comparison of natural and artificial atoms.

full-fledged universal quantum computer of the future will likely be a hybrid system that combines a classical processing part with a number of different special purpose quantum components selected based on their respective merits.

Before, however, the first 2048-bit number[4] will be factorized by a quantum computer using Shor's algorithm [10], a different subfield of quantum information processing is likely to deliver on its promise first: quantum simulation [11]. Following Feynman's idea of using one controllable quantum system to mimmic the behavior of another, already simulations using only tens of quantum bits can offer new insights into fundamental quantum mechanical models that underpin research in applied fields such as materials science or pharmaceutical chemistry. Here, one particular method known as *digital quantum simulation* is poised to play a large role in the quantum computer implementation of the complex Hamiltonians that are associated with these models. The first proof-of-principle implementation of this method in a trapped ion architecture is discussed in Chapter 5.

The large amount of progress made in quantum information processing using trapped ions [12–15] also has had its merits in the field of precision spectroscopy. High-accuracy single-ion clocks have been demonstrated in the recent years [16–18] – accurate enough to detect the gravitational red-shift affecting the passage of time at distances as small as 30 cm [19]. A technique known as *quantum logic spectroscopy* [20] was instrumental in the most recent experiments and provides a tool to perform spectroscopic measurements on formerly inaccessible atomic and molecular species. In this context, the experiment discussed in Chapter 6 adds another variation of the technique to the toolbox of quantum metrology [21], which is aimed at exploiting non-classical states to perform more precise measurements.

In parallel to the scientific work reported in this thesis, a large amount of technical work was carried out to enable the next steps on the way to more complex quantum simulations. Large parts of this text are therefore devoted to the experimental setup and the methods used in the initial characterization and daily operation of a newly built linear ion trap.

The remainder of this thesis is structured as follows:

Chapter 2 introduces the theoretical framework used for the description of quantum bits and the foundations of the interactions employed in the concrete implementation with Ca^+.

---

[4] This is NIST's 2007 recommendation for an RSA key length that is estimated to be secure until 2030.

Chapter 3 showcases the experimental setup and the performance of a few selected components such as the high-finesse reference cavity of the laser used to manipulate the optical qubit (Section 3.3.3), site-resolved state detection (Section 3.4) and a novel implementation of single ion addressing using acousto-optics (Section 3.5).

Chapter 4 discusses a selection of experimental methods used in the manipulation of trapped ion qubits. In addition, the chapter offers a hands-on description of the first steps taken when setting up a new ion trap “from scratch”.

Chapter 5 summarizes an experiment demonstrating the first implementation of digital quantum simulations on the trapped-ion architecture.

Chapter 6 reports on the work contributed to the field of precision spectroscopy. The method of cat-state spectroscopy is applied to the detection of single-photon scattering events in a mixed-isotope crystal of $^{40}\mathrm{Ca}^+$ and $^{44}\mathrm{Ca}^+$.

Chapter 7 concludes the thesis with a brief summary and provides an outlook towards future work.

2. Foundations and theoretical framework

The key to all experiments presented in this text is the experimental control attained over quantum bits encoded in a system of trapped calcium ions. This chapter introduces the foundations and underlying concepts in quantum information, atomic physics and quantum optics that enable these experiments. Considering the large number of books and theses already available on these topics, each section is kept concise and cites more detailed references. A compilation of useful relations used in or resulting from the derivations below is given in Appendix B.

2.1. Quantum bits

In a calculation on a digital computer, information is processed in the form of so-called binary digits or *bits*, representing its smallest unit. Each bit can have the value 0 *or* 1, corresponding to two discrete states commonly realized by two voltage levels in a transistor. Underlying each of the millions of transitions in today's electronic devices are quantum mechanical processes – still, at the level of bits, the binary "either-or" is the signature of classical logic. Moving the processing of information itself into the quantum mechanical domain, one can, again, identify a two-level system now called quantum bit, or *qubit* that is based on two distinguishable quantum states, e.g. $|\uparrow\rangle$ and $|\downarrow\rangle$. In contrast to the classical bit however, the qubit can also be in a superposition state $|\psi\rangle$, which corresponds to an arbitrary linear combination of these basis states and is described by the relation

$$|\psi\rangle = c_\uparrow |\uparrow\rangle + c_\downarrow |\downarrow\rangle \,. \tag{2.1}$$

Here $c_\uparrow$ and $c_\downarrow$ are complex coefficients bound by the normalization $|c_\uparrow|^2 + |c_\downarrow|^2 = 1$. Their values cannot be determined in a single measurement. It is only after a number of N measurements that one finds $|\uparrow\rangle$ with probability $|c_\uparrow|^2$ and $|\downarrow\rangle$ with probability $|c_\downarrow|^2$, where the corresponding uncertainty is determined by N and the respective probability $p \in [0,1]$ in what is known as *quantum projection noise* $\Delta p = \sqrt{p\,(1-p)\,/\,N}$ [22].

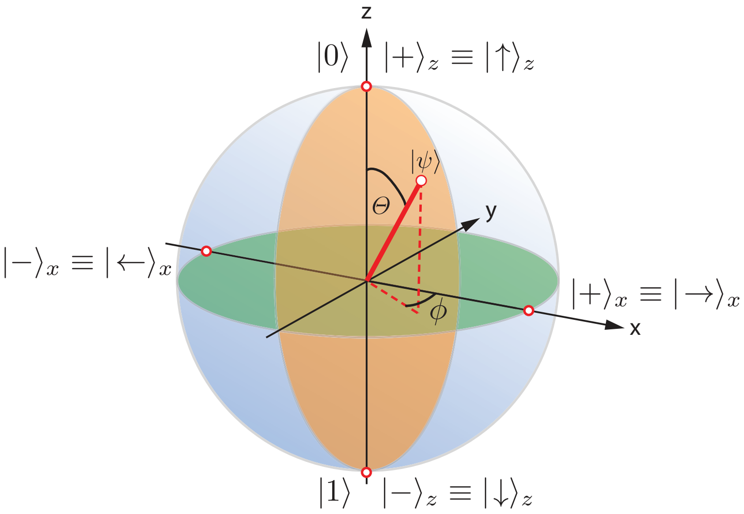

Figure 2.1.: Bloch sphere represenation of a qubit.
The two-dimensional state space of complex vectors that describes all possible (pure) states of a single qubit can be represented by the surface of a unit sphere in three dimensions. Two exemplary pairs of orthogonal basis states are labeled (red points) and can each be used to describe an arbitrary state $|\psi\rangle$ using the spherical coordinates Θ and φ, cf. Eq. (2.2).

Figure 2.1 shows a graphical representation of possible quantum states of a single qubit on the so-called *Bloch sphere*. The basis states introduced before are associated with the north and south pole of the sphere, following the usual convention. In the context of quantum information they are often labeled as $|0\rangle$ and $|1\rangle$, in analogy to classical bits. Throughout this text, however, the spin notation will be used. Making use of the normalization, Eq. (2.1) can be rewritten in terms of spherical coordinates of a unit vector as

$$|\psi\rangle = e^{i\gamma}\Big(\cos\frac{\theta}{2}\,|\uparrow\rangle_z + e^{i\phi}\sin\frac{\theta}{2}\,|\downarrow\rangle_z\Big), \tag{2.2}$$

where γ, θ and ϕ are real numbers. Since it has no effect on the measured probabilities $|c_\uparrow|^2$ and $|c_\downarrow|^2$, one can set γ (the *global phase*) to zero. The coefficients for a given basis can be written as a column vector represented by a "ket" in Dirac notation, e.g.

$$\begin{pmatrix} c_\uparrow \\ c_\downarrow \end{pmatrix} = \begin{pmatrix} \cos\frac{\theta}{2} \\ e^{i\phi}\sin\frac{\theta}{2} \end{pmatrix} \Longrightarrow \begin{pmatrix} 0 \\ 1 \end{pmatrix} \equiv |\downarrow\rangle_z\,,$$

for $\theta = \pi, \phi = 0$ in the z-basis. The choice of basis states is arbitrary as long as they are orthonormal, i.e. orthogonal and of unit length. Counterintuitively, in the Bloch sphere representation this is true for every pair of points on opposite sides of the sphere's surface. Each basis state can be represented by a superposition in another basis, e.g. $|\pm\rangle_x = \left(|+\rangle_z \pm |-\rangle_z \right)/\sqrt{2}$. The $|\pm\rangle$ notation used here relates to the eigenstates of the Pauli spin matrices with eigenvalues ±1 introduced below. The complex vector space spanned by all $|\psi\rangle$ is generally referred to as *Hilbert space*.

2.1.1. Single qubit gate operations

Gate operations that manipulate the state of a single qubit amount to rotations of its state vector $|\psi\rangle$ on the Bloch sphere. A convenient way to describe rotations around the set of axes $k = \{x, y, z\}$ shown in Figure 2.1 is given by the Pauli matrices

$$\sigma_x = \begin{pmatrix} 0 & 1 \\ 1 & 0 \end{pmatrix}, \qquad \sigma_y = \begin{pmatrix} 0 & -i \\ i & 0 \end{pmatrix}, \qquad \sigma_z = \begin{pmatrix} 1 & 0 \\ 0 & -1 \end{pmatrix}, \tag{2.3}$$

which are Hermitian unitary matrices whose eigenstates $|\pm\rangle_k$ (denoted by eigenvectors, cf. Appendix B.1) are the points where the respective axis k intersects the Bloch sphere's surface. To express a rotation around an axis k, one can make use of Euler's formula $\exp(\pm i x \sigma_k) = \cos(x)\mathbb{1} \pm i \sin(x)\sigma_k$, where $\mathbb{1}$ is the identity matrix and σ_k is the k-th Pauli matrix. It follows from Euler's rotation theorem [23, and refs. therein] that an arbitrary rotation by an amount θ can be described by a concatenation of at most three (non-commuting) rotation matrices out of a set defined by

$$U_z(\theta) = e^{-i\frac{\theta}{2}\sigma_z} = \begin{pmatrix} e^{-i\frac{\theta}{2}} & 0 \\ 0 & e^{i\frac{\theta}{2}} \end{pmatrix} \quad \text{and} \tag{2.4}$$

$$U_\phi(\theta, \phi) = e^{-i\frac{\theta}{2}\sigma_\phi} = \begin{pmatrix} \cos\frac{\theta}{2} & -ie^{-i\phi}\sin\frac{\theta}{2} \\ -ie^{i\phi}\sin\frac{\theta}{2} & \cos\frac{\theta}{2} \end{pmatrix}, \tag{2.5}$$

with $\sigma_\phi = \cos(\phi)\,\sigma_x + \sin(\phi)\,\sigma_y$. Here, U_ϕ corresponds to a clockwise rotation around an axis at angle ϕ in the x-y-plane and U_z represents a clockwise rotation around the linearly independent z-axis.

To give an example, a σ_x-rotation ($\phi = 0$) of $\theta = \pi$ around $|+\rangle_x$ applied to $|\downarrow\rangle_z$ causes a spin flip

$$U_\phi(\pi, 0)\,|\downarrow\rangle_z = \begin{pmatrix} 0 & -i \\ -i & 0 \end{pmatrix} \begin{pmatrix} 0 \\ 1 \end{pmatrix} = \begin{pmatrix} -i \\ 0 \end{pmatrix} = e^{-i\frac{\pi}{2}} \begin{pmatrix} 1 \\ 0 \end{pmatrix} \equiv |\uparrow\rangle_z\,. \tag{2.6}$$

The example illustrates a property shared by qubits and spin-1/2 particles like electrons: in order to fully return to the initial state, a rotation of $\theta = 4\pi$ is needed. Upon measurement, however, any global phase incurred during operations (like $-i$ in Eq. (2.6) above) drops out as it has no effect on the measured probabilities.

2.1.2. Multiple qubits and entanglement

The description in terms of pure states denoted by the "ket"-vectors introduced above can be extended to a system of N qubits (multipartite system). Here, a pure N-qubit state $|\Psi\rangle$ is given by a tensor product of their state vectors ψ_i (Eq. (2.1)), a so-called *product state*, e.g.

$$|\Psi\rangle = |\psi\rangle_1 \otimes \ldots \otimes |\psi\rangle_N \, , \tag{2.7}$$

or a superposition of tensor products. An example in a two qubit (bipartite) system is the state vector

$$\begin{aligned} |\Psi\rangle &= (c_{\uparrow,1} |\uparrow\rangle + c_{\downarrow,1} |\downarrow\rangle\,) \otimes (c_{\uparrow,2} |\uparrow\rangle + c_{\downarrow,2} |\downarrow\rangle\,) \\ &= \quad a_1 |\uparrow\uparrow\rangle + a_2 |\uparrow\downarrow\rangle + a_3 |\downarrow\uparrow\rangle + a_4 |\downarrow\downarrow\rangle \, , \end{aligned} \tag{2.8}$$

where the (in general 2^N) complex state amplitudes a_k again obey the normalization $\sum |a_k|^2 = 1$. Given the arbitrary single qubit gate operations of Eq. (2.3) on all N qubits, only one multi-qubit gate operation is needed in order to be able to build up all arbitrary operations on $|\Psi\rangle$ [24]. One example of such a multi-qubit gate operation is the Mølmer-Sørensen (MS) gate (Section 2.5.2) which is represented by the operation

$$U_{\mathrm{MS}}(\theta, \phi) = e^{-i\frac{\theta}{2}\sum_{i<j} \sigma_\phi^i \otimes \sigma_\phi^j}, \tag{2.9}$$

where the indices denote the i-th and j-th qubit and ϕ is the rotation axis in the N-qubit Hilbert space. As an example, in the two-qubit case of Eq. (2.8), starting with both qubits in the ground state $|\downarrow\downarrow\rangle$, the MS gate with $\theta = \pi/2$ and $\phi = 0$ creates the Bell state

$$|\Psi\rangle = \frac{1}{\sqrt{2}}\Big(|\uparrow\uparrow\rangle - i\,|\downarrow\downarrow\rangle \Big). \tag{2.10}$$

It belongs to a class of states that are referred to as *entangled*, meaning that they exhibit perfect correlations (or anti-correlations) in more than one measurement basis. Hence, depending on the state prepared (angle ϕ), there are corresponding measurement bases in which a measurement on one of the two qubits immediately reveals the value that would be found if the same measurement were to be performed on the second qubit.

The generally used formal definition of entanglement is:
If a state $|\Psi\rangle$ *cannot be written as a product state of its constituents in the form of equation* (2.7)*, it is entangled.*
Indeed, attempting to factor Eq. (2.10) immediately leads to a violation of the normalization and the appearance of cross-terms that do not exist in the original state. These non-classical correlations are at the core of many applications of quantum bits in quantum computation and cryptography. A more thorough treatment of entanglement and the description of pure and mixed quantum states of qubits can be found in the quantum information textbooks listed in references [25–27].

2.2. Atomic structure of Ca$^+$

The experiments presented in this thesis employ two isotopes of the alkaline-earth element calcium (Table 2.1). Both have zero nuclear spin and consequently no hyperfine structure. In order to confine them in a linear Paul trap (Section 3.1) they are ionized in a two-step photoionization process illustrated in Figure 2.2.a. In the scheme depicted, a tunable laser at a wavelength around $\lambda = 422.79\,\mathrm{nm}$ provides isotope selectivity in the first step. The second step is less crucial and can be performed with a free running laser diode at 375 nm (as done in this thesis) or even an LED. An overview of other photoionization schemes for neutral calcium can be found in reference [28].

In its singly ionized form, the calcium ion has one remaining outer valence electron and therefore an electronic level structure similar to that of hydrogen. However, akin to the alkali atoms often used in neutral atom experiments (e.g. rubidium), the inner electrons do not entirely screen their associated charge in the nucleus. This situation is commonly described by quantum defect theory [32] and leads to a deformation of the outer electron's orbitals, which gives rise to metastable electronic states in the energy spectrum. Figure 2.2.b provides an overview of the electronic level structure of the three lowest orbitals in Ca$^+$. Following the ground state S-orbital, the lowest excited state is

Table 2.1.: Properties of two neutral calcium (Ca I) isotopes

Property	^{40}Ca	^{44}Ca	ref.
natural abundance	96.941(156)%	2.086(110)%	[29]
atomic mass (relative to ^{12}C)	39.962 590 98(22)	43.955 481 8(4)	[30]
$\lambda(4s^2\ {}^1S_0 - 4s4p\ {}^1P_1)$ and isotope shift	422.791 71 nm	+773.8(2) MHz	[31]

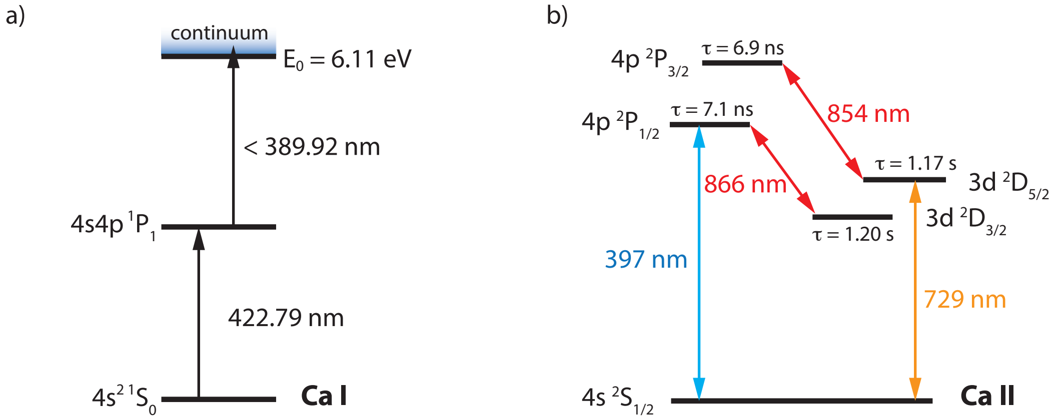

Figure 2.2.: Reduced energy level scheme of calcium.
a) Energy levels and light wavelengths used in the photoionization process of neutral calcium. **b)** Energy levels and transition wavelengths in Ca II relevant for this text. Not shown are the transitions 4p $^2P_{3/2} \leftrightarrow$ 3d $^2D_{3/2}$ at 850 nm, 4s $^2S_{1/2} \leftrightarrow$ 4p $^2P_{3/2}$ at 393 nm and 4s $^2S_{1/2} \leftrightarrow$ 3d $^2D_{3/2}$ at 732 nm.

a metastable D-orbital with the two fine-structure components[5] $3D_{3/2}$ and $3D_{5/2}$. The latter has a lifetime of $\tau = 1.168(7)$ s [33] and can be reached from the $S_{1/2}$ ground state via an electric quadrupole transition at 729 nm with a linewidth of $\Gamma/(2\pi) = 136$ mHz. The $4P_{1/2}$ excited state connects to the $4S_{1/2}$ ground and the $3D_{3/2}$ metastable state via electric dipole transitions at 397 nm and 866 nm. Its lifetime of $\tau = 7.1$ ns [34] leads to a comparably large linewidth of $\Gamma/(2\pi) = 22.4$ MHz. Lastly, the short-lived $4P_{3/2}$

Table 2.2.: Transition wavelengths for $^{40}Ca^+$, relative isotope shift (IS) of $^{44}Ca^+$ and branching ratios of the dipole transitions.

transition	$^{40}Ca^+$ (nm)	ref.	$^{44}Ca^+$ IS (MHz)	ref.	branching ratio	ref.
$4S_{1/2} \leftrightarrow 4P_{3/2}$	393.366	[35]	842(13)	[36]	93.47(3)%	[37]
$4S_{1/2} \leftrightarrow 4P_{1/2}$	396.849 934	[38]	842(3)	[36]	93.565(7)%	[39]
$4S_{1/2} \leftrightarrow 3D_{3/2}$	732.389	[35]	5344(5)	calc.		
$4S_{1/2} \leftrightarrow 3D_{5/2}$	729.152 176	[40]	5337(14)	calc.		
$3D_{3/2} \leftrightarrow 4P_{3/2}$	849.802	[35]	−4498(3)	[41]	0.661(4)%	[37]
$3D_{3/2} \leftrightarrow 4P_{1/2}$	866.214	[35]	−4502(4)	[41]	6.435(7)%	[39]
$3D_{5/2} \leftrightarrow 4P_{3/2}$	854.209	[35]	−4495(4)	[41]	5.87(2)%	[37]

---

[5] Instead of the full spectroscopic notation for multi-electron atoms $nl^x\ {}^{2S+1}L_J$, where nl is the electron configuration with x electrons in orbital l, and S and J represent the total spin and angular momentum, the reduced notation nL_J is used for compactness in the following.

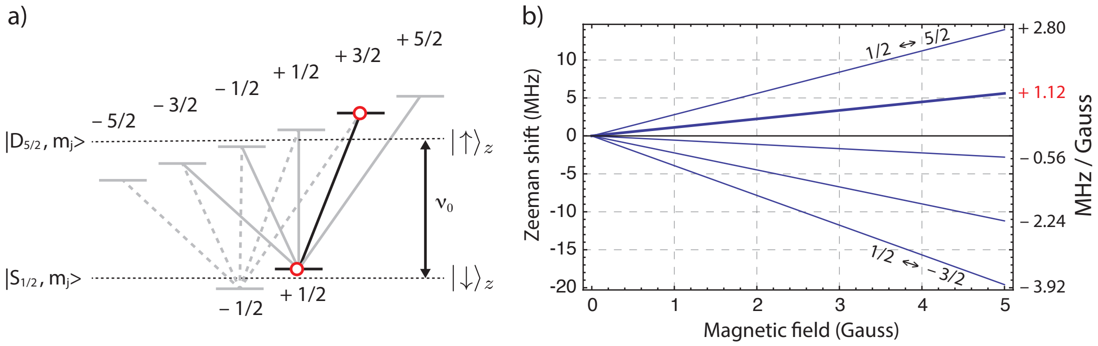

Figure 2.3.: Encoding an optical qubit in Zeeman levels of a quadruple transition. **a)** Magnetic fields lift the degeneracy of the Zeeman states, each identified by their quantum number m_j. The marked transition is used as the default qubit in most experiments. **b)** Zeeman shift with respect to ν_0 of each of the transitions indicated in a). Their field sensitivity is given on the right with the default qubit's sensitivity marked in red.

state couples to the $3D_{5/2}$, $3D_{3/2}$ and $4S_{1/2}$ states via electric dipole transitions with a linewidth of ~23 MHz. Table 2.2 provides a summary of all transition wavelengths and branching ratios as well as the isotope shift (IS) between $^{40}Ca^+$ and $^{44}Ca^+$ caused by their respective mass difference.

The basis states $|\downarrow\rangle_z$ and $|\uparrow\rangle_z$ introduced before can now be identified with the $S_{1/2}$ and $D_{5/2}$ state, respectively, thereby allowing one to encode an *optical qubit* [42]. In the presence of a magnetic field B, both fine structure states split into $2j+1$ Zeeman levels. With respect to the bare transition frequency ν_0 in the absence of a magnetic field, the magnetic field-induced energy level shift changes the transition frequency by

$$\Delta\nu_{(\mathrm{S,D})} = \frac{\mu_B}{h}\Big(g_j(\mathrm{D}_{5/2})\, m' - g_j(\mathrm{S}_{1/2})\, m\Big) B, \tag{2.11}$$

where μ_B is the Bohr magneton[6], g_J the Landé g-factors[7] and m', m are the magnetic quantum numbers of the $D_{5/2}$ and $S_{1/2}$ state, respectively. The selection rules for an electric quadrupole transition ($\Delta m = 0, \pm 1, \pm 2$) [44] allow for a total of 10 transitions that can be used to encode and manipulate a qubit (Figure 2.3).

The following experiments are carried out at a quantization field of $B \approx 4\,\mathrm{G}$ and use the states $\left|\mathrm{S}_{1/2}, m_j = 1/2\right\rangle$ and $\left|\mathrm{D}_{5/2}, m_j = 3/2\right\rangle$ to encode a qubit, compromising between high coupling strength (Section 2.3.3) and low sensitivity to B-field fluctuations.

---

[6] A useful quantity to remember is the value of $\mu_B/h = 1.399\,\mathrm{MHz/G}$.

[7] $g_j(\mathrm{S}_{1/2}) = 2.00225664(9) \approx 2$ [43] and $g_j(\mathrm{D}_{5/2}) = 1.2003340(3) \approx 1.2$ [40]

2.3. Fundamental interactions

This section introduces the theoretical framework underlying the description of an ion in a harmonic trapping potential that is coherently manipulated by laser beams. First, a useful transformation into an interaction picture is presented. Then, this approach is applied separately to the inner (electronic) and external (motional) degree of freedom.

2.3.1. Interaction picture

The evolution of the state vector $|\psi\rangle$ of a quantum system follows the time-dependent Schrödinger equation

$$i\hbar\frac{\partial}{\partial t}|\psi\rangle = H|\psi\rangle$$

which is governed by the Hamiltonian H corresponding to the energy of the system. The operator can be split into two parts $H = H_0 + H_1$, where H_0 is time-independent and H_1 is the time-dependent part that allows us to manipulate the system's state. To investigate the dynamics induced by H_1 it is useful to change into the so-called *interaction picture*. In this way, the evolution driven by the interaction-energy is separated from the time evolution of the unperturbed system. An interaction Hamiltonian H_{int} is derived via the transformation

$$H_{\text{int}} = U_0^\dagger H_1 U_0,$$

where $U_0 = e^{-iH_0t/\hbar}$ is the time evolution operator of the time-independent part of the Hamiltonian. Appendix B.2 lists a few relations that are useful in simplifying the ensuing calculations. With knowledge of H_{int}, the time-evolved state following an interaction $U_I = e^{-iH_{\text{int}}t/\hbar}$ can now simply be calculated as

$$|\psi(t)\rangle = U_0 U_I U_0^\dagger |\psi(0)\rangle\,.$$

Interaction Hamiltonians H_{int} and the corresponding unitary matrices U derived in the following sections always follow the principle outlined above.

2.3.2. Two-level atom interacting with a laser beam

In the following, a two-level atom encoding a qubit (or pseudo-spin-1/2) is interacting with a laser beam described by an electrical field $E = E_0\cos(\omega_l t + \phi_l)$ with frequency ω_l and phase ϕ_l. The goal of this section is to illustrate how the resulting interactions allow us to practically implement the single qubit gates introduced in Section 2.1.1.

The energy of the bare two-level atom is described by the Hamiltonian

$$H_a = \frac{\hbar\omega_0}{2}\sigma_z, \tag{2.12}$$

where $\hbar\omega_0$ is the energy difference between the two eigenstates $|\uparrow\rangle = |+\rangle_z$ and $|\downarrow\rangle = |-\rangle_z$ of the Pauli operator σ_z (cf. Section 2.1.1)[8]. The perturbation introduced by a light field (close to resonance) applied for time t leads to spin flips between the two states (cf. Eq. (2.6)) induced by the interaction energy described by the Hamiltonian

$$H_l = \hbar\Omega\sigma_x\cos(\omega_l t + \phi_l),$$

where the Rabi frequency $\Omega \propto E_0$ (see Section 2.3.3 below) represents the coupling strength between the field and the atom. With the overall Hamiltonian $H = H_a + H_l$, a transformation to an interaction picture with respect to H_a yields

$$H_{\text{int}} = \hbar\frac{\Omega}{2}\Big(\cos(\Delta\,t + \phi_l)\sigma_x + \sin(\Delta\,t + \phi_l)\sigma_y\Big),$$

where $\Delta = \omega_l - \omega_0$ is the detuning of the laser frequency from the atomic transition. Here, a *rotating wave approximation* has been performed, dropping sum frequency terms $\{(\omega_l + \omega_0)\,t\}$ that oscillate much faster than the time scale given by the induced dynamics. Using the electronic raising and lowering operators $\sigma_\pm = (\sigma_x \pm i\sigma_y)/2$ and trigonometric identities (Appendix B.4) the Hamiltonian can be rewritten as

$$H_{\text{int}} = \hbar\frac{\Omega}{2}\Big(e^{-i(\Delta t+\phi_l)}\sigma_+ + e^{i(\Delta t+\phi_l)}\sigma_-\Big). \tag{2.13}$$

A laser beam on resonance ($\Delta = 0$) then implements the unitary operation

$$U(\theta,\phi_l) = \exp\left(-i\frac{H_{\text{int}}t}{\hbar}\right) = \begin{pmatrix} \cos\frac{\theta}{2} & -ie^{-i\phi_l}\sin\frac{\theta}{2} \\ -ie^{i\phi_l}\sin\frac{\theta}{2} & \cos\frac{\theta}{2} \end{pmatrix}, \tag{2.14}$$

in which one can immediately recognize the rotation described by Eq. (2.5). Here, $\theta = \Omega t$ corresponds to the *pulse area*, i.e. how far the state vector $|\psi\rangle$ is being rotated in time t, and the optical phase of the light wave ϕ_l determines the axis of rotation in the equatorial plane of the Bloch sphere (cf. Section 2.1.1).

---

[8] This definition of H_a follows from setting the zero energy value to be in the middle of the two qubit levels.

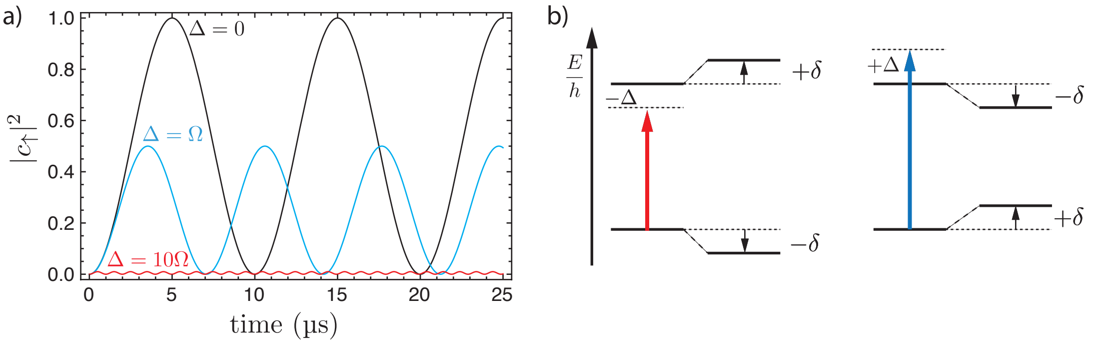

Figure 2.4.: Rabi oscillations and AC Stark shifts.
a) Rabi oscillations for $\Omega = 2\pi \times 100\,\mathrm{kHz}$ and different detunings Δ from the atomic transition frequency. The curves follow Eq. (2.15) given below. **b)** Energy level shifts induced by a negative and positive detuning with respect to the atomic transition frequency.

The oscillating electric field of the resonant laser beam leads to a continuous exchange between the probability amplitudes (populations) of both states $|c_\uparrow|^2$ and $|c_\downarrow|^2$ at the Rabi frequency Ω. While a higher electric field amplitude of the laser beam leads to faster *Rabi oscillations*, their effective amplitude and frequency depends on the laser detuning. From a solution of the optical Bloch equations [45, 46] one can obtain an expression for the probability $|c_\uparrow|^2$ of finding the atom in the excited state $|\uparrow\rangle$ as a function of the time t the laser field is applied for to an atom initially in $|\downarrow\rangle$:

$$p_\uparrow = |c_\uparrow|^2 = \frac{\Omega^2}{\Omega^2 + \Delta^2} \sin^2\left(\frac{1}{2}\sqrt{\Omega^2 + \Delta^2}\, t\right). \tag{2.15}$$

The oscillations follow an effective Rabi frequency $\Omega_{\mathrm{eff}} = \sqrt{\Omega^2 + \Delta^2}$ at a reduced amplitude $\propto 1/\Omega_{\mathrm{eff}}^2$ (Figure 2.4.a). For detunings $\Delta \gg \Omega$ the population exchange is largely suppressed but one is still left with a shift of the energy levels due to the presence of the oscillating electric field. In order to see the magnitude of this *dynamical or AC Stark shift*, it is convenient to change into a different interaction picture with respect to the frequency of the applied laser field. By expressing the perturbation introduced by the light field as $H_l = -\frac{\Delta}{2}\sigma_z + \Omega\sigma_x \cos(\omega_l t)$ a transformation with $U_0 = \exp(-i\omega_l t \sigma_z/2)$ followed by a rotating wave approximation yields

$$H_{\mathrm{int}} = -\frac{\Delta}{2}\sigma_z + \frac{\Omega}{2}\sigma_x = \begin{pmatrix} -\Delta/2 & \Omega/2 \\ \Omega/2 & \Delta/2 \end{pmatrix}.$$

The eigenvalues $\lambda_{\pm} = \pm\frac{1}{2}\sqrt{\Delta^2 + \Omega^2}$ of the Hamiltonian above are obtained from setting $|H_{\text{int}} - \lambda\mathbb{1}| = 0$ and correspond to energy levels shifted by

$$\delta = \lambda_{\pm} - \lambda_{\pm}(\Omega = 0) = \pm\frac{\Omega^2}{4\Delta}.$$

The detuning Δ determines the sign of δ for the individual levels (as illustrated in Figure 2.4.b) such that the overall shift of the atomic transition amounts to

$$\Delta_{\text{AC}} = -\frac{\Omega^2}{2\Delta}.$$

To arrive at the effective Hamiltonian for large detunings one can start at Eq. (2.13) and take a shortcut following the approach of reference [47]. Here, the time average over a period $T \gg 2\pi/\Delta$ neglects the rapidly oscillating terms yielding the simple formula

$$H_{\text{eff}} = \frac{1}{\hbar\Delta}\left[\sigma_-, \sigma_+\right] = \frac{\hbar\,\delta_{\text{AC}}}{2}\sigma_z.$$

The corresponding unitary evolution under this Hamiltonian is then given by

$$U(\delta_{\text{AC}}) = \exp\left(-i\frac{H_{\text{eff}}t}{\hbar}\right) = \begin{pmatrix} \exp(-i\frac{\delta_{\text{AC}}}{2}t) & 0 \\ 0 & \exp(i\frac{\delta_{\text{AC}}}{2}t) \end{pmatrix}, \tag{2.16}$$

in which the remaining single qubit rotation of Eq. (2.4) can immediately be recognized.

2.3.3. Rabi frequency

For the Rabi frequency Ω introduced above there are two different conventions in use throughout the literature. Following the first convention, which this text will adhere to, Ω corresponds to the (angular) frequency at which population is exchanged between the ground and excited state of the two-level system such that for every time $t = \pi/\Omega$ a spin flip occurs (cf. Figure 2.4.a). The alternative definition $\Omega' = \Omega/2$ corresponds to the frequency at which the wave function $\Psi(\mathbf{r}, t)$ or state vector $|\Psi\rangle$ returns to its initial value (which accounts for the global phase factor, cf. Eq. (2.6)).

In the case of the optical qubit encoded in $^{40}\text{Ca}^+$ (Section 2.2) the coupling mechanism between a light field and the electronic state is based on the interaction of the atomic quadrupole moment Q with the gradient of the electric field $H_I = Q \cdot \nabla E(t)$. The value of the Rabi frequency can then be calculated from the expression [48, 49]

$$\Omega = \frac{eE_0}{2\hbar}\sqrt{\frac{15}{c\alpha_0}\frac{\Gamma(\mathrm{D}_{5/2})}{k^3}}\,\Lambda(m,m')\,g_{\Delta m_j}, \tag{2.17}$$

where c is the speed of light, α_0 the fine structure constant, Γ the linewidth of the excited qubit state, k the absolute value of the light beam's wave vector and $\Lambda(m,m')$ is the Clebsch-Gordan coefficient (given in Table 2.3 below) of the chosen transition. The term $g_{\Delta m_j}$ [48–50] accounts for geometrical factors in respect to the angle between the laser beam and the magnetic field quantization axis as well as the light polarization when considering a specific transition $\Delta m_j = |m' - m|$ (see also Figure 4.5).

Table 2.3.: Clebsch-Gordan coefficients $\Lambda(m,m')$ for the $^{40}\mathrm{Ca}^+$ quadrupole transition $|\mathrm{S}_{1/2}, m_j = 1/2\rangle \leftrightarrow |\mathrm{D}_{5/2}, m_j = m'\rangle$ (for $|\mathrm{S}_{1/2}, m_j = -1/2\rangle$ exchange $m_j' \to -m_j'$).

m'	-3/2	-1/2	1/2	3/2	5/2
$\Lambda(1/2, m')$	$\sqrt{1/5}$	$\sqrt{2/5}$	$\sqrt{3/5}$	$\sqrt{4/5}$	1

2.3.4. Quantum harmonic oscillator and coherent states

Laser cooling techniques (Section 4.2) allow us to reduce the energy of an ion confined in a linear Paul trap (Section 3.1) to a regime in which a quantized description of its motional energy becomes warranted. This section introduces the quantum harmonic oscillator, coherent states and the operators acting on both, which will be fundamental to the description of the light-matter interaction in ion traps discussed in the following. Coherent states in the context of the quantum harmonic oscillator are treated in textbooks [45, 51] and the well-readable original paper by Roy Glauber [52].

The prime example of a classical harmonic oscillator is a particle of mass m moving in a 1D quadratic potential $V(x_c) = m\omega^2 x_c^2/2$, where x_c is the position coordinate and ω is its (angular) oscillation frequency within the potential. Like any harmonic motion, the oscillation can be described in the complex plane of phase space, where the oscillator's state traces out a circle following the relation $\alpha_c(t) = |\alpha_c|\,e^{i\omega t}$, with $\alpha_c = x_c + ip_c$ and momentum coordinate p_c.

Moving to a quantum mechanical description, x_c and p_c are replaced by operators $\hat{x}$ and $\hat{p}$. Analog to the classical case, the total energy of the particle is given by the sum of its kinetic and potential energy in the form of Hamiltonian

$$H_{\text{h.o.}} = \frac{\hat{p}^2}{2m} + \frac{1}{2}m\omega^2\hat{x}^2. \tag{2.18}$$

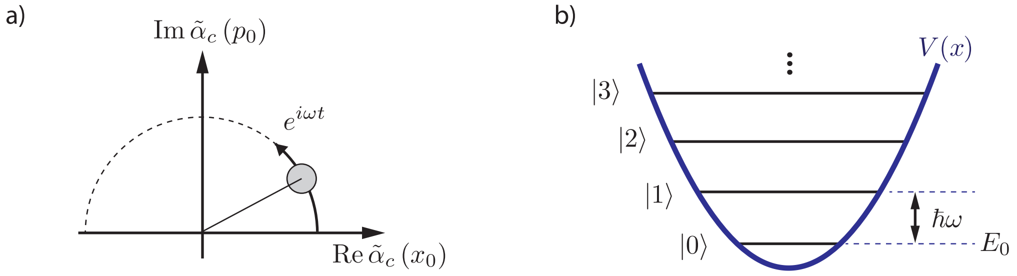

Figure 2.5.: Graphical descriptions of a harmonic oscillator
a) Motion of an excited harmonic oscillator in phase space (normalized). A full oscillation corresponds to a full circle in phase space, only half of which is shown. **b)** The quantized states of a quantum harmonic oscillator with ground state energy $E_0 = \hbar\omega/2$ form an equidistant ladder of energy levels.

Introducing the creation and annihilation operators

$$a^\dagger = \sqrt{\frac{m\omega}{2\hbar}}\Big(\hat{x} - \frac{i}{m\omega}\,\hat{p}\Big) \quad \text{and} \quad a = \sqrt{\frac{m\omega}{2\hbar}}\Big(\hat{x} + \frac{i}{m\omega}\,\hat{p}\Big) \tag{2.19}$$

the position and momentum operators can be expressed as

$$\hat{x} = (a + a^\dagger)\,x_0 \qquad \text{and} \qquad \hat{p} = i(a^\dagger - a)\frac{\hbar}{2x_0}, \tag{2.20}$$

where $x_0 = \sqrt{\hbar/(2m\omega)}$ defines a characteristic length scale for the harmonic oscillator.[9] For a $^{40}\mathrm{Ca}^+$ ion oscillating in a harmonic potential at frequency $\omega = (2\pi) \times 1.23\,\mathrm{MHz}$, its value is close to 10 nm and corresponds to the RMS spatial extent of the ion's ground state wave function.
Using the operators a and $a^\dagger$ defined above, Eq. (2.18) can now be cast into its familiar form

$$H_{\mathrm{h.o.}} = \hbar\omega\Big(a^\dagger a + \frac{1}{2}\Big) = \hbar\omega\Big(\hat{N} + \frac{1}{2}\Big).$$

The states $|n\rangle$ illustrated in Figure 2.5.b are called *Fock*[10] *or number states*. They are simultaneous eigenstates of $H_{\mathrm{h.o.}}$ and the *number operator* $\hat{N} = a^\dagger a$ whose eigenvalues $n \in \mathbb{N}$ correspond to the number of motional excitations (phonons) present in the oscillator. Their ground state $|0\rangle$ with $n = 0$ and energy $E_0 = \hbar\omega/2$ is the starting point of an equally spaced ladder of states.

---

[9] Analogously, the characteristic momentum scale is given by $p_0 = \sqrt{(m\omega\hbar)/2}$. These natural units allow us to work with normalized amplitudes $\tilde{\alpha}_c = x/(2x_0) + ip/(2p_0)$ in phase space.

[10] Vladimir Fock, Soviet physicist (1898-1974)

As the name suggests, the application of creation and annihilation operators to a given state $|n\rangle$ raises or lowers its energy by one phonon, respectively:

$$\begin{aligned} a^\dagger |n\rangle &= \sqrt{n+1}\, |n+1\rangle \\ a\, |n\rangle &= \sqrt{n}\, |n-1\rangle\,, \quad \text{with} \quad a\,|0\rangle = 0. \end{aligned}$$

All Fock states $|n\rangle$ can be created by repeatedly applying the creation operator to the ground state

$$|n\rangle = \frac{1}{\sqrt{n!}}(a^\dagger)^n\, |0\rangle\,.$$

The closest quantum mechanical analogy to an excited motional state of a classical harmonic oscillator presents itself in the form of a coherent state $|\alpha\rangle$. The following illustrates how such a state can be created by the action of an oscillating force.

The application of a time-dependent force

$$F(t) = A\sin(\omega_d t + \phi_d) = \frac{A}{2i}[e^{i(\omega_d t+\phi_d)} - e^{-i(\omega_d t+\phi_d)}]$$

of amplitude A, (drive) frequency ω_d and phase ϕ_d to the quantum harmonic oscillator leads to an additional interaction energy corresponding to $H_i(t) = -\hat{x}F(t)$ and the new Hamiltonian $H = H_{\text{h.o.}} + H_i(t)$. Just like in the previous section, the effect of the perturbation introduced by the oscillating force can be separated out by going to an interaction picture via the transformation $U = \exp(-iH_{\text{h.o.}}t/\hbar)$. The interaction Hamiltonian then is given by

$$H_{\text{int}} = (ae^{-i\omega t} + a^\dagger e^{i\omega t})\, x_0 F(t)$$

where Equations (B.7) and (B.8) from Appendix B.2 have been used in the transformation. For a drive frequency resonant with the eigenfrequency of the oscillator ($\omega_d = \omega$) and omitting the sum frequency terms (rotating wave approximation), the Hamiltonian reduces to

$$H_{\text{int}} = \frac{Ax_0}{2i}(ae^{i\phi_d} + a^\dagger e^{-i\phi_d}). \tag{2.21}$$

It is worth pointing out the similarity to the on-resonance case of Eq. (2.13), clearly illustrating the analogy between $\sigma_\pm$ and the annihilation and creation operators $a, a^\dagger$ introduced above.

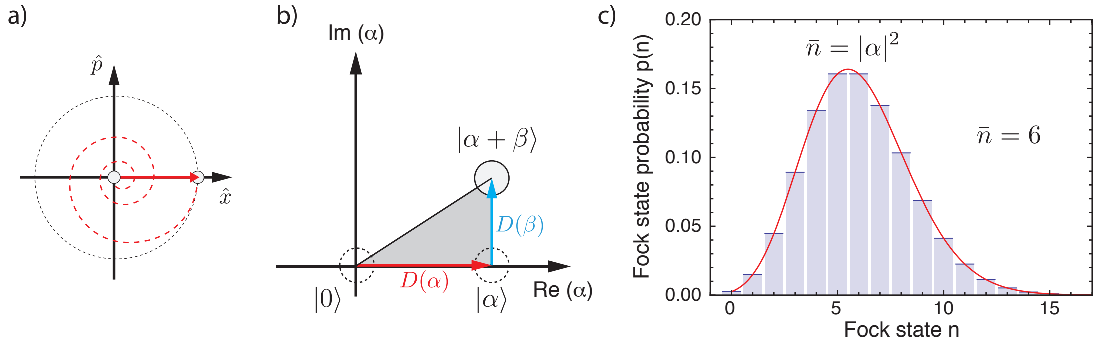

Figure 2.6.: Coherent state in phase space and Fock space
a) Phase space picture of a resonantly driven harmonic oscillator initially at rest. The state vector rotates counter-clockwise while growing in amplitude. Once the drive stops, the state continues to move on a circular trajectory around the origin at frequency ω. **b)** Phase space picture in a frame co-rotating at frequency ω. Displacement of the motional ground state $|0\rangle$ creates a coherent state $|\alpha\rangle$. A subsequent displacement (resonant but with phase $\phi_D = \pi/2$) creates a new coherent state $|\alpha + \beta\rangle$. All coherent states, including the ground state, are represented by a disc corresponding to a Gaussian wave packet of minimum uncertainty that retains its shape over time. **c)** Fock space representation of a coherent state with an amplitude of $\alpha = \sqrt{6}$.

By defining a complex, dimensionless[11] amplitude

$$\alpha = e^{-i\phi_d} A x_0 t/(2\hbar) \tag{2.22}$$

the corresponding unitary evolution $U = \exp(-iH_{\text{int}}t/\hbar)$ can now be written in terms of the *displacement operator*

$$D(\alpha) = e^{\alpha a^\dagger - \alpha^* a}. \tag{2.23}$$

Applied to the harmonic oscillator ground state $|0\rangle$, it creates a displaced *coherent state*

$$|\alpha\rangle \;=\; D(\alpha)\,|0\rangle \;=\; \sum_n \underbrace{e^{-|\alpha|^2/2}\frac{\alpha^n}{\sqrt{n!}}}_{c_n}|n\rangle\,, \tag{2.24}$$

Its Fock state probability amplitudes $p_\alpha(n) = |c_n|^2$ follow a Poisson distribution with average phonon number $\bar{n} = |\alpha|^2$ and variance $\sqrt{\bar{n}}$ as illustrated in Figure 2.6.c. Just like the oscillator's wave packet, the distribution retains its shape over time. Here, the transition from the quantum to the well localized classical harmonic oscillator can be seen for large values of $n \to \infty$ as the dispersion ratio $\sqrt{\bar{n}}/\bar{n}$ goes to zero.

---

[11] To see this, recall that $[A] = \mathrm{N}$, $[x_0] = \mathrm{m}$, $[t] = \mathrm{s}$ and $[\hbar] = \mathrm{J \cdot s} = \mathrm{N \cdot m \cdot s}$.

Using Eq. (B.15) one can see that two consecutive displacements

$$D(\alpha)D(\beta) = D(\alpha+\beta)e^{\frac{1}{2}(\alpha\beta^* \ -\alpha^*\beta)} = D(\alpha+\beta)e^{i\,\mathrm{Im}\{\alpha\beta^*\}} \tag{2.25}$$

are additive up to a phase factor (corresponding to the grey shaded area in Figure 2.6.b). Their respective direction in phase space is determined by the phase relationship between the harmonic oscillator and the driving force given by ϕ_d in Eq. (2.22).

2.4. Hamiltonian of the laser–ion interaction

Combining the previous discussions of the two-level atom and the harmonic oscillator model, the following section derives a description for the interaction of a trapped ion with a coherent laser beam [see 13, and references therein].

The unperturbed system is governed by the Hamiltonian $H_0 = \frac{\hbar\omega_0}{2}\sigma_z + \hbar\omega_t\left(a^\dagger a + \frac{1}{2}\right)$, where ω_t is the ion's oscillation frequency in the trapping potential and ω_0 the bare atomic transition frequency. Since the ion is now trapped, the phase of an incident light field depends on the ion's changing position. In the ion's rest frame, the Doppler shift caused by its motion results in a frequency modulation of the incoming laser light. As a result, the appearance of corresponding motional sideband transitions at $\omega_0 \pm \omega_t$ allows for a joint manipulation of the ion's internal ("spin") and external (motional) degrees of freedom, now described by the ladder-like state space of Figure 2.7.a.

To formally describe the interaction between laser and trapped ion, Eq. (2.13) has to be modified by an additional term $\exp(ik\hat{x}) = \exp\{i\eta(a+a^\dagger)\}$ which yields

$$H_1 = \hbar\frac{\Omega}{2}(\sigma_+ + \sigma_-)\left(e^{i\eta(a+a^\dagger)}e^{-i(\omega_l t-\phi_l)} + e^{-i\eta(a+a^\dagger)}e^{i(\omega_l t-\phi_l)}\right).$$

Here, the Lamb-Dicke factor

$$\eta = kx_0\cos\theta = k\sqrt{\frac{\hbar}{2m\omega_t}}\cos\theta, \tag{2.26}$$

accounts for the ratio of the ion's (confinement-dependent) ground state wave packet size x_0 and the laser's wavelength $\lambda = 2\pi/k$ as well as its angle θ with respect to the ion's direction of motion.

In the transformation to an interaction picture with respect to H_0, Eq. (B.6) helps to simplify the first bracketed term, Eq. (B.9) the second. Following a rotating wave

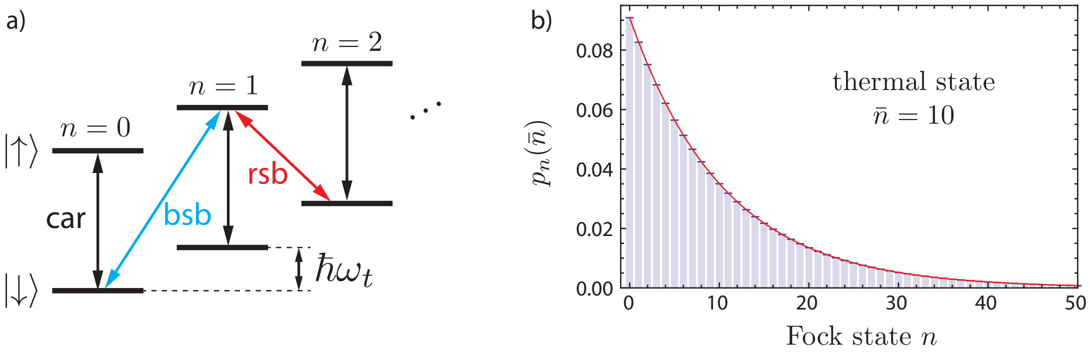

Figure 2.7.: Fock space ladder of states and thermal distribution
a) Ladder of joint spin-motional states ($|\psi\rangle \otimes |n\rangle$) offset in energy by multiples of the motional trap frequency ω_t and connected via *carrier* (car), red (rsb) and blue (bsb) sideband transitions. **b)** Thermal distribution of Fock states for a mean phonon number of $\bar{n} = 10$.

approximation (ignoring sum frequency terms at optical frequencies) one arrives at

$$H_{\text{int}} = \hbar\frac{\Omega}{2}\left(e^{-i(\Delta t-\phi_l)}\sigma_+ \exp\left\{i\eta\left(a\,e^{-i\omega_t t} + a^\dagger\,e^{i\omega_t t}\right)\right\} + h.c.\right), \tag{2.27}$$

where $\Delta = \omega_l - \omega_0$ is the laser detuning and $h.c.$ refers to the hermitian conjugate.

The interaction Hamiltonian can be simplified further under the assumption that the ion's motional wave packet is confined to an extent x_0 much smaller than the light's wavelength. This *Lamb-Dicke approximation* holds as long as $\eta^2(2\bar{n}+1) \ll 1$, where $\bar{n}$ is the mean number of phonons in the harmonic oscillator[12]. In this case, the exponential can be Taylor-expanded to

$$\exp\left\{i\eta\left(a\,e^{-i\omega_t t} + a^\dagger\,e^{i\omega_t t}\right)\right\} = \mathbb{1} + i\eta\left(a\,e^{-i\omega_t t} + a^\dagger\,e^{i\omega_t t}\right) + \mathcal{O}(\eta^2). \tag{2.28}$$

In typical situations with $\bar{n} < 20$, one can neglect the higher order terms $\mathcal{O}(\eta^2)$ and approximate Eq. (2.27) by

$$H_{\text{int}} = \hbar\frac{\Omega}{2}\left(e^{-i(\Delta t-\phi_l)}\sigma_+\left\{\mathbb{1} + i\eta\left(a\,e^{-i\omega_t t} + a^\dagger\,e^{i\omega_t t}\right)\right\} + h.c.\right). \tag{2.29}$$

An ion's motional state after laser cooling is given by a thermal distribution with a mean phonon number of $\bar{n}$ (Figure 2.7.b) following

$$p_n(\bar{n}) = \left(\frac{\bar{n}}{\bar{n}+1}\right)^n. \tag{2.30}$$

---

[12] This is usually satisfied at the end of Doppler laser cooling with $\bar{n} \approx 10-20$ (cf. Section 4.2).

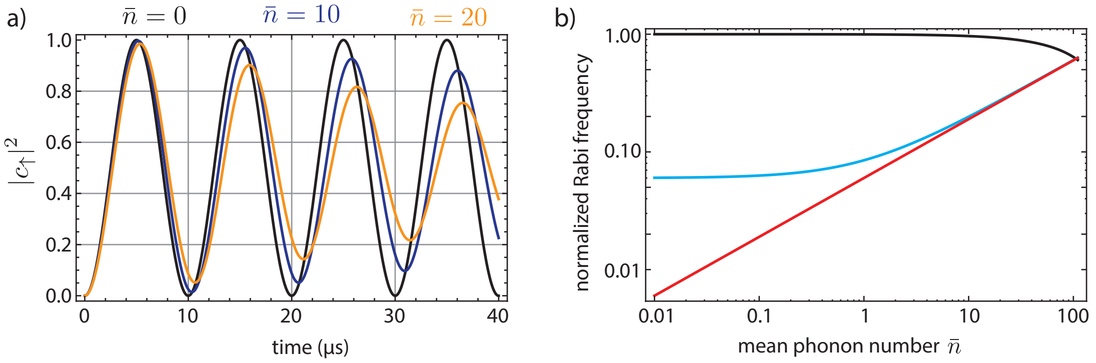

Figure 2.8.: Relative coupling strength as a function of $\bar{n}$
a) Rabi oscillations on a carrier transition with $\Omega_0 = 2\pi \times 100\,\text{kHz}$ for a range of mean phonon numbers reachable by Doppler and resolved sideband cooling. **b)** Normalized coupling strength of the carrier and first order motional transitions for $\eta = 0.06$.

Consequently, Rabi oscillations

$$|c_\uparrow|^2 = \sum_{n=0}^{\infty} p_n(\bar{n}) \sin^2\left(\frac{\Omega(n)}{2}t\right), \text{ where } \Omega(n) = (1-\eta^2 n)\Omega_0, \tag{2.31}$$

now have frequency components $\Omega(n)$ whose weight corresponds to the motional state distribution. The result is a damping of the oscillation around the steady-state average of 0.5 at a rate proportional to $\bar{n}$ (Figure 2.8.a), which can be used to assess the quality of Doppler cooling.

Provided one operates in the *resolved sideband limit* ($\Omega \ll \omega_t$), one can perform a second rotating wave approximation in Eq. (2.29) neglecting terms oscillating at ω_t. Taking the fundamental coupling strength (at $\bar{n} = 0$) to be Ω_0, one can now distinguish three cases corresponding to the transitions marked in Figure 2.7.a:

- For a resonant laser beam ($\Delta = 0$) one finds

$$H_{\text{car}} = \hbar\frac{\Omega_n}{2}\left(e^{i\phi_l}\sigma_+ + e^{-i\phi_l}\sigma_-\right), \tag{2.32}$$

which couples $|\downarrow, n\rangle \leftrightarrow |\uparrow, n\rangle$ and is called *carrier* transition as it leaves the motional state unchanged ("car" in Figure 2.7.a). The coupling strength is given as $\Omega_n = (1-\eta^2 n)\,\Omega_0$. Here, a second order term in Eq. (2.28) has been included, which is responsible for the damping of the Rabi oscillations seen in Figure 2.8.a.

- The second case is the *red motional sideband* transition at negative laser detuning $\Delta = -\omega_t$ which couples $|{\downarrow}, n\rangle \leftrightarrow |{\uparrow}, n-1\rangle$ at rate $\Omega_{n,n-1} = \eta\sqrt{n}\,\Omega_0$ according to

$$H_{\text{rsb}} = i\hbar\eta\frac{\Omega_{n,n-1}}{2}\left(e^{i\phi_l}a\sigma_+ - e^{-i\phi_l}a^\dagger\sigma_-\right). \tag{2.33}$$

- Lastly, the *blue motional sideband* at positive detuning $\Delta = +\omega_t$ is described by

$$H_{\text{bsb}} = i\hbar\eta\frac{\Omega_{n,n+1}}{2}\left(e^{i\phi_l}a^\dagger\sigma_+ - e^{-i\phi_l}a\sigma_-\right), \tag{2.34}$$

  coupling $|{\downarrow}, n\rangle \leftrightarrow |{\uparrow}, n+1\rangle$ with coupling strength $\Omega_{n,n+1} = \eta\sqrt{n+1}\,\Omega_0$.

As Figure 2.8.b illustrates in a log-log plot, in the limit of small mean phonon numbers $\bar{n} \lesssim 1$ the blue sideband coupling strength barely depends on the phonon population. Here, the ratio of red and blue sideband strength provides a good measure of $\bar{n}$.

2.5. Bichromatic light field

Two superimposed laser fields at positive and negative detuning $\pm\Delta$ from a common center frequency, respectively, produce a bichromatic light field. Their phase-coherent addition effectively results in a light beam at the common center frequency that is amplitude modulated at the absolute value of their frequency difference (Figure 2.9).

To arrive at a laser-ion interaction Hamiltonian describing this case, one can consider an ion simultaneously excited on the blue and red sideband. With their coupling strengths made equal ($\Omega = \Omega_{n,n-1} = \Omega_{n,n+1}$) simply summing up Equations (2.33) and (2.34) yields the Hamiltonian

$$H_{\text{bic}} = i\hbar\eta\frac{\Omega}{2}\left\{\left(e^{i\phi_r}a\sigma_+ + e^{-i\phi_r}a^\dagger\sigma_-\right) + \left(e^{i\phi_b}a^\dagger\sigma_+ + e^{-i\phi_b}a\sigma_-\right)\right\},$$

where ϕ_b and ϕ_r are the respective phases of the light fields blue and red detuned by ω_t, respectively. This expression can be recast into the more convenient form

$$H_{\text{bic}} = \hbar\eta\frac{\Omega}{2}\left(\sigma_x\cos\phi_+ - \sigma_y\sin\phi_+\right)\left((a+a^\dagger)\cos\phi_- + i(a^\dagger - a)\sin\phi_-\right), \tag{2.35}$$

where

$$\phi_+ = \frac{\phi_b+\phi_r}{2} + \frac{\pi}{2} \quad \text{and} \quad \phi_- = \frac{\phi_b-\phi_r}{2}$$

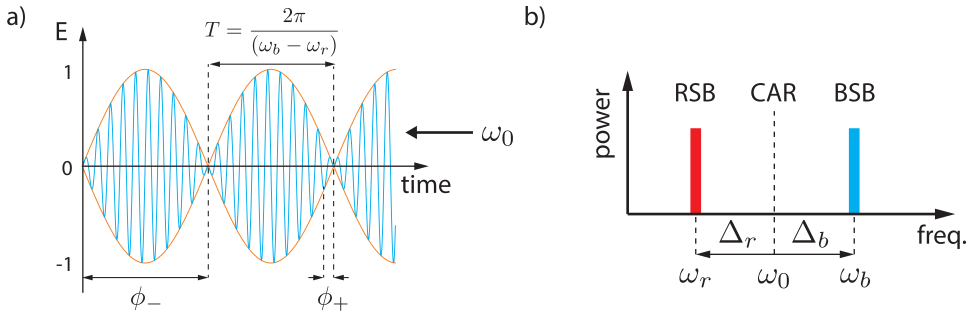

Figure 2.9.: Bichromatic light field.
a) Electric field of a bichromatic light field from two beams of equal amplitude. The time domain is fully characterized by an amplitude modulation at the beat frequency ($1/T$) and the sum- and difference phases ϕ_+ and ϕ_- of the two components. **b)** Spectral power density. In the frequency domain, equal powers in both components provide a perfect cancellation of the intermediate carrier (CAR) frequency at ω_0 maintaining all the power in the components resonant with the blue (BSB) and red (RSB) sidebands at detuning $\Delta_{b,r}$.

are the sum and difference of the phases of the two fields and the prefactor i has been lumped into ϕ_+. As opposed to the pairwise coupling on the individual sidebands the bichromatic Hamiltonian H_{bic} couples all Fock states

$$|{\uparrow},0\rangle \leftrightarrow |{\downarrow},1\rangle \leftrightarrow |{\uparrow},2\rangle \ldots \text{ and}$$
$$|{\downarrow},0\rangle \leftrightarrow |{\uparrow},1\rangle \leftrightarrow |{\downarrow},2\rangle \ldots$$

shown in Figure 2.7.a simultaneously. It effectively realizes an oscillating force resonantly driving the harmonic oscillator that describes the ion's motional state. In this case, however, the force is *spin dependent* and acts differently on the two electronic eigenstates selected by the sum-phase ϕ_+ (Figure 2.9.a). Both eigenstates of Eq. (2.35) lie in the equatorial plane of the Bloch sphere (cf. Figure 2.1) and are displaced in opposite directions in phase space, where the principal direction is determined by the difference phase ϕ_- (analog to ϕ_d in Eq. (2.21) before).

2.5.1. Coherent displacements

For the specific choice of $\phi_+ = \phi_- = 0$, Eq. (2.35) reduces to

$$H_{\text{bic}} = \hbar\eta\frac{\Omega}{2}\sigma_x(a + a^\dagger), \tag{2.36}$$

with the two eigenstates $|+\rangle_x$ and $|-\rangle_x$.

Here one can distinguish two interesting cases:

- If a bichromatic pulse of duration t is applied to the initial state $|\psi\rangle = |+\rangle_x |0\rangle$, where $|0\rangle$ is the coherent ground state of the harmonic oscillator, a displaced coherent state is created

  $$|\psi(t)\rangle = e^{-iH_{\mathrm{bic}}t/\hbar} |\psi\rangle = |+\rangle_x D\left(-i\frac{\eta\Omega t}{2}\right) |0\rangle \equiv |+\rangle_x |\alpha\rangle$$

  in which, recalling that $\eta = kx_0$, one can recognize the displacement operator $D(\alpha)$ of Eq. (2.23) with $\phi_d = \pi/2$.

- The ground state $|\psi\rangle = |\downarrow\rangle |0\rangle$ can be rewritten as $|\psi\rangle = \frac{1}{\sqrt{2}} (|+\rangle_x - |-\rangle_x) |0\rangle$ using a superposition of the electronic eigenstates $|\pm\rangle_x$ of the displacement operator D. Here, the application of a bichromatic light pulse creates a *motional Schrödinger cat state*

  $$|\psi(t)\rangle = \frac{1}{\sqrt{2}} (|+\rangle_x |\alpha\rangle - |-\rangle_x |-\alpha\rangle) , \tag{2.37}$$

  corresponding to a superposition of two coherent states $|\pm\alpha\rangle$ that are maximally entangled with the internal qubit states $|\pm\rangle_x$.

2.5.2. Mølmer-Sørensen interaction creating entanglement

If the respective detuning of the bichromatic components is increased by an amount δ to $\Delta = \pm(\omega_t + \delta)$, the result is a state evolution corresponding to an off-resonantly driven harmonic oscillator. Just like in the classical case, under the application of such a Hamiltonian, a quantum harmonic oscillator initially at rest will return to its original state at multiples of time $t = 2\pi/|\delta|$.

This type of interaction was first investigated by A. Sørensen and K. Mølmer as well as E. Solano [53–55] and allows us to create entanglement in a string of N ions sharing a common motional mode. The details of the Mølmer-Sørensen gate operation and its application to trapped ions have been thoroughly covered in [56, 57]. Here, only a brief summary of the most important features for the simplest case of two ions is provided.

Due to the additional detuning δ, the light phases ϕ_l of the blue and red motional sidebands in Eq. (2.33) and Eq. (2.34) become time-dependent resulting in $\phi_r = \phi_r(0) - \delta t$ and $\phi_b = \phi_b(0) + \delta t$, respectively. In the bichromatic Hamiltonian given in Eq. (2.35) the time-dependence is only relevant in the difference phase $\phi_- = (\phi_r(0) - \phi_b(0))/2 - \delta t$.

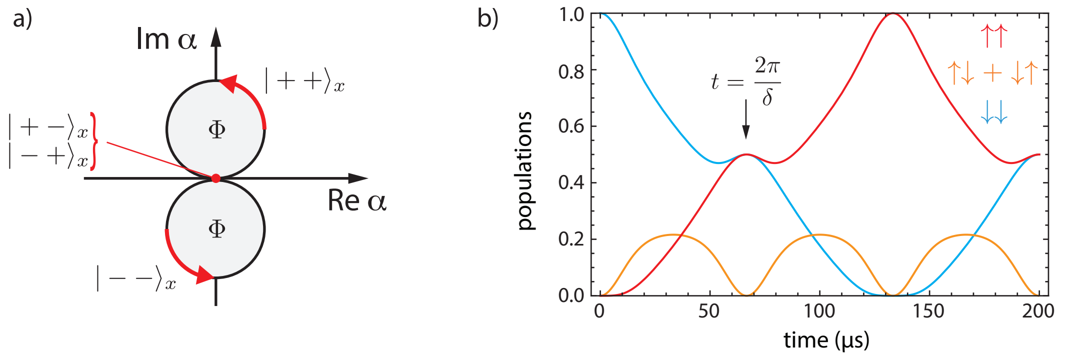

Figure 2.10.: Mølmer-Sørensen gate operation.
a) Phase space picture of the gate operation. The electronic eigenstates $|{+}{+}\rangle_x$ and $|{-}{-}\rangle_x$ of the two ions are displaced on a trajectory following a circle of radius $\propto \eta\Omega/\delta$ that closes every $t_{\text{gate}} = 2\pi/|\delta|$. The geometric phase Φ imprinted on the state corresponds to the enclosed area. The electronic eigenstates $|{+}{-}\rangle_x$ and $|{-}{+}\rangle_x$ (red dot at the origin) do not couple to the motion. **b)** Numerical simulation of the population evolution for $\delta = 2\pi \times 15\,\text{kHz}$. A maximally entangled state is created after $t_{\text{gate}} \approx 66\,\mu\text{s}$. Note that these correlations appear in the z-basis and not the x-basis depicted in (a).

Consequently, the Mølmer-Sørensen interaction is described by

$$\begin{aligned} H_{\text{MS}} &= \hbar\eta\Omega' \left(\sigma_x^{(1)} + \sigma_x^{(2)}\right) \left((a^\dagger + a)\cos\delta t - i(a^\dagger - a)\sin\delta t\right) \\ &= \hbar\eta\Omega' \left(\sigma_x^{(1)} + \sigma_x^{(2)}\right) \left(a^\dagger e^{-i\delta t} - a e^{i\delta t}\right), \end{aligned} \tag{2.38}$$

where it was assumed that $\phi_r(0) = \phi_b(0) = \pi/2$.

Noting that the electronic ground state in the z-basis $|{\downarrow}\rangle\,|0\rangle = |-\rangle_z\,|0\rangle$ can be represented as a superposition in the x-basis $\frac{1}{\sqrt{2}}\left(|+\rangle_x - |-\rangle_x\right)|0\rangle$, the action of the gate operation is as follows: The two electronic states $|{+}{+}\rangle_x$ and $|{-}{-}\rangle_x$ are displaced in a direction in phase space that changes continuously with δt, while the states $|{+}{-}\rangle_x$ and $|{-}{+}\rangle_x$ remain stationary. The resulting circular trajectory shown in Figure 2.10.a can be approximated by a sum of (integral over) small consecutive displacements according to Eq. (2.25). It encloses an area in phase space that corresponds to a geometric phase [58] which is given by $\Phi(t) = (\Omega/\delta)^2(\delta t - \sin\delta t)$. States $|{+}{+}\rangle_x$ and $|{-}{-}\rangle_x$ to which the spin-dependent force couples, therefore become entangled with the driven motional degree of freedom. Whenever the N^{th} circle is closed at time $\tau_N = 2\pi N/\delta$, spin and motion become disentangled again and, while the latter has retuned to its initial state, the accumulated phase $\Phi(\tau_N) = 2\pi N(\Omega/\delta)^2\text{sgn}(\delta)$ is left in the electronic state(s).

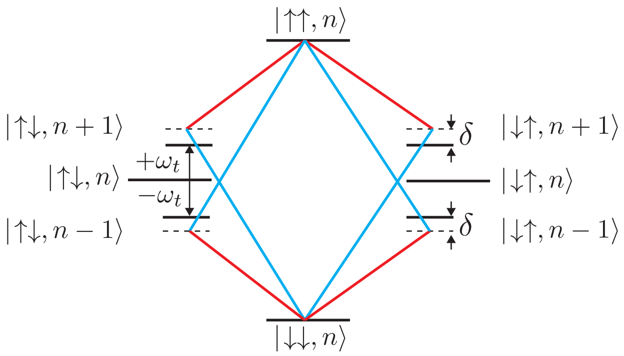

Figure 2.11.: Spin-motional manifold associated with the two-ion MS-gate operation. A bichromatic laser field with components slightly detuned by δ from the motional sidebands at ω_t connects the qubit states $|\downarrow\downarrow\rangle \leftrightarrow |\uparrow\uparrow\rangle$ via four possible paths. The motional states are denoted by $|n\rangle$ and form a joint manifold with the qubit's electronic states.

The unitary evolution induced by Eq. (2.38) can be described by

$$U_{\mathrm{MS}}(t) = D\left(\alpha(t)S_x\right)\exp\left(i\Phi(t)S_x^2\right), \tag{2.39}$$

with the time-varying displacement amplitude $\alpha(t) = i\frac{\Omega}{\delta}(1 - e^{i\delta t})$ and the global spin operator $S_x = \sigma_x^{(1)} + \sigma_x^{(2)}$, where the superscript corresponds to the ion number. It is easy to see that every $t_N = 2\pi N/|\delta|$ with $N = 1, 2, \ldots$ the displacement D vanishes, resulting in an effective spin-spin interaction $H_{\mathrm{eff}} \propto \sigma_x^{(1)} \otimes \sigma_x^{(2)}$ that leads to pairwise-correlated spin flips, i.e. spin 1 only flips if spin 2 flips at the same time.

If the Rabi frequency is set to $\Omega = \delta/(4\eta)$, Eq. (2.39) effectively realizes the entangling gate operation of Eq. (2.9) and creates at the gate time $t_{\mathrm{gate}} = 2\pi/\delta$ the maximally entangled Bell state $|\Psi\rangle = (|\uparrow\uparrow\rangle - i\,|\downarrow\downarrow\rangle)/\sqrt{2}$.

A numerical simulation of the state evolution for a detuning of $\delta = 2\pi \times 15\,\mathrm{kHz}$ is shown in Figure 2.10.b. The electronic state populations plotted arise from the time-dependent interference of the 4 possible interaction paths depicted in Figure 2.11. The population, in which only a single ion spin is flipped, disappears every t_{gate}, leaving the system either in $|\downarrow\downarrow\rangle$, $|\uparrow\uparrow\rangle$ or a Bell state.

3. Experimental setup

The experiments presented in this text have been carried out in two different linear Paul traps located at the Institute for Quantum Optics and Quantum Information (IQOQI) of the Austrian Academy of Sciences (OEAW). The laser systems and computer control were set up alongside with trap I by Jan Benhelm, Gerhard Kirchmair and others, initially to investigate $^{43}\text{Ca}^+$ as a qubit candidate. The original setup is described in detail in the corresponding theses [50, 59–61] and, to a large extent, was still used in the quantum simulation experiment described in Chapter 5. In parallel, a new linear ion trap design (trap II) was modeled and optimized, subsequently built, set up and characterized. The quantum enhanced measurement presented in Chapter 6 marked the starting point of the new setup's productive operation. All changes and additions to the physical setup and software aim at enabling future work with long(er) ion strings and have recently led to results using up to 15 particles (see Appendix A).

3.1. Ion trap

The blade design of the linear Paul traps [2] used in Innsbruck and elsewhere date back to a design by Stefan Haslwanter from the early 2000s [62] that was aimed at increasing the machining and alignment precision of the radial electrodes. The first trap built in such a way has been successfully employed at the University of Innsbruck's quantum optics laboratory in numerous experiments over the last 13 years [63–66]. The relatively large ion-electrode distances in the design lead to low heating rates (Section 4.7) and allow for good optical access with little stray light. Trap I at the IQOQI laboratory follows the same macroscopic design and is depicted in figure 3.1. The original blade trap at the university laboratory has been used to entangle strings of up to 14 ions [67]. It has only very rarely seen a chemical reaction with residual background gas in the vacuum vessel which turn a trapped atomic into an unwanted molecular ion. The (almost identical) trap I at IQOQI, however, is not able to stably confine strings of more than three ions and suffered from chemical reactions often more than twice a day.

While the exact reasons remain unknown, in 2009, efforts went underway to build a new setup to remedy these problems. Table 3.1 provides a comparison between the old and the new ion trap (again designed and manufactured by Stefan Haslwanter).

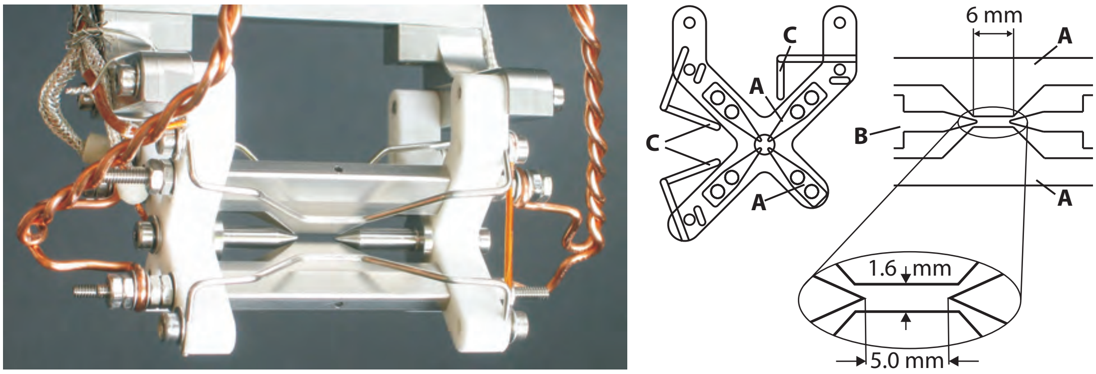

Figure 3.1.: Trap I (2006)
The ion trap consists of four blade-shaped electrodes (**A**) and two tip-shaped end-cap electrodes (**B**) made from stainless-steel that are held together by two Macor® pieces. Twisted oxygen-free high-conductivity (OFHC) copper wires deliver a radio frequency (RF) voltage to two opposite blades while the other two are held at ground potential. Kapton-insulated copper wires connect the tip (**B**) and stray-field compensation (**C**) electrodes to a high voltage feedthrough. (modified from references [50, 59])

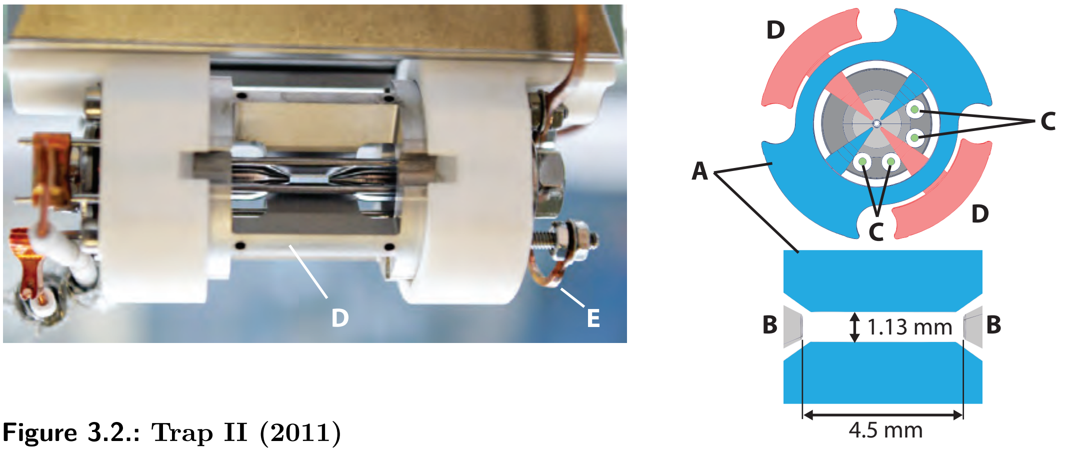

Figure 3.2.: Trap II (2011)
The tip-shaped end-caps (**B**) include a 0.5 mm diameter hole for optical access. Alignment rods used during assembly and groves machined into the Macor® holders ensure proper alignment of the ground (**A**) and RF blade (**D**) electrodes. Compensation (**C**) and tip (**B**) electrodes are connected using OFHC copper wires insulated with Macor beads. The RF blades are connected in series via a copper “bridge” (**E**). The photo, taken by M. Rambach, corresponds to the view from the W viewport in Figure 3.6.

Table 3.1.: Comparison of the two ion traps used for the experiments presented in the thesis. The efficiencies refer to Figure 3.3 on the following page and the 2D quadrupole approximation is equal to the ratio of the RF potential curvature in the (axial) z to the (radial) x,y directions.

	trap I	**trap II**	**unit**
Characteristic dimensions			
distance blade to blade	1.6	1.131	mm
distance between tip electrodes	5.0	4.5	mm
length of blades	6	4.02	mm
tip hole diameter	—	0.5	mm
Simulation results			
axial voltage conversion efficiency (η_{ax})	8.6	7.2	%
radial voltage conversion efficiency (η_{RF})	93.5	92.4	%
2D quadrupole approximation at center	99	99.6	%

The newly built trap II, depicted in figure 3.2, also builds on the proven blade design but again improves on mechanical stability and alignment precision ($\leq$10 µm). The minimal electrode-ion distance is reduced to 565 µm to achieve sufficiently strong radial confinement already at lower RF drive powers. Further changes include the addition of holes in the tip electrodes, which allows for direct optical access along the principal trapping axis (z-direction, cf. Figure 3.6), and the ability to apply a DC offset voltage to the two blade electrodes held at ground potential. To find a balance between the achievable trapping depths and constraints given by the manufacturing and desired assembly precision, several iterations of this geometry were modeled using finite element method (FEM) simulations in Comsol Multiphysics (versions 3 and 4).

Ramsey experiments (Section 4.8) using a spin-echo sequence, in which the RF drive power was rapidly changed to a different value for the second half of the free evolution, later revealed that the geometry of the RF connection (possibly the “bridge” (E) in Figure 3.2) produces an *AC magnetic field* in the trap region. This results in an energy level shift of the Zeeman states[13] in addition to the one created by the quantization magnetic field (Section 3.6). A second trap of the same design (located in a neighboring lab) uses a different wiring geometry and does not exhibit this behavior.

As detailed treatments of the classical dynamics of ion traps are readily available in many places in the literature (for example, refs. [12, 13, 68] and almost every thesis published in the field), the remainder of this section offers only a brief summary of the equations used to characterize trap II in FEM simulations.

---

[13] 360(21) Hz/$\mathrm{W_{RF}}$ between the $m = \pm 1/2$ Zeeman levels of the $\mathrm{S}_{1/2}$ state and 67(7) Hz/$\mathrm{W_{RF}}$ between $m = 1/2$ and $m = 3/2$ of the $\mathrm{D}_{5/2}$ state; for $\Omega_{\mathrm{RF}} = 28.8\,\mathrm{MHz}$ at a DC bias field of $B \approx 4$ G

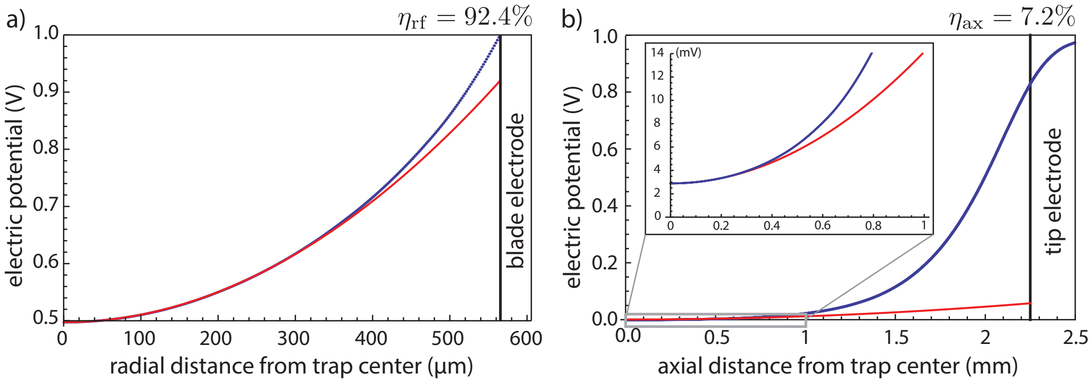

Figure 3.3.: Trap efficiencies from harmonic approximation
FEM simulation data (blue) and second-order polynomial fits (red) to regions ±200 µm around the trap center. The ratio of the respective values at the location of the radial (a) and axial (b) electrodes yields a trap "efficiency" η with respect to the generated harmonic pseudo-potential.

The trapping potential Φ can be divided into a dynamical radial part Φ_{rad} and a static axial part Φ_{ax} [13]. Using a Taylor expansion around the center of the trap $\Phi_{\mathrm{rad}} = \Phi_{\mathrm{rad}}^{(0)} + \Phi_{\mathrm{rad}}^{(2)} + \Phi_{\mathrm{rad}}^{(4)} \ldots$, the dynamical part can be approximated by

$$\Phi_{\mathrm{rad}}^{(2)}(x, y, z, t) = \frac{V_{\mathrm{RF}} \cos(\Omega_{\mathrm{RF}} t) + U_r}{2} \left(\alpha_x x^2 + \alpha_y y^2 + \alpha_z z^2 \right). \tag{3.1}$$

Here, V_{RF} is the peak amplitude of the applied AC voltage oscillating at frequency Ω_{RF} and U_r is a DC bias voltage applied to one of the blade pairs. The *geometric factors* $\alpha_x, \alpha_y, \alpha_z$ account for the difference between blade/tip and ideal hyperbolic electrode shapes *as well as* the possible 2D symmetry breaking in the case the RF voltage is only applied to one pair of blades (as done in this thesis) and not both. In order to fulfill the Laplace equation $\Delta\Phi = 0$, they are bounded by the requirement $\alpha_x + \alpha_y + \alpha_z = 0$. Similarly, the static axial confining potential is approximated by

$$\Phi_{\mathrm{ax}}^{(2)}(x, y, z) = U_{\mathrm{DC}} \left[\beta_z z^2 - \frac{1}{2} \left(\beta_x x^2 + \beta_y y^2 \right) \right],$$

where U_{DC} is the voltage applied to the tip electrodes and, again, $\beta_x + \beta_y + \beta_z = 0$.

In the limit of small excursions around the trap center, the harmonic motion of an ion of charge e and mass m in direction i can be described by

$$e\phi_i = \frac{1}{2} \sum_i m \omega_i^2 r_i^2 \quad \text{with} \quad i \in \{x, y, z\}, \tag{3.2}$$

with (secular) motional frequency ω_i and the associated potential curvature ϕ_i / r_i^2.

In this *pseudo-potential* approximation of independent harmonic oscillators, anharmonic terms of the generating potential Φ (such as $\Phi_{\mathrm{RF}}^{(4)}$) are neglected. A static FEM simulation at $t = 0$ allows us to extract the potential curvatures in each spatial direction via second-order polynomial fits. Figure 3.3 shows the simulation results for 1 V applied to the blade and tip electrodes, respectively. In both cases (a) and (b), the fits, indicated in red, were made to a range of ±200 µm around the trap center which was simulated with a high-resolution mesh. In the inefficient axial direction (b), a $\sim 1\%$ deviation between fit and the simulated potential is reached only at a distance of ±280 µm from the trap center. Therefore, even for longer chains of tens of ions (e.g. Figure 3.18) anharmonicities of the trapping potential should not be a concern. A discussion of the effects related to anharmonic trap potentials can be found in reference [69].

The extracted pseudo-potential curvatures can also be used to asses the overall quality of the 2D quadrupole potential generated by the blade electrodes at the center of the trap. A non-zero value along the axial (z) direction leads to an RF-induced driven motion (“micromotion”, see also Section 4.5) which - especially when working with longer chains of ions, where the effect cannot be circumvented - has to be minimized. Both linear traps used in the experiment do well in this regard (cf. Table 3.1).

From solutions of Mathieu equations [13, 68], the secular frequencies of Eq. (3.2) can be derived as a function of the electrode voltages to be

$$\omega_r = \frac{e}{\sqrt{2}m\Omega}\alpha_r V_{\mathrm{RF}} \quad \text{and} \quad \omega_z = \sqrt{\frac{2e}{m}\beta_z U_{\mathrm{DC}}}, \tag{3.3}$$

where $\alpha_r = (\alpha_x + \alpha_y)/2$ and it was assumed that α_z and $U_r = 0$. In practice, however, the axial trapping potential leads to a weakening of the radial confinement, effectively lowering the radial oscillation frequency to a value $\tilde{\omega}_r = \sqrt{\omega_r^2 - 0.5\,\omega_z^2}$.

The potential (trap) depth $D = \frac{1}{2}m\omega^2 r^2$ reaches 5 eV to 32 eV for radial frequencies $\omega_r/(2\pi)$ between 1.4 MHz to 3.5 MHz, which allows even hot ions from a thermal source to be captured and retained easily.

When an RF voltage is applied to both pairs of blades with opposite phase and no electric field lines end on the end caps, the radial oscillation frequency ω_r is the same in both radial directions x and y. However, when V_{RF} is applied to only one pair of blades the radial modes differ due to the symmetry breaking.

In Figure 3.4.b and Figure 3.5.b on the next page, the measured mean radial frequency $\omega_r = (\omega_x + \omega_y)/2$ is plotted as a function of RF drive power and corresponding voltage, respectively. The splitting of the radial modes depends on the radial confinement and

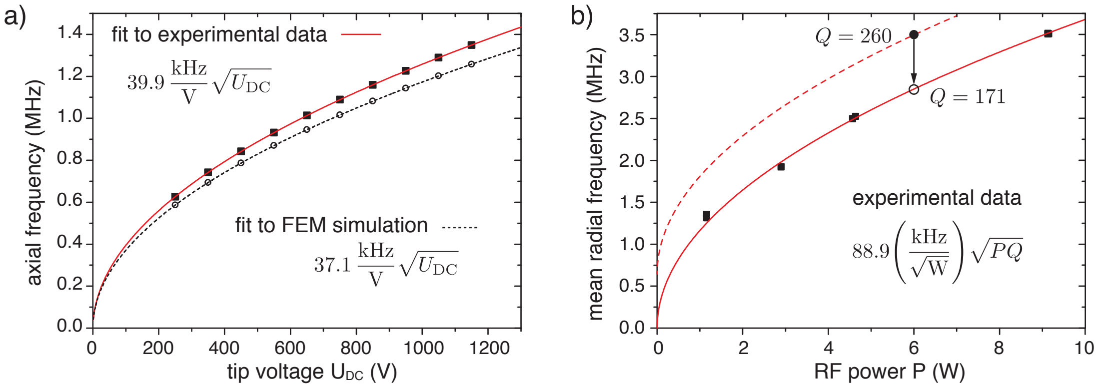

Figure 3.4.: Trap frequencies of the center of mass (COM) modes
a) Axial frequency $\omega_z/(2\pi)$ as a function of tip voltage in FEM simulation (dashed line) and experiment. The scaling factors relate to Eq. (3.3). **b)** Measured radial center frequencies $\omega_r/(2\pi)$ for different RF powers P sent to a helical resonator. Its quality factor Q degraded over time (see text) shifting the frequencies from the dashed to the solid line following $\omega_r = \epsilon\sqrt{PQ}$. The single datapoint at $Q = 260$ was taken right after the resonator was first installed.

can be tuned using a DC offset voltage U_r applied to the blade electrode(s) held at ground potential. In our case, this feature, illustrated in Figure 3.5.a is essential for efficient Doppler cooling; see also Section 4.2.

To reach the AC voltage amplitude necessary for the radial confinement shown in Figures 3.4 and 3.5, the trap is set up as part of a quarter-wave resonator that is driven by amplified[14] RF from a signal generator[15]. The current setup uses a tapped helical resonator [70, 71]; see reference [72] for information on inductive coupling. The (loaded) quality factor Q = bandwidth/(resonance frequency) of the resonator was determined from a measurement of the full width at half maximum (FWHM) of the reflected power (=bandwidth) with an RF network analyzer. Using the relation $\omega_r = \epsilon\sqrt{PQ}$, the measurement of $Q = 260$ at $P = 6\,\mathrm{W}$ and $\omega_r = 2\pi \times 3.51\,\mathrm{MHz}$ allows us to calculate the constant $\epsilon = 88.9\ \mathrm{kHz}/\sqrt{\mathrm{W}}$, which is determined by the resonator geometry and drive frequency [70]. Combined with a fit of the equation (solid line in Figure 3.4.b) we infer the Q-factor at the time the other measurements shown in the figure were taken.

The observed degradation of the resonator's quality factor over the course of many months seems to be due to tarnishing of the coils copper surfaces (skin depth $\approx 12\,\mu\mathrm{m}$ for $\Omega_\mathrm{RF}/(2\pi) = 28.8\,\mathrm{MHz}$) as mechanical cleaning of the resonator's inner helix using organic solvents always led to improvements. A conductive coating that is less susceptible to corrosion (e.g. silver) could be used to address this problem in the future.

---

[14] Minicircuits LZY-1
[15] Rhode+Schwarz SML 01

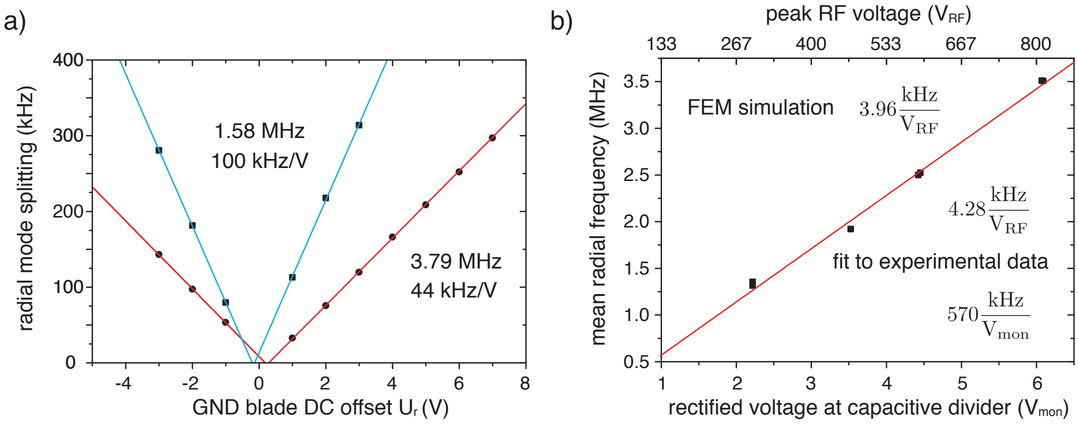

Figure 3.5.: Radial COM mode frequency splitting and corresponding blade voltages **a)** Induced splitting of the radial COM mode for different confinements. For each offset voltage U_r added to the blade electrodes at ground potential the radial mode splitting was measured. Extrapolation from linear fits yields a mode splitting of 13.4 kHz at $\omega_r = 1.58\,\mathrm{MHz}$ and 8 kHz at $\omega_r = 3.79\,\mathrm{MHz}$ when no offset is applied. **b)** Observed mean radial frequency for different peak RF voltages. The RF voltage is monitored as V_mon after rectification following a capacitive divider that is placed at the vacuum feedthrough of the resonator. The top axis shows the estimated peak RF voltage based (only) on the capacitive divider ratio of 1:133.3. The 8% scaling difference between FEM simulation and experiment is comparable to that of Figure 3.4.a.

The DC voltages used for confinement in the axial direction via the tip electrodes are derived from a dedicated high voltage supply[16]. The DC voltages applied to compensate for stray electric fields (micromotion compensation, cf. Section 4.5) and the DC blade offset inducing the additional radial mode splitting are supplied by standard laboratory power supplies[17]. All voltages are low-pass filtered at the high voltage feedthrough of the vacuum vessel (tip: $R = 33\,\mathrm{k\Omega}$, $C = 820\,\mathrm{pF}$, compensation: $R = 2\,\mathrm{M\Omega}$, $C = 820\,\mathrm{pF}$).

3.2. Vacuum vessel

The vacuum chamber (Figure 3.6) enclosing the ion trap (Figure 3.2) is a 316 stainless steel octagon with eight CF63 flanges and a CF200 flange on top and bottom, both modified to carry additional flanges. The trap carrier is attached to the top flange right beneath a central CF40 power feedthrough that directly connects to the helical resonator. An adjacent CF16 high-voltage feedthrough[18] directly connects to a low-pass filter board that provides connectivity for the compensation electrodes and each tip electrode individually.

---

[16] EHS8020x-K2; iseg Spezialelektronik GmbH

[17] models PS 3646A and 3644A; EA Elektro-Automatik GmbH & Co. KG

[18] CeramTec 9871-08-CF

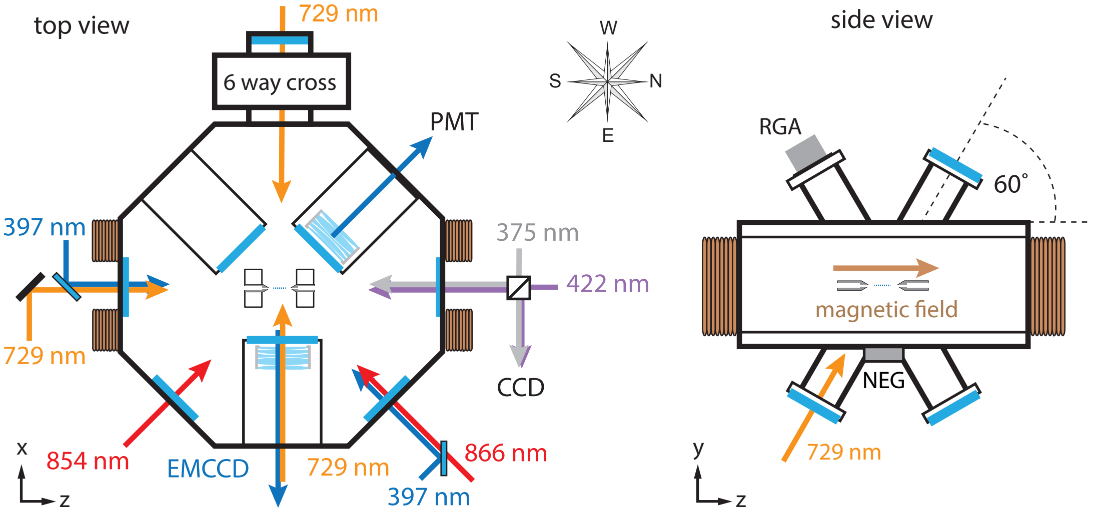

Figure 3.6.: Laser beam directions
The schematic drawing (not to scale) of the vessel relates the laser beam and imaging directions to the laboratory coordinate system and the cardinal directions (indicated by the compass rose). The pair of coils at the north and south viewports provide the magnetic quantization field (Section 3.6) along the axial (z) direction of the ion trap. A non-evaporative getter (NEG) and a residual gas analyzer (RGA) provide vacuum pumping and analysis in addition to the pumps and an ion gauge (not shown), which are attached to a 6-way cross. All laser beams are delivered by optical fibers and directly focussed to the trap center by standard fiber collimators and, in one case, dedicated focussing optics (addressed beam). Dichroic mirrors are used to overlap the laser beams at 397 nm and 866 nm (729 nm) in front of the trap.

Five of the eight in-plane directions are equipped with standard vacuum viewports[19] located at a distance of 18.6 cm (W viewport: 39.5 cm) from the trap center. Another three directions are fitted with recessed (inverted) viewports[20] that allow the placement of custom-made objectives[21] on three-axis translation stages very close to the ion trap while still keeping them outside the vacuum. Two additional CF40 flanges are welded each to the top and bottom CF200 flange and provide additional optical access at an angle of 60° to the horizontal plane.

A commercial calcium source[22] is mounted directly to a CF16 electrical feedthrough underneath the trap. A non-evaporative getter (NEG)[23] is located next to it. The western horizontal flange is connected to a six-way cross carrying a titanium sublimation

---

[19] Caburn, fused silica with two-sided anti-reflection coating X/UIMCP/43 from Tafelmaier GmbH
[20] UKAEA, fused silica with one-sided anti-reflection coating X/UIMCP/43 from Tafelmaier GmbH
[21] Silloptics GmbH, Wendelstein
[22] Alvatec AS-2-Ca-50-C
[23] SAES Capacitorr D100

pump[24], a 20 L/s ion pump[25], a Bayard-Alpert ion gauge[26] and a CF40 all-metal valve[27].

Motivated by repeated vacuum problems during multiple trap assembly runs, a residual gas analyzer (RGA)[28] was added to one of the 60° viewports for in-situ vacuum diagnostics. The problems manifested themselves in an increased rate of molecule formation during trap operation (mostly CaOH^+ and very rarely CaH^+)[29] – all while the base pressure at the ion gauge remained at the low 10^{-11} mbar level. We later identified contaminations on the blade electrodes facing the oven as a likely cause: As Ca-deposits on stainless steel reduce its work function, light at 397 nm, used for laser cooling and state detection, can produce photoelectrons when striking contaminated parts[30]. The electrons are subsequently accelerated by the trap's RF field and gain enough energy to release and ionize all kinds of contaminants from surfaces close to the ions.

The ensuing problems have now been reduced to an acceptable level by rearranging the UV laser beams to prevent illumination of the affected areas and the use of careful focussing to keep all residual stray light at a minimum. The latter includes the separate delivery of the laser beams at 422 nm and 375 nm used in the photoionization. When delivered through the same fiber collimator (as done in many experiments), its lens' focal length shift between the two wavelengths leads to foci that can be many centimeters apart, causing a significant amount of stray light and markedly reducing photoionization efficiency. Light delivery through separate optical fibers and careful overlapping of the $2\omega \approx 100\,\mu\mathrm{m}$ foci allows us to send the two beams through the tip electrodes without stray light, achieving decent loading rates for $10\,\mu\mathrm{W}$ to $20\,\mu\mathrm{W}$ optical power in each beam. The beam overlap at the location of their foci is monitored via a CCD camera that is placed at the same distance from a polarizing beam combiner as the trap.

The trap vacuum vessel is mounted onto a two-level breadboard support-structure that is located inside a magnetic field shielding enclosure (Section 3.6). To allow for precise manipulations with the enclosure doors closed, some of the opto-mechanical elements next to the vacuum chamber are controlled remotely using stepper motors[31].

---

[24] Varian/Agilent cartridge model 916-0050

[25] Varian/Agilent VacIon Plus 20 StarCell

[26] Varian/Agilent UHV-24p

[27] Series 540 "Easy close" all-metal angle valve; VAT Vacuumvalves AG

[28] RGA 100; Stanford Research Systems

[29] Photodissociation of both molecules is possible but requires deep-UV wavelengths [73, 74].

[30] With a large positive DC bias voltage applied to one set of blade electrodes via a large in-series resistor, the voltage drop across the resistor was used to measure small photocurrents that were induced by targeted UV-illumination. Visually contaminated parts gave large readings, while others did not.

[31] Newport NSC200 with NSA12 actuators

3.3. Laser systems

A total of seven solid-state laser systems are used for the work presented in this text. As the corresponding optical setups have already been described in detail in references [50, 59–61], only schematics of the most relevant parts are presented in the following.

With the exception of the multi-mode fibers connecting to the wavelength meter, all laser beams are carried by single-mode polarization maintaining fibers (PMF) with angle-polished end-facets (FC/APC). To preserve the linear input polarization at the output, half-wave plates in front of each fiber are carefully adjusted with the help of commercial polarization analyzers[32] to match the polarization direction to the fiber axes. This way, polarization extinction ratios (PER) of 33 dB (23 dB) are achieved for fibers in the infrared[33] (UV-A)[34]. The quoted values correspond to the worst case, i.e. the farthest point from the equator on a circle traversed on the Poincaré sphere when stress (mechanical or thermal) is applied to the fiber. They are calculated from the polarization ellipse as $\mathrm{PER} = -10\log_{10}\{\tan^2(|\eta| + |\Delta\eta|)\}$, where η is a constant ellipticity (caused by non-linear input polarization, imperfect alignment to the fiber's axes and/or stress in the input connector) and $\Delta\eta$ is an additional stress-induced ellipticity.

Due to the lack of practical atomic references at the Ca^+ wavelengths, all lasers are locked to Fabry-Pérot cavities using a Pound–Drever–Hall (PDH) scheme [75, 76]. The diode lasers are referenced to piezo-tunable cavities of finesse $\mathcal{F} \approx 300$ [59].

3.3.1. Diode lasers

Laser cooling, detection and optical pumping (397 nm)

The strong $\mathrm{S}_{1/2} \leftrightarrow \mathrm{P}_{1/2}$ dipole transition in $^{40}\mathrm{Ca}^+$ is used for laser cooling, state detection and optical pumping. The corresponding light at 397 nm is generated by a commercial master oscillator power amplifier (MOPA) system[35] through second harmonic generation (SHG) in a resonant doubling cavity. The system is capable of producing more than 100 mW of UV light but is usually operated with an output power between 25 mW and 30 mW. This is done in order to prolong the lifetime of its tapered amplifier (TA) chip (and its coatings) and also to reduce the wear on optical elements in contact with the UV light. The laser's output is decoupled from the down-stream optics using

---

[32] Schäfter+Kirchhoff, polarimeter models SK010PA-UV & SK010PA-NIR
[33] Schäfter+Kirchhoff PMC-630-4.1-NA012-3-APC-1500-P at 729 nm
[34] Schäfter+Kirchhoff PMC-S400Si-2.7-NA012-3-APC-1200-V at 397 nm
[35] Toptica DL-SHG pro

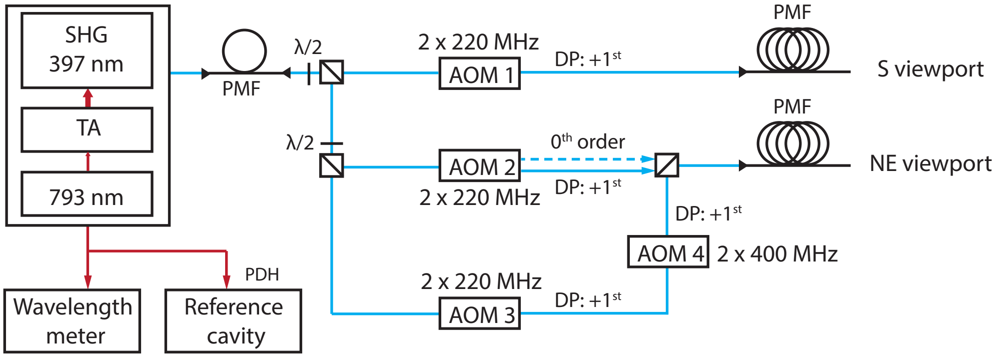

Figure 3.7.: 397 nm laser setup
Light at 397 nm is passed through a short end-capped polarization-maintaining fiber (PMF) and is subsequently split into three beam paths. AOM 1 provides light for optical pumping, AOM 2 for Doppler cooling. Here, a mechanical shutter allows the non-diffracted 0^{th} order light to be sent to the trap as well. The third beam path (AOM 3 and 4) bridges the isotope shift to $^{44}\mathrm{Ca}^{+}$ and is combined with the Doppler cooling beam for delivery through the same fiber.

a short PM-fiber that also acts as a mode cleaner. At 397 nm wavelength – even at the seemingly low power levels used – it is important to use fiber connectors with coreless end-caps. Their design effectively lowers the light intensity at the silica–air interface, which significantly reduces light-induced damage at the fiber facets that is otherwise observed to develop over a few months of operation. Each of the beam paths shown in Figure 3.7 uses an acousto-optic modulator (AOM) at 220 MHz[36] in a double-pass (DP) setup[37] to switch the corresponding light beam on or off. In addition, a mechanical shutter in the beam path of AOM 2 allows for propagation of the undiffracted light beam, which is used to help re-crystallize longer ion strings after collisions with background gas. For the experiments using $^{44}\mathrm{Ca}^{+}$, the $\mathrm{S}_{1/2} \leftrightarrow \mathrm{P}_{1/2}$ isotope shift of 842(3) MHz (cf. Section 2.2) made it necessary to add an additional beam path along AOMs 3[36] and 4[38].

Repumping and qubit reset (866 nm / 854 nm)

Commercial diode lasers[39] provide the light necessary to repump the ion from the $\mathrm{D}_{3/2}$ and $\mathrm{D}_{5/2}$ metastable states via the P-manifolds. Their light beams are controlled

---

[36] Crystal Technology, model 3220-120

[37] Note: Opposed to a standard double pass setup [77], the polarization sensitivity of quartz- and fused-silica crystals used in many UV-grade AO devices require the use of a right angle folding prism (e.g. FRP-040-UV, Rainbow Research Optics) to provide a vertical beam offset on the second pass.

[38] Brimrose FQM-400-100-393

[39] Toptica DL-100 and DL-pro

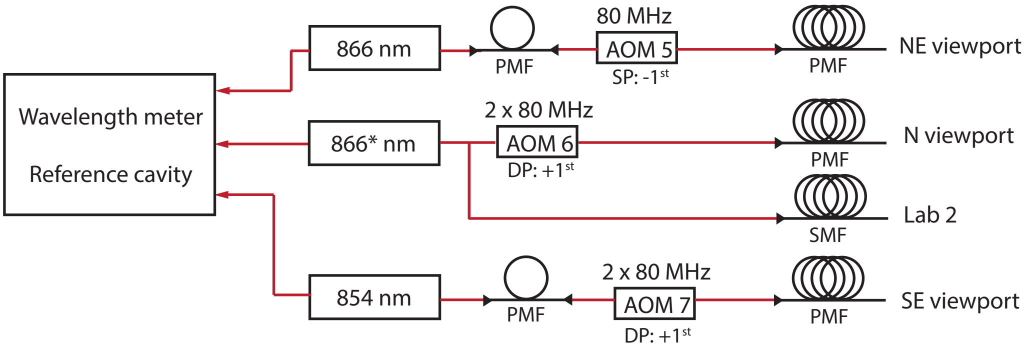

Figure 3.8.: Repumper laser setups
All light beams are switched using acousto-optic modulators in single (SP) or double-pass (DP) configuration. The laser marked by * is used to address the $D_{3/2} \leftrightarrow P_{1/2}$ transition in $^{44}Ca^+$ and has a separate single-mode fiber (SMF) connection to an adjacent laboratory (Lab 2) for precise wavelength monitoring.

with AOMs[40] running at 80 MHz (cf. Figure 3.8). As the $D_{3/2} \leftrightarrow P_{1/2}$ transition of $^{44}Ca^+$ is shifted by -4.5 GHz with respect to $^{40}Ca^+$, a separate laser (866*) is used for repumping and spectroscopy. During the experiment described in Chapter 6 the laser's wavelength was recorded on a high-precision wavelength meter[41] in an adjacent laboratory. To maintain the wavelength meter's accuracy, the device was calibrated every 60 s by referencing it to the Ti:Sapphire laser discussed in the following (see Section 3.7 for more details on the wavelength meter's performance).

3.3.2. Ti:Sapphire laser for qubit manipulation (729 nm)

An ultra-stable narrow-linewidth laser at 729 nm [60] provides the ability to coherently manipulate the optical qubit encoded in the $^{40}Ca^+$ $S_{1/2}/D_{5/2}$ states. The setup consists of a diode-pumped $Nd{:}YVO_4$ laser at 532 nm[42] that pumps a titanium-doped sapphire (Ti:Sa) crystal inside a modified dye laser[43]. Equipped with an intra-cavity electro-optic modulator (EOM)[44] for high-bandwidth feedback, a three-fold laser lock to a high-finesse cavity (Section 3.3.3) provides a short-term linewidth of 1-10 Hz [50, 60]. The system's performance is regularly checked via beat-measurements using a 400 m optical path-length stabilized fiber to a similar setup located at the university's laboratories.

---

[40] Crystal Technology, model 3080-120
[41] Highfinesse WSU/2
[42] Coherent Verdi V-10
[43] Coherent model 899
[44] Qioptiq (formerly Linos) PM-25

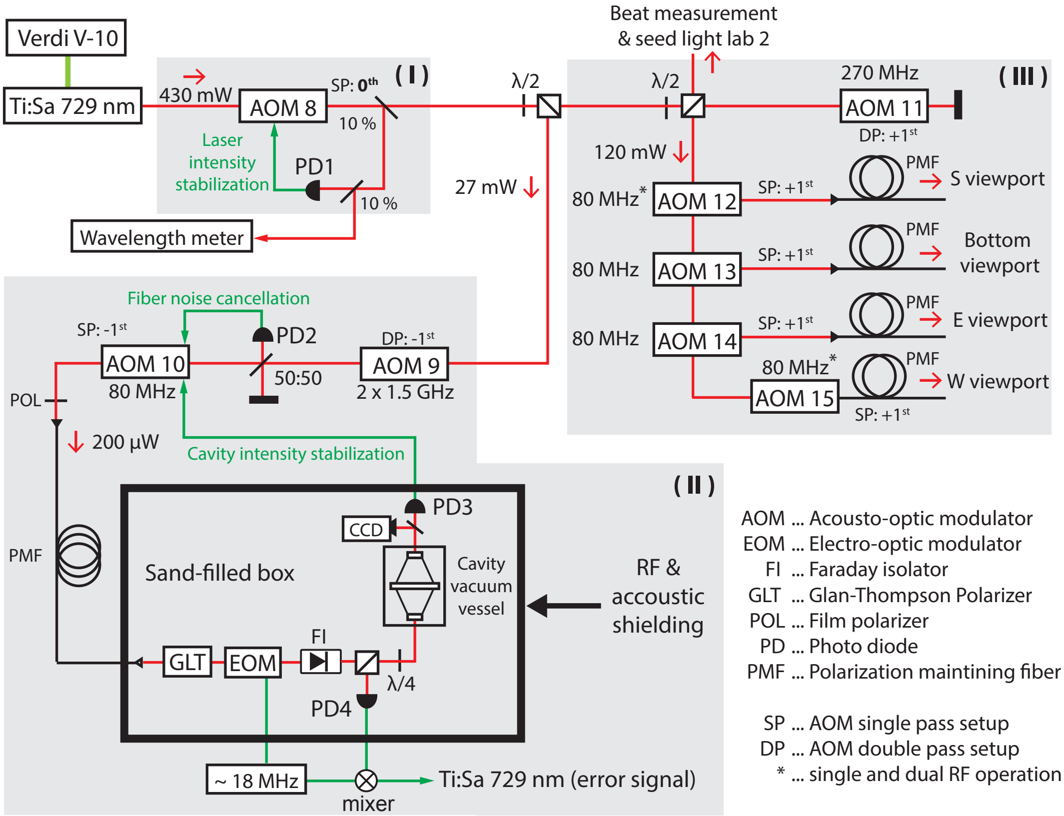

Figure 3.9.: 729 nm laser setup for coherent qubit manipulation (simplified)
The setup consists of three separate parts: (I) laser intensity stabilization at AOM 8, (II) cavity light preparation (AOM 9 & 10), and (III) light preparation (AOM 11) and distribution to the trap access ports (AOM 12-15). Part of the generated light is branched off for beat measurements with the university laboratory and for seeding a TA system in the adjacent laboratory 2.

Figure 3.9 above shows a simplified schematic of the laser setup, split into three parts: intensity stabilization (I), high-finesse cavity locking (II), and light preparation and delivery (III).

(I) The laser intensity is stabilized in a PID[45] loop with 100 kHz bandwidth by directing 9% of its output light onto PD1[46] and adjusting the amount of RF power sent to AOM 8[40] accordingly. Residual fluctuations in the transmitted 0th order light are smaller than 1% [60]. However, vibration-[47] and thermally-induced beam pointing throughout the downstream optics following AOM 8 add fluctuations and drifts (up to $\sim 2\%$), such that this value does not hold at the location of the ion trap.

---

[45] Stanford Research Systems PID 960 analog PID controller

[46] Thorlabs PDA100A-EC

[47] The main source of vibrations is a HEPA fan/filter unit used to keep the laser area dust-free.

(II) The short-term frequency reference for the laser is provided by a high-finesse cavity (Section 3.3.3). To match the frequency of one of its TEM_{00} modes to the atomic transition, high-frequency AOM 9[48] is set up in double-pass configuration, allowing to scan over more than one free spectral range of the cavity.

The reference cavity vacuum vessel is housed in a sand-filled wooden box, into which light is carried via a PM-fiber. Inside the box, a Glan-Thompson polarizer[49] ensures a match of the incoming light polarization to the Brewster-cut windows and crystals of an EOM[44] used to phase-modulate the laser light at 18 MHz. Careful alignment of the Brewster-cut windows with respect to each other minimizes the residual amplitude modulation that would distort the error signal generated in a PDH locking scheme using PD4[50]. An optical isolator (FI)[51] is placed into the cavity beam path to suppress etalon effects between flat surfaces, which were found to be responsible for laser frequency shifts on the order of $50-100$ Hz induced by thermal drifts and, with the enclosure open, air-currents. The light intensity sent to the cavity is kept constant by detecting the transmitted power on PD3[52] and controlling the RF power sent to AOM 10[40] in a feedback loop[45]. The same AOM is used to stabilize the optical path length of the fiber carrying light to the cavity, actively cancelling out the effect of refractive index modulations induced by acoustics and temperature changes. This method of *fiber noise cancellation* [78] is implemented using a home-built, VCO-based phase-locked loop [60] that is controlled via a beat-note detected on PD2[53] between laser light at the fiber input and light reflected from the flat-polished (FC-PC) end of the fiber.

(III) A fraction of the laser light is branched off to seed a tapered amplifier in an adjacent laboratory and to implement the beat measurement with laser light delivered from the university setup (see [50, 60, 64] for details). The remaining light is sent to AOM 11[54] which is used to tune it into resonance with arbitrary transitions between the Zeeman-split $^{40}\mathrm{Ca}^{+}$ $\mathrm{S}_{1/2}$ and $\mathrm{D}_{5/2}$ manifolds. The modulator also performs amplitude shaping of the optical pulse [79] in order to adiabatically eliminate off-resonant excitations, e.g. during gate operations [56]. AOMs $12-14$[40] deflect the produced light pulse into polarization maintaining optical fibers that deliver it to the desired viewport at the

---

[48] Brimrose GPF-1500-100, 75 µm active aperture, diffraction efficiency ~15 %
[49] Bernhard Halle Nachfl. GmbH, Germany
[50] home-built, based on Hamamatsu S5971
[51] QiOptiq FI-680-5 SV
[52] Thorlabs PDA520
[53] home-built, based on Hamamatsu S5973
[54] Brimrose, model TEF-270-100-800

ion trap. Optionally, two RF signals can be sent simultaneously to one of the AOMs marked with an asterisk* to convert the incoming laser beam to a bichromatic light field (Section 2.5). They are set up in single-pass configuration as a double pass setup would produce unwanted, co-propagating sum-frequency components that are resonant with the carrier. Hence, the two 1st order diffracted beams after the first pass have to be directly coupled into the fiber, off-center, on the side of their Gaussian profiles, which worsens their sensitivity to vibrations. Here, the fiber-coupled AOM 15[55] provides increased mechanical stability, which is helpful especially when the bichromatic light field is made from RF components with a large separation in frequency ($> 2\,\mathrm{MHz}$). This is the case, e.g., when transverse motional modes at $\pm\omega_r$ are addressed.

3.3.3. High-finesse cavity (729 nm)

The Ti:Sa laser's short term frequency stability is derived from a PDH lock to a vertical Fabry-Pérot cavity[56] with a spacer made from ULE[57] glass, which possesses a near zero[58] linear *coefficient of thermal expansion (CTE)* at an optimal temperature T_m, which allows for very high dimensional stability that is surpassed only by cryogenic single crystal cavities [80, 81].

The cavity's design and mounting structure is optimized to ensure that the mirror distance remains largely unaffected by vertical accelerations[59]. Complemented by an in-vacuum temperature stabilization keeping the cavity temperature close to T_m, residual linear drift rates of $63\,\mathrm{mHz/s}$ have been observed [83]. Figure 3.10 shows the cavity vacuum vessel used in the experiment following a design similar to reference [83]. The midplane-mounted cavity is placed inside a two-stage heat shield, which is actively temperature stabilized using two pairs of Peltier elements that are located between the surrounding vacuum chamber and the outer shield. A quartz crystal, a fast-responding NTC thermistor, as well as a slower but more accurate PT1000 provide access to the temperature of the cavity surroundings. Contaminants outgassing from the unbaked cavity or the Peltier elements are removed by a $20\,\mathrm{L/s}$ ion pump that is connected to the vessel via a $20\,\mathrm{cm}$ bellows (not shown). After more than 3 years of continuous operation, the assembly remains at a base pressure of $2 \times 10^{-9}\,\mathrm{mbar}$.

---

[55] Gooch+Housego, model MM080-1C2V14-5-F2SH-B

[56] Advanced Thin Films, Boulder, CO, USA

[57] Corning, *ultra low-expansion* (ULE) titania silicate glass

[58] $0 \pm 30 \times 10^{-9}\,\mathrm{K}^{-1}$ from $5\,^\circ\mathrm{C}$ to $35\,^\circ\mathrm{C}$ (Corning ULE data sheets)

[59] See ref. [82] for FEM simulations of the strain and acceleration sensitivity of various cavity designs.

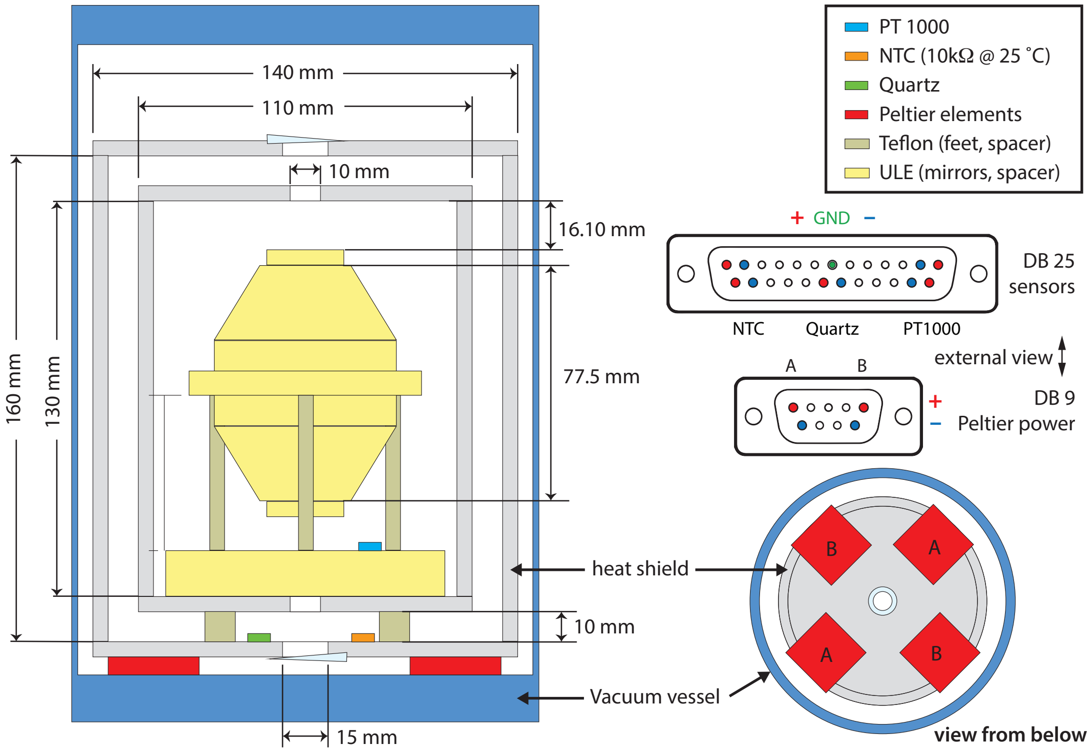

Figure 3.10.: Cavity vacuum vessel and electrical connections
A 316 stainless steel vacuum chamber encloses two stacked aluminum heat shields of 5 mm thickness. The outer shield is temperature stabilized via in-vacuum Peltier elements using either a quartz crystal or an NTC element as in-loop sensor. A PT1000 sensor mounted at the cavity base inside the second shield is used for out-of-loop temperature monitoring. All sensors and the 4 Peltier elements (A,B – pair-wise in series) are connected to the outside via Sub-D vacuum feedthroughs. (Figure based on a drawing by Michael Chwalla; private communication)

The cavity length of $L = 77.5\,\mathrm{mm}$ corresponds to a free spectral range (FSR) of $1.934\,\mathrm{GHz}$, which allows us to determine the cavity finesse $\mathcal{F}$ according to

$$\mathcal{F} = \tau \frac{c\pi}{L} = 2\pi\,\tau\,\mathrm{FSR} \approx 407000,$$

where the exponential decay time $\tau = 33.49\,\mathrm{\mu s}$ has been determined in a ring-down measurement. The ratio of $\mathrm{FSR}/\mathcal{F}$ yields a cavity linewidth of $\Delta\nu = 4.75\,\mathrm{kHz}$.

The assembly shown in Figure 3.10 was installed in October 2010 replacing an older cavity of the same design. The older cavity, installed in 2006 [60], could only be heated and thus not be operated near its optimal temperature T_m.

To determine the CTE-minimum temperature T_m before permanent installation of the new cavity, the Peltier elements inside the vessel were used to cool/heat the outer heat shield to various temperatures. For each temperature value, the corresponding

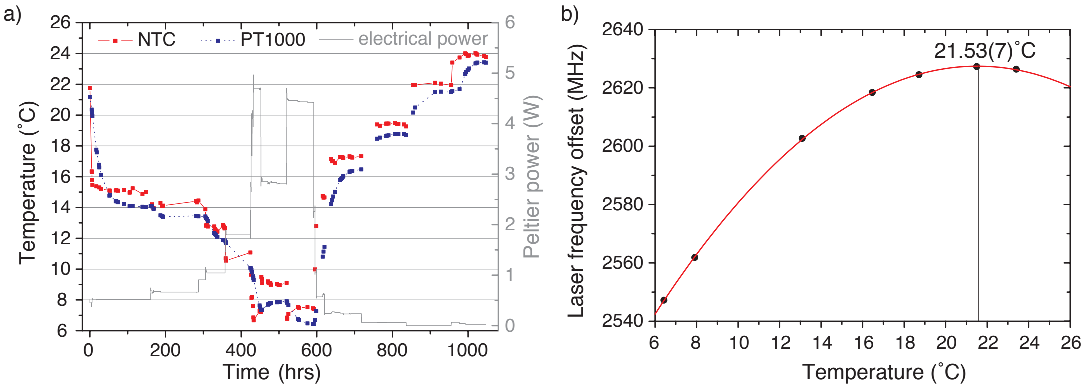

Figure 3.11.: Measurement of the thermal expansion minimum
a) Temperature readings of the resistors and electrical power applied to the Peltier elements over ~ 43 days. **b)** Frequency offset of the tracked cavity TEM_{00} mode with respect to the 729 nm laser locked to the old reference cavity as a function of PT1000 temperature. The red line is a fit of $y = A + B(T - T_\mathrm{m})^2$ to the data, yielding $B = -352(4)\,\mathrm{kHz/K}^2$ and $T_\mathrm{m} = 21.53(7)\,°\mathrm{C}$.

frequency of a particular TEM_{00} mode was determined by tuning AOM 9 to bring the frequency of the 729 nm laser, while it was locked to the old high-finesse cavity, into resonance with the new cavity. The measurements were taken over many weeks to allow the cavity to thermalize after each temperature step. A polynomial fit to the data then yields T_m (Figure 3.11.b). Later fine-tuning of the temperature setpoint by tracking the laser frequency in beat measurements with laser light from the university lab *during* a temperature change, indicate a T_m closer to 21.8 °C – which illustrates the error margin brought on by the trade-off between a thermally well-isolated cavity and reliable measurements of T_m.

Figure 3.11.a also indicates the amount of electrical power needed to reach and maintain a given temperature. For temperatures T_m significantly below room temperature this may become an issue as an equivalent heat load needs to be dissipated and water cooling or electrical fans outside the vessel introduce additional vibrations that translate to laser frequency noise. In this context, it is worth noting that a majority of ULE-based cavities, albeit specified with a T_m close to room temperature, actually have their thermal expansion minimum at lower temperatures. The two cavities investigated in ref. [83] were found to have an optimum temperature at 7 °C and 12.5 °C, respectively. In Innsbruck, a second vertical cavity of the same type was found to have a T_m at 7 °C. Based on discussions with colleagues in a number of laboratories, it is believed that this discrepancy is related to a calibration issue in Corning's ultrasound-method to determine the CTE zero crossing, which, reportedly (late 2013)[60], has improved since.

---

[60] Mark Notcutt of Stable Laser Systems, Boulder, CO, USA (private communication)

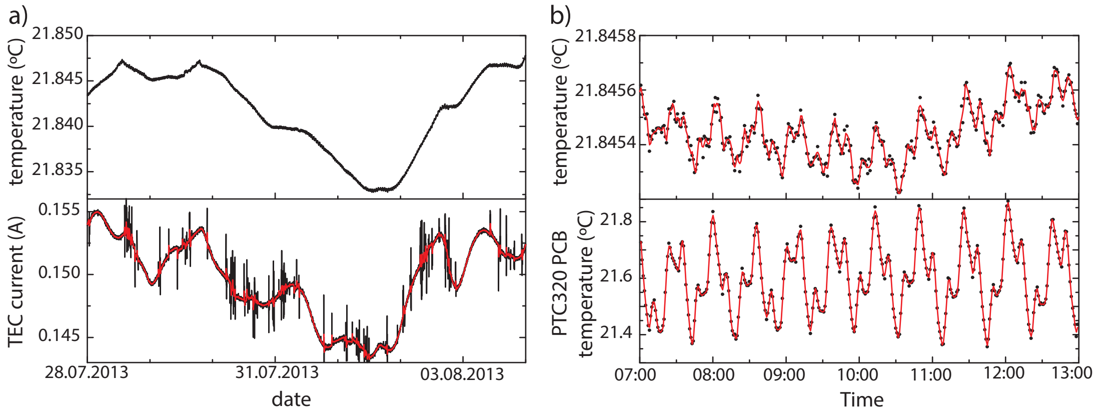

Figure 3.12.: Cavity temperature stability and measurement resolution
The temperature at the cavity base measured by the out-of-loop sensor over 1 week **(a)** and 6 hours **(b)**. The spikes visible in the TEC current are caused by electromagnetic interference. The range shown is equivalent to an electrical cooling power of 76-88 mW. The regular pattern visible in b) is an artifact caused by the laboratory air conditioning temperature cycle that changes the temperature of the sensor card (PTC320 PCB) used to read out the PT1000 sensor at the cavity base. (Red lines are produced by a 2nd order Savitzky-Golay filter of 10 (a) and 4 (b) points, allowing for an easier comparison of the pattern in both signals.)

Temperature stabilization

The cavity temperature is actively stabilized using a commercial digital PID controller rack[61]. It is equipped with a single-channel sensor card[62] for out-of-loop measurements of the temperature at the cavity base and a thermoelectric cooler (TEC) driver card[63] for stabilizing the NTC temperature at the in-vacuum Peltier elements. Figure 3.12 shows the effective temperature stability over the course of one week. The spikes seen in the Peltier current are caused by changes in the magnitude of RF cross-talk from sources surrounding the cavity into the temperature stabilization circuitry[64]. During “refreeze events”, in which the trap’s RF drive power is briefly lowered to help re-crystalize longer ion strings, these current spikes can reach up to 30 mA. Brief current changes are not expected to cause major temperature changes at the location of the cavity as the thermalization time of the outer aluminum heat shield is estimated to be around 300 s. However, temporary offsets of longer duration can induce a “heat wave” of a magnitude sufficient to shift the cavity temperature. Occasionally, this effect did lead to noticeable

---

[61] SRS PTC10

[62] SRS PTC320

[63] SRS PTC440

[64] Diodes on the TEC driver card could be rectifying RF signals picked up by the measurement leads that go to the cavity which is likely to cause DC offsets in the measured values.

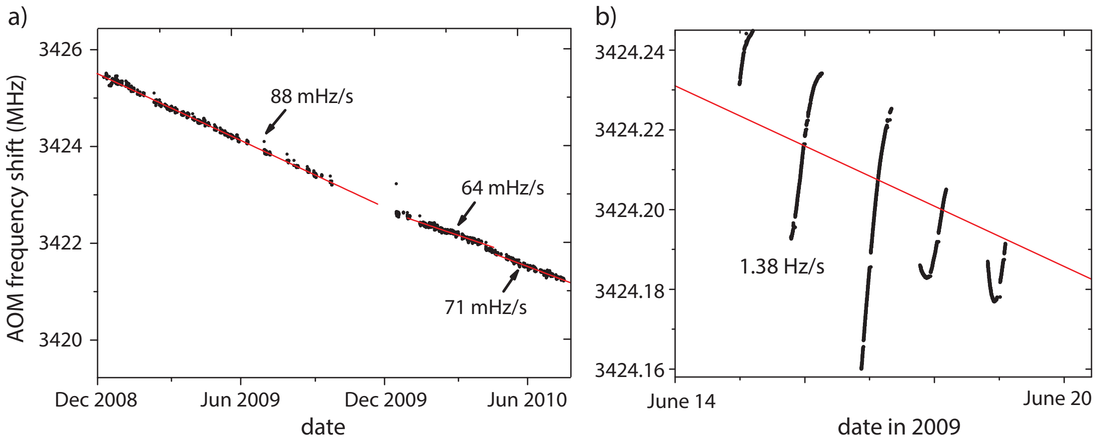

Figure 3.13.: Drift rate of the old high-finesse cavity
The optical frequency shift introduced by AOM 9 is plotted as a function of time. **a)** Long-term frequency drift rates of the old high finesse cavity obtained from linear fits to subsets of the data. **b)** Short-term frequency drifts over the course of a week. The long term average of 88 mHz/s is shown as a red line.

changes in the short-term frequency drift rate. To mitigate this problem, the in-loop sensor of the temperature stabilization will be operated via an additional dedicated sensor card[65] in the future. The residual long term drift of the cavity base temperature is likely due to the thermally “floating” inner heat shield following the black-body radiation-induced drifts of the outer shield’s average temperature. A straightforward improvement could be the addition of an inner-shield Peltier element (as done in [83]).

The quartz crystal shown in Figure 3.10 is meant for an alternative field-programmable gate array (FPGA)-based temperature stabilization system, which was not being used at the time of writing. During testing, its temperature sensitivity has been determined to be ~3.1 kHz/K.

Cavity drift rate

In order to correct for medium and longterm cavity drifts as well as possible changes of the magnetic field at the position of the ions, Ramsey experiments are performed every 2-5 minutes (Section 4.8.1). A linear fit to the measurements taken within a certain time-window is then used to *continuously* compensate the cavity drift and keep the 729 nm laser on resonance during experiments. Figures 3.13 and 3.14 show the measured data points of multiple years in terms of the frequency shift at AOM 9. The old high

---

[65] In the SRS PTC320 card run in AC mode, offsets caused by electromagnetic interference are rejected by reversing the sensor excitation current at every measurement.

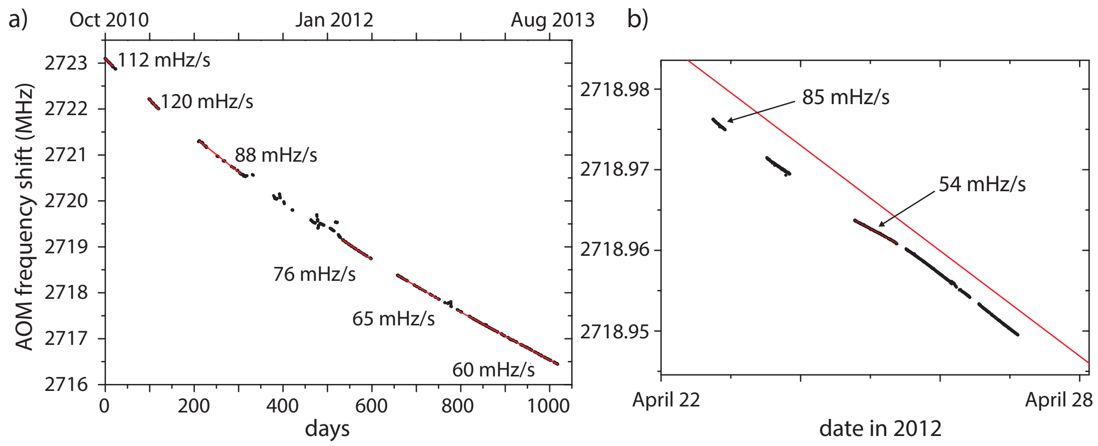

Figure 3.14.: Drift rate new high finesse cavity
The optical frequency shift introduced by AOM 9 is plotted as a function of time. **a)** Long term frequency drift rate over the course of almost 3 years. **b)** Short term frequency drift rate over the course of a week. The red line corresponds to the local long term average of 76 mHz/s.

finesse cavity installed in 2006 did not have in-vacuum temperature stabilization or heat shields inside the vacuum vessel. To provide temperature stability, the outside of the cavity vessel was heated to ~30 °C and the surrounding wooden box was temperature stabilized using water cooling [60]. While the longterm drift rate was similar to that of the new cavity, short term drifts during the course of a day were found to be two orders of magnitude larger, reaching one to a few Hz/s and sometimes even reversing directions mid-day. The new high finesse cavity solved this problem (Figure 3.14) and allows for a reliable feed-forward drift correction during measurements.

To put these numbers in perspective, one can relate the residual cavity drift to the cavity length $\Delta\nu/\nu \approx \Delta L/L$. A linear drift rate of 60 mHz/s ($\Delta\nu/\nu = 1.46 \times 10^{-14}$) corresponds to a cavity length change close to 24 proton diameters per hour, which translates to just about 7 Bohr radii per year. The origin of this (locally linear) drift is related to aging of the ULE material superimposed with a slow relaxation of the optically contacted surfaces [84]. Using a decade-old ULE cavity, drift rates as low as 13(2) mHz/s have been reported in the literature [84].

3.4. Fluorescence and state detection

As long as the valence electron of a calcium ion is in the $S_{1/2}$ state ($\equiv |\downarrow\rangle$), laser excitation on the strong $S_{1/2} \leftrightarrow P_{1/2}$ dipole transition at 397 nm combined with repumping light on the $P_{1/2} \leftrightarrow D_{3/2}$ transition at 866 nm (cf. Section 2.2) causes scattering of millions of photons per second[66]. If the electron is in the $D_{5/2}$ state instead, no light is scattered and the ion remains dark. This profound difference is at the core of the detection technique known as *electron shelving* [86, 87] (see also Section 6.1) that is used to detect the quantum state of the qubit encoded in the $S_{1/2}$ and $D_{5/2}$ manifolds with almost unity fidelity (>99.99 % can be realized [88, 89]).

PMT detection

To detect the quantum state at the end of an experimental sequence (Section 3.8) and monitor Doppler cooling at its beginning, light at 397 nm wavelength, emitted by the trapped ions during those stages, is collected by the two custom-made 5-lens objectives[67] shown in Figure 3.6. At the on-axis working distance of 58 mm between trap center and the first lens surface, the numerical aperture (NA) is 0.289, which corresponds to a collection efficiency of 2.5 % of the full 4π solid angle [59]. On the way to the detectors about 4 % absorption loss occur in the objective and another 3.2 % at a band-pass filter[68] used to suppress light at other wavelengths. Further suppression of stray light is performed using a variable slit aperture[69]. Despite these numbers, a photomultiplier tube (PMT)[70] still detects around 24×10^3 photons/s or 24 kilocounts/s (kcps) from a single fluorescing ion and around 2 kcps when the ion is dark. In general, the photon count numbers are normalized by the duration of the detection time window, which is usually on the order of a few ms. Given the PMT's dark count rate of ~100 Hz, around 95% of the "clicks" recorded when the ion is dark are from background light originating from the detection laser beam.

By recording the number of detected PMT pulses N times, two photon count distributions corresponding to the two cases above can be identified in a histogram. Due to the low overall detection efficiency, they can always be approximated by Poissonian distributions with a mean value of $\bar{x}$ and standard deviation of $\Delta x = \sqrt{\bar{x}}$ [90]. Ignoring the finite lifetime of the $D_{5/2}$ state for the moment (see below), the threshold to optimally discriminate between the two distributions is then given by $\sqrt{\bar{x}_0 \cdot \bar{x}_1}$. Figure 3.15.a shows an example histogram for a single ion and illustrates, how the relative weight of each *population* is derived from the number of counts that fall into each distribution.

---

[66] To calculate the actual scattering rate, eight-level Bloch equations describing the full $S_{1/2}-P_{1/2}-D_{3/2}$ Λ-system have to be solved numerically [85] for a given set of experimental parameters.

[67] Silloptics, Germany; effective focal length f = 66.8 mm, pupil diameter D = 34 mm

[68] Semrock, SEM-FF01-390/18-25

[69] Owis, Spalt 40

[70] Sens-Tech, P25PC; quantum efficiency at 397 nm ~27 %

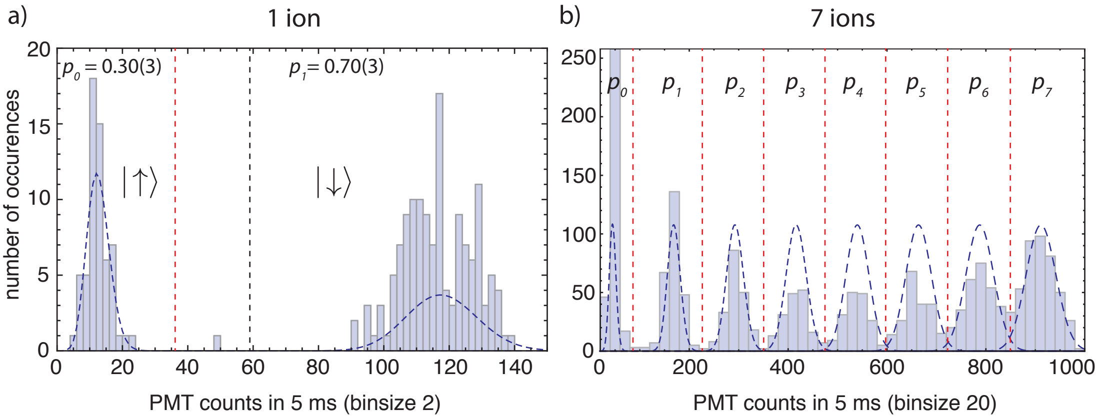

Figure 3.15.: PMT detection histograms
State discrimination thresholds are indicated by the red line(s) and dashed blue lines correspond to Poisson distributions calculated for the mean dark and (multiples of) the mean bright photon counts of a single ion. **a)** Histogram of photon counts registered in 200 trials after a superposition state has been prepared in a single ion. Here, one can infer the coefficients of Eq. (2.1) directly from the populations: $p_0 = |c_\uparrow|^2$ and $p_1 = |c_\downarrow|^2$. The single, well-separated event at 50 photon counts is likely to correspond to a decay of the D-state during the second half of the detection period. To reduce these effects, the threshold should be set around 50% of the bright count rate (black dashed line). **b)** Cumulative histogram over 2050 experiments entailing collective Rabi oscillations of 7 ions. The Poissonian distributions are shown scaled to the same height to better illustrate their increasing overlap.

Extending this approach to n ions, one finds n thresholds and $n+1$ photon count distributions, corresponding to populations $(p_0, \ldots, p_n)$. The subscript refers to the number of bright ions associated with each population. An example of a histogram for 7 ions is shown in Figure 3.15.b. Here, the main problem with the thresholded detection of the overall fluorescence becomes apparent: for large count rates the first distributions are well separated but the following ones begin to overlap at higher mean count rates, leading to state discrimination errors.

A second source of errors is the finite lifetime τ of the $D_{5/2}$ state, which leads to a (small) "tail" of counts extending towards the bright count distribution(s). The likelihood that the D-state decays during a detection time window T can be expressed as $1 - e^{-T/\tau}$ [49]. For the commonly used detection time of $T = 5\,\text{ms}$ this would add an error probability of 0.5%, which can be reduced to ~0.25 % by setting the first threshold a bit higher (Figure 3.15.a). However, with more ions, the decay probabilities add up, yielding 1.75% for 7 ions in the D-state. Clearly, the shortest possible detection time, in which the count distributions can still be separated, is desirable.

For each set of N experiments (*cycles*) carried out on n ions, the raw number of detected counts in each cycle as well as the following derived numbers are recorded:

populations p_j where j ranges from 0 to n, are derived from the ratios of the number of events recorded in each thresholded range and the total number of experiments N. Assuming perfect discrimination, the uncertainty of each probability value p is governed solely by quantum projection noise [22]:

$$\Delta p = \max\left(\sqrt{\frac{p(1-p)}{N}}, \frac{1}{N+2}\right), \tag{3.4}$$

where the second term is given by Laplace's rule of succession for N trials and 2 possible outcomes (bright or dark). It accounts for the non-zero probability that the $N+1^{\text{st}}$ trial yields a different outcome [65]. Without this correction, the extreme cases $p = \{1, 0\}$, which have no projection noise, would underestimate the uncertainty in the measurements made.

mean excitation is the overall probability of finding the n-ion string in state $|\uparrow\rangle$ over N experimental cycles. It is determined as

$$p_\uparrow \equiv p_{n\mathrm{D}} = 1 - \frac{\#\text{ of bright ions detected over all } N \text{ cycles}}{N \cdot n},$$

with an uncertainty given by quantum projection noise, as above.

parity corresponds to the product of the eigenvalues of the σ_z-Pauli operators (Eq. (2.3)) over all n ions: $P = \sigma_z^1 \sigma_z^2 \ldots \sigma_z^n$. It can be calculated from the populations p_j as

$$P = \sum_{j=0}^{n} (-1)^j p_j. \tag{3.5}$$

P is a measure of the mean excitation rescaled to $[-1, 1]$, which effectively corresponds to the summed-up probability of all even populations minus the summed-up probability of all odd populations [65]. In a Ramsey experiment (Section 4.8), this quantity can be used to directly measure the coherence in a joint quantum system of n ions [91, 92]. It is obtained from the amplitude of its $\cos(n\phi)$ oscillation between 1 and -1, where ϕ is the phase of the analysis pulse in the Ramsey experiment.

Camera detection

Aside from the challenges in separating count distributions for larger numbers of ions, threshold-based detection with a PMT cannot uniquely identify the actual quantum state of an ion string. In order to do this, the fluorescence of the individual ions needs to be spatially resolved. For this purpose, a back-lit EMCCD[71] camera[72] is set up about 1.50 m from the objective behind the eastern inverted viewport.

Numerical calculations of the distance of two trapped ions [48] for a given axial confinement allows us to calibrate the spatial resolution of the imaging system. This is done by relating the calculated real space distance to a distance in (fractional) pixels of the camera image. These are obtained from a fit to distributions that result from a summation of pixel brightness values orthogonal to the orientation of the ion string. The procedure is illustrated in Figure 3.16 below and yields a magnification of 24.6 for the current imaging setup.

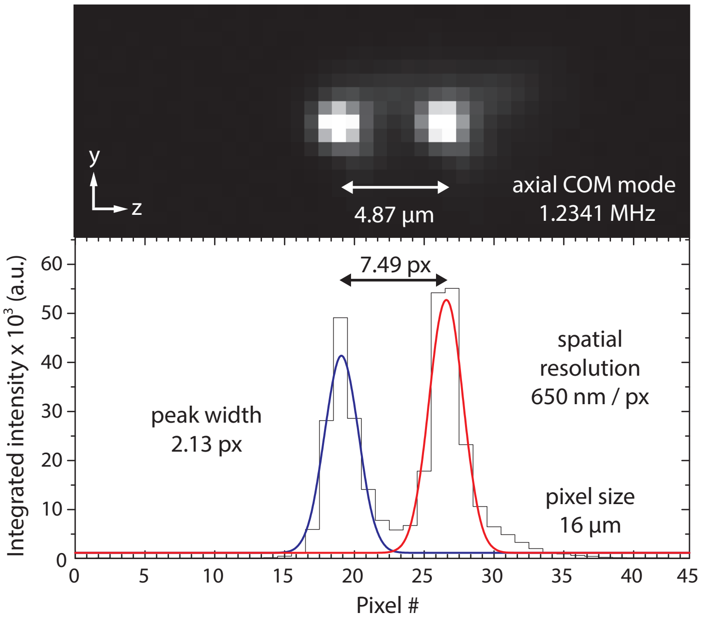

Figure 3.16.: Camera calibration
Using the calculated distance between two ions in a linear string [48] the spatial resolution of the imaging system can be calibrated using fits to the intensity integrated along the y-direction. Here, simple Gaussian fits are used to obtain the center pixel coordinates of the ion positions.

---

[71] electron-multiplying charge-coupled device

[72] Andor iXon “blue” DU-897-DCS-BBB, 512 × 512 pixel of 16 × 16 µm size; quantum efficiency at 397 nm ∼74 %; custom AR-coated front window with 98.27 % transmission at 397 nm

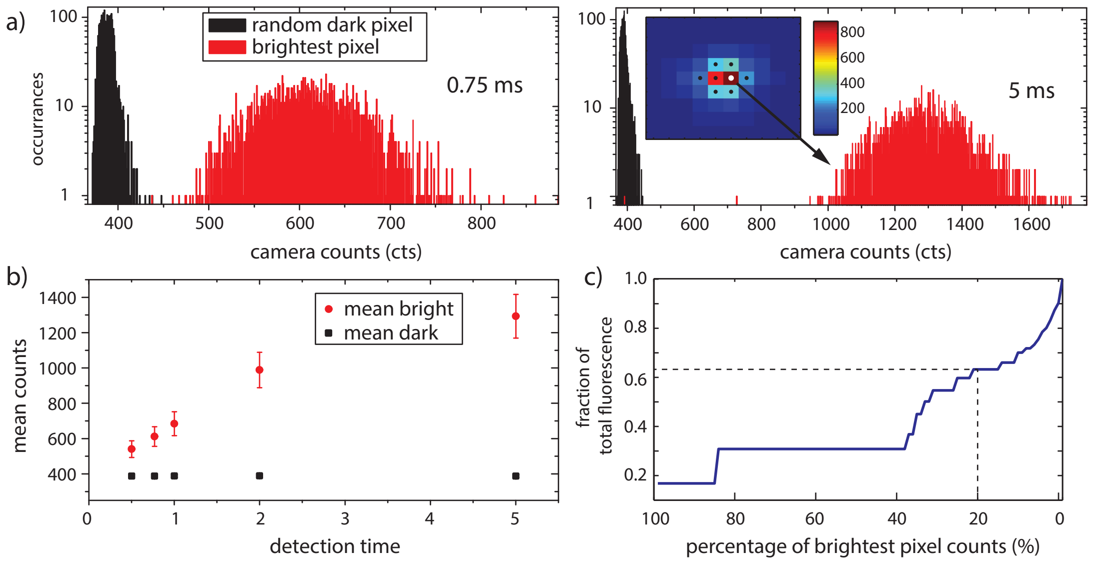

Figure 3.17.: EMCCD camera performance
a) Count rate histograms of the brightest pixel (white dot in the inset picture) and a randomly chosen dark pixel for different detection times. Due to the electronic gain, the distributions are wider than Poissonian statistics would suggest. Additional *pixels of interest* with at least 20 % of the bright pixel's fluorescence are marked with a black dot. **b)** Scaling of the mean count values of a dark and the brightest pixel for different detection times. At longer detection times starting between 2-5 ms the number of counts seems to saturate. **c)** Total fluorescence used in state detection (white and black dots in inset) as a function of the cut-off percentage with respect to the brightest pixel (white dot). An identical curve is obtained for 0.75 ms and 5 ms detection time. [2100 images of a 20x20 pixel region of interest, EMCCD gain 200]

A Labview[73] program running on a dedicated computer determines the state of each ion and the corresponding state of the whole quantum register in each of the N camera images taken per data point. It uses an algorithm, implemented in Matlab[74], similar to the maximum likelihood detection method discussed in ref. [89].

Initially, a set of reference images is used to determine dark and bright reference histograms for a selection of bright pixels clustered around the location of each ion. The histograms shown in Figure 3.17.a represent only the single brightest pixel which amounts to about 17 % (18 %) of the total detected fluorescence in 0.75 ms (5 ms). Starting at the maximum fluorescence, additional *pixels of interest (POI)* are added up to a 20 % of the maximum brightness value. In this way, more than 60 % of the total detected fluorescence is taken into account in the state detection (Figure 3.17.c)

---

[73] "Laboratory Virtual Instrument Engineering Workbench", visual programming language by National Instruments

[74] programming language for mathematical computing developed by Mathworks

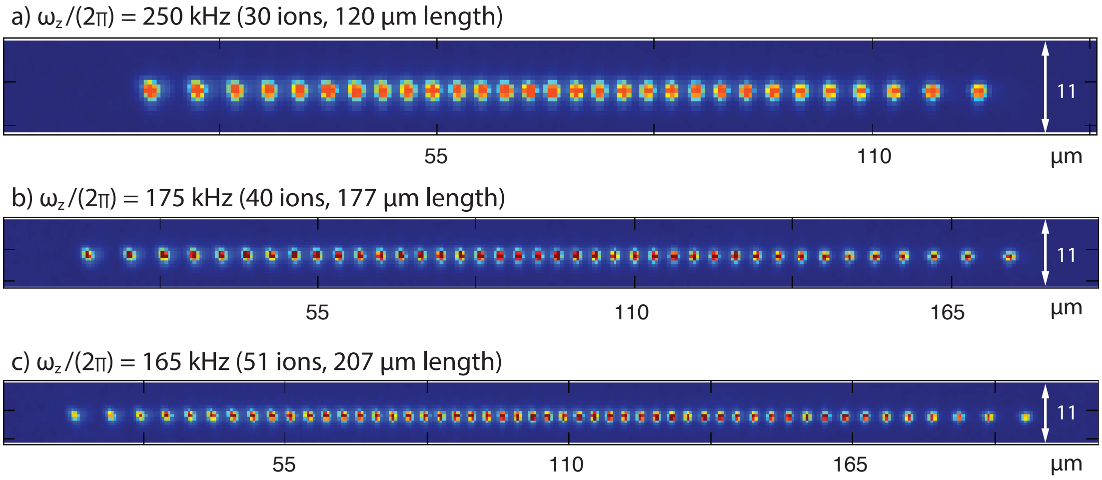
a) $\omega_z/(2\pi)$ = 250 kHz (30 ions, 120 µm length)

b) $\omega_z/(2\pi)$ = 175 kHz (40 ions, 177 µm length)

c) $\omega_z/(2\pi)$ = 165 kHz (51 ions, 207 µm length)

Figure 3.18.: Imaging performance
False color images of long linear ion chains at a radial confinement $\omega_r/(2\pi) \approx 3.2\,\text{MHz}$. The innermost of the 51 ions are 3.3 µm apart at the axial confinement given above.

that proceeds as follows: For each ion, the POI provide sets of pixel coordinates whose log-likelihood sum is calculated for each ion in every image in order to decide whether it was bright ($s = 1$) or dark ($s = 0$) with respect to the reference data.

The specific quantum state Q of a string of n ions is labeled by associating the leftmost[75] ion with the least significant bit of a binary string:

$$Q = \sum_{i=1}^{n} s_i\, 2^{i-1}.$$

Examples for a 7-ion mapping are: 1111111 = 127, 0111111 = 126 and 1111110 = 63. The corresponding value for each of the N cycles is stored and, over all cycles, the mean excitation per ion is calculated. In addition to storing the online-processed data, the raw images are archived to a compressed file to have the ability to post-process data at later times and to allow for consistency checks independent of the analysis algorithm.

The spatial resolution provided by the camera makes it possible to perform ion-resolved state detection in longer strings (Figure 3.18), which was crucial in the more recent experiments listed in Appendix A.

---

[75] This deliberately goes against the binary convention to facilitate working with tensor products, where the individual quantum systems are counted from the left.

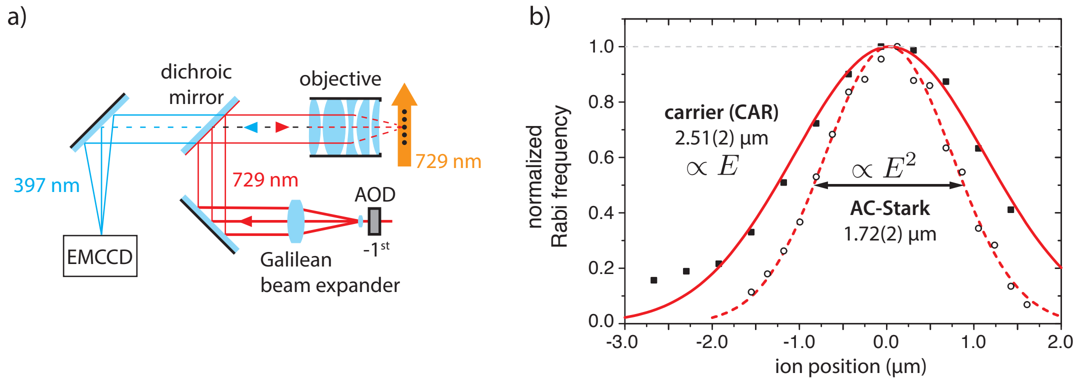

Figure 3.19.: Single ion addressing
a) Optical setup of the laser beam used to address single ions within a string. The collimating lens of the Galilean beam expander (1:22) is mounted on a motorized 3-axis translation stage.
b) Beam profiles obtained from fitting Rabi oscillations of a single ion recorded at different positions along the trap axis. The *carrier* measurement uses a single laser pulse of the focussed beam, while the *AC-Stark* measurement uses the pulse sequence depicted in Figure 3.20 on the following page. With the magnetic field shielding enclosure (cf. Figure 3.24) open, beam pointing induced by slow thermal drifts (∼1 min measurement time for each data point) lead to an estimated additional 100 nm uncertainty for both beam diameters.

3.5. Single ion addressing

In addition to collecting fluorescence light at 397 nm, the custom objective at the eastern viewport is also used to focus a laser beam at 729 nm to a small spot at the location of the ions. In order to achieve a spot size close to the diffraction limit[76], a Galilean beam expander enlarges the incoming beam before it is focussed by the objective as shown in Figure 3.19.a. Its final FWHM diameter can be measured by recording Rabi oscillations on the carrier transition of a single ion shifted to different positions along the orthogonal trap axis. A high spatial resolution[77] is obtained by applying an additional small DC offset voltage of opposite sign, e.g. ±30 V, to the tip electrodes. A constrained Gaussian fit to the normalized Rabi frequencies Ω then allows us to extract the beam width in relation to the electric field E of the focussed laser beam. The same measurement can be made in relation to its intensity ($\propto E^2$) using the composite pulse sequence described in the following. The measurement results shown in Figure 3.19.b above illustrate how the composite sequence leads to a narrower beam which is routinely used to address single ions in chains like those shown in Figure 3.18 before.

---

[76] *theoretical* $1/e^2$ diameter: $2\omega = (4\lambda/\pi)(f/D) \approx 1.8\,\mu\mathrm{m} \rightarrow \mathrm{FWHM} = 2\omega/1.699 = 1.1\,\mu\mathrm{m}$

[77] At 950 V tip voltage the resolution is 186 nm/dV where dV is the voltage difference between the tips.

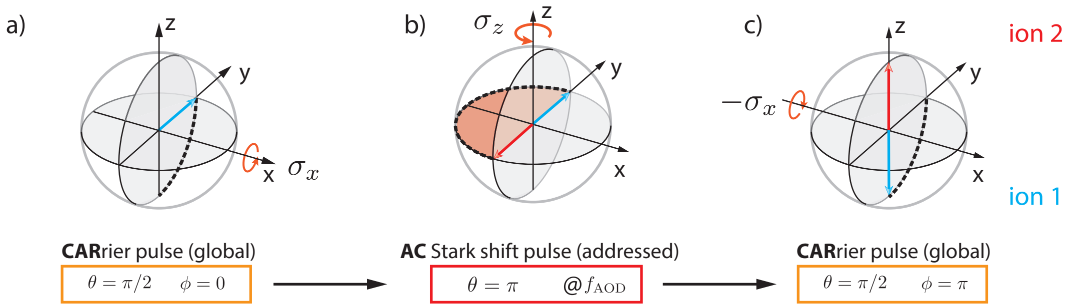

Figure 3.20.: Composite pulse sequence affecting two ions
a) A beam illuminating both ions equally induces a $\sigma_x(\pi/2)$ rotation on the carrier that takes them from the electronic ground state $|{\downarrow}\rangle \equiv |-\rangle_z$ to $|+\rangle_y$. **b)** The tightly focussed laser beam is directed at ion 2, which is located at the acousto-optic deflector (AOD) position associated with f_{AOD} (see text). The light field induces an AC Stark shift equivalent to a $\sigma_z(\pi)$ rotation. **c)** A final $-\sigma_x(\pi/2)$ rotation brings ion 1 back to $|-\rangle_z$ while ion 2 is brought to $|+\rangle_z$.

The composite laser pulse sequence, illustrated in Figure 3.20, affects two ions as follows: First, a global $\pi/2$ laser pulse resonant with a carrier transition rotates both ion's state vector into the equatorial plane of the Bloch sphere. Then, an addressed laser pulse of length t is sent in with a frequency detuning between $-50\,\mathrm{MHz}$ and $-90\,\mathrm{MHz}$ from the carrier transition (depending on the specific f_{AOD}, see below). Given its large detuning from the carrier transition, the pulse only induces an AC-Stark shift following Eq. (2.16). It effectively rotates the addressed ion's state vector within the equatorial plane by an amount proportional to $\delta_{\mathrm{AC}}\, t = (\delta_{\mathrm{D}} - \delta_{\mathrm{S}})\, t$, where δ_{S} and δ_{D} are the energy level shifts induced by the off-resonant light field in the respective states of the chosen qubit. A final, third laser pulse is set to be a global $\pi/2$ pulse on the carrier transition again. With its optical phase shifted by π, it effectively undoes the first $\pi/2$ pulse for the non-addressed ion and completes the rotation to for the addressed ion.

Note that at this large detuning from the carrier frequencies, the AC-Stark shifts δ_{S} and δ_{D} induced by the light field mainly result from couplings to the far-detuned dipole transitions $\mathrm{S}_{1/2} \leftrightarrow \mathrm{P}_{1/2}, \mathrm{S}_{1/2} \leftrightarrow \mathrm{P}_{3/2}$ and $\mathrm{D}_{5/2} \leftrightarrow \mathrm{P}_{3/2}$, respectively. Compared to the values $\delta_{\mathrm{AC}}/(2\pi)$ on the order of $10\,\mathrm{kHz}$ seen in reference [93], the tight focus of the laser beam allows us to reach AC-Stark Rabi frequencies of up to $\Omega_{\mathrm{AC}}/(2\pi) \approx 100\,\mathrm{kHz}$.

Due to the strongly off-resonant nature of the AC-Stark pulse, phase coherence is only required between the two $\pi/2$ pulses. Therefore, they can be sent onto the ions using a beam path different from that of the tightly focussed laser beam.

To ensure that the $\pi/2$ pulses interact equally along a string of ions, they are sent into the trap using the *global* 729 nm beam of the southern viewport (cf. Figure 3.6).

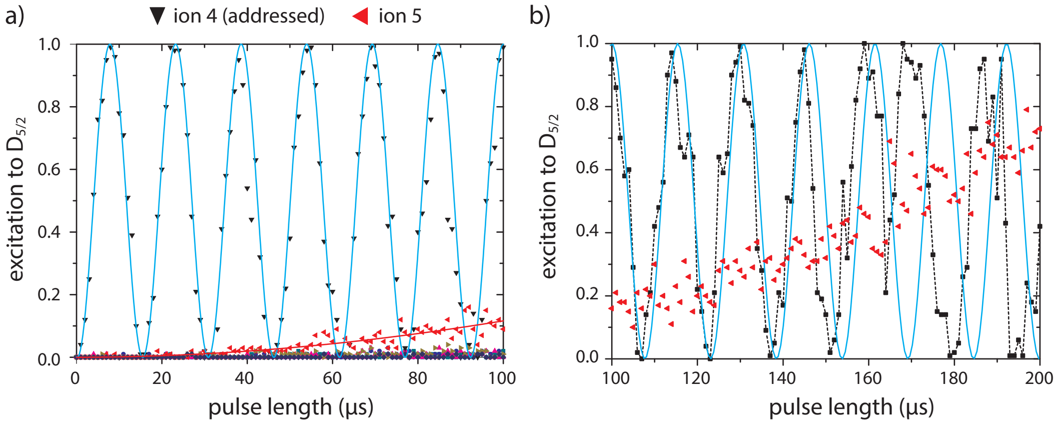

Figure 3.21.: Addressing error and intensity fluctuations
a) Addressed Rabi flops on the center ion of a 7-ion string held at 500 V tip voltage, which corresponds to $(\omega_z/(2\pi) = 898\,\text{kHz})$. The beam is slightly misaligned leading to a weak excitation of the neighboring ion 5 (but not 3) at a distance of 3.3 µm. The ratio of the fit Rabi frequencies $\Omega_{\text{ion4,AC}}/\Omega_{\text{ion5,AC}}$ reveals an addressing error of $\epsilon(4)_{\text{AC}} \approx 3.5\%$. **b)** At longer times, variations due to intensity fluctuations become apparent in phase-jumps that lead to a visible mismatch of the initially fit Rabi oscillation (continued in cyan) and the observed data (black squares). In this second data set black lines connect the individual data points to help visualize the phase-jump around a pulse length of $\sim 165\,\mu\text{s}$ and provide a guide to the eye.

This beam is focussed through the tip electrodes with a $2\omega_0$ diameter chosen such that its Rayleigh range[78] ensures equal illumination of all ions in a string.

Figure 3.21 shows *AC-Stark* Rabi oscillations driven on the center ion in a string of seven ions, held at an axial confinement where the neighboring ions are $\pm 3.3\,\mu\text{m}$ away. As a figure of merit for the addressing quality on ion n, the ratio $\epsilon(n) = \max(\Omega_{n\pm1}/\Omega_n)$ is specified as *addressing error* associated with cross-talk. Careful alignment of the focussing objective and the beam expander's collimating lens in relation to the objective is crucial for the composite pulse sequence. Alignment errors in which an ion is left on the slope of the laser beam's Gaussian envelope worsen the effect of vibration-induced beam pointing, which is translated into intensity variations as illustrated Figure 3.21.b.

Despite a nonzero addressing error, however, in most cases only a single π-pulse on an addressed ion is needed to "hide" it in a $D_{5/2}$ Zeeman level different from the one used to encode the qubit in the remaining ions. Once separated in frequency space in this way, global beams can be used for most operations. It should be noted though, that a superposition state hidden in the D-manifold will still acquire (small) phase shifts from the off-resonant beams, which may need to be taken into account in later operations.

---

[78] $z_{\text{R}} = (\pi\omega_0)/\lambda$ is the distance at which the area of the beam's $1/e^2$ intensity doubles.

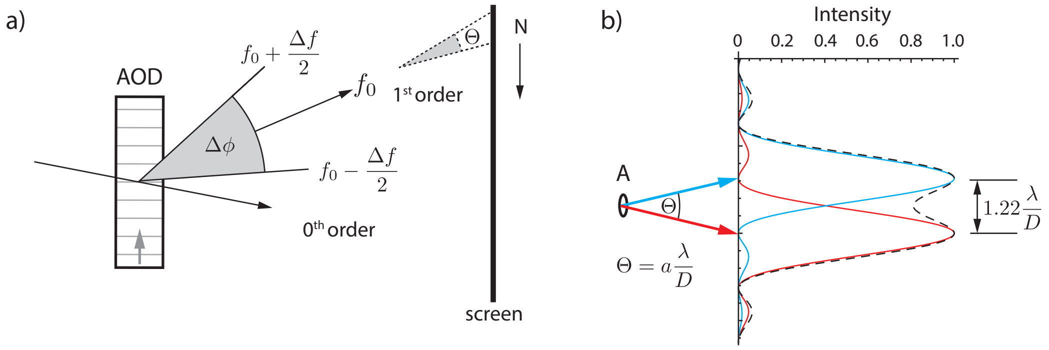

Figure 3.22.: Deflector resolution
a) Number of resolvable spots N as the ratio of the angular deflector range $\Delta\phi$, here given by the AO bandwidth Δf and center frequency f_0, and the beam divergence Θ (angles not to scale). **b)** Rayleigh criterion: two spots can be resolved at wavelength λ, if the brightest spot of the first diffraction pattern coincides with the first dark fringe of the second one. The aperture factor a is 1.22 for a uniformly illuminated circular aperture of diameter A and $4/\pi \approx 1.273$ for a non-truncated ($A \geq 1.7D$) Gaussian beam of $1/e^2$ diameter D [94].

A key addition to the newly built setup of trap II is the ability to address individual ions in long strings like those shown in the preceding section. The predecessor trap I used offset voltages on the tip electrodes to shuttle the desired ion into the tightly focussed addressed beam over a distance of 10 µm within 40 µs [50]. For longer strings in trap II, however, this approach becomes impractical as the switching speed has to be kept low enough to avoid motional heating during ion transport and yet high enough to allow for arbitrary addressing of multiple ions that could be at opposite ends of a string[79]. The $^{40}\mathrm{Ca}^+$ linear trap experiment at the university has long been using an electro-optical deflector (EOD) to, instead, move the focussed beam between different ions [96]. Here, the switching speed ($\sim$ 30 µs) is given by the time it takes to (dis)charge the deflector's electrodes. However, its deflection range is limited to 3-5 mrad/kV, depending on the specific model[80], and its speed is mainly determined by the amount of current the high voltage amplifier used to drive the device can deliver.

Apart from speed, a central figure of merit for optical deflectors is the number of resolvable spots N, i.e. the number of non-overlapping angular beam widths within the deflection range $\Delta\phi$. It is given by $N = \Delta\phi/\Theta$, where Θ is the angular spreading of the optical beam derived from the Rayleigh criterion illustrated in Figure 3.22.b.

---

[79] Fast adiabatic switching using more complex electrode configurations and waveforms has been demonstrated in Boulder and Mainz (see reference [95] for a summary).

[80] Leysop Ltd., United Kingdom

To achieve a larger deflection range with a small deflector footprint, the setup of trap II has been equipped with an acousto-optic deflector (AOD) [97, 98]. In such a device, the switching speed is given by the acoustic transit time $\tau_a = D/v_a$ of an acoustic wavefront travelling at speed v_a through the optical beam of diameter D. The deflection range is given by the ratio of optical wavelength λ to the range of acoustic wavelengths supported by the AOD's crystal as $\Delta\phi = \lambda\Delta f/v_a$. Here, Δf is the frequency bandwidth of the device as illustrated in Figure 3.22.a. From this, the number of resolvable spots N, if one assumes a non-truncated Gaussian input beam, can be calculated to equal

$$N = \frac{\pi}{4}\frac{D\Delta f}{v_a} = \frac{\pi}{4}\tau_a\Delta f,$$

illustrating its equivalence to the time-bandwidth product $\tau_a\Delta f$ that is often specified for AO devices. Consequently, in contrast to an acousto-optic modulator where speed and extinction ratio are the main concern, a deflector is optimized for a large diameter, highly collimated beam and often employs a different crystal orientation to derive benefit from lower acoustic velocities[81].

The shear-mode deflector[82] used in the experiment runs at an RF center frequency of $f_0 = 70\,\text{MHz}$ and is specified for a bandwidth of $\Delta f = 40\,\text{MHz}$. The corresponding deflection range of $\Delta\phi = 47\,\text{mrad}$ even surpasses the acceptance angle of the addressing optics (cf. Figure 3.19.a) and no longer is a limiting factor in the experiment.

The AOD's first order diffraction efficiency (measured at 633 nm for 0.7 W RF power) shows a relatively flat plateau close to a value of 92 % over a frequency range of ±10 MHz around f_0 with a fall-off to ~72 % at the ±20 MHz bandwidth edges. The resulting changes in light intensity are taken into account by calibrating the addressed Rabi frequency $\Omega_{n,\text{AC}}$ for each ion n individually at its corresponding location f_{AOD}. This approach is also necessitated by the fact that aberrations in the addressing optics are only corrected for beam paths that traverse the center of the focussing objective – for larger deflection angles this is no longer the case in the current setup.

The switching time (random access) is close to 12 µs for the currently employed beam position and diameter. Here, about 8 µs correspond to the response time between the application of an RF signal and the rising edge of the optical signal and about 4 µs are contributed by the optical rise time to $\geq 98\%$ intensity. The warmed-up device exhibits less than 1 % intensity variations during optical pulses of typically $\leq 20\,\mu\text{s}$ duration.

---

[81] e.g. TeO_2: $v_a = 4.2\,\text{mm}/\mu\text{s}$ (longitudinal mode [001]), $v_a = 0.62\,\text{mm}/\mu\text{s}$ (shear mode [110]) [98]

[82] Gooch&Housego, model 45070-5-6.5DEG-633

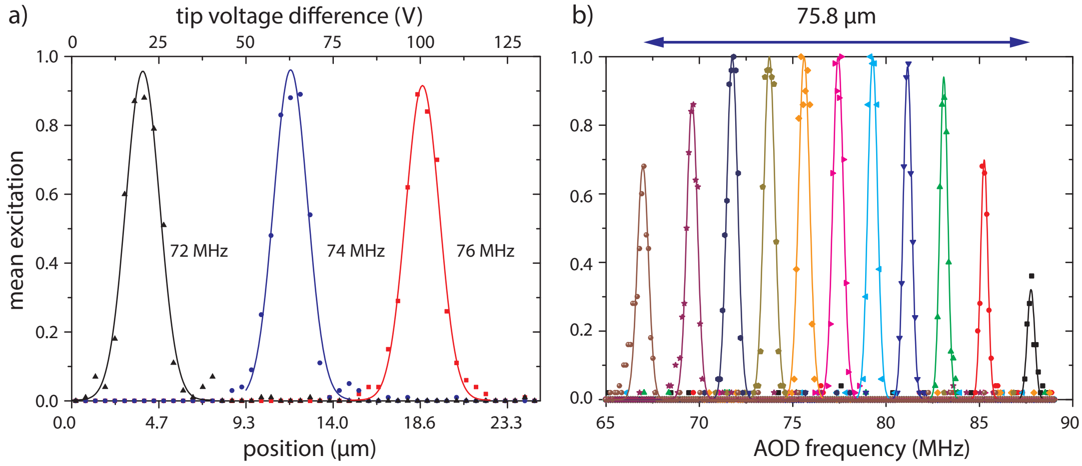

Figure 3.23.: Addressing range
a) For three different values of f_{AOD} a single ion is shifted along the trap axis using offset voltages applied to both tip electrodes held at 950 V. The corresponding center positions of the addressed beam are obtained from Gaussian fits and allow to calibrate the lateral focus shift at the location of the ions to 3.79 µm/MHz. **b)** AOD frequency scan across 11 ions confined at a tip potential of 30 V ($\omega_z = 214\,\mathrm{kHz}$) using an AC pulse length that corresponds to a π-pulse on the center ion. At this confinement the innermost ions are 6.7 µm apart.

In order to calibrate the lateral focus shift at the location of the ions provided by the deflector, for three RF values sent to the AOD a single ion is shifted perpendicular to the focussed beam using an offset voltage applied symmetrically around 0 V to both tip electrodes. The mean excitation to the $D_{5/2}$ state is measured at each location and a subsequent Gaussian fit determines the center positions of the focussed beam. The results, illustrated in Figure 3.23.a, yield a resolution of 3.79 µm/MHz showing that a very precise control of the focus position is possible by adjustments of the RF sent to the AOD. With the current set of relay and focussing optics, at least 11 ions can be addressed even at a relatively low axial confinement corresponding to large ion separations (Figure 3.23.b). However, for deflections >90 µm, beam clipping sets in, leading to significant aberrations.

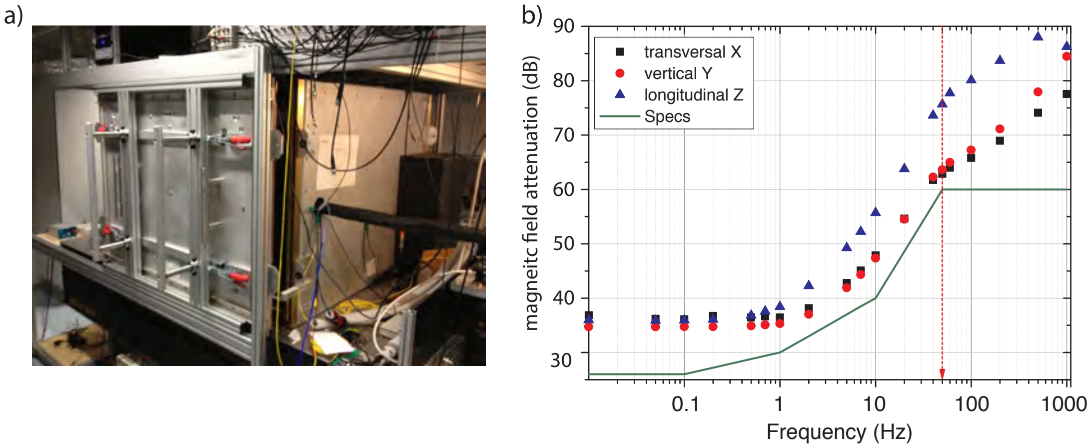

Figure 3.24.: Magnetic field shielding enclosure
a) Shielding enclosure with additional sliding mechanism for easier handling of the removable doors (> 30 kg each). **b)** Factory test results of the empty shielding enclosure measured with a Bartington MAG-03 MCL-70 sensor according to industry norm ASTM A 698-A. Static fields are attenuated by 35 dB (corresponding to an amplitude ratio of 56). The red line marks the strongest magnetic field noise component at 50 Hz, where an attenuation of 62 dB (factor 1256) was measured.

3.6. Magnetic field shielding and quantization field

To attenuate (fluctuating) ambient magnetic fields, the trap vessel is placed inside a magnetic field shielding enclosure[83]. The shield consists of a shell made from a soft magnetic nickel-iron alloy (Magnifer[84]) enclosed in a welded aluminum case fitted with two removable doors weighing ∼ 330 kg in total. Using electrically isolated feet, the vacuum assembly is directly mounted to the optical table through 6 small holes in the bottom of the shield. In addition, a further 6 openings are distributed on the remaining 3 sides to allow access for electrical wires, fiber optic cables and imaging optics. According to the factory measurement shown in Figure 3.24.b the shielding properties extend from high values at AC fields down to DC fields[85]. However, due to a number of electric cables running to and from the trap assembly the effective AC magnetic field amplitudes at the location of the ion cannot be reduced as much. A Ramsey experiment allows us to determine the 50 Hz magnetic field amplitude to be

---

[83] IMEDCO AG, Switzerland

[84] trademark of ThyssenKrupp

[85] According to the current WMM2010 model (`http://www.ngdc.noaa.gov/geomag-web/`) the earth's magnetic field in Innsbruck, Austria (2° declination, 63° inclination) has three components: 215 mGauss horizontal north, 9 mGauss horizontal east and 429 mG towards the ground. However, deviations due to locally varying rock compositions should be expected in the Alps.

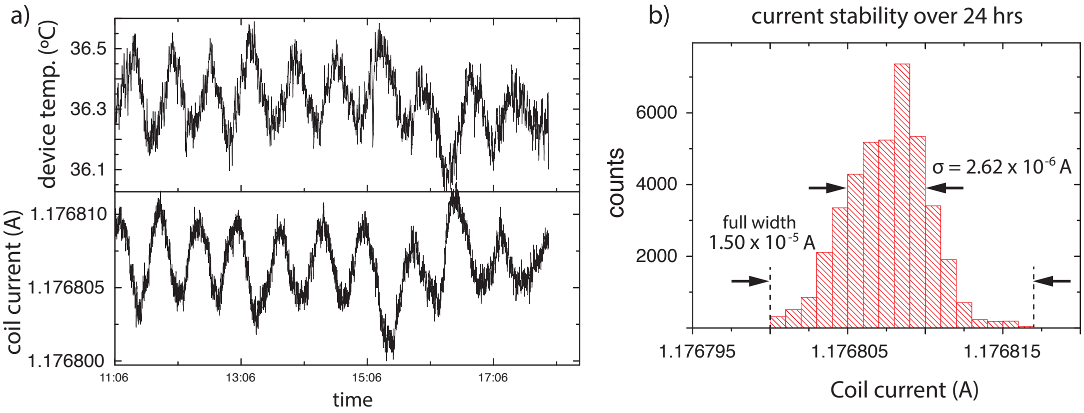

Figure 3.25.: Current driver stability over 24 hours
a) Correlation between the (measured) current driver temperature (PT100 resistor) and the output current (Keithley DMM 2002). The oscillations directly line up with the laboratory air conditioning temperature cycle. **b)** Histogram of the DC current values measured over 24 hours.

around 30 to 40 µG (cf. Section 4.8.2). Under these conditions, parity oscillations fit to data computed from Eq. (3.5) show a contrast of $\geq 80\,\%$ at a wait time of 10 ms.

To lift the degeneracy of the Zeeman levels (Section 2.2), a pair of magnetic field coils with 350 windings[86] each is mounted to the north and south viewports (cf. Figure 3.6). A current of 1 A produces a magnetic field of 3.62 G[87] at the trap center. For practical reasons, the ratio of the distance between the coils (l = 300 mm) and their inner diameter ($2r$ = 115mm) does not fulfill the Helmholtz criterion ($l = r$). However, the dominant part of a small magnetic field gradient, observed along the trap axis, is linear (potentially generated by the ion pumps magnets). When working with longer strings and the most magnetic field sensitive transitions, additional coils in quadrupole configuration can be used for compensation.

The current sent through the coils is actively stabilized using a home-built PI-regulator with a stable reference resistor[88]. The driver's stability, investigated over 24 hours in Figure 3.25, shows a relative stability of the DC value around the 10^{-6} level, even without a dedicated temperature stabilization. In measuring the voltage across the coils on a spectrum analyzer, AC fluctuations can be compared in relative strength. The strongest noise component is found at the power-line frequency of 50 Hz with a total magnitude of 2×10^{-5}.

---

[86] Oswald Elektromotoren, Germany; copper wire with a cross section of 2.0×1.25 mm^2

[87] 1 G = 10^{-4} T

[88] Vishay, VCS 302

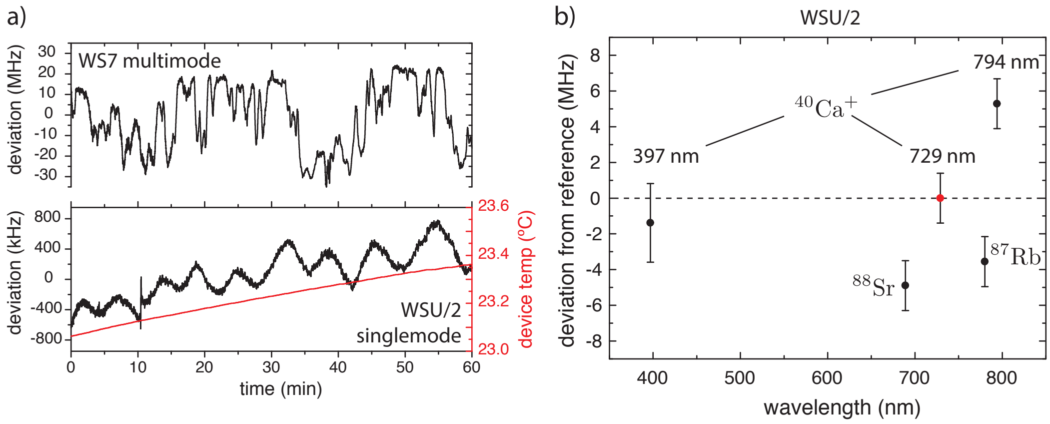

Figure 3.26.: Wavelength meter accuracy and stability
a) Comparison of two different models of HighFinesse wavelength meters monitoring the same cavity-locked Toptica DL pro laser at 866 nm. The deviations are given with respect to the median of all measured frequency values. **b)** Accuracy of the WSU/2 wavelength meter with respect to published literature values (see text).

3.7. Wavelength meter

The laser wavelengths used in the experiment are monitored using a HighFinesse WS7 wavelength meter in conjunction with an 8-channel multimode fiberswitch. Its absolute measurement accuracy is specified to be 60 MHz (150 MHz when using multimode fibers) with a measurement resolution of 10 MHz. For the spectroscopy experiment discussed in Chapter 6, a HighFinesse WSU/2 model with a resolution ≤ 1 MHz was used in parallel. Figure 3.26.a demonstrates the relative stability of the two devices with respect to the median of the values measured over 60 minutes.

The absolute accuracy of the WSU/2 model is specified to be 2 MHz within ±2 nm of the calibration wavelength. The accuracy over a wider range was checked in collaboration with the Sr-Rb experiment of Florian Schreck (formerly IQOQI, now University of Amsterdam) [99]. Figure 3.26.b shows data taken with the device continuously referenced to the laser at 729 nm. The line center of the $S_{1/2} \leftrightarrow P_{1/2}$ transition in ^{40}Ca$^+$ was determined with the help of coherent population transfers and analysis on the $|S_{1/2}, m_j = +1/2\rangle \leftrightarrow |D_{5/2}, m_j = +3/2\rangle$ transition by first initializing a single ion in $|S_{1/2}, m_j = -1/2\rangle$ and then varying the frequency of an optical pumping pulse at 397 nm for various laser powers and pulse lengths. As the UV light is generated by frequency doubling, the laser's fundamental wavelength at 794 nm could be compared as well. In addition, the $5s\,^1S_0 \rightarrow 5p\,^3P_1$ intercombination line of atomic ^{88}Sr at 689 nm and the $5s\,^2S_{1/2} \rightarrow 5p\,^2P_{3/2}$ D2 line of atomic ^{87}Rb at 780 nm were measured.

Both Fizeau-interferometer-based wavelength meters should be regularly calibrated (at least every 6-12 months for the WS7) using a reference laser at a known wavelength for which the device shows a deviation of at most 400 MHz. If this is not possible, an interferometer spectrum of a known reference can be recorded and sent to the manufacturer, who can manually convert it into a usable calibration file. With the calibration, the overall offset *and* fringe shifts *between* the built-in interferometers are corrected. Without regular calibration – especially at short wavelengths – the correlations between the different interferometers can break down, resulting in deviations or jumps of many GHz or even nanometers[89]. In fact, due to at least 5 years without calibration, a systematic shift of around 18 GHz was observed in the WS7 readings when compared with known reference wavelengths of $^{40}\mathrm{Ca}^+$ and $^{88}\mathrm{Sr}$. The necessary re-calibration subsequently had to be performed with the help of the manufacturer.

The WSU/2 provides a second fiber port to allow for near-continuous calibration during measurements. Its measured frequency value, however, differs from the main input port by around 30-40 MHz (changing with device temperature and air pressure). Accounting for this correction, however, the data shown in Figure 3.26.b shows a remarkable accuracy over a range much larger than that guaranteed by the manufacturer's specification.

3.8. Experiment control and sequencing

A schematic overview of the different components involved in the data collection and control of the experiment is shown in Figure 3.27 on the next page.

Its central node is a *Control PC* on which a large multi-threaded Labview[73] program[90] coordinates the various devices used in the experiment and provides a graphical user interface (GUI) to the user. A companion program running in Labview on a separate *Camera PC* is dedicated to the EMCCD camera and performs a Matlab-based state detection in real time. Throughout the course of this thesis, both programs have been heavily extended and modified to support work on long ion strings and the simultaneous handling of two Ca^+ isotopes. The changes include the implementation of a completely new camera detection and state discrimination routine, as well as the addition of an adaptive "refreeze feature" that takes various escalating measures to recrystallize an ion string quickly after a collision with background gas has been detected.

---

[89] private communication, HighFinesse GmbH (April 2013)

[90] "QFP 2.1": "Quantized Fluorescence Program" (version 2.0 originally written by Timo Körber)

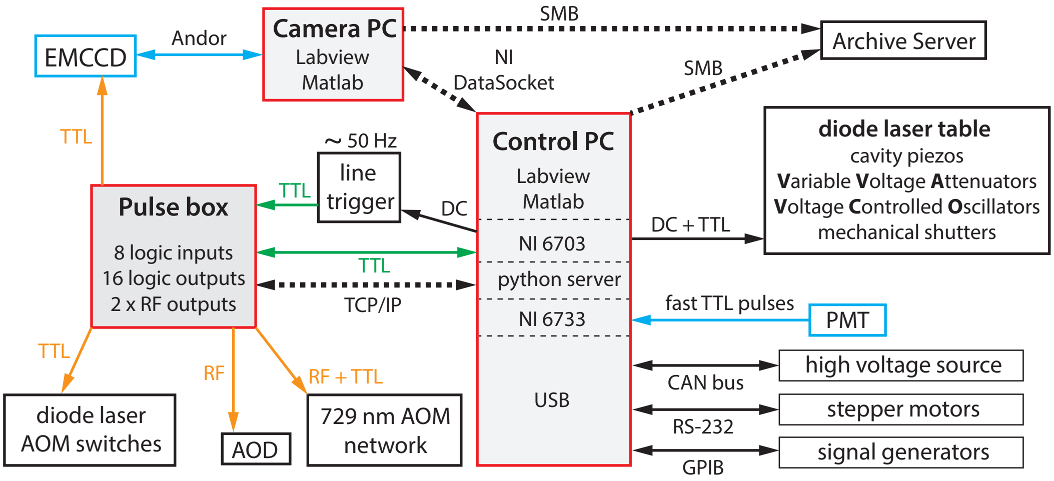

Figure 3.27.: Computer control and interconnects
(red boxes) The three central control components of the experiment are two PCs and the "Pulse box" (see text). The latter provides timing control with nanosecond resolution within each of the programmed sequences and generates phase-controllable radio frequencies (orange arrows). TTL trigger signals *(marked in green)* mark the start and stop of the execution of a set of *cycles* implementing a pre-programmed sequence. Optionally, each cycle itself is synchronized to the power line frequency using an additional line trigger. The data gathered via PMT and EMCCD *(marked in blue)* is acquired and processed by the camera and control PCs. Asynchronous interconnects are marked in *black*. The dashed lines correspond to Ethernet connections.

Pulse sequences, written in python[91], correspond to one complete experimental cycle and are compiled for a given parameter set by a software server based on the Innsbruck branch [79] of the MIT-NIST-ARDA pulse sequencer[92] project [100]. The compiled program is then sent over Ethernet to the FPGA-based "Pulse box", which is equipped with two independent direct digital synthesizers (DDS) and multiple digital in- and outputs. The device coordinates all laser pulses in their relative timings and durations as well as the phase, pulse shape and frequency of the RF signals sent to the AOMs used in coherent optical manipulations. Fluorescence counts (cf. Section 3.4) are gathered by the control and camera PCs within triggered acquisition windows and processed in batches of N experiment cycles.

Once acquisition and processing are complete, the results are displayed to the user or automatically analyzed to implement feedback, e.g., in the laser frequency drift lock described in Section 4.8.1.

---

[91] high-level programming language

[92] http://sourceforge.net/projects/pulse-sequencer/

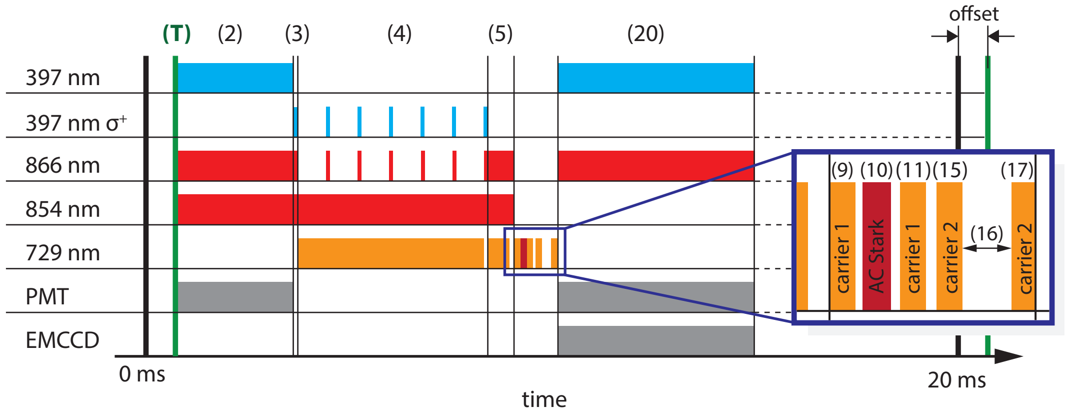

Figure 3.28.: Typical sequence of single experimental cycle.
The numbered labels correspond to the lines in listing 3.1 below. (T) Line trigger with offset, (2) Doppler cooling (3 ms), (3) optical pumping at 397 nm (20 µs), (4) continuous sideband cooling (5 ms), (5) frequency resolved optical pumping at 729 nm (500 µs), (9–17) Coherent operations, (20) Detection (5 ms)

An exemplary pulse sequence is shown in Figure 3.28. Electric power supplies emit spurious magnetic fields at the power line frequency (50 Hz in Europe), which cause time-dependent Zeeman shifts of the states that encode the qubit and, consequently, lead to a loss of coherence. To mitigate this problem, a line trigger device[93] can be used to synchronize the experiment with the line cycle (cf. Section 4.8.2). Ideally, a variable offset is introduced as well in order to shift the coherent operations into a part of the line cycle at which the rate of change of the magnetic field amplitude is smallest.

Each pulse sequence is stored in a text file, which is initially parsed by the control software. There, XML-style tags (`<TAG>` ... `</TAG>`) are used to identify parts that command the setting of GUI parameters, the acquisition mode (processed data or raw photon counts) and list the variables and transitions to be used in the specified experiment. All the relevant data together with the actual `<SEQUENCE>` commands (see listing 3.1 for an example) is then passed to the python server where it is translated to machine code that is subsequently sent to the Pulse box over Ethernet.

Coherent manipulations to be carried out with laser pulses at 729 nm can be invoked with a dedicated command that is structured as follows:

$$\texttt{rf\_729}(\textit{ion}, \textit{rotation angle } \theta, \textit{phase } \phi, \textit{transition}, \text{musec\_timebase} = \textit{FALSE}).$$

For each *transition* defined in the GUI, the desired laser beam power, transition frequency (both parameters for AOM 11), pulse shape as well as the information which

---

[93] home-built circuit based on STMicroelectronics M74HC123AB1R

beam path is supposed to be used (TTL combination that activates a specific AOM branch shown Figure 3.9.III) are stored globally. In addition, each *transition* holds an array of "π-times" $t_\pi = \pi/\Omega$, specific to each *ion*, representing the time it takes to carry out a π-pulse at the current coupling strength Ω (determined by laser power and beam focus). Generally, array elements beyond the first are only needed in addressed transitions, where the array index is used further to access a list of f_{AOD} values that correspond to each ion's location (AOD frequency). Laser power, together with pulse shape and duration t yield the pulse area that corresponds to the *rotation angle* $\theta = \Omega t$. It is given to the command in terms of multiples of t_π or, depending on the setting of the musec_timebase boolean, directly as a pulse duration t in µs. Finally, the *phase* argument ϕ allows the user to chose the phase of the RF sent from the Pulse box's DDS to AOM 11 that eventually produces the pulses.

With these arguments, the `rf_729` command can be used to implement arbitrary rotations around the z- or any equatorial axis of the Bloch sphere on either all or a chosen single ion. For the x,y and z axes the map to the rotation matrices is as follows:

$$\texttt{rf\_729}(1, \theta, 0 * \text{math.pi}, \text{"carrier"}) \quad \longleftrightarrow \quad U_x(\theta) = \exp\left(-i\frac{\theta}{2}\sigma_x\right) \tag{3.6}$$

$$\texttt{rf\_729}(1, \theta, 0.5 * \text{math.pi}, \text{"carrier"}) \quad \longleftrightarrow \quad U_y(\theta) = \exp\left(-i\frac{\theta}{2}\sigma_y\right) \tag{3.7}$$

$$\texttt{rf\_729}(2, \theta, 0 * \text{math.pi}, \text{"AC-Stark"}) \quad \longleftrightarrow \quad U_z(\theta) = \exp\left(-i\frac{\theta}{2}\sigma_z\right) \tag{3.8}$$

Here, the mapping in (3.6) of the *phase* $\phi = 0$ to a σ_x rotation is an arbitrary choice since the atomic states supporting the qubit are identified with the eigenstates of the σ_z operator. The first pulse in a coherent set of laser pulses sets the absolute phase reference $\phi = 0$ and is thereby simply defined to be a σ_x rotation around $|+\rangle_x$. More information on the effects of the different rotations is given in Appendix B.1.

The z-axis rotation in (3.8) (corresponding to an AC-Stark shift as described in Section 3.5) is carried out on *ion* 2. To do this, the addressed beam path has to be set in the *transition* object "AC-Stark". A global stark shift on all ions is implemented by typing a large (> 40 MHz) frequency shift directly into the GUI's transition object. The same technique (using shifts that are only on the order of a few MHz) is used to globally address motional sideband transitions.

The pulse sequence illustrated in Figure 3.28 is realized by the python command sequence shown on the following page.

Listing 3.1: Python section of a sequence file parsed by QFP

```
 1 <SEQUENCE>
 2 incl.DopplerCooling40(gl_doppler_length, gl_repump_length)
 3 incl.OpticalPumping40(gl_pump_length)
 4 incl.SBCooling40(gl_SBCool_time, gl_SBCool_reps, gl_pump_length)
 5 incl.OpticalPumping40_729(gl_pump_length_729)
 6
 7 # use composite pulse sequence to "hide" ion number 2 in carrier 1 qubit
 8 if hide_ion :
 9 ␣rf_729(1,0.5,0,"carrier1")
10 ␣rf_729(2,1,0,"AC Stark")
11 ␣rf_729(1,0.5,math.pi,"carrier1")
12
13 # Ramsey experiment using carrier two on all ions that "see" carrier 2
14 if Ramsey :
15 ␣rf_729(1,pulse_length,0,"carrier2", musec_timebase=TRUE)
16 ␣seq_wait(wait_time)
17 ␣rf_729(1,pulse_length, phase * math.pi,"carrier2", musec_timebase=TRUE)
18
19 # simultaneous PMT and camera detection
20 incl.PMTDetection(gl_det_time, gl_cam_time)
21 </SEQUENCE>
```

All arguments marked in blue, are defined in the `<VARIABLES>` section (not shown) of the sequence file such that they are extracted from the GUI before the sequence is passed on to the python server for compilation. Transition objects defined in the GUI, marked in red, are referred to by strings in quotation marks.

In lines 2–5 of the sequence, the `incl` commands embed standard sequence blocks used for laser cooling and optical pumping that will be described in the following chapter. They are separate files that contain definitions in terms of TTL pulses and repetitions. The `If` statements (line 8 and 14) query the boolean value of a corresponding GUI variable such that the following (tab-indented!) blocks of commands can be switched on and off at will, without the need to modify the sequence file.

The control software also provides an additional scripting language that can be used to implement complete multi-part measurement sequences combined with automated evaluation and (if desired) feedback to experiment parameters. The calibration of laser beam coupling strengths, measurements of the cavity drift and current magnetic field are implemented in this fashion.

4. Trap characterization and experimental techniques

This chapter provides a brief hands-on overview of experimental techniques. It is written as a practical guideline based in the context of the setup, characterization and everyday use of trap II. Hence, the first sections cover the initial steps in setting up an ion trap before moving on to the basic techniques and calibrations required for high-fidelity qubit manipulations.

4.1. First steps

The assembly and bake-out procedure used for trap II along with residual gas analyzer spectra obtained during the process is provided in Appendix C. At this point, it is assumed that the setup's calcium oven has undergone its activation procedure and that the residual pressure of the vacuum vessel has reached the low 10^{-10} to 10^{-11} mbar level. The next steps involve the optics setup, neutral atom fluorescence detection, single ion trapping as well as coarse stray field compensation and trap frequency calibration.

1. **Imaging setup**
   An appropriate lens or multi-lens objective is set up to image the center of the ion trap onto a PMT and/or EMCCD camera for detection. Here it is useful to be able to send in light from the opposite side of the detector and image the trap's shadow onto a white sheet of paper at the detector's location. In case of a single PMT, imaging and the specific magnification are not that important as there is no spatial resolution. However, as much fluorescence as possible should be collected by using large NA optics as close to the trap as possible.

2. **Atomic fluorescence**
   With the detector(s) in place and shielded against stray light, the laser beam at 422 nm is sent through the tip electrodes. If such an arrangement is not possible,

care has to be taken that the beam runs through the field of view of the detectors and – *most importantly* – that it runs at a 90° angle to the atomic beam such that the Doppler shift due to the motion of the hot atoms is minimized.

Now, the laser's frequency is scanned slowly around the atomic resonance while PMT or camera are checked for a correlated signal. It is worthwhile to keep possible wave meter deviations in mind (cf. Section 3.7) and, if no other reference is available, set up a Doppler-free [59, 101] or photogalvanic spectroscopy [102] for cross-checks. Also, be aware that the light intensity of many diode laser sources varies as they are scanned over many GHz, which should not be mistaken as a correlated PMT signal.

3. **Ion fluorescence**

   For the next step, the trap's AC and DC voltages need to be operational. It is also advantageous to already have a magnetic field applied, which provides a well-defined quantization axis in order to prevent unwanted optical pumping and dark resonances that could reduce the resonance fluorescence yield. The 866 nm repumper and 397 nm cooling/detection beam (both linearly polarized) are now overlapped and sent into the imaged trap region. Ideally, the 397 nm beam direction has a projection onto all three trapping axes to improve laser cooling and fluorescence. However, even sending both beams through the tip electrodes, i.e. perfectly along one the weak trap axis, will yield some fluorescence that can be used as a starting point. With the ion trap operating at low voltages[94], the oven and both photoionization beams are turned on, which should lead to a continuous accumulation of ions. To make fluorescence detection easier, an optical bandpass filter[68] should be installed in front of the PMT/camera to block all but the ion's fluorescence wavelength. To further help distinguishing an ion fluorescence signal from the background light, it is useful to employ a differential detection technique. Here, the 866 nm repumper light is turned off periodically and the count rate difference between the on and off state is used to extract a signal while suppressing PMT counts from background scatter. As soon as a signal is visible, the beam alignment can be optimized while iteratively loading fewer and fewer ions at stepwise lowered oven currents.

   Compared to a single or a few crystalized ions, the fluorescence signal of an ion cloud will have a very *weak* frequency response as the lasers at 397 nm and 866 nm

---

[94] In our case, we used around 20 V tip voltage and sent 1.5-2 W to the helical resonator (cf. Figure 3.4).

are scanned. On the PMT, the transition from an ion cloud to an ion crystal is visible as a kink (sudden decrease in fluorescence) on the red-detuned side of the 397 nm resonance. Towards the resonance frequency, a higher fluorescence yield is obtained as, once crystalized, the ions experience a much smaller Doppler-shift and spend more time near the resonance's transition frequency [103, 104].
Once the beams are aligned, the signal-to-noise ratio (SNR) can be further increased by a variable-slit aperture[69] to cut off stray light. Combined with spatial filtering using a pinhole at an intermediate focus in the imaging system, SNRs exceeding 200 can be achieved [105] even in the presence of stray light. A background-free detection method [106], which requires two more laser wavelengths at 850 nm and 854 nm, provides an alternative approach.

4. **Coarse micromotion compensation (see also Section 4.5)**
Using a single ion, a first attempt can now be made to compensate stray electric fields in the trapping region that shift the ion away from the nodal line of the trap's RF field. Depending on their magnitude, the stray fields can lead to a significant degradation of the fluorescence signal and result in unstable trapping conditions that cause frequent ion losses. Another clear hint of strong micromotion is the observation of fluorescence counts when the 397 nm laser is blue-detuned from the $S_{1/2} \leftrightarrow P_{1/2}$ resonance. Here, the fast RF-driven micromotion induces Doppler shifts that broaden the fluorescence spectrum symmetrically [107] and wash out the sharp edge otherwise observed at the resonance (cf. Section 4.2 below).
Two strategies can be employed to achieve a coarse compensation: (I) Using a fast RF switch or directly controlling the RF power, the ion's position is marked on the camera at high RF confinement, where it is forced into the RF null in the radial direction. Reducing the radial confinement again, the stray field-induced shift becomes visible in the imaging plane. With the appropriate compensation electrode, the ion can now be shifted back to the previously marked position. No information, however, can be obtained in the direction orthogonal to the imaging plane. (II) Stray fields *perpendicular* to the 397 nm beam cause a driven motion *in* the direction of the beam (cf. Figure 4.7), which leads to the already mentioned Doppler-broadening of the resonance line. Through variation of the compensation voltage perpendicular to the 397 nm laser beam (as it is kept red-detuned from the resonance), one can then attempt to narrow the observed width of the transition by minimizing the observed fluorescence count rate.

5. **First measurement of the motional oscillation frequencies**
   At this point, it is worthwhile to perform a measurement of the motional oscillation frequencies in the trap. This can be done by applying an oscillating drive voltage to one of the compensation electrodes. The 397 nm laser frequency is first set to a point where the fluorescence rate is at roughly half of its maximum value and then the drive frequency is varied. As soon as it becomes resonant with a motional oscillation frequency, the ion is resonantly heated which leads to a Doppler broadening of the transition and a corresponding increase in the fluorescence count rate. In this way, the radial mode splitting naturally present in the trap can be determined. When the frequency difference between the radial modes is very small, efficient Doppler cooling will only be possible with the addition of a DC offset potential U_r (Eq. (3.1)), applied to one pair of the blade electrodes.

4.2. Doppler cooling and fluorescence detection

The $S_{1/2} \leftrightarrow P_{1/2}$ transition at 397 nm wavelength is used for both laser cooling and state detection. About one in fifteen excitations of the $P_{1/2}$ state (cf. Table 2.2) will decay to the metastable $D_{3/2}$ state. Hence, the 397 nm laser is always used in conjunction with a repumper laser at 866 nm that returns the ion to the cooling or detection cycle by coupling the metastable state to the $P_{1/2}$ manifold. The Zeeman manifolds of the $S_{1/2}$, $P_{1/2}$ and $D_{3/2}$ states contain a total of eight energy levels that can give rise to dark resonances induced by the simultaneous presence of a magnetic field and the two laser fields. In order to minimize the ensuing modification of the lineshape(s) (see, e.g., [49, 85]), it is advisable to keep the 866 nm repumper laser tuned to a frequency slightly above the $P_{1/2} \leftrightarrow D_{3/2}$ resonance.

In the simplified picture of a two-level atom interacting with a traveling laser field of a power level much below the transition's saturation intensity, Doppler cooling achieves a minimum temperature (Doppler limit) of $T_\mathrm{D} = \hbar\Gamma/(2k_\mathrm{B})$ at a detuning of $-\Gamma/2$ [108]. Here, $\Gamma = 2\pi \times 22.4\,\mathrm{MHz}$ is the linewidth of the transition and k_B is the Boltzmann constant. The Doppler temperature ($\sim$0.5 mK for Ca^+) can be related to a mean phonon number $\bar{n} = k_\mathrm{B}T_\mathrm{D}/(\hbar\omega) = \Gamma/(2\omega)$ at a given oscillation frequency ω in the trap. For a typical axial confinement of $\omega/(2\pi) \approx 1\,\mathrm{MHz}$ and a Lamb-Dicke parameter η between 0.06 and 0.08, this shows that the Lamb-Dicke regime $\eta^2(2\bar{n}+1) \ll 1$ (cf. Section 2.4) can easily be reached with Doppler cooling alone. At the detuning of $-\Gamma/2$, however, the fluorescence count rate is lower than on resonance, which goes against the aim of

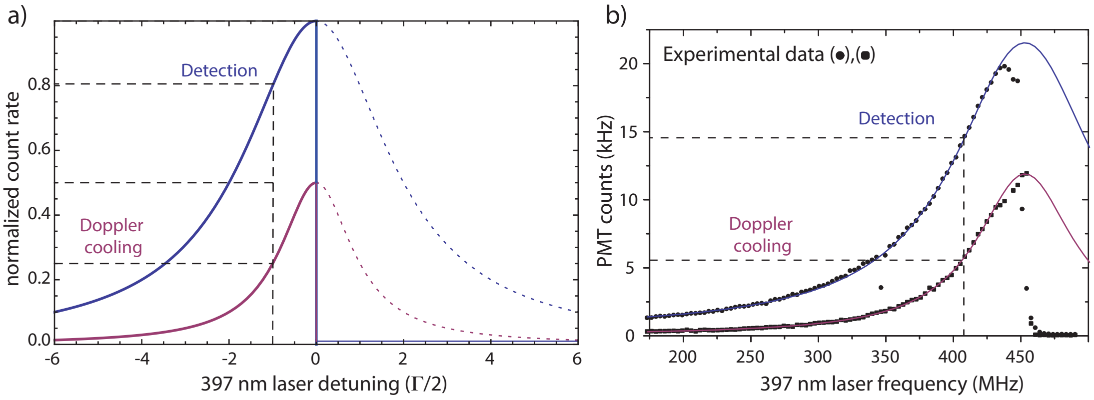

Figure 4.1.: $S_{1/2} \leftrightarrow P_{1/2}$ **line profile at 397 nm**
a) Lorentzian line shapes for different laser powers. After establishing a maximum fluorescence count rate for the state detection, the Doppler cooling power is set to produce at most half the number of counts on resonance, before the laser frequency is red detuned until, again, half the counts are observed. **b)** Experimental data illustrating the broadening of the transition's natural linewidth $\Gamma = 2\pi \times 21.6\,\mathrm{MHz}$ [38] by the magnetic quantization field of $B = 4.2\,\mathrm{G}$ and the presence of the repumper light field at 866 nm. Lorentzian fits to the data yield widths of 127 MHz for the detection and 87 MHz for the Doppler cooling power level. They are certainly not ideal and it would be advisable to further vary the settings to narrow them. Additionally, imperfect micromotion compensation could be contributing to the observed line broadening.

scattering as many photons as possible during state detection (Section 3.4). Therefore, a higher laser power level is used during the detection phase. This way, much more fluorescence can be obtained with minimal danger of heating the ion, which happens as soon as the 397 nm laser frequency crosses the resonance. This is illustrated in the theoretical fluorescence profiles shown in Figure 4.1.a by the sharp cut-off at the resonance. The adjacent Figure 4.1.b shows experimental data of the same cases together with Lorentzian fits. Here, the difference between the ideal two-level approximation and the real experiment becomes apparent as Zeeman shifts and the presence of the second light field at 866 nm broaden the line significantly beyond its natural linewidth.

Doppler cooling in ion traps is usually carried out using only a single laser beam as opposed to the six-beam geometry found in, for example, an optical molasses used to cool neutral atoms. This is made possible by the three-dimensional confinement provided by the trapping potential. It necessitates, however, that the direction of the cooling beam has a projection on all trap axes and that the oscillation frequencies in all directions differ [108]. In an ideal linear Paul trap, symmetric application of the radial voltages (i.e. $+U_{\mathrm{rf}}$ to one electrode pair and $-U_{\mathrm{rf}}$ to the other) generates a potential that is cylindrical around the axial direction, yielding radial frequencies that are degenerate ($\omega_x = \omega_y$). The absorption of photons from the laser beam provides cooling in a direction determined by its k-vector, while orthogonal to it, the spontaneously emitted photons will cause heating. A splitting in the radial mode frequencies, either present naturally due to imperfections and voltage geometry or induced by U_r in Eq. (3.1), turns the radial trapping potential's circle into an ellipse. This breaks the symmetry in the direction of the radial electrodes and leads to radial motional modes that now both have a projection onto the cooling beam's k-vector. The rate at which energy is being transferred between the two degrees of freedom is inversely proportional to their frequency difference $\Delta\omega_{x,y}$. In practice, it is therefore desirable to have a radial splitting between a few tens and 100 kHz to reach the Doppler limit in the radial motion.

4.3. Optical pumping

For fully coherent state manipulations, the qubit ground state first needs to be initialized by *optical pumping*, which transfers all population into one of the two $\mathrm{S}_{1/2}$ Zeeman levels. It exploits dipole selection rules ($\Delta m = 0, \pm 1$) to realize a laser-driven pumping cycle in which the decay of the excited state accumulates population in a target state, to which the cycle does not couple. The experiment employs two different ways of optical pumping in direct succession allowing to reach $\gg 99.9\%$ state initialization fidelity.

The first pumping cycle, shown in Figure 4.2.a, uses circularly polarized light at 397 nm to drive a σ^+-transition between $\mathrm{S}_{1/2}$ and $\mathrm{P}_{1/2}$. It relies on the purity of the light polarization seen by the atom to prevent leakage from the $m = +1/2$ state back into the pumping cycle. While the beam geometry (cf. Figure 3.6) ensures an agreement between the direction of the applied quantization magnetic field $\vec{B}$ and the laser beam's $\vec{k}$-vector, stray magnetic fields (e.g. by an ion pump magnet) may rotate the effective B-field vector at the location of the ions slightly, which also allows unwanted $\Delta m = 0$ transitions to be driven. Equally so, a high degree of circular polarization of the light itself has to be ensured by careful alignment using a polarizing element and a quarter wave plate. Commercial equipment[32] can be helpful and allows us to measure a degree of polarization $> 99\%$ for the desired left circularly polarized (LCP) light.

In this context, it is worth noting that there are two naming conventions in use with respect to circular polarizations (Figure 4.2.c): convention 1 uses the handedness of the polarization in respect to the direction of the photon's spin angular momentum ($\vec{p} = \pm\hbar\vec{k}$); convention 2 (often used in engineering and a number of optics contexts) refers to the direction in which the electric field is rotating when the viewer looks towards the source (left = counter-clockwise).

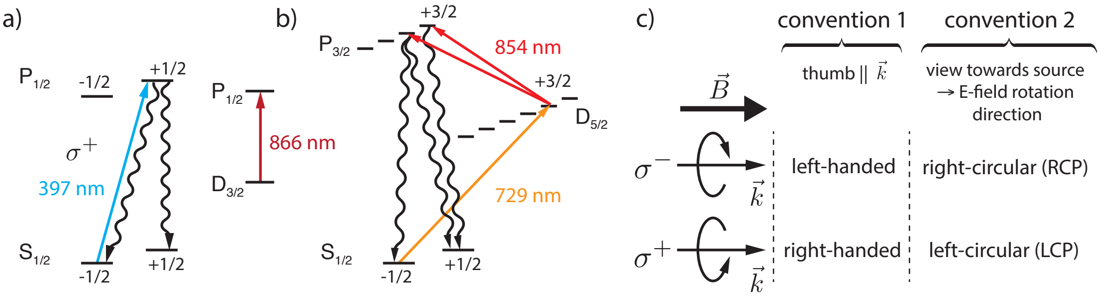

Figure 4.2.: Optical pumping and polarization conventions
a) By dipole selection rules σ^+-polarized light only drives the $\Delta m = +1$ transition, leaving the $m = +1/2$ state dark (transparent to the light). **b)** Frequency resolved optical pumping uses the narrowband laser at 729 nm to selectively couple the $m = -1/2$ state to the $\mathrm{D}_{5/2}$ manifold, from where it is pumped out using light at 854 nm. In both pumping cycles, repumper light at 866 nm ensures that decays to the $\mathrm{D}_{3/2}$ state are returned to the pumping cycle. **c)** Naming conventions for circular polarizations with respect to the direction of propagation and the magnetic field.

The second pumping cycle, illustrated in Figure 4.2.b, does not rely on the magnetic field and light polarization but comes at the price of a much slower cycle time as it incorporates the quadrupole transition at 729 nm, which is much weaker than the dipole transitions. Its narrow linewidth, however, allows for a direct frequency selection of the $|\mathrm{S}_{1/2}, m_j = -1/2\rangle \leftrightarrow |\mathrm{D}_{5/2}, m_j = +3/2\rangle$ transition which is further coupled to the $\mathrm{P}_{3/2}$ manifold in a continuous fashion. Assuming no specific light polarization, the dipole selection rules allow the coupling-laser at 854 nm only to populate the $m = 1/2, 3/2$ Zeeman levels of the P state, such that decays to the $m = +1/2$ target state dominate. Decays to the $\mathrm{D}_{3/2}$ are returned to the pumping cycle by repumper light at 866 nm.

4.4. Rabi spectroscopy

When an experiment is first set up, the magnitude of the magnetic field at the location of the ion is usually not known well enough to calculate the transition frequencies between the Zeeman levels. Therefore, the initial step is to perform spectroscopy over a wide range around the suspected $\mathrm{S}_{1/2} \leftrightarrow \mathrm{D}_{5/2}$ center frequency ν_0 (cf. Figure 2.3).

First, a spectroscopy laser beam needs to be aligned onto the ion. This can be done using *quantum jumps* (Section 6.1): The 729 nm light is shone into the trapping region simultaneously with the detection and repumper lasers at 397 nm and 866 nm. The presence of the additional light fields coupling to the strong dipole transitions leads to a broadening of the $\mathrm{S}_{1/2} \leftrightarrow \mathrm{D}_{5/2}$ transition to a linewidth on the order of that of the $\mathrm{S}_{1/2} \leftrightarrow \mathrm{P}_{1/2}$ transition (Figure 4.1.b). Occasionally, the coherent transfer to the $\mathrm{D}_{5/2}$

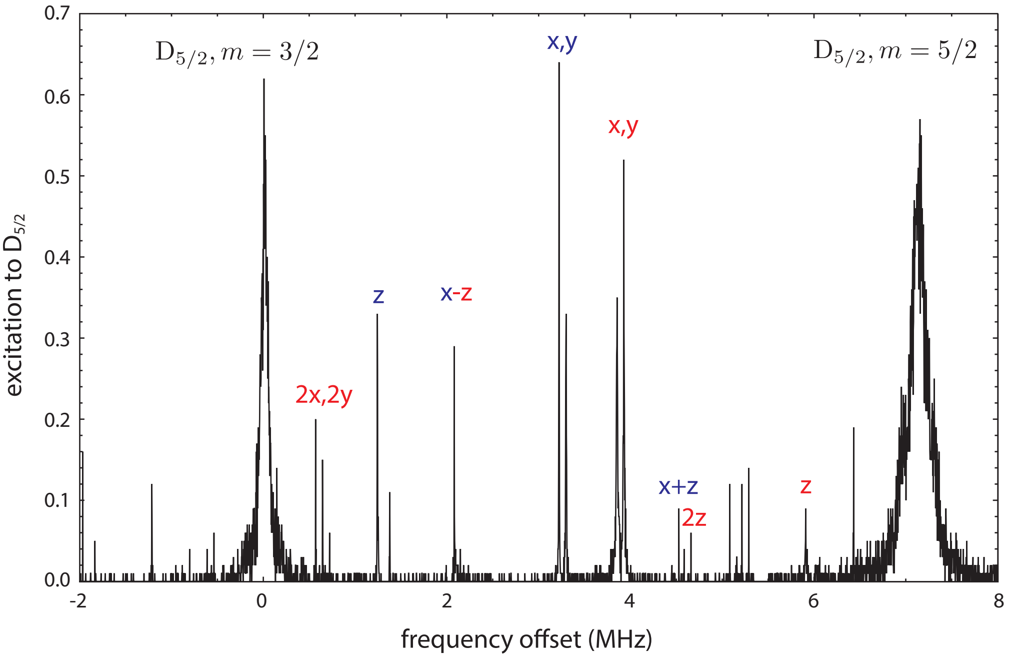

Figure 4.3.: Spectroscopy on the $S_{1/2} \leftrightarrow D_{5/2}$ transition of a single trapped ion
The excitation probability to the $D_{5/2}$ manifold is plotted as a function of the laser frequency offset from the $|S_{1/2}, m_j = 1/2\rangle \leftrightarrow |D_{5/2}, m_j = 3/2\rangle$ carrier transition. The spectrum was obtained using a single 2 ms long laser pulse at a quantization magnetic field of 4.236 G with $\omega_z/(2\pi) = 1.23\,\mathrm{MHz}$ axial and $\omega_{x,y}/(2\pi) = (3.22, 3.30)\,\mathrm{MHz}$ radial confinement, where the radial splitting was induced by a DC offset voltage of $U_\mathrm{r} = 1.5\,\mathrm{V}$. A number of motional sidebands appear around the carriers at multiples of the motional oscillation frequencies, as well as their sums and differences.

state will be successful and a quantum jump occurs causing the fluorescence to cease. The rate at which this happens is directly proportional to the coupling strength Ω of the 729 nm laser. As Ω is proportional to the square of the electric field strength at the location of the ion, it can always be used as an alignment help.

Once the quantum jump rate cannot be increased further, the laser frequency of a single pulse at 729 nm is scanned around ν_0. The resulting spectra, like the one shown in Figure 4.3 above, are recorded by repeating the following sequence N times at each frequency value: (1) Doppler cooling and optical pumping at 397 nm, (2) excitation of the $S_{1/2} \leftrightarrow D_{5/2}$ transition by a single 729 nm laser pulse and (3) state detection using 397 nm light. In addition to the *carrier* transitions between the Zeeman states of the $S_{1/2}$ und $D_{5/2}$ manifolds, the motion of the ion leads to a number of blue and red *sideband* transitions. They appear symmetrically around the carriers at multiples of the motional oscillation frequencies as well as their sum and difference frequencies. These sidebands can be easily identified from their response to a change in

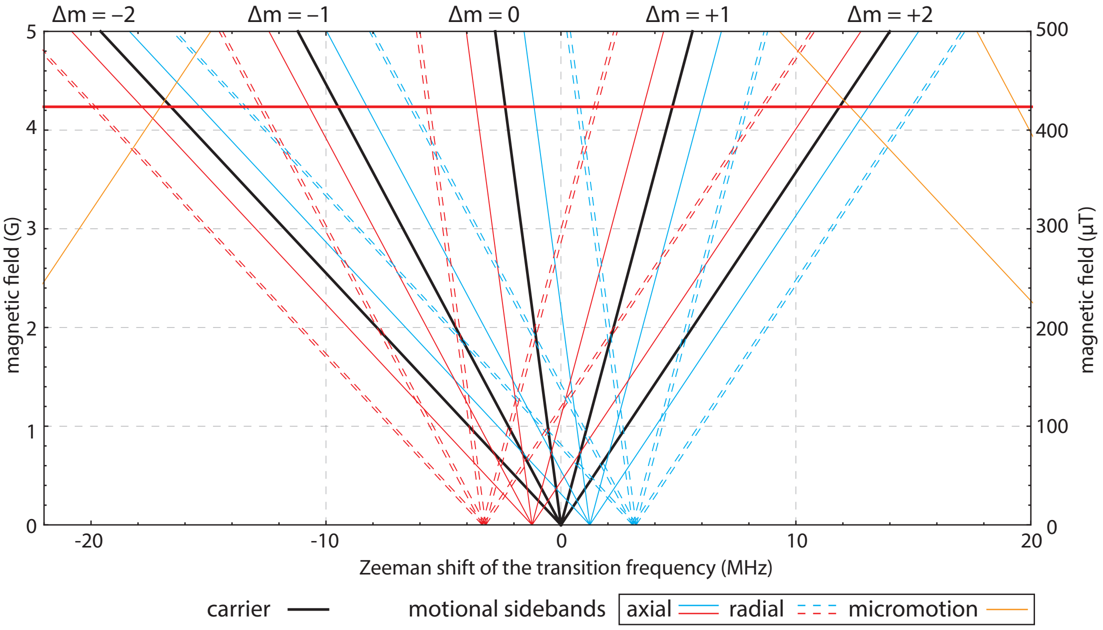

Figure 4.4.: Zeeman shift of the five $|\mathrm{S}_{1/2}, m_j = 1/2\rangle \leftrightarrow |\mathrm{D}_{5/2}, m_j\rangle$ transitions The magnetic field induced Zeeman shift of the carrier transitions (black) following Eq. (2.11) is depicted together with their axial and radial sidebands at $\omega_z/(2\pi) = \pm 1.23\,\mathrm{MHz}$ and $\omega_{x,y}/(2\pi) = (3.2, 3.35)\,\mathrm{MHz}$, respectively. Also shown are parts of the micromotion sideband manifolds at $\Omega_{\mathrm{RF}}/(2\pi) = \pm 28.9\,\mathrm{MHz}$. The red horizontal line marks the quantization magnetic field strength used in Figure 4.3.

the trap's confinement parameters. While optical pumping limits the number of carrier transitions to five (based on the quadrupole selection rules $\Delta m = 0, \pm 1, \pm 2$), a possible complication arises from micromotion that leads to additional sidebands around the carriers at the trap drive frequency $\pm\Omega_{\mathrm{rf}}$. Depending on its strength, they can appear as strong as or even stronger than the carrier transitions, underlining the importance of the coarse micromotion compensation at the beginning.

As illustrated in Figure 4.4 above, at sufficiently high quantization magnetic fields overlaps between carrier and sideband transitions can be easily avoided. In cases where the identification of resonances in the spectrum remains ambiguous, it can be further simplified through the use of the geometrical factors $g_{\Delta m_j}$ in Eq. (2.17). For example, a linearly polarized spectroscopy beam sent in perpendicular to the magnetic field axis ($\vec{k} \perp \vec{B}$ and $\vec{E} \perp \vec{B}$) can only drive $\Delta m = \pm 2$ transitions, which are well separated in frequency. A $\sigma^{\pm}$ circularly polarized beam sent in along the direction of the magnetic field, leaves only one resonance corresponding to $\Delta m = \pm 1$ that can be uniquely identified. Useful plots for other geometries are shown in Figure 4.5 on the following page.

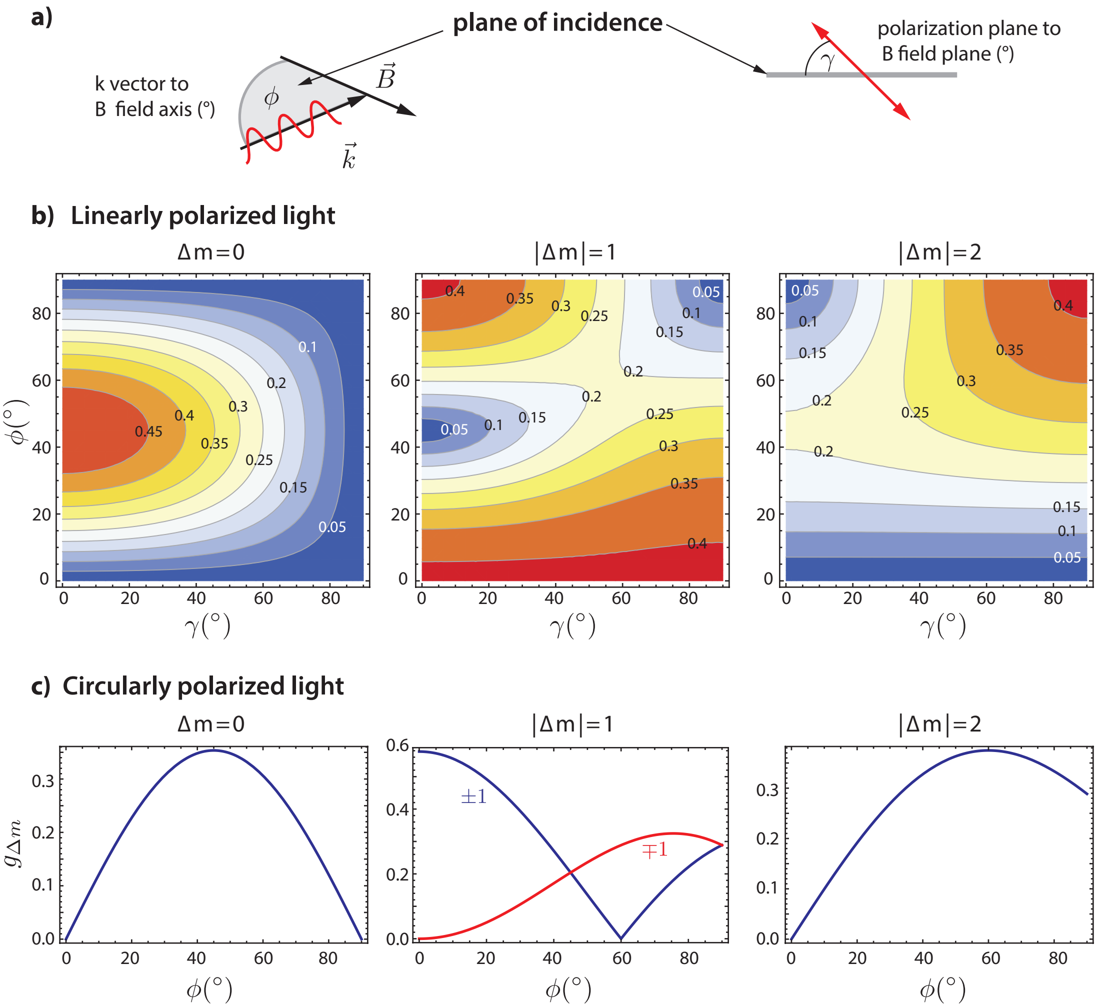

Figure 4.5.: Geometrical factor $g_{\Delta m_j}$ of the coupling strength Ω
The Rabi frequency Ω of the quadrupole transition at 729 nm is scaled by a geometrical factor [48–50] in Eq. (2.17) that can be used to maximize or minimize the coupling strength of specific transitions. **a)** Angles relevant in the definition of the geometrical factor. The angle ϕ between the incoming light beam characterized by its k-vector and the magnetic field direction spans the plane of incidence. A linear polarization vector can be in plane or rotated out of it by an angle γ. Circular polarization is defined with respect to the light beam's k-vector (see also Figure 4.2). **b)** Values of $g_{\Delta m_j}$ given along contour lines for linearly polarized light as a function of incidence angle ϕ and orientation of the linear polarization γ. **c)** Values of $g_{\Delta m_j}$ for circularly polarized light. Only the angle ϕ is relevant as every the circular polarization can be represented as a superposition of two orthogonal linear polarizations. The middle panel illustrates that beyond the desired $\Delta m = \pm 1$ transitions also $\Delta m = \mp 1$ transitions can be driven at every non-zero angle ϕ between the magnetic field vector and the laser beam.

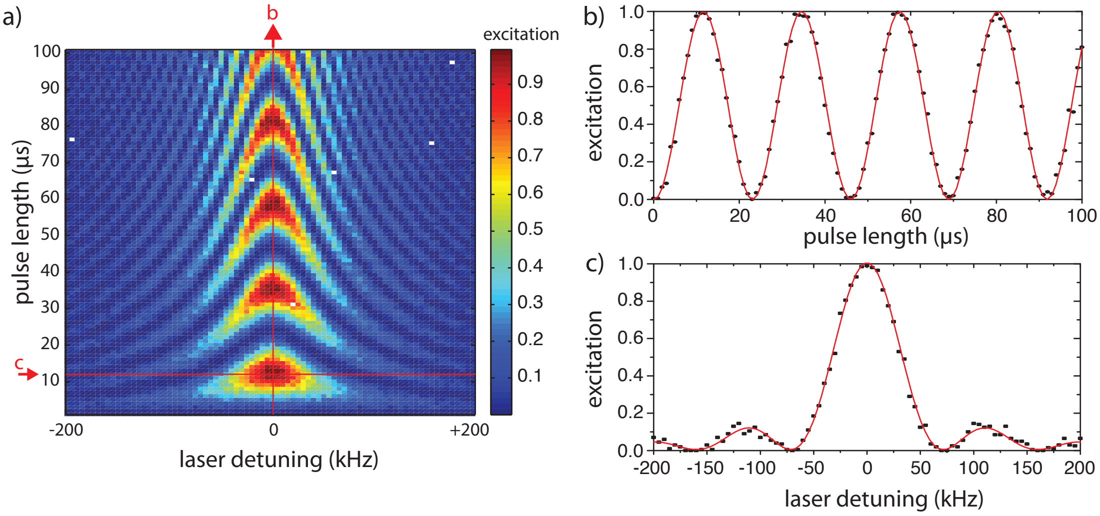

Figure 4.6.: Rabi spectroscopy
a) 2D plot of the mean electronic excitation to $D_{5/2}, m = 5/2$ with a resolution of 1 µs and 5 kHz. Each data point corresponds to the average excitation of two ground state cooled ions in 100 experiments ($\sim$ 6 h total measurement time). The few white points correspond to erroneous (empty) datapoints that the control software failed to reject and retake. **b)** Rabi oscillations as seen in a cut through (a) along the indicated line on resonance. **c)** Fit of Eq. (2.15) to data from a cut through (a) at a fixed pulse time of $t_\pi = 12$ µs.

For illustrative purposes, Figure 4.6.a shows how the excitation to $D_{5/2}$ around one of the carriers changes, depending on the length of the excitation pulse and its respective detuning. The familiar *Rabi oscillations* are obtained when the length of the laser pulse is varied. In the example, a ground state cooled ion ($\bar{n} \ll 1$) was used, such that oscillations do not damp over the time frame observed in Figure 4.6.b. In general, however, higher motional excitations (cf. Figure 2.8) and other decohering processes (for example magnetic field noise) lead to a damping over time, which leads to values close to 0.5 for long pulses. Keeping the time fixed at or close to a π-pulse of length $t_\pi = \pi/\Omega$ while scanning the laser frequency detuning around a resonance, a sinc-like pattern emerges in Figure 4.6.c. Its central peak becomes more and more narrow for longer interrogation times, nicely illustrating the Fourier transform relationship between the time and frequency domain in spectroscopy. Even at short times, this approach is a good way to find the center frequency of a transition, e.g. when refining the position of a motional sideband. An alternative that allows for even more precise frequency measurements on short time scales, is the method of separated oscillatory fields invented by and named after Rabi's student Norman Ramsey, which will be described in Section 4.8 below.

4.5. Micromotion compensation

At any position away from the exact RF null (or nodal line) along the trap's symmetry axis, the ion experiences a force from the electric field gradient generated by the radial electrode voltage(s) V_{rf} at distance r_0. The gradient oscillates at the RF drive frequency Ω_{rf}, which causes a driven motion in addition to the ion's secular motion at frequency ω_r and amplitude x_a characteristic for the (time-averaged) harmonic confinement after laser cooling. The resulting ion motion is well approximated by [109]

$$x(t) = x_a \left(1 + \frac{q}{2} \sin \Omega_{\mathrm{rf}} t\right) \cos \omega_r t,$$

where $q = 2eV_{\mathrm{rf}}/(\Omega_{\mathrm{rf}}^2 m r_0^2)$ with ion mass m and $\omega_r = q\Omega/\sqrt{8}$. Note that in order to avoid unnecessary clutter, the axial DC confinement (cf. Section 3.1) is neglected in this description.

If stray electric fields shift the center of the secular motion away from the nodal line of the RF field, *excess micromotion* along the RF field lines sets in leading to Doppler shifts due to the driven motion of the ion. In the rest frame of the ion, a laser beam exciting the ion with an electric field $E(t) = E_0\, e^{-i\omega_{\mathrm{l}} t}$ at frequency ω_{l} will therefore appear frequency modulated at the RF trap drive frequency. Hence, the effective electric field is given by

$$\begin{aligned} E(t) &= E_0\, e^{-i\omega_{\mathrm{l}} t}\, e^{ikx_a \frac{q}{2} \sin(\Omega_{\mathrm{rf}} t)} \\ &= E_0\, e^{-i\omega_{\mathrm{l}} t} \sum_{n=-\infty}^{\infty} J_n(\beta)\, e^{in\Omega_{\mathrm{rf}} t}, \end{aligned}$$

where the second exponential was expanded in terms of Bessel functions $J_n(\beta)$ that relate the micromotion strength to the *modulation index*

$$\beta = kx_a \frac{q}{2}. \tag{4.1}$$

Here, x_a is the position of the ion with respect to the RF null and $k = 2\pi/\lambda$ is the wavevector of the incoming laser beam at wavelength λ. The field strength of a static electric stray field E_s displacing the ion to x_a can be calculated from the condition that it settles at a position where the restoring force of the trapping field equals the electric force of the stray field, $m\omega_r^2 x_a = eE_{\mathrm{s}}$. As illustrated in Figure 4.7.a, *horizontal* micromotion is caused by *vertical* electric fields while *horizontal* stray fields lead to *vertical*

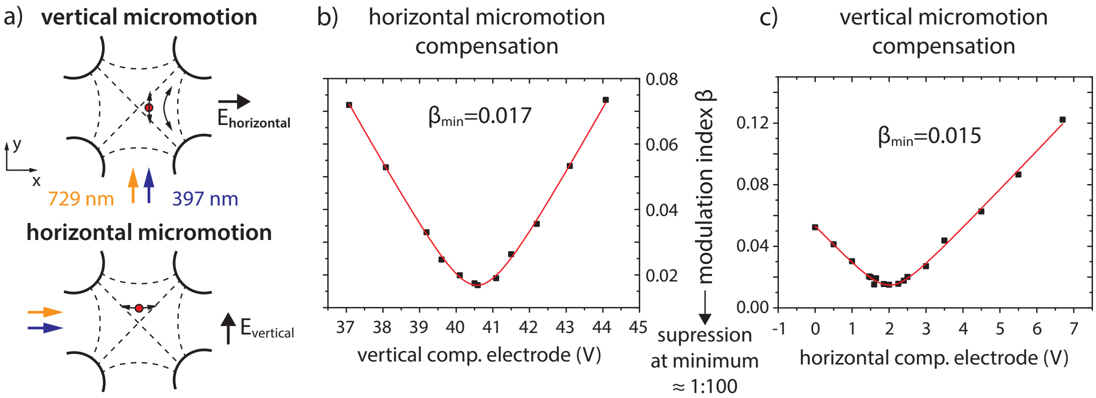

Figure 4.7.: Micromotion compensation in horizontal and vertical direction
a) Radial micromotion directions, affected laser beams and the direction of the responsible electric stray fields. Note that a laser beam *along* the micromotion's direction has to be used to observe it. The coordinate system on the left relates the directions to those used in Figure 3.6. **b) and c)** Horizontal and vertical micromotion compensation voltages in trap II (see Section 3.1). The hyperbolic fit following $\beta(U_\mathrm{C}) = A\sqrt{(U-U_\mathrm{C})^2+V^2}$ takes into account an offset field related to a potential V that is likely caused by a phase shift between the radial blade voltages and, hence, cannot be compensated.

micromotion. It is worth noting that any phase shift between the voltages V_rf applied to the blade electrodes results in a dipolar offset field that cannot be compensated and leaves a minimal modulation index $\beta > 0$ [49, 109].

A number of methods are available [109] to determine the compensation voltages in horizontal and vertical direction shown in Figure 4.7. Using light at 397 nm, measurements correlating scattered fluorescence photons with the phase of the RF drive field can be made. Less technically demanding is the minimization of the observed width of the cooling transition, as discussed in Section 4.1. A refined method of this technique has recently been demonstrated in reference [107], which uses time-separated laser pulses at 866 nm and 397 nm to circumvent the additional broadening effects that result from the simultaneous presence of both beams. The most accurate measurements, however, can be made using the sideband-resolved $\mathrm{S}_{1/2} \leftrightarrow \mathrm{D}_{5/2}$ transitions at 729 nm. Here, in the limit of low modulation, β can be calculated directly from the coupling strength ratio of the micromotional sideband Ω_SB to its carrier transition Ω_car as

$$\frac{\Omega_\mathrm{SB}}{\Omega_\mathrm{car}} = \frac{J_1(\beta)}{J_0(\beta)} = \frac{\beta}{2} + \mathcal{O}(\beta^2). \tag{4.2}$$

Figure 4.8.a on the following page illustrates this approach for a measurement of the axial micromotion that is accessible with a laser beam sent through the tip electrodes.

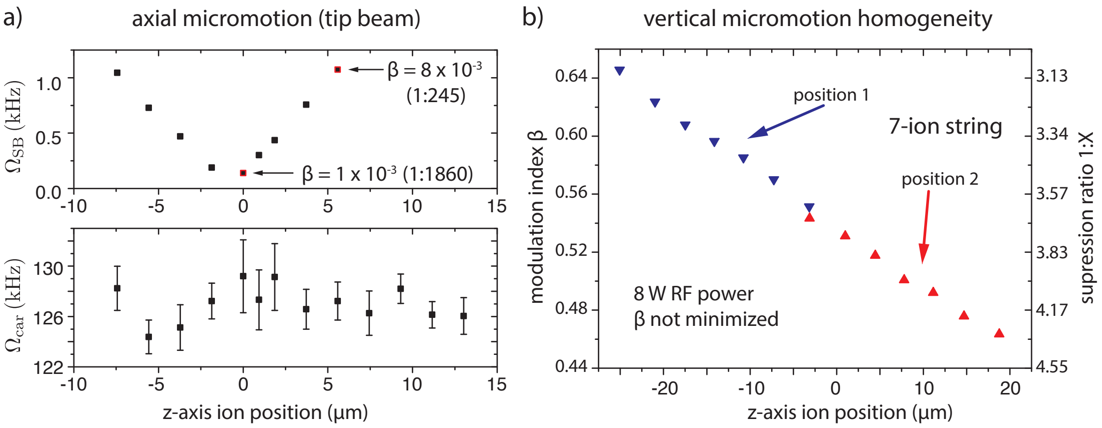

Figure 4.8.: Axial micromotion and inhomogeneity along the trap axis
a) Axial micromotion measurements that allow us to determine the micromotion suppression (given in brackets) from the ratio of the carrier and sideband coupling strengths, which is calculated from the respective π-times t_π. The modulation index β is then given by Eq. (4.2). **b)** A 7 ion crystal is shifted along the axial direction by tip voltage imbalancing (cf. Section 3.5). The measurement was made after increasing the radial confinement from a lower value without re-optimizing the horizontal compensation voltage. The z-axis center position corresponds to the equilibrium position of a single ion at an axial confinement of $\omega_z/(2\pi) \geq 1\,\text{MHz}$.

The very small, but non-zero modulation index is likely due to the asymmetric connection of the RF electrodes (Section 3.1). The homogeneity of the vertical micromotion along the trap axis is investigated in Figure 4.8.b. The results can point to either a dominant, localized stray potential or to an angle between the trap's z-axis and the horizontal compensation electrodes. With $q \approx 0.33$ and $\omega_r/(2\pi) = 3.35\,\text{MHz}$, the relatively large modulation index of $\beta = 0.54$ seen in the center of the figure corresponds to a displacement from the RF nodal line of $x_0 \approx 380\,\text{nm}$ caused by a field of $E_\text{s} \approx 70\,\text{V/m}$.

4.6. Sideband cooling

While the Doppler cooling technique discussed in Section 4.2 can reach the Lamb-Dicke regime, its lowest attainable phonon number $\bar{n} = \Gamma/(2\omega)$ is limited by the decay rate Γ of the excited $\text{P}_{1/2}$ state used for cooling and the trap frequency ω. Utilizing the narrow linewidth of the $\text{S}_{1/2} \leftrightarrow \text{D}_{5/2}$ qubit transition, it is possible to create a sideband-resolved cooling cycle that brings the thermal vibrational population after Doppler cooling to the motional ground state $|n = 0\rangle$. Such a cycle is similar to the optical pumping discussed in Section 4.3 in that the target state is decoupled from the cooling cycle.

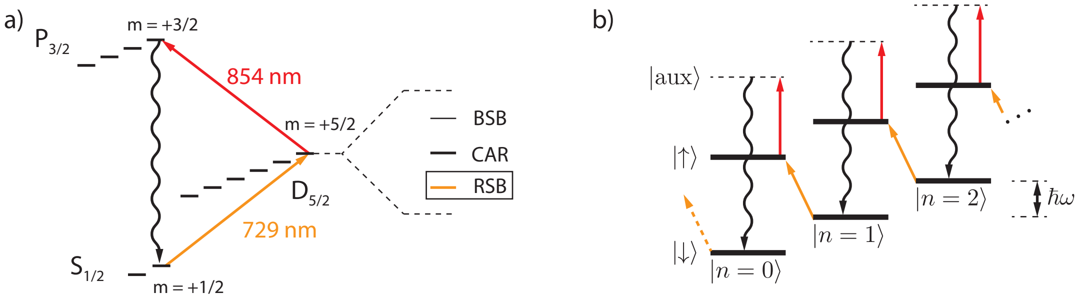

Figure 4.9.: Sideband cooling
a) Sideband cooling cycle consisting of a 729 nm laser beam resonant with a motional red sideband (RSB) of the $|\mathrm{S}_{1/2}, m_j = 1/2\rangle \leftrightarrow |\mathrm{D}_{5/2}, m_j = 5/2\rangle$ transition and a laser beam at 854 nm. Not shown is the decay channel to $\mathrm{D}_{3/2}$ which necessitates brief repumping pulses of 866 nm and 397 nm σ^+ light. **b)** Sideband cooling in Fock space. Absorption of a photon on an RSB transition incorporates the energy of one phonon $\hbar\omega$ into an electronic excitation to $|\uparrow\rangle$. A laser at 854 nm "quenches" the excitation via an auxiliary state, from which a spontaneously emitted photon at 393 nm provides the desired energy dissipation. The motional ground state $|n = 0\rangle$ no longer couples to the RSB transition.

The sideband cooling cycle [110, 111] shown in Figure 4.9.a follows Doppler cooling and optical pumping (cf. Figure 3.28). Its first stage drives the red sideband (RSB) of a particular motional mode via the quadrupole transition at 729 nm. Starting from the $|\mathrm{S}_{1/2}, m_j = 1/2\rangle$ ground state, photon absorption populates the upper Zeeman manifold's "stretched state"[95] $|\mathrm{D}_{5/2}, m_j = 5/2\rangle$ while at the same time lowering the ion's motional excitation in the particular mode. An auxiliary light field at 854 nm resonant with the $\mathrm{D}_{5/2} \leftrightarrow \mathrm{P}_{3/2}$ transition is used to artificially shorten the lifetime of the excited state[96] from ~1.2 s to a few µs such that energy is quickly dissipated via a spontaneously emitted photon at 393 nm and the cycle can begin anew. Figure 4.9.b illustrates this process in Fock space: with every completed cycle the phonon number is reduced by one until the motional ground state $|n = 0\rangle$ has been reached. Dipole selection rules ensure that the 854 nm light couples only to the $|\mathrm{P}_{3/2}, m = +3/2\rangle$ state, which itself can only decay back to the $|\mathrm{S}_{1/2}, m = +1/2\rangle$ ground state. However, due to a small branching ratio of ~0.7 % associated with decays to the $\mathrm{D}_{3/2}$ level, it is necessary to repeatedly send in repump pulses using the 866 nm and 397 nm σ^+ laser beams. In case of polarization imperfections, the latter could lead to unwanted re-heating from the scattering of multiple photons. To minimize this, it is advisable to keep the 397 nm pulses during and at the end of the cooling sequence as short as possible.

---

[95] The state has the largest angular momentum quantum number within a manifold of spin states.
[96] This process is often referred to as "quenching" the excitation.

The effective decay rate $\Gamma_{\mathrm{D}'}$ of the quenched $\mathrm{D}_{5/2}$ state is given by [112]

$$\Gamma_{\mathrm{D}'} = \frac{\Omega_{\mathrm{aux}}^2}{\Gamma_{\mathrm{aux}}^2 + 4\Delta_{854}^2}\Gamma_{\mathrm{aux}},$$

where Γ_{aux} is the decay rate of the auxiliary $\mathrm{P}_{3/2}$ state and Δ_{854} the detuning of the quenching laser from the $\mathrm{D}_{5/2} \leftrightarrow \mathrm{P}_{3/2}$ transition. Its coupling strength Ω_{aux} is a function of both power *and* polarization [48], which, in the specific cycle described before, corresponds to its degree of σ^- polarization. "Pump-out" experiments, illustrated and described in panels a and b of Figure 4.10, provide an easy way to determine $\Gamma_{\mathrm{D}'}$ and to verify the stability of the 854 nm beam's polarization, as drifts would translate to variations in the sideband cooling performance. The presence of the 854 nm light induces a positive AC-Stark shift (Section 2.3.2) on the $\mathrm{S}_{1/2} \leftrightarrow \mathrm{D}_{5/2}$ transition. Consequently, the RSB resonance frequency shifts upwards as well by a few kHz, which is illustrated in Figure 4.10.c for two values of Ω_{aux} chosen via the 854 nm light intensity.

Under the assumption that the Rabi frequency of the 729 nm beam is small compared to the effective decay rate ($\eta_{\mathrm{a}}\Omega \ll \Gamma_{\mathrm{D}'}$), the cooling limit close to the motional ground state ($\bar{n} \ll 1$) can be calculated [49] to

$$\bar{n} = \left\{ \left(\frac{\eta_d}{\eta_a}\right)^2 + \frac{1}{4} \right\} \frac{\Gamma_{\mathrm{D}'}^2}{4\omega^2}. \tag{4.3}$$

Here, the Lamb-Dicke factor η_a takes the photon recoil of the stimulated absorption at 729 nm into account. The *effective* Lamb-Dicke factor η_d captures both the recoil of the photon absorption at 854 nm and the subsequent, randomly directed spontaneous emission at 393 nm, which form the cooling cycle's dissipation process. Expression (4.3) is calculated from a balance of the cooling rate

$$\Gamma_{\mathrm{C}} = \Gamma_{\mathrm{D}'}\frac{(\eta_a\Omega)^2}{\Gamma_{\mathrm{D}'}^2 + 2(\eta_a\Omega)^2} \qquad \text{and} \qquad \Gamma_{\mathrm{laser-heat}} = \left(\frac{\Omega}{2\omega}\right)^2 \eta_{\mathrm{d}}^2\Gamma_{\mathrm{D}'} + \left(\frac{\eta_{\mathrm{a}}\Omega}{4\omega}\right)^2 \Gamma_{\mathrm{D}'},$$

which is a laser-induced heating rate where the first term corresponds to off-resonant carrier excitations and the second term represents blue sideband excitations.

Moving away from the assumption used above, the cooling rate begins to saturate while the Ω^2-dependent off-resonant carrier excitations raise the minimum temperature that can be attained. For this reason, the coupling strengths Ω_{aux} and Ω should always be chosen such that $(\eta_{\mathrm{a}}\sqrt{\bar{n}}\Omega) \leq \Gamma_{\mathrm{D}'}$, where $\bar{n}$ is the mean phonon number reached after Doppler cooling in the respective mode.

In practice, sideband cooling is set up as follows: First, the 854 nm laser is put on resonance by minimizing the quantum jump rate observed at low laser powers.

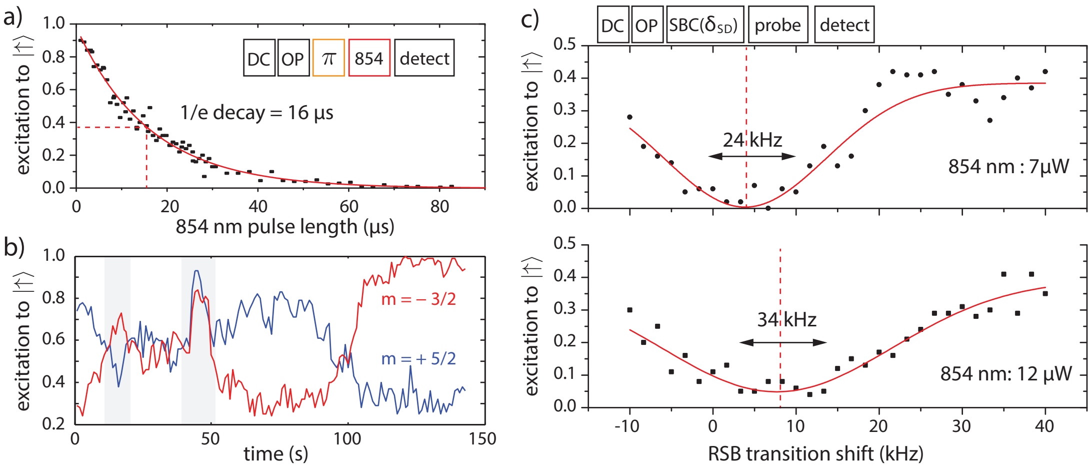

Figure 4.10.: Sideband cooling in practice
a) After Doopler cooling (DC) and optical pumping (OP) a π-pulse is used to prepare the $|D_{5/2}, m_j = 5/2\rangle$ state. A separate pulse at 854 nm is varied in length before the remaining population in $|\uparrow\rangle$ is detected. An exponential decay fit to the data yields an effective decay rate $\Gamma_{D'} = (2\pi)\,9.95\,\mathrm{kHz}$. **b)** Stability check of Ω_{aux}. The pulse sequence shown in a) is used to prepare two different initial states in an alternating fashion followed by an 854 nm pulse length of fixed length. Thermal and mechanical stress applied to the optical fiber carrying the light to the ion trap result in (anti-)correlated changes (marked in gray) between the two traces which provides a way to distinguish power from polarization changes. **c)** The residual population in states $n > 0$ after sideband cooling (SBC) is probed by a weak 2 ms laser pulse resonant with the red sideband (RSB). The increase of the AC Stark shift $\delta_{\mathrm{SD}} = -\Omega^2_{\mathrm{aux}}/(2\Delta_{854-729})$ and the cooling transition's effective linewidth $\Gamma_{D'}$ with the 854 nm power can be seen in the fit to the data. A suitable choice of parameters yields a residual excitation ($\simeq \bar{n}$) close to 0.

Then, the sequence shown in Figure 4.10.c is used to check for residual population in $n > 0$. This is repeated while the frequency of the RSB pulse used *during* the cooling cycle is scanned around its bare resonance frequency. The minimum value of the observed excitation is now compared for different 854 nm laser powers to find an optimal combination similar to the one shown in the figure's upper panel.

Thus far, motional heating by electric field noise has been neglected. Depending on its strength with regards to the specific motional mode in question, it can prevent the sideband cooling cycle from reaching the ground state and will increase the ion's motional energy during experiments. The corresponding heating rate is discussed below.

4.7. Heating rate measurements

A sideband-cooled ion does not stay in the ground state of its confining potential indefinitely and gains motional energy over time. This heating process can have a variety

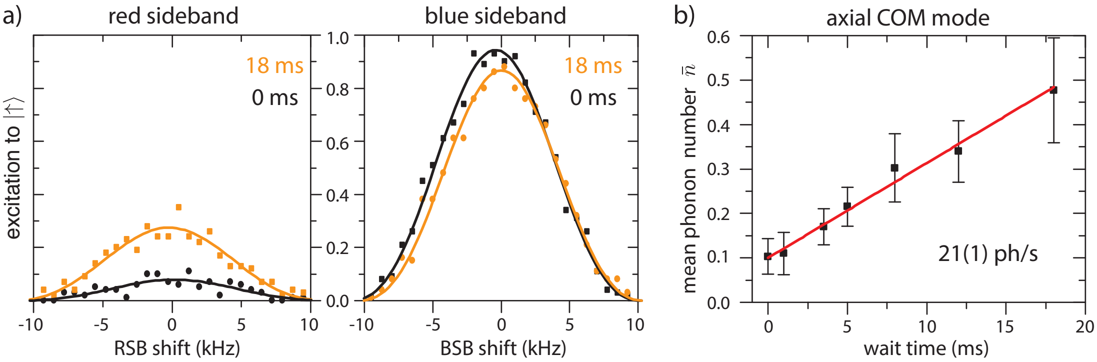

Figure 4.11.: Heating rate measurement of the axial COM mode
a) Spectrum of the red and blue sideband of the axial COM motional mode using a pulse duration close to $t = \pi/\Omega$. The lines are sinc-fits to the data and provided as a guide to the eye to distinguish the traces recorded at different times after the completion of sideband cooling. **b)** By repeatedly probing both sidebands on resonance using pulses of *equal length* in an alternating fashion, the mean phonon number $\bar{n}$ can be determined from the ratio of the respective excitations to $|\uparrow\rangle$ using Eq. (4.4). The measurement is carried out at various wait times and a linear fit to the data reveals the motional heating rate of the axial COM motional mode at $\omega_z/(2\pi) = 1.23\,\text{MHz}$.

of origins [113], the most obvious one being electric field noise that is brought in via the trap electrodes. The noise fields couple to the ion's charge and heat it by exerting randomly fluctuating forces. However, even with dedicated filtering of the trapping voltages, a mechanism persists that has been dubbed "anomalous heating" in the literature [114]. Its origin appears to be related to surface contaminants on the trap electrodes and fluctuating patch potentials associated with these. While the exact mechanisms are still under investigation, two recent experiments [115–117] have used in-vaccum cleaning methods to remove surface contaminants and observed impressive reductions in the heating rate of surface ion traps by up to two orders of magnitude.

As shown in Figure 4.11.b, the heating rate of a particular motional mode is obtained by measuring its mean phonon number $\bar{n}$ at various delay times after the completion of sideband cooling. Each datapoint is derived from two successive measurements consisting each of a single pulse resonant with the k-th motional sideband. For equal pulse lengths, $\bar{n}$ is directly obtained from the ratio

$$\frac{p_k^{\text{rsb}}}{p_k^{\text{bsb}}} = \left(\frac{\bar{n}}{\bar{n}+1}\right)^k \quad \xrightarrow{k=1} \quad \bar{n} = \frac{p^{\text{rsb}}}{p^{\text{bsb}} - p^{\text{rsb}}}, \tag{4.4}$$

where p^{rsb} (p^{bsb}) correspond to the excitation probability found after resonant excitation (cf. Figure 4.11.a) on the red (blue) sideband [113]. While Eq. (4.4) is valid even for

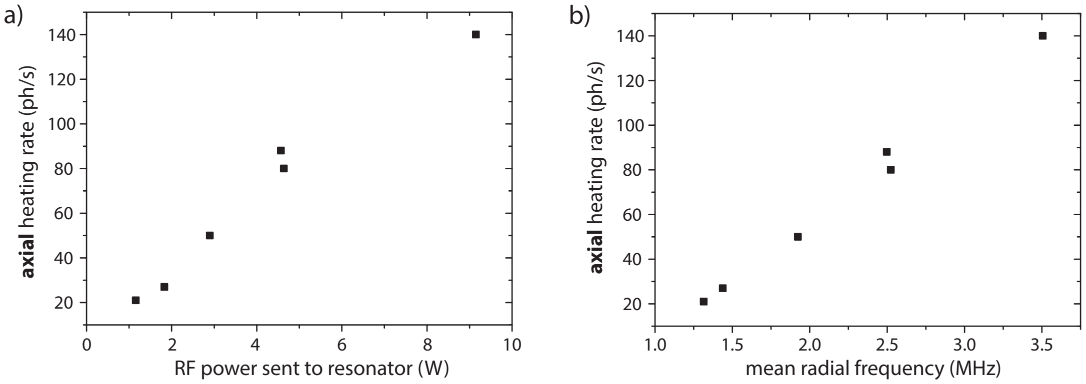

Figure 4.12.: Axial heating rate dependence on radial confinement
The heating rate of the axial COM mode is measured at different RF powers sent to the resonator **(a)** using the technique outlined in the text. For each power setting, the axial COM mode frequency as well as the mean radial mode frequency **(b)** were determined anew to ensure the reliability of the technique. The exact cause of the increase in the heating rate is unknown, but a (very rapid) temperature increase of the trap assembly at higher RF powers is suspected to play a role (see text). No fits are made to the data in order to avoid suggesting a specific relationship. Error bars are smaller than point size.

thermal states outside the Lamb-Dicke regime, high sensitivity is only achieved when using a sideband order k that matches the expected mean phonon number $\bar{n}$ [113].

Trap I maintained a heating rate around $R_{\mathrm{H}} = 3$ phonons/s [50]. Due to the reduced ion-electrode distance (800 µm → 565 µm), trap II was expected to show a higher heating rate. Initially a value around $R_{\mathrm{H}} = 20$ ph/s was found in February 2012. 18 months later, however, a heating rate of around $R_{\mathrm{H}} = 40 - 50$ ph/s was found repeatedly under otherwise identical conditions. The heating rate also appeared to fluctuate on some days over the course of multiple hours. The origin of this radical change could not yet be identified with certainty and remains under investigation.

Additionally, a very significant increase in the axial COM mode heating rate as a function of the radial confinement was observed (Figure 4.12), which – to the author's knowledge – has not been reported in the literature before[97]. However, the behaviour was *not* found in a similar trap with identical dimensions that is available in an adjacent laboratory. There, instead of the stainless steel and Macor holder of trap II, the setup employs gold-coated titanium blades and a blade holder made from sapphire. It also allowed us to monitor the trap's temperature at the different RF powers using an in-vacuum sensor. As opposed to trap II, where the trap temperature is likely around 100 °C (cf. Fig.3.5 in [64]), the other setup remains within ∼ 10 K of room temperature.

---

[97] A similar behavior was seen at NIST using a surface ion trap with 40 µm ion-electrode distance that was used in the experiments of reference [115] (Y. Colombe, private communication).

4.8. Ramsey spectroscopy

An alternative to the Rabi spectroscopy illustrated before is the method of separated oscillatory fields invented by and named after Norman Ramsey [118]. Whereas in the original experiments with molecular beams, the oscillatory fields were separated in space, interrogation of the trapped ion makes use of laser pulses separated in time. The basic pulse sequence is illustrated in Figure 4.13.a alongside experimental data in panel b. It proceeds as follows:

Starting with an ion in the electronic ground state $|{\downarrow}\rangle \equiv |-\rangle_z$, a $\pi/2$ pulse rotates the state vector into the Bloch sphere's equatorial plane. Being the first in a series of coherent interactions, the initial pulse's optical phase sets the reference $\phi_1 = 0$ to which all of the later pulses refer. As such, the corresponding rotation in the equatorial plane can be arbitrarily defined, e.g., to be around the x-axis as σ_x in Eq. (2.3), which is the convention adopted in this text. The resulting superposition state $|+\rangle_y$ is then allowed to evolve freely for a time τ_R as described by the state vector $|\psi\rangle = \frac{1}{\sqrt{2}}\left(|{\downarrow}\rangle + ie^{-i\omega_0\tau_\mathrm{R}}|{\uparrow}\rangle\right)$. Here, the frequency $\omega_0/(2\pi) = \nu_0 \approx 4 \times 10^{14}\,\mathrm{Hz}$ corresponds to the energy splitting between the two basis states of the qubit, yielding a rapidly varying $|\psi\rangle$. To see the effect of the second $\pi/2$ pulse in the sequence, it is convenient to change into an interaction picture (Section 2.3.2). This amounts to changing into a co-rotating frame in which the new state vector $|\psi'\rangle = \frac{1}{\sqrt{2}}\left(|{\downarrow}\rangle + ie^{-i\Delta\omega\tau_\mathrm{R}}|{\uparrow}\rangle\right)$ remains stationary as long as the laser frequency ω_l and qubit remain in resonance ($\Delta\omega = \omega_l - \omega_0 = 0$). Depending on its optical phase ϕ_2 relative to the first pulse, the final $\pi/2$ pulse now rotates the state vector to $|+\rangle_z$ for $\phi_2 = 0$ ($\equiv \sigma_x$) or back to $|-\rangle_z$ for $\phi_2 = \pi$ ($\equiv -\sigma_x$). In the experiment, the optical phase can be changed by varying the phase of the RF signal that is sent to an AOM in the path of the laser beam. (Recall that the phase of the diffracted light is the sum of the optical and acoustic phases in the device [97, 98].)

A detuning $\Delta\omega \neq 0$ is the result of a change in the energy separation of the qubit levels ω_0 (e.g., due to a change in the ambiant magnetic field) or a drift of the laser frequency ω_l. In the co-rotating frame, this causes a rotation of the state vector around the z-axis by an amount[98] $\delta = \Delta\omega\,\tau_\mathrm{R}$, which is eventually mapped onto the observable σ_z ($|{\uparrow}\rangle$, $|{\downarrow}\rangle$) by the second $\pi/2$ pulse. With knowledge of τ_R, the detuning $\Delta\omega$ can then be directly extracted from the mean excitation probability to the $D_{5/2}$ state.

---

[98] For the moment only the free evolution period is considered; for the effective τ_R used in measurements, see Section 4.8.1 below.

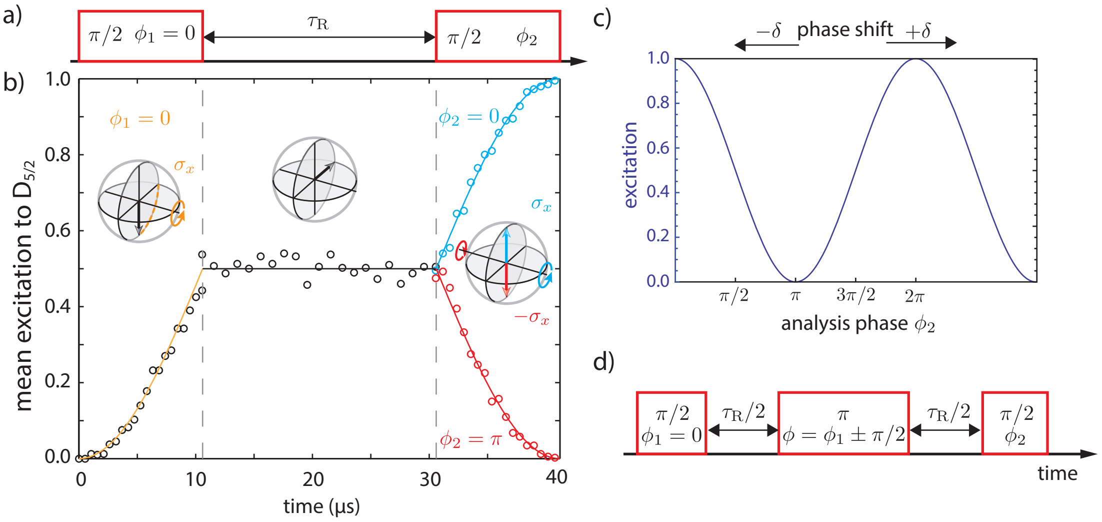

Figure 4.13.: Ramsey experiments
a) Pulse sequence for a Ramsey experiment. Two $\pi/2$ pulses of length $t = \pi/(2\Omega)$ are separated by a waiting time τ_R. The coupling strength Ω is usually controlled by the light intensity. The optical phase ϕ allows us to select the rotation angle of the second $\pi/2$ pulse. **b)** Excitation at various times of the pulse sequence shown in a) for a detuning $\Delta\omega = 0$. The insets show a Bloch sphere representation (cf. Section 2.1) of the state vector at the end of each step (gray dashed line). **c)** Excitation as a function of the analysis phase ϕ_2 of the second pulse, assuming no decoherence (= full amplitude). Phase shifts δ accumulated during τ_R shift the fringe pattern left or right, depending on their sign. **d)** Extension of a Ramsey experiment to a spin-echo sequence. A π pulse of duration $t = \pi/\Omega$ after half the waiting time exchanges the qubit state populations allowing for the inverse free evolution in the second part of the sequence.

Deliberate variation of the second $\pi/2$ pulse's phase ϕ_2 at a fixed wait time reveals the fringe pattern shown in Figure 4.13.c. Phase shifts by $\pm\delta$ translate the pattern in the horizontal directions. Its amplitude can be directly related to the qubit coherence or Bloch vector length using Eq. (3.5).

A Ramsey experiment can readily be extended to the spin-echo [119] sequence shown in Figure 4.13.d. Here, an intermediate π pulse is used to swap the electronic populations halfway during the wait time. Its phase ϕ is set such that it carries out a 180° rotation of $|\psi'\rangle$ around a Bloch sphere axis orthogonal to that of the first $\pi/2$ pulse. As a result, frequency shifts $\Delta\omega$ that are common to both free evolution periods are cancelled, unless they match the condition $\Delta\omega = 1/\tau_\mathrm{R}$.

In the context of what is known as dynamical decoupling [120, and references therein] a variation of the spin-echo technique can be used to suppress noise-induced decoherence or, deliberately using the condition given above, to identify the particular noise frequencies acting on the qubit [121, 122].

4.8.1. "The clock" – frequency drift correction via the qubit transition

Ramsey experiments, as outlined above, provide the foundation for a frequency drift lock of the qubit laser at 729 nm, which allows us to compensate the drifts of its high finesse cavity (Section 3.3.3). In the same way, changes in the magnetic field at the location of the ion(s) can be detected. The gathered data is used in a feed-forward correction that updates the frequency of AOM 9 (cf. Figure 3.9) every second. Once changes in the ambient magnetic field are detected, all transition objects (cf. Section 3.8) are automatically updated with the corresponding transition frequency shifts.

The lock is implemented using a total of four independent Ramsey experiments with an equal wait time τ_R probing two transitions in the $\mathrm{S}_{1/2} \leftrightarrow \mathrm{D}_{5/2}$ manifold. For each transition, two separate measurements with a different optical phase in the second $\pi/2$ pulse are carried out [40]: measurement 1 uses the optical phase $\phi_2 = +\pi/2$ and measurement 2 uses $\phi_2 = -\pi/2$ such that two complimentary points on the fringe pattern shown in Figure 4.14 are obtained. Their respective distance allows us to directly calculate the laser frequency detuning $\Delta\omega$ from the $\mathrm{S}_{1/2} \leftrightarrow \mathrm{D}_{5/2}$ resonance at $2\pi \times \nu_0$ using

$$\Delta\omega = \frac{1}{(\tau_\mathrm{R} + 2\tau_\pi/\pi)} \arcsin\left(\frac{p_\mathrm{B} - p_\mathrm{A}}{p_\mathrm{A} + p_\mathrm{B}}\right). \tag{4.5}$$

Here, the first denominator includes an *effective Ramsey time* that takes both $\pi/2$-pulses of duration $\tau_\pi/2$ into account [59]. The denominator $(p_\mathrm{A} + p_\mathrm{B})$ of the arcsin-function ensures that the measurement results are normalized, which allows the lock to operate even in cases where optical pumping is incomplete or the pulse lengths τ_π have not been calibrated accurately (dashed lines in Figure 4.14). By probing the detuning $\Delta\omega$ on two different transitions, their measured frequency values[99] can be used in combination with Eq. (2.11) to extract the magnetic field strength B at the location of the ion.

Typical parameters used in the experiment are $\pi/2$ pulse lengths of $t_\pi/2 \approx 6\,\mu\mathrm{s}$ and a Ramsey time of $50\,\mu\mathrm{s} \leq \tau_\mathrm{R} \leq 1\,\mathrm{ms}$. The latter gives the lock a capture range between ±5 kHz and ±250 Hz, corresponding to the increased frequency resolution. Frequency measurements are repeated every 1-5 minutes and their results are stored together with a timestamp and the relevant experimental parameters. A polynomial fit (usually only to first order, cf. Figure 3.14) is automatically applied to a subset of the data in a user-selected time window. After weighing each measurement based on its timestamp with an exponential decay, the fit results are used in the feed-forward correction of the

---

[99] Transition frequencies are stored in terms of the frequency shift induced by DP AOM 11. It is centered around frequency f_0, where $\nu_0 = \nu_\mathrm{laser} + 80\,\mathrm{MHz} + f_0$ (cf. Figure 3.9).

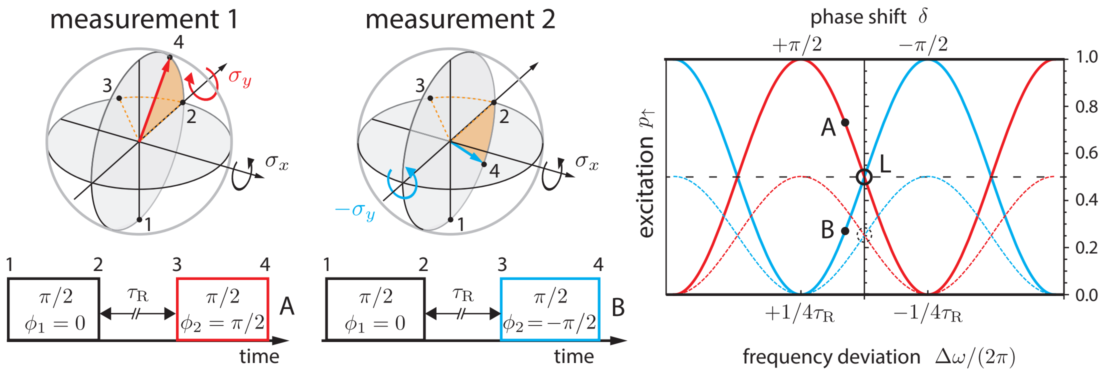

Figure 4.14.: Laser drift lock via Ramsey measurements
Two separate measurements with a Ramsey wait time τ_R are carried out on a single $S_{1/2} \leftrightarrow D_{5/2}$ transition. The phase ϕ_2 of the analysis pulse is set to be shifted by ±90° with respect to the first pulse. Without a phase shift δ both measurements yield an excitation of $p_\uparrow = 0.5$. The positive detuning $\Delta\omega$, indicated on the left, shifts the measured excitations (A, B) along the fringe lines in opposite direction. Incomplete optical pumping or inaccurate $\pi/2$ pulses, i.e. a pulse length τ_π that is either too large or too small, shift the lockpoint (L) to lower values (dashed lines), thereby reducing the frequency lock's overall gain.

laser frequency (→ AOM 9) and, optionally, the magnetic field value employed in the calculation of the transition frequencies (→ AOM 11).

4.8.2. Line cycle induced frequency shifts

The mains electricity at 50 Hz alternating current (AC) used to power devices in the laboratory produces spurious AC magnetic fields that affect the energy levels encoding the qubit. The fields originate from insufficiently shielded power supplies and ground loops that can form when two devices that are already grounded via the power outlet are directly connected. Common culprits are connections to oscilloscopes in which the cable's outer conductor may provide an additional path to ground for the connected device, effectively forming a loop between the two ground points.

Mains electricity is commonly delivered via a three-phase-AC system. The three line phases (L1, L2, L3) shown in Figure 4.15.a share the same neutral return line, in which their currents will cancel *if* all of them are under equal load. Different loads yield a current in the neutral conductor at the third (and higher) odd harmonic, producing a strong noise component at 150 Hz in addition to the 50 Hz.

If the equipment in the vicinity of the experiment is powered by only one line-phase (which is highly recommended), the effect of the ambient magnetic field noise can be greatly mitigated through the use of a *line trigger* (see also page 66). The device

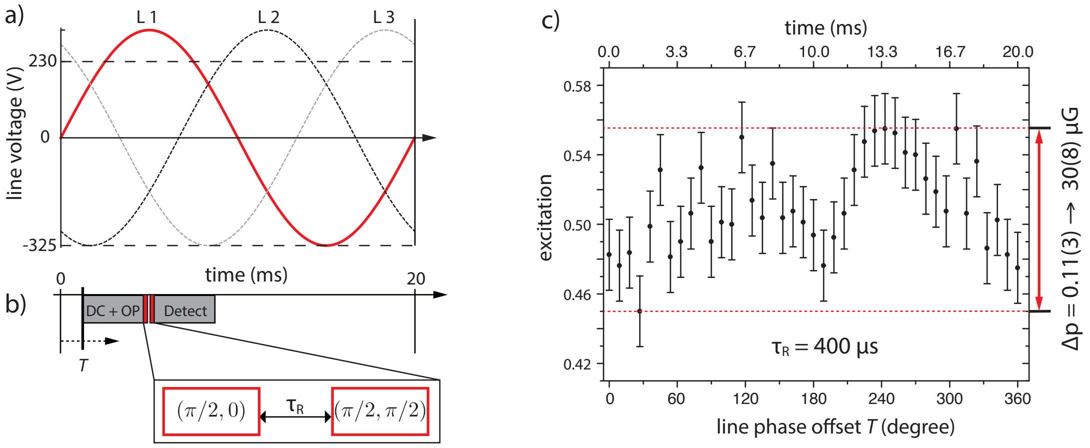

Figure 4.15.: Line cycle measurements and line trigger
a) Mains voltage over one 50 Hz power line cycle. The power usually is supplied over three different phases (L1, L2, L3) that are each shifted by 120° and referred to the same neutral line and protective earth. Each phase is usually distributed to standard single phase outlets via separate fuses. **b)** Ramsey pulse sequence used to measure the magnetic field associated with the power line cycle. The sequence is triggered at a fixed line phase offset (T) and comprises Doppler cooling (DC), optical pumping (OP) and detection in addition to the coherent manipulations ($\theta = \pi/2$, $\phi = \{0, \pi/2\}$). **c)** Result of a Ramsey experiment shown in b) performed on the $|\mathrm{S}_{1/2}, m_j = 1/2\rangle \leftrightarrow |\mathrm{D}_{5/2}, m_j = 5/2\rangle$ transition with $\tau_\mathrm{R} = 400\,\mu\mathrm{s}$ and 600 experiments per datapoint. The line cycle amplitude at 50 Hz calculated from the pattern is 30(8) µG.

generates a TTL signal synchronous with the power line frequency at a variable phase offset. It relies on the fact that the commonly used switching power supplies only draw current close to the peak of the power line voltage. Consequently, the noise magnetic field amplitude changes over time and usually shows a few "quiet" periods in which very little change occurs. A line trigger offset phase (T) is then selected such that coherent operations happen during the quiet periods in experimental cycle.

To identify the quiet periods and quantify the overall magnitude of the line cycle-induced shifts, the amplitude of the magnetic field at various points in the cycle is obtained using the Ramsey sequence shown in Figure 4.15.b. Here, the analysis phase of the second pulse is set such that the sensitivity to shifts is maximized (cf. Figure 4.13). Its results, shown in Figure 4.15.c, can be evaluated as follows:

Without any wait time τ_R between the $\pi/2$ pulses, the excitation signal would remain centered around a value of $p = 0.5$. Introducing a wait time $\tau_\mathrm{R} > 0$, small changes around this value ($0.3 \leq p \leq 0.7$) can be approximated as

$$p = \frac{1}{2}\Big[1 + \sin\Big(\Delta\omega\,\tau_\mathrm{R}\Big)\Big] \approx \frac{1}{2}\Big(1 + \Delta\omega\,\tau_\mathrm{R}\Big) \rightarrow \Delta p = \frac{1}{2}\Delta\omega\tau_\mathrm{R}.$$

The frequency shift $\Delta\nu = \Delta\omega/(2\pi)$ can now be used in combination with Eq. (2.11) to directly relate the overall signal change Δp to the 50 Hz magnetic field strength

$$B_{50\mathrm{Hz}} = \frac{2\Delta p}{\pi\gamma\tau_\mathrm{R}}.$$

Here, γ is the field sensitivity (cf. Figure 2.3) of the $S_{1/2} \leftrightarrow D_{5/2}$ transition probed in the measurement. The field amplitude measured inside the magnetic shielding enclosure of trap II (30-40 µG) constitutes a significant improvement over that measured in trap I (1.4 mG, [57]). However, given the 50 Hz attenuation factor of 10^3 shown in the factory calibration (Section 3.6), one would hope to measure even lower values. Residual AC noise in the quantization magnetic field coils has been excluded by driving both the coils as well as the regulator from batteries. The likely source therefore is electrical equipment that remains in close proximity to the ion trap.

More information on electrical power distribution and how to avoid noise problems related to ground loops etc. can be found in reference [123].

4.8.3. Motional coherence

Ramsey experiments are not just limited to the electronic, internal degree of freedom. With the addition of coherent sideband pulses, the motional coherence can be probed as well. In this case, illustrated in Figure 4.16, a superposition of Fock states is prepared by a carrier $\pi/2$ pulse that is followed by a π pulse on the blue motional sideband of the mode of choice. After a wait time τ_R, the same sequence is applied in reverse. A scan of the optical phase of the second $\pi/2$ pulse then allows one to recover the same fringe pattern as before in Figure 4.13. The phase shift $\delta = \Delta\omega\tau_\mathrm{R}$ is now related to changes in the motional oscillation frequency ω and, with the electronic state being entirely in state $|{\uparrow}\rangle$ during the wait time, largely independent of changes in the laser frequency or ambient magnetic field. By repeating the same experiment at a fixed wait time over and over, changes of the motional frequencies, which are equivalent to changes of the trapping voltages (c.f. Section 3.1), can be quantified based on the observed changes in the excitation signal.

The experiment presented in Chapter 6 relies on the motional stability of the axial center of mass (COM) mode and future experiments will make use of the radial modes of motion. Therefore, the stability of both COM modes has been checked yielding the results shown in Figure 4.16.c and d on the next page. While the axial motional mode relies solely on the intrinsic stability of the high-voltage power supply connected to the

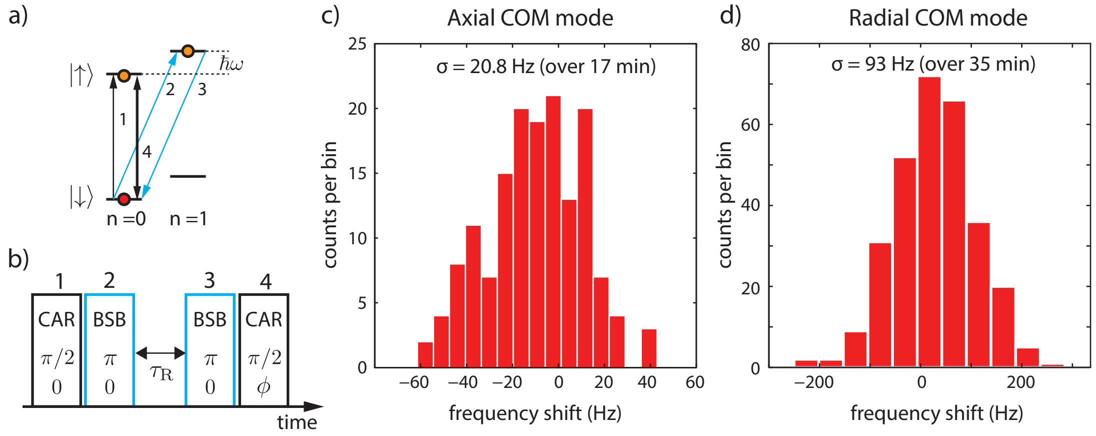

Figure 4.16.: Motional Ramsey experiment
a) The motional Ramsey experiment uses a superposition of two Fock states to probe the stability of the trap frequency $\omega_t = 2\pi\nu_t$. **b)** Two additional pulses on a motional sideband make the experiment sensitive to the motional phase, while at the same time the electronic state remains largely unaffected by magnetic field noise. Again, by scanning the analysis phase ϕ of the second $\pi/2$ pulse, the fringe pattern of Figure 4.13.c can be observed. **c)** Axial COM mode. The frequency stability of $\Delta\nu_z/\nu_z = 1.7 \times 10^{-5}$ is based only on the internal stabilization of the high voltage power supply connected to the tip electrodes. **d)** Radial COM mode. The frequency stability of $\Delta\nu_r/\nu_r = 3.1 \times 10^{-5}$ shown in the histogram is seen only with active feedback to the amplitude of the RF drive signal. It is based on an error signal derived from the rectified voltage of a capacitive divider placed at the end of the helical resonator. Without the active feedback, the distribution has a width on the order of 10 kHz.

tip electrodes, the RF voltage responsible for the radial confinement does not reach the level of stability seen in the figure just by itself. Here, the rectified signal from a capacitive divider at the output of the helical resonator has been used to implement active feedback to the amplitude of the signal generator that produces the RF used to drive the resonator. The data shown in Figure 4.16 represents the best case of an early attempt to stabilize the radial confinement over the course of $\sim$ 30 min and has to be compared to drifts on the order of 10 kHz with the feedback turned off.

5. Quantum simulation

published in: Science **334**, 57–61 (2011)
arXiv:1109.1512 [quant-ph]

With significant progress in experimental control, the field of quantum simulation has grown significantly in the 21$^{\mathrm{st}}$ century, establishing itself as a cornerstone in today's quantum physics research [124–126]. This chapter is about one particular contribution to the field: the proof-of-principle demonstration of digital quantum simulations using trapped ions. All of the experiments presented in the following have been performed using trap I (cf. Section 3.1) and, for experiments with more than two ions, an almost identical setup [62] at the university laboratory was used. The chapter begins with a brief review illustrating the fundamental obstacle associated with the simulation of many-body quantum systems: the memory problem. Two approaches to overcome this problem are outlined in the following, namely analog and digital quantum simulation. The remainder of the chapter is then devoted to the experimental demonstration of the first digital quantum simulations in a system of trapped ions.

5.1. Introduction – the quantum simulation problem

Quantum mechanics is one of *the* fundamental theories of physics. It is at the basis of many phenomena observed in many-body systems in physics and chemistry and, as recent investigations show, possibly even biology [127, 128]. Given the wide success and vast impact that its formalism has had in the description of nature, as well as the technological breakthroughs it helped to achieve in applied fields, it is an imperative to be able to efficiently simulate quantum mechanical models. This need is furthered by the fact that, in many systems described by quantum mechanical models, the underlying parameters cannot, or only with extreme difficulty, be accessed and controlled experimentally. However, already for rather small physical systems, the required calculations very quickly become computationally inefficient on classical computers as the resources needed to carry them out scale exponentially with the size of the problem.

To understand the fundamental issue underlying this problem, one can start with the smallest possible simulation of a simple quantum mechanical two-level system. An electron is a spin-1/2 particle with the two states $|{\uparrow}\rangle$ and $|{\downarrow}\rangle$ as demonstrated in the famous Stern-Gerlach experiment [129] in the connection to magnetism at its most fundamental level. It behaves just like the qubit or "pseudo-spin-1/2" introduced in Section 2.1 and can exist in a superposition $|\Psi\rangle = \alpha\,|{\uparrow}\rangle + \beta\,|{\downarrow}\rangle$ of its two logical basis states. Any simulator therefore needs to store the complex coefficients α, β to faithfully represent its quantum state. Advancing to two qubits, as described by Eq. (2.8), four coefficients have to be stored. More generally, to simulate an n-qubit system, the simulator has to store 2^n coefficients just to record its state. Notably, each additional qubit doubles the amount of memory needed for this task – which leads to the memory problem that is further illustrated in the box below. (Note that only the internal spin degree of freedom has been taken into account here. Just a single qubit with quantized motional degrees of freedom, like a trapped ion, can pose a similar challenge [e.g. 130].)

Qubits vs. bits – memory requirements on a classical computer

qubits	1	2	42	51	69	...
coefficients	2	4	4.3×10^{12}	2.2×10^{15}	5.9×10^{20}	...
state vector	32 Bytes	64 Bytes	64 TB	32 PB	8 ZB	...
(classical) bits	256	512	5.6×10^{14}	2.8×10^{17}	7.5×10^{22}	...

A general n qubit state is described by a complex-valued state vector of length 2^n. Using double-precision floating-point numbers (8 bytes each) one needs 2^{n+4} bytes of memory, just to encode all of the vector's elements corresponding to the complex coefficients. The associated memory demand is indicated for a few examples in the table above. Classical computer simulations of a universal quantum computer have been run on supercomputers with results for 36 simulated qubits published in reference [131] and a press release in 2010 reporting the factoring of 15707 into 113 × 139 using **42** *simulated* qubits ("JUGENE": IBM BlueGene/L at the Jülich supercomputing center). However, given the memory scaling shown above, it will not be possible to increase the size of the simulated register much further: just the storage of the state of **69** qubits (in zetabytes) surpasses, by almost an order of magnitude, the number of bits stored by humanity in all of its technological devices by the end of 2014 (based on estimates given in reference [132]). The number of **51** qubits corresponds to the ion chain shown in Figure 3.18.

Proceeding to the actual simulation itself, the next step after the encoding is to calculate the evolution of the simulated system. In the general case, this comes down to solving a time-(in)dependent Schrödinger equation, that is represented by a $2^n \times 2^n$ Hamiltonian matrix in addition to the 2^n state vector. The ensuing exponentially scaling number of differential equations can in some cases be significantly reduced by the use of symmetries, approximations and optimized numerical methods. With their help, only a subset of the full matrix has to be stored at a given time, which allows for some larger problems of tens of spins to still be simulated on a classical computer. However, many other simulations, especially when reaching a size relevant to practical applications, still remain out of reach even for state-of-the-art supercomputers.

It is this "exponential explosion", both in the size of the Hilbert/computational space and the number of equations describing the quantum state dynamics, that prompted Richard Feynman in 1981 [5] to suggest that one might be able to escape the associated problems by employing a (well-controlled) quantum system itself to perform quantum calculations. Implementations following this paradigm, generally involve three steps performed on a given number of qubits:

1. repeated, controlled preparation of the initial state
2. simulation of the desired dynamics and
3. read-out of the result.

For this to work well, the Hamiltonian underlying the quantum simulator needs to be very well understood and has to be controllable with high fidelity over the parameter range of interest. In addition, the read-out has to be possible in a way that allows one to infer the quantities relevant to the simulation result.

As candidates for such *quantum simulators*, a variety of quantum systems have been suggested, ranging from atoms in optical lattices, to ions in linear strings or 2D arrays, to solid state implementations in arrays of quantum dots or superconducting circuits, to photons in integrated waveguides. An overview of the different approaches can be found in references [125, 133]. The implementations mainly differ in

- the number of particles (qubits) involved,
- the degree of control that can be exerted over the simulator,
- the interactions naturally present in the respective system and
- the fidelity with which a simulation result can be retrieved.

5.2. Analog vs. digital quantum simulation

There are two distinct approaches to quantum simulation, commonly referred to as *analog quantum simulation* and *digital quantum simulation* [124, 133]. Both differ in the requirements as to what interactions have to be naturally present in the simulator and in the way the Hamiltonian of the system to be simulated is implemented and processed in the simulator.

Analog quantum simulators take the approach of finding a one-to-one correspondence between the terms of the Hamiltonian $H_{\mathrm{sys}} = \sum_i h_i$ to be simulated and those terms corresponding to interactions $\{h_{\mathrm{sim}}\}$ directly available in the simulator. This mapping ($H_{\mathrm{sys}} \leftrightarrow H_{\mathrm{sim}}$) between the Hamiltonians essentially allows the simulator to directly mimic the unitary evolution of the system to be simulated. Here, the main task is to identify and relate the accessible simulator variables to the relevant parameters of the simulated system.

While in this approach the fidelity of the simulation itself is only limited by the quality of the three steps listed in Section 5.1 above, the class of problems that can be simulated is bounded by the interactions that are directly available in the simulator. An early application of this technique in trapped ions investigated non-linear interferometers [134]. Later, the analog approach has been successfully used to perform simulations of a basic quantum magnet [135], Ising interactions with more than 100 spins [136], quantum phase transitions in frustrated systems [137–141], a model of interacting polaritons [142] and even mimic relativistic quantum dynamics [130, 143]. Additionally, the scope of analog simulations in trapped ions has been extended towards open quantum systems, where the coupling to the environment is no longer a bug detrimental to the simulation but instead a well controlled feature [144].

Digital quantum simulation translates the unitaries describing the dynamics of the system to be simulated into quantum circuits built up from elementary gate operations on a quantum computer [25]. This is the kind of quantum simulation Feynman suggested in his 1981 lecture, but only in 1996 Seth Lloyd showed [145] that by simply turning on and off a special but finite set of Hamiltonians, a quantum system can be made to evolve in close correspondence to *any* unitary operator involving local interactions, i.e. interactions that decay in strength with distance. In this way, one is effectively using the universal operations set [24] of a quantum computer to calculate the simulated system's evolution. As such, the errors resulting from the approximation $H_{sys} \simeq H_{sim}$ can be directly controlled, quantified and potentially corrected.

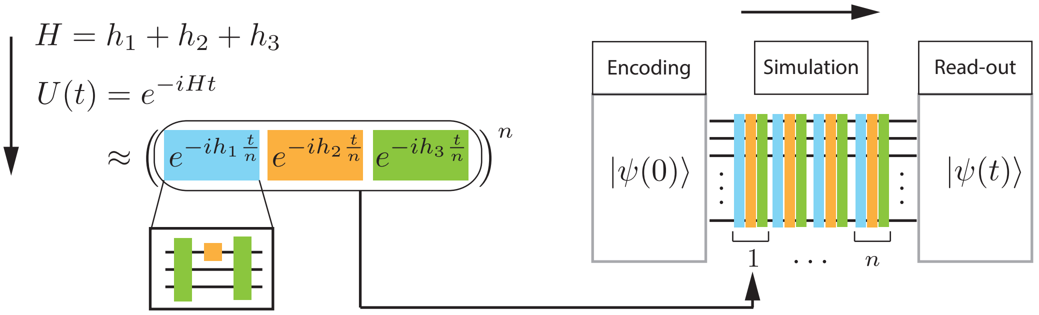

Figure 5.1.: Trotter approximation in a digital quantum simulation algorithm. Each local evolution operator h_i of the full Hamiltonian H is implemented either via an interaction directly available in the simulator (h_2, h_3) or as a composite sequence that effectively realizes the desired interaction (h_1). The interactions h_i do not necessarily commute. Following the Trotter approximation, they are only switched on for a fraction t/n of the simulated time step t. The resulting sequence is then concatenated n-times to arrive at the total time step t.

To demonstrate the procedure used in this approach, one can imagine the case of a time-independent Hamiltonian where the solution of the Schrödinger equation takes the form $\psi(t) = e^{-iHt/\hbar}\psi(0) = U\psi(0)$. In general, the global unitary evolution operator U can be directly implemented on the simulator only in certain specific cases (cf. analog simulation). Local evolution operators $U_k = e^{-ih_k t/\hbar}$, however, can always be realized as long as a fixed number of operations from a universal set is available on the simulator degrees of freedom. Even so, the corresponding terms generally do not commute $\left(U \neq \prod_k e^{-ih_k t/\hbar}\right)$ and can therefore not be applied in an arbitrary order, as would be necessitated by the composite operation shown in Figure 5.1. This is where the Trotter formula [146], the central part of a digital simulation, comes to the rescue:

$$e^{-iHt} = \lim_{n\to\infty}\left(\prod_k e^{-\frac{i}{\hbar}h_k t/n}\right)^n, n \in \mathbb{N}. \tag{5.1}$$

In such a Trotter decomposition, the Hamiltonian H describing the system dynamics is divided up into its individual terms, each of which is then sequentially applied for a time t/n within a discrete block or single Trotter step. The length of each of its parts, hence, depends on the total number n of blocks used in the discretization of the real time step t. As n is always finite, the corresponding error in this approximation of the global unitary is bounded and can be made arbitrarily small at the expense of a *polynomially* growing number of additional operations [147]. Notably, in many cases n does not need to be very large as the approximation often converges rather quickly.

5.3. Digital quantum simulation using trapped ions

A digital quantum simulation following the algorithm outlined above can be implemented using the universal operations set presented in Section 2.1 in combination with the single ion addressing capability introduced in Section 3.5. To recap and introduce respective shorthands, we define:

1. a ***local* AC Stark shift** on ion j, rotating its state by θ

$$O_1(\theta, j) = \exp(-i\theta\sigma_z^j),$$

2. a ***global* AC Stark shift**, shifting the phase on all ions equally by θ

$$O_2(\theta) = \exp(-i\theta\sum_j \sigma_z^j),$$

3. a **global carrier rotation** on all ions by θ around an axis set by phase ϕ

$$O_3(\theta, \phi) = \exp(-i\theta\sum_j \sigma_\phi^j) \quad \text{and}$$

4. a **Mølmer-Sørensen (MS) gate** entangling all ions in a basis set by phase ϕ

$$O_4(\theta, \phi) = \exp(-i\theta\sum_{j<k} \sigma_\phi^j\sigma_\phi^k), \quad \text{where}$$

σ_k^j denotes the k-th Pauli matrix acting on the j-th qubit and $\sigma_\phi^j = \cos\phi\ \sigma_x^j + \sin\phi\ \sigma_y^j$.

Each operation uses one of two beam paths that impinge on the trapped ions from different directions. The first beam, referred to as “global beam”, illuminates the ions equally and is used to perform the global spin rotations of O_2 and O_3 as well as the effective ion-ion (spin-spin) interaction O_4. The second beam, referred to as “addressed beam”, is sent in at an angle of 90° to the z-axis (68° for the trap at the university laboratory), along which the ions form a linear string. It is tightly focused close to the diffraction limit and can be used to address individual ions using the composite pulse sequence described in Section 3.5, which effectively implements O_1. In the experiments involving more than two ions the position of the beam can be changed within $\approx 30\,\mu\text{s}$ using an electro-optic deflector.

In the case of the resonant operation O_3 the interaction between the j-th qubit and the laser beam with optical phase ϕ is described by the Hamiltonian $H_3 = \hbar\Omega\sigma_\phi^j$. The rotation angle $\theta_3 = \Omega t$ is given by the Rabi frequency Ω (cf. Section 2.3.3) that can be tuned via the optical power as well as a variable pulse length t.

The off-resonant interaction O_2 additionally employs a large detuning $\Delta \gg \Omega$ of the laser frequency with respect to the qubit transition frequency. Its effective Hamiltonian hence becomes $H_2 = \frac{\hbar\Omega^2}{4\Delta}\sigma_z^j$ (cf. page 15).

Operation O_4 makes use of the global beam's projection onto the z-axis of the ion string which allows the laser to couple to that direction's motional COM mode at frequency $\omega_z \approx 1.2\,\mathrm{MHz}$. The laser beam is then simultaneously detuned from the qubit carrier frequency by $\pm(\omega_z \pm \delta)$ realizing a bichromatic light field (cf. Section 2.5) that implements an effective spin-spin interaction following the approach of Sørensen and Mølmer. Values of δ vary between 10 kHz and 100 kHz and every $t_{\mathrm{MS}} = 2\pi/\delta$ the interaction effectively generates the unitary operation O_4 with $\Theta_4 = \eta^2\Omega^2/\delta^2$.

The following sections begin with a proof-of-principle test of the convergence of the Trotter decomposition with increased digital resolution and higher order approximations. Then, a time-dependent Hamiltonian is investigated in a protocol for adiabatic state preparation. The final sections demonstrate the versatility and scaling behavior of the digital simulation by (I) adding more interactions and (II) adding more qubits to the experiments. Finally, Hamiltonian spectroscopy is presented as a direct application enabled by the digital approach. Quantum state or process tomography carried out for certain points in the observed dynamics of each simulation, provide a way to directly quantify the simulation quality in a comparison with analytical solutions and theoretical predictions based on the Trotter approximation.

Note: To make it easier to calculate and visualize the simulated system's time evolution for the different input states, Hamiltonians H and terms h_k used in the experiment, we define dimensionless Hamiltonians $\tilde{H} = H/E$ such that unitary evolutions $U(t) = e^{-i\tilde{H}Et/\hbar}$ are quantified by a unitless phase $\Theta = Et/\hbar$.

5.3.1. Ising model / Proof-of-principle demonstration

A simple model of ferromagnetism and phase transitions is the Ising model of interacting spin-1/2 particles which is described by the Hamiltonian

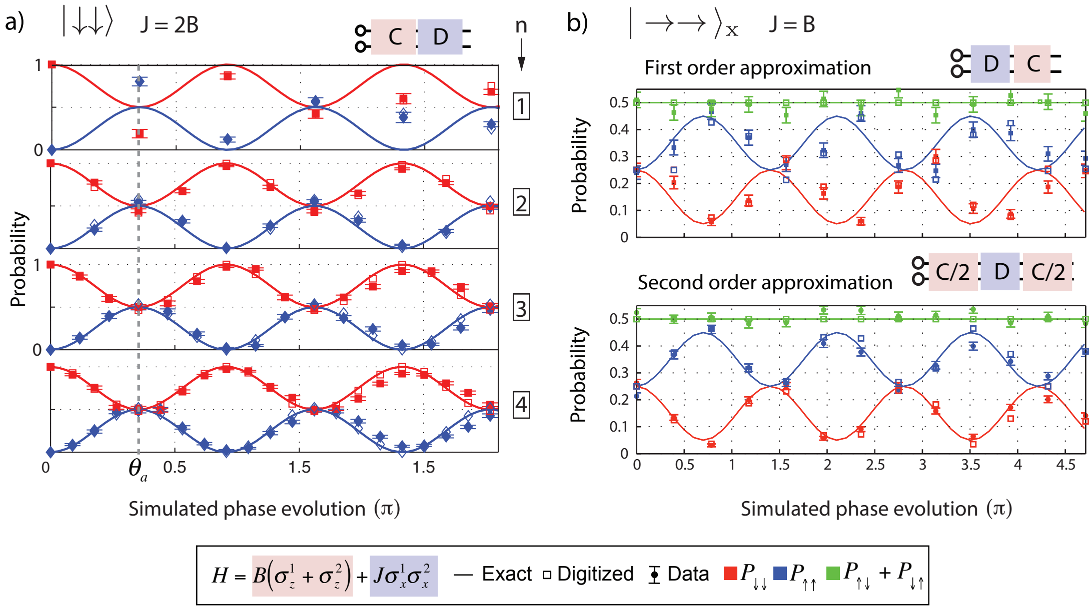

Figure 5.2.: Digital simulation of a two-spin Ising system
a) Dynamics for the initial state of $|{\downarrow\downarrow}\rangle$ for increasing levels of digital resolution ($n = 1, 2, 3, 4$). A single digital step corresponds to $D.C = O_4(\theta_a/n, 0).O_2(\theta_a/2n)$, where $\theta_a = \pi/(2\sqrt{2})$. **b)** First and second order Trotter-Suzuki approximations with their respective pulse sequences employing $D = O_4(\pi/8, 0)$ and $C = O_2(\pi/8)$ are compared for the initial state $|{\rightarrow\rightarrow}\rangle_x$.

$$H = J\sum_{i\neq j}\sigma_x^i\sigma_x^j + B\sum_i \sigma_z^i. \tag{5.2}$$

Here, B determines the strength of a uniform external magnetic field in the z-direction and J quantifies a uniform spin-spin interaction strength along an orthogonal direction in space. The indices i, j refer to the i-th and j-th spin-1/2 particle. The simplest case of the model employs two particles and serves as a building block of more complex spin models investigated later. While an analog simulation of the Ising model is possible in trapped ions [135], we implement a digital approach to investigate the convergence of and errors accumulated in the Trotter approximation. Mapping the spin states $|{\uparrow}\rangle$ and $|{\downarrow}\rangle$ to our optical qubit's logical states, we realize sequences of *Trotter steps* using operation O_2 to simulate the interaction with the external magnetic field and operation O_4 to realize the spin-spin interaction in an orthogonal direction.

First, we investigate a time-independent case with $J = 2B$, where Eq. (5.2) couples the state $|{\downarrow\downarrow}\rangle$ to the maximally entangled superposition $1/\sqrt{2}(|{\uparrow\uparrow}\rangle + |{\downarrow\downarrow}\rangle)$. Results of the simulation using the *"trotterized"* unitary $U(t) \approx \left(e^{-iCt/n}e^{-iDt/n}\right)^n$ are shown in

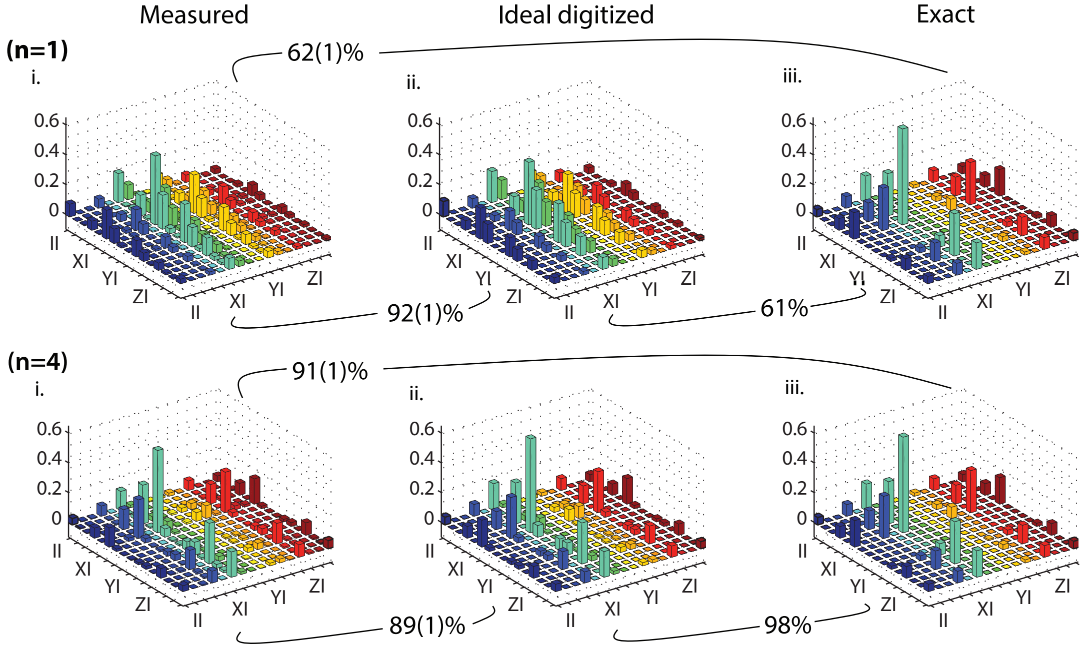

Figure 5.3.: Quantum process matrices at θ_a for $n = 1$ and $n = 4$ in Figure 5.2
The absolute values of the experimentally reconstructed process matrices (i.) are shown in the Pauli basis next to theoretical calculations of a simulated digitized evolution (ii.) and the exact analytical calculation (iii.). The overlaps given as percentage are calculated using the full, complex process matrices and the mixed-state fidelity [148]. One standard deviation of uncertainty, given in brackets, is obtained from a Monte-Carlo bootstrapping technique [149].

Figure 5.2.a for increasing digital resolutions using $n = 1$ up to $n = 4$ pairs of (O_2, O_4) operations. In each case, the size (in terms of θ) of an individual Trotter step is set by adjusting the pulse length t_2 in O_2 and the detuning δ in O_4.

The simulator state at the point marked by θ_a, is investigated by full *quantum process tomography* [150–152]. The tomography entails feeding a complete set of the possible input states into the simulation process and measuring each output, again, in a complete basis. As quantum projection noise can lead to unphysical results, the most likely quantum process matrix is determined in the following by an iterative maximum-likelihood reconstruction algorithm [153], which yields the results shown in Figure 5.3.

Errors of a first-order Trotter approximation are on the order of t^2/n. A second-order Trotter-Suzuki approximation [25, 154] implementing $U(t) \approx \left(e^{-iDt/2n}e^{-iCt/n}e^{-iDt/2n}\right)^n$ readily improves on this, yielding an error of t^3/n at the expense of more operations. The results of both cases are directly compared in Figure 5.2.b for the initial state $|{\rightarrow\rightarrow}\rangle_x$, showcasing the improved convergence.

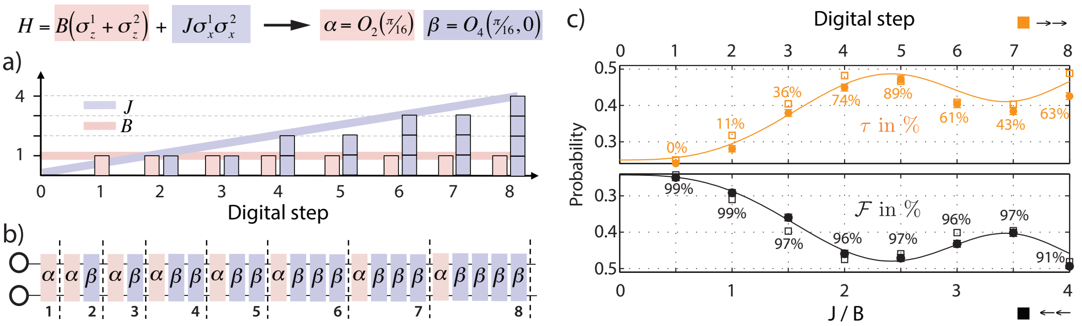

Figure 5.4.: Time-dependent Ising model
a, **b**) A linear increase in the spin-spin coupling strength J from 0 to 4B is divided into sequences of discrete building blocks α, β. **c)** The initial state $|{\downarrow\downarrow}\rangle$ evolves into an entangled superposition $\frac{1}{\sqrt{2}}(|{\leftarrow\leftarrow}\rangle_x + |{\rightarrow\rightarrow}\rangle_x)$, which is close to the ground state of the final Hamiltonian (step 8). The black percentages are calculated mixed-state fidelities $\mathcal{F}$ between the measured state (●) and the ideal digitized state (□). Orange percentages quantify the amount of entanglement in the measured state by its tangle τ.

Digital simulations are not limited to time-independent cases. In figure 5.4 we now investigate a case in which J increases linearly from 0 to $4B$. Starting in the ground state $|{\downarrow\downarrow}\rangle$ of the external magnetic field, the system evolves adiabatically into the anti-ferromagnetic entangled ground state $\frac{1}{\sqrt{2}}(|{\leftarrow\leftarrow}\rangle_x + |{\rightarrow\rightarrow}\rangle_x)$ of the final Hamiltonian. With a total simulated phase spanning $\theta = [0, \pi/2]$, the ramp increasing the spin-spin coupling strength J is divided into 8 digital steps, leading to oscillations that can be understood as non-adiabatic effects. Full *quantum state tomography* [151, 155, 156] is used to calculate the mixed-state fidelity $\mathcal{F}$ [148] and tangle τ [157] at each digital step in the simulation. As Figure 5.4.c shows, the data is in good agreement with the theoretically calculated states expected for the chosen discretization and rate of change of the control parameter J.

The procedure used in the simulation of the time-dependent Hamiltonian can also be regarded as a protocol for quasi-adiabatic digital state preparation, which provides us with a way to initialize ground states of system Hamiltonians that cannot be encoded directly.

5.3.2. Scaling up to more complex Hamiltonians

Additional spin-spin interactions in the y and z directions can be added by simply extending the operation sequence in each Trotter step accordingly. Figure 5.5 shows the dynamics of the initial state $|{\rightarrow\leftarrow}\rangle_x$ under three increasingly complex spin models.

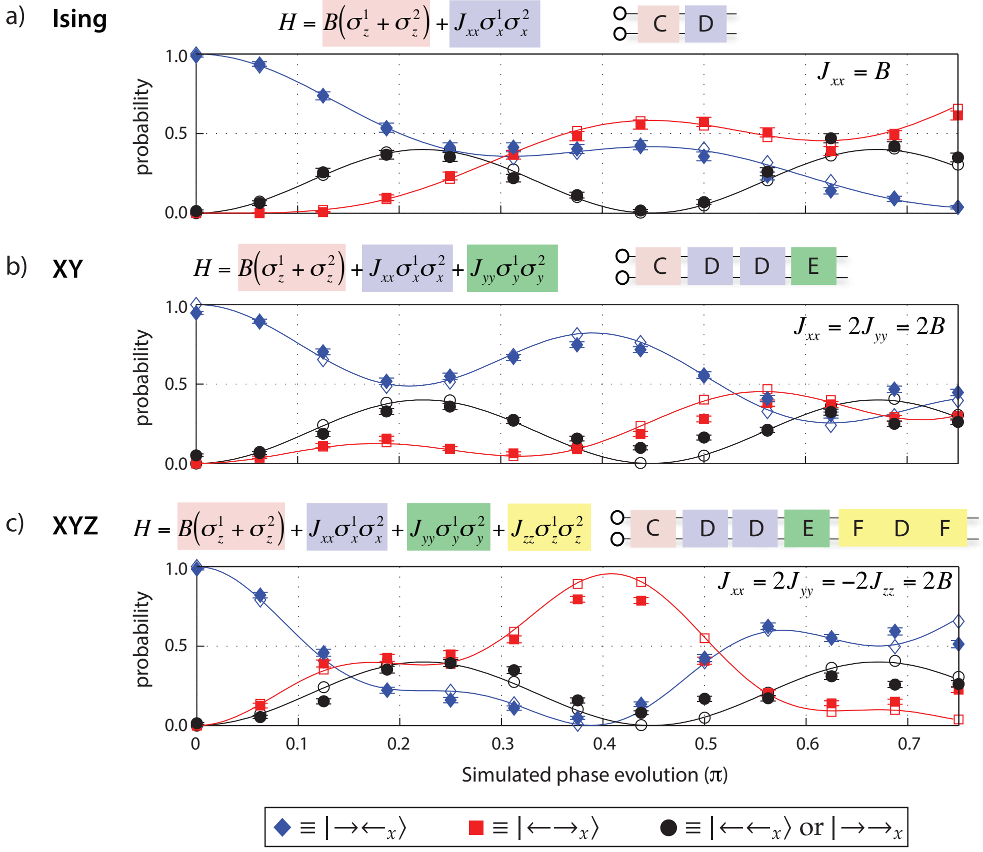

Figure 5.5.: Scaling up to more complex Hamiltonians
a to c) Dynamics of the initial state $|\rightarrow\leftarrow\rangle_x$. A single digital step is built up according to the diagram shown in each panel. The operations used in the simulations are $C = O_2(\pi/16)$, $D = O_4(\pi/16, 0)$, $E = O_4(\pi/16, \pi)$, $F = O_3(\pi/4, 0)$. Unfilled shapes correspond to the ideal digitized dynamics, filled shapes are data and lines represent the exact dynamics obtained from analytical calculations.

The particular input state has been chosen because the ideal evolution is markedly different in each model. In all cases the digital resolution (size of a Trotter step) is fixed to $\theta = \pi/16$. In terms of the basic building blocks, this corresponds to a total of 24, 48 and 84 gate operations in the Ising, XY and XYZ model, respectively. After 4 steps, process fidelities were determined as before yielding values of 88(1)%, 85(1)% and 79(1)% for the respective models. Estimates based on a numerical simulation assuming perfect operations in the digital simulation yield process fidelities of 98% in all cases, already hinting at inaccuracies due to imperfect operations beyond the expected Trotter errors.

5.3.3. Scaling up to a larger number of spins

Starting at three spins, the question of non-symmetric interaction distributions arises. They can be implemented with sequences of O_4 and O_1 operations, where the single particle manipulation of the latter allows us to restrict the effect of the former's spin-spin interaction to a subset of the whole simulator register. An example is given in Figure 5.6.a, where one coupled state $|\uparrow\downarrow\downarrow\rangle$ is populated faster than the others owing to the broken symmetry.

A long-range 4-spin Ising interaction is investigated in Figure 5.6.b. The increased complexity of the multi-body interactions leads to a rich structure in the dynamical evolution. The different oscillation frequencies observed in the data can be used, for example, to extract information about the energy gaps in the spectrum of the simulated Hamiltonian, which is demonstrated in the following section.

The largest simulation implemented in this project is the six-spin many-body interaction shown in Figure 5.6.c. It directly couples the states $|\uparrow\uparrow\uparrow\uparrow\uparrow\uparrow\rangle$ and $|\downarrow\downarrow\downarrow\downarrow\downarrow\downarrow\rangle$ which periodically creates a maximally entangled Greenberger-Horne-Zeilinger (GHZ) state.

In any simulation beyond two qubits the direct characterization of the simulation quality via quantum process tomography becomes impractical. The required number of different experimental configurations that needs to be measured scales as 12^n, where n is the number of qubits. In the four- and six-ion cases above, this would correspond to 20 736 and 2 985 984 measurement settings, respectively. However, an average process fidelity F_p can be bounded more efficiently [158]. Following this approach, it is sufficient to perform $2^n(n+2)$ (512 for $n=6$) measurements in order to at least put a bound on the simulation quality. To keep this discussion brief, the reader is referred to the comprehensive (32 page) supplementary material available with the publication for further details and data tables of parity measurements used in the analysis.

Especially in simulations involving operation O_1 and those that populate highly entangled GHZ states, a damping of the dynamics is observed which results from accumulated errors over the course of many gate operations. In case of the former, single ion addressing errors (cf. Section 3.5) multiply while the latter is influenced by "superdecoherence" [67] corresponding to the increased fragility of an n-body entangled state.

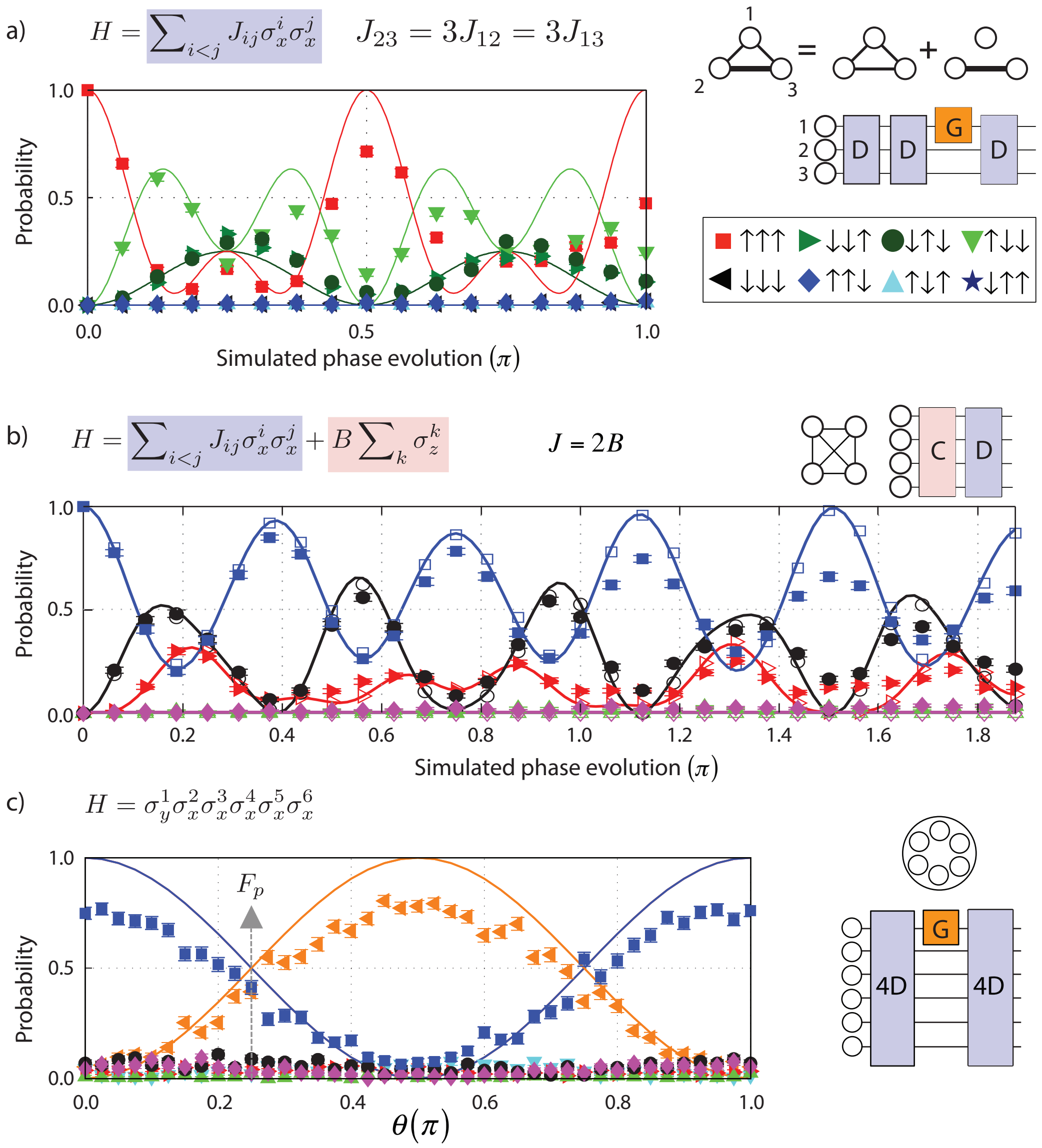

Figure 5.6.: Scaling up to a larger number of spins
a) Example for the implementation of an anisotropic spin-spin interaction in a system of three ions. The addressed operation $G = O_1(\pi/2, 1)$ allows us to selectively manipulate spin 1 and compose the desired Hamiltonian from an equal-strength interaction and another with twice the strength between one pair. **b**) Simulation of a four-spin long-range Ising system with the initial state $|\downarrow\downarrow\downarrow\downarrow\rangle$. The blue, black and red lines (symbols) correspond to cases where an even number of spins are pointing down. Each digital step corresponds to $D.C = O_4(\pi/16, 0).O_2(\pi/32)$.
c) Six-body interaction using the operations $4D = O_4(\pi/4, 0)$ and $F = O_1(\theta, 1)$. At $\theta = \pi/4$ (marked by the gray line) the average process fidelity F_p is bounded to have a value between $56(1) \leq F_p \leq 77(1)$ (see text). — In b) and c) the symbol key is given by the probability P_i of finding i spins pointing up (■P_0 ◆P_1 ●P_2 ▲P_3 ▶P_4 ▼P_5 ◀P_6).

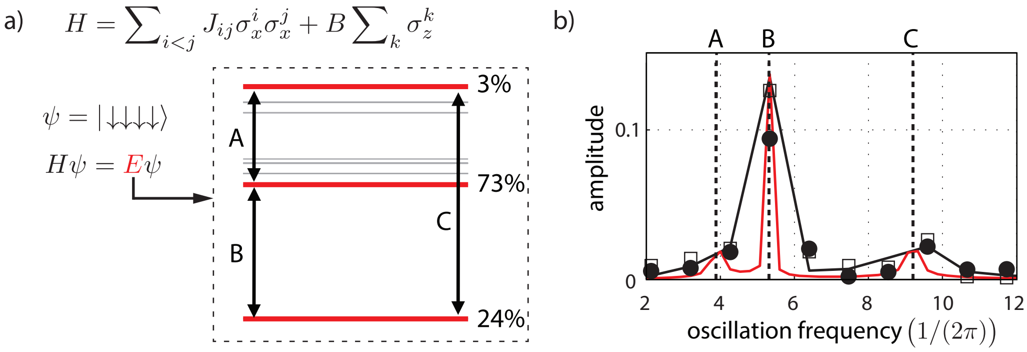

Figure 5.7.: Hamiltonian spectroscopy
a) Energy level diagram of the 4-body Hamiltonian simulated in Figure 5.6.b. The initial state $|{\downarrow\downarrow\downarrow\downarrow}\rangle$ is a superposition of three different energy eigenstates (marked in red) with the respective population probabilities given as percentages. Unpopulated energy levels are shown in gray. The energy gaps between the populated states are labeled A, B and C. **b)** Frequency spectrum obtained from a Fourier transformation of the time evolution data (black trace, P_2 in Figure 5.6.b), together with the values theoretically expected from a digitized simulation (unfilled squares) and the actual spectrum calculated analytically (red line).

5.3.4. Hamiltonian spectroscopy

The oscillation frequencies seen in the time evolution of the various observables of a quantum system correspond to energy gaps in the underlying Hamiltonian. A Fourier transformation can be used to extract them and infer information about the energy spectrum of the simulated Hamiltonian. Specific energy gaps of interest could be targeted by preparing superpositions of eigenstates via an initial quasi-adiabatic digital evolution as shown before in Figure 5.4 [159].

An example for this method is given in Figure 5.7. Here, the spectral components of the 4-body Ising interaction shown in Figure 5.6.b are obtained with the input state $|{\downarrow\downarrow\downarrow\downarrow}\rangle$ from the observable corresponding to the probability of finding all combinations of two spins pointing up and two spins pointing down. While at least one energy gap can be clearly identified, the results also show the limitation of this approach: depending on the coupling strength of the laser-mediated simulator Hamiltonian (and thereby the speed of the time evolution) the spectral resolution remains limited. However, the recording of longer time-domain traces is further hampered by decoherence whose strength generally is state- and protocol-dependent, as shown in the prior section.

5.4. Conclusion

Digital quantum simulation provides access to arbitrarily engineered interactions and facilitates the quantification of intrinsic simulation errors. However, the concatenated approach mandated by the Trotter approximation comes at the price of a higher sensitivity to errors in the experimental implementation of the repeatedly applied “building blocks” of the simulated interactions. Whereas analog simulations can often be tailored to correct for systematic experimental errors and fluctuations in control parameters, digital simulations rely on the overall constant quality of each individual operation. Depending on the simulation protocol, small errors can accumulate and be detrimental to the quality of the obtained results. However, the gate-based digital model provides the advantage that it is readily compatible with protocols for quantum error correction which can be used to counteract these adverse effects. First results of repetitive quantum error correction have been shown in reference [160] and are certainly needed for larger simulations than those presented in this chapter. Recently, the digital approach has been extended to include the controlled simulation of dissipation [161], further extending the range of models accessible by quantum simulations.

6. Entanglement-enhanced detection of single-photon scattering events

published in: Nature Photonics **7**, 630–633 (2013)
arXiv:1304.3270 [quant-ph]

This chapter presents a spectroscopy technique designed to enhance the detection sensitivity for scattering events on a broad optical transition towards the single photon level. The method relies on sensing the small recoil that the scattering of a single photon imparts on an atomic or molecular ion. Its novelty lies in the "amplification" of this very weak "momentum kick" by means of a Schrödinger cat state's high sensitivity to external perturbations. It is demonstrated in a proof-of-principle experiment in the newly-built trap II (cf. Section 3.1).

The chapter begins with a brief discussion of ways to investigate the light-matter interaction at the single particle level. Then, it expands on the effect of a photon recoil on a trapped ion and provides a description in terms of displacement operators in phase space. In the following, motional Schrödinger cat states are introduced and their creation using an optical qubit and as well as their size and coherence are investigated. Finally, the cat state spectroscopy protocol is described, demonstrated and benchmarked in a two-ion crystal of $^{40}\mathrm{Ca}^{+}$ and $^{44}\mathrm{Ca}^{+}$. The chapter concludes with a discussion on heating-rate-induced decoherence and its adverse effects on the protocol's attainable detection sensitivity.

6.1. Light-matter interactions at the single particle level

A fundamental element of quantum optics and spectroscopy is the interaction of a *single* photon with a *single* atom or molecule. The many advances in atomic, molecular and optical (AMO) physics made over the 20th century [162] have brought investigations of this fundamental light-matter interaction into reach. However, to this day – even with

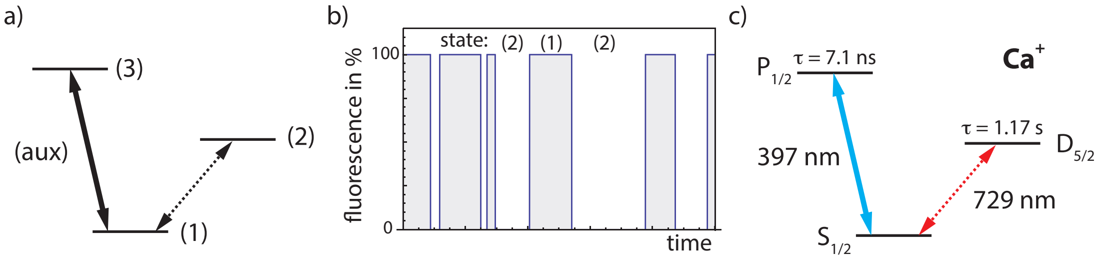

Figure 6.1.: Electron shelving
a) Energy level structure considered in the electron shelving method. Photon absorption on the targeted (1) ↔ (2) transition is detected via the cessation of fluorescence observed from the scattering of photons on the auxiliary transition (1) ↔ (3). **b)** Under the influence of a (near) resonant excitation on the (1) ↔ (2) transition, changes between two fluorescence levels occur at random, indicating "quantum jumps" between states (1) and (2). **c)** Mapping of the electron shelving method to the energy level structure of Ca$^+$.

state of the art technology – the detection of single photons emitted or absorbed by an atom or molecule remains a formidable challenge.

In fluorescence measurements it is crucial for the detection optics to cover a large solid angle to efficiently collect the emitted photon(s) in the first place. Absorption measurements, taking the inverse approach, rely on a good mode-matching between the atom and the light field used to probe it. Both techniques require detectors with a high quantum efficiency specifically tailored to the wavelength in question. However, even with sophisticated optical setups, such as those in references [163, 164], no more than a few percent *overall* detection efficiency have been achieved thus far.

A way around this issue has been proposed by Hans Dehmelt already in 1975 [86, 87]. His indirect detection method, known by the name *electron shelving*, is applicable to the following case (illustrated in Figure 6.1 above): Suppose one wants to detect the absorption or emission of a photon on a transition between a ground (1) and an excited state (2) in a single atom. The atom's electronic level structure additionally contains a third level (3), that also connects to the ground state (1) but has a much higher decay rate than state (2). Suppose finally, one can drive the strongly allowed (1) ↔ (3) *auxiliary* transition with resonant light and collect at least a fraction of the scattered fluorescence photons. If a photon now gets absorbed on the (1) → (2) transition, the electron "jumps" to state (2) and the *single* absorption event is immediately indicated by the sudden cessation of the previously abundant fluorescence observed from the (1) ↔ (3) transition. The electron, figuratively speaking, has been "shelved" to the (2)-state, which gave the detection technique its name.

One of the fundamental questions arising from the quantum mechanical description of light-matter interactions is *"Do quantum jumps (really) exist?"*. Already in 1952, Erwin Schrödinger published his respective doubts in a two-part article [3, 165] with that very question as its title. Still, only in the mid-1980s, ion trapping and laser technology had advanced sufficiently to approach that (up to then thoroughly debated) question [see, e.g., references in 4]. Dehmelt's electron shelving technique, with its very high signal to noise ratio and near 100 % detection efficiency, was the essential ingredient to perform an experiment. Finally, in 1986, using single trapped ions, the first observations of "quantum jumps" were reported [166–168]. In its use for spectroscopy, however, the electron shelving's prerequisite of a suitable level scheme limits its applicability to only a few ionic species.

Almost 20 years later, following significant progress in the development of methods conceived for quantum information processing using trapped atomic ions [12–15], a new technique was devised to enable the application of the electron shelving method to atomic species that lack suitable transitions. Bearing a name that provides a clear indication of its origin, *quantum logic spectroscopy* (QLS) [20] confines a "spectroscopy ion" of interest together with an auxiliary "logic ion" of a different species. A joint vibrational mode shared by the two particles is then used to map the internal state of the spectroscopy ion to the internal state of the logic ion, where it can subsequently be read out using electron shelving. In addition to enabling precision spectroscopy on atomic species previously out of reach, the strong Coulomb interaction between both trapped particles allows this approach to extend the benefits of laser cooling to elements where direct laser cooling is not feasible. Recently, such *sympathetic cooling* [169] via the logic ion made it possible to develop extremely accurate single-ion optical atomic clocks [17, 18] that interrogate the $^1\mathrm{S}_0 \leftrightarrow {}^3\mathrm{P}_0$ clock transition of $^{27}\mathrm{Al}^+$.

A key requirement needed for quantum logic spectroscopy is the ability to spectrally resolve motional sidebands of the transition in question. Typical motional frequencies $\omega/(2\pi)$ are in the range of one to a few MHz, which again limits the kind of transitions that can be investigated to those with a linewidth $\Gamma \ll \omega$.

Furthermore, the linewidth of a transition is not the only concern in the investigation of optical spectra in atomic and molecular ions. In some cases, scattering events are limited to only a few or even just a single photon. This can be due to technical reasons, e.g. difficulties in producing or delivering the light needed for spectroscopy, or simply result from the fact that a transition is not closed. In this case, a decay does not lead back to the initial state, preventing repeated scattering events on the same transition.

6.2. Photon recoil

Instead of detecting the spectroscopy ion's electronic state directly or via QLS, one can also use another signature of a scattering event: the mechanical recoil experienced by the ion upon absorption or emission of a photon characterized by wavelength λ, momentum $p = \hbar k$ and wavenumber $k = 2\pi/\lambda$. In order to quantify its magnitude, the "momentum kick" has to be compared to the energy of a motional quantum $\hbar\omega$ of the ion oscillating at (angular) frequency ω in the harmonic trapping potential (cf. Section 2.3.4). The square root of this ratio takes the form of the dimensionless Lamb-Dicke parameter $\eta = \sqrt{E_\text{rec}/\hbar\omega}$ as seen before in Eq. (2.26), which for experiments on optical transitions typically satisfies $\eta \ll 1$. Here, the recoil energy is given by $E_\text{rec} = p^2/(2\,m)$, where m is the mass of the ion.

For an ion cooled to the motional ground state, the action of a photon recoil is described by a coherent displacement $D(i\eta)$ in phase space (Figure 6.2.a) as the following calculation, using Eqs. (2.20) and (B.12), shows:

$$\begin{aligned}
\langle 0|\, D^\dagger(i\eta)\hat{p}D(i\eta)\,|0\rangle &= p_0 i \,\langle 0|\, D^\dagger(i\eta)(a^\dagger - a)D(i\eta)\,|0\rangle \\
&= p_0 i \,\langle 0|\, D^\dagger(i\eta)D(i\eta)((a^\dagger - i\eta) - (a + i\eta))\,|0\rangle \\
&= p_0(2\eta)\,\langle 0|\, D^\dagger(i\eta)D(i\eta)\,|0\rangle \\
&= p_0 2\eta = p_0 2kx_0 \\
&= \sqrt{\frac{\hbar m\omega}{2}}\,2\sqrt{\frac{\hbar}{2m\omega}} = \hbar k.
\end{aligned}$$

Consequently, the probability P of being promoted out of the ground state by absorption of a single photon is (Figure 6.2.b)

$$P_{(0\to 1)} = 1 - |\langle 0|D(i\eta)|0\rangle|^2 \approx \eta^2.$$

This makes a direct detection of the recoil imparted by a single photon rather inefficient. While each scattering event contributes very little motional energy, the scattering of 100's of photons does lead to a measurable heating and has been used to reconstruct spectral lines of broad transitions from the observed fluorescence change of a Doppler-cooled control ion [170]. Using a ground state cooled ion crystal of $^{24}\text{Mg}^+$ and $^{40}\text{Ca}^+$, a very recent experiment [38] has determined the line center of the $^{40}\text{Ca}^+$ $\text{S}_{1/2} \leftrightarrow \text{P}_{1/2}$ transition by detecting the recoil-induced heating of as little as 15 scattered UV photons.

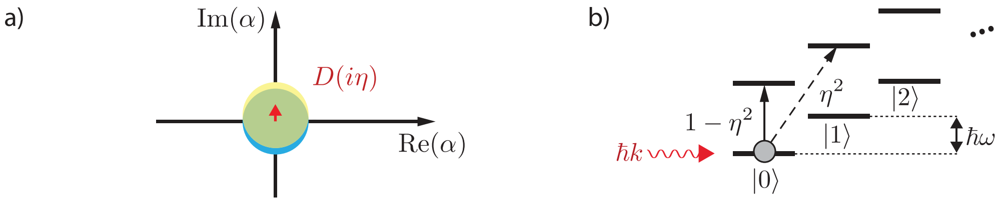

Figure 6.2.: Photon absorption by a ground state cooled ion
a) Phase space representation. An absorption event displaces the motional ground state (circle) by a small amount in phase space. **b)** Fock space representation. Most scattering events of a photon of momentum $p = \hbar k$ do not change the motional state. The likelihood of increasing the ion's energy by one motional quantum $\hbar\omega$ is η^2.

The next sections will show how one can apply a non-classical state of motion to amplify the photon recoil to a level that allows for a very efficient detection of events in which only a single infrared photon is scattered. Unlike any of the techniques mentioned above, the method of Schrödinger cat state spectroscopy introduced in Section 6.4 below is able to maintain a similar sensitivity even in the absence of ground state cooling.

6.3. Schrödinger cat states of motion

In 1935, Erwin Schrödinger put forward his famous thought experiment involving a cat whose fate is entangled with the state of an atom, leaving it simultaneously dead and alive for as long as it is not observed [171]. This superposition of distinguishable, macroscopic quantum states, since then referred to as "Schrödinger cat states", was meant to exemplify the inherent peculiarities of quantum theory. In order to create and preserve states with the same properties in the laboratory, a well-controlled and well-isolated quantum system is needed. A single trapped ion confined in a harmonic potential is an ideal candidate. With the ability to perform coherent manipulations of the motion using laser beams that couple to the trapped ion's internal states, proposals on how to create various non-classical states of motion where put forward, e.g. references [172–174]. Shortly afterwards, the first "mesoscopic" Schrödinger cat state, in which the ion's motion becomes entangled with its internal electronic states, was created in the laboratory [175]. Now accessible experimentally, investigations into the decoherence of such states under controlled coupling to the environment followed [176, 177]. Both of these experiments made use of a two-photon Raman coupling that coherently displaced the $|\uparrow\rangle$ state of a qubit encoded in the hyperfine ground states of $^9\mathrm{Be}^+$ in phase space. By interleaving the displacement operation with a carrier $\pi/2$ and a π pulse, both qubit states were sequentially displaced in opposite directions, effectively creating a cat state.

Creation of single-ion motional cat states using an optical qubit

The optical qubit in $^{40}\mathrm{Ca}^+$ allows us to create a Schrödinger cat state using only a single bichromatic laser pulse [178]. With the appropriate choice of optical sum and difference phase, the bichromatic Hamiltonian of Eq. (2.35) directly implements the state-dependent coherent displacement $D(\alpha)$ introduced in Eq. (2.23). To illustrate the effect of its application to the trapped ion, we start with the ground state of both the ion's internal and external degree of freedom

$$|\Psi_0\rangle \equiv |-\rangle_z\,|0\rangle = \frac{1}{\sqrt{2}}\Big(|+\rangle_x - |-\rangle_x\Big)\,|0\rangle\,.$$

Here, the electronic ground state $|-\rangle_z$ has been *rewritten* in the form of a superposition of the σ_x basis states $|\pm\rangle_x$, which are eigenstates of the specific bichromatic Hamiltonian in Eq. (2.36). The motional ground state $|0\rangle$ corresponds to a Gaussian distribution of position and momentum in phase space (green circle in Figure 6.3). Application of the displacement operator now creates the state

$$|\Psi_{\mathrm{cat}}\rangle = D(\alpha)\,|\Psi_0\rangle = \frac{1}{\sqrt{2}}(|+\rangle_x|\alpha\rangle - |-\rangle_x|-\alpha\rangle),$$

in which the $|+\rangle_x$ electronic eigenstate has become entangled with a coherent state displaced to $|\alpha\rangle$ and likewise $|-\rangle_x$ has become entangled with a coherent state displaced to $|-\alpha\rangle$. A this point, the spin-motional cat state $|\Psi_{\mathrm{cat}}\rangle$ is fully characterized by the distance $d = 2|\alpha|$ of the two coherent states in phase space, where α is the dimensionless displacement amplitude of Eq. (2.22).

If a projective measurement in the qubit's logical basis $\langle\sigma_z\rangle = \langle\Psi_{\mathrm{cat}}|\,\sigma_z\,|\Psi_{\mathrm{cat}}\rangle$ is carried out on $|\Psi_{\mathrm{cat}}\rangle$, the probability to find the ion in its electronic state $|\uparrow\rangle$ is

$$p_\uparrow = \frac{1}{2}\Big(\langle\sigma_z\rangle + 1\Big) = \frac{1}{2}\left(1 - e^{-2|\alpha|^2}\right). \tag{6.1}$$

As the measurement ignores the motional part of $|\Psi_{\mathrm{cat}}\rangle$, a complete statistical mixture of the qubit's basis states ($p = 0.5$) is found for $\alpha \to \infty$. However, even at $\alpha \approx 1.8$ ($p_\uparrow = 0.499$) the remaining overlap of the two Gaussian distributions in phase space is already negligible, as is illustrated in Figure 6.3.

In the experiment, we first prepare the initial state $|\Psi_0\rangle$ by optical pumping and sideband cooling (Sections 4.3 and 4.6). Then, the displacement is applied in the form of a single bichromatic laser pulse of duration t whose spectral components are resonant

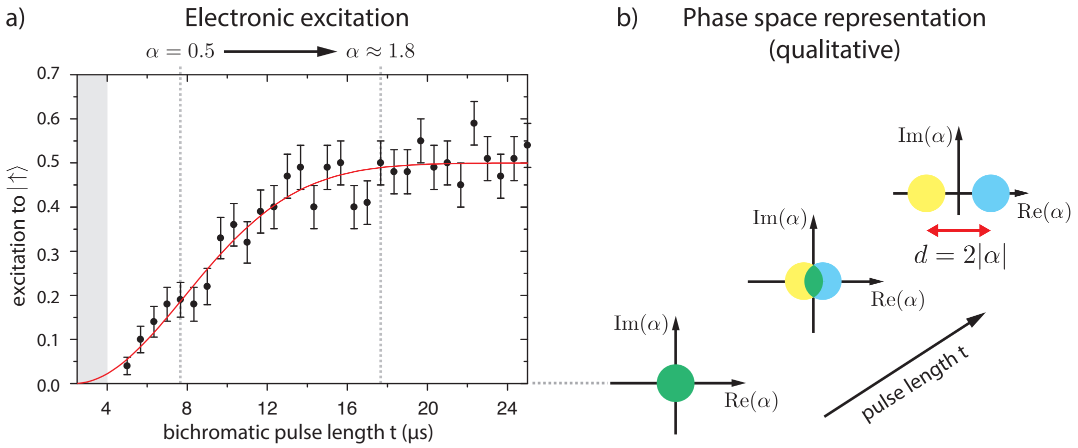

Figure 6.3.: Creation of a Schrödinger cat state using a bichromatic light field
a) Mean excitation to $|\uparrow\rangle$ as a function of bichromatic pulse length. Based on Eq. (6.1), the red line is a fit of $p_\uparrow = \frac{1}{2}(1 - e^{-2(a(t-t_0))^2})$ to the data. The experimental parameters relating to the displacement $\alpha = \eta\Omega t$ were determined independently to be $\eta = 0.08$ and $\Omega \approx 2\pi \times 294\,\text{kHz}$. Pulse shaping with a 4 µs Blackman window (cf. page 42) is used to suppress off-resonant excitation of the carrier transition and restricts data points to those $\geq$5 µs. **b)** The coherent ground state wave packet splits further and further into two parts, the longer the bichromatic light field is applied for. The size of the resulting cat state is given by their distance d and directly determined by the length of the applied pulse t.

with the red and blue sideband of the chosen motional mode. The two corresponding frequency components are produced by AOM 12 (cf. Figure 3.9) and subsequently coupled into the same single-mode optical fiber. In terms of the experimental parameters, the displacement amplitude $\alpha = \eta\,\Omega\,t$ is directly proportional to the bichromatic pulse length t, the Lamb-Dicke factor η and the coupling strength Ω of the laser beam used in the experiment. The latter assumes an equal intensity in the beam's red- and blue-detuned frequency components ($\Omega_{n,n-1} = \Omega_{n,n+1}$). After a first optimization during fiber coupling, this condition is regularly checked by sequentially shifting either component onto the carrier frequency (using AOM 11) and comparing Rabi-flops. The RF power levels sent to AOM 12 are used for fine-tuning.

Cat state size

Once the cat state has been created, its size $d = 2|\alpha|$ can be determined from the mean number of phonons $\langle n\rangle = |\alpha|^2$ that characterize the coherently displaced parts moving back and forth in the harmonic oscillator (c.f Section 2.3.4). The value of $\langle n\rangle$ can be obtained from a fit to Rabi-flops driven on resonance with the blue motional sideband (BSB). In this case, the excitation probability $p_\uparrow$ is fit by Eq. (2.31) with $\Omega = \Omega_{n,n+1}$.

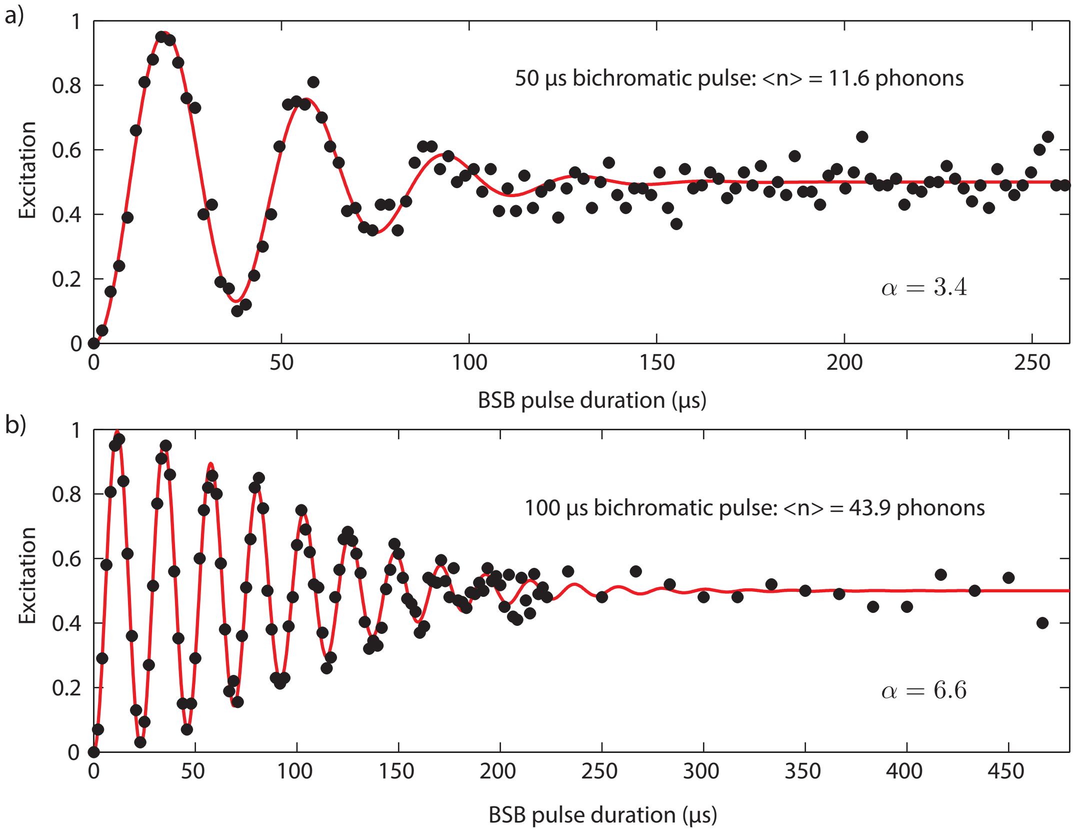

Figure 6.4.: Cat state size
Fits to Rabi flops on the blue motional sideband (BSB) after a Schrödinger cat state has been produced by a resonant bichromatic excitation of different length. Before the traces are recorded, the electronic excitation was "traced out" by incoherent light at 854 nm.

Beforehand, the electronic state components have to be recombined in $|-\rangle_z$ or "*traced out*" [25] from the joint state $|\Psi_{\text{cat}}\rangle$ using an incoherent pulse of 854 nm light. This leaves the motional state unchanged (for all practical purposes) and "frees" the internal state for excitation on the blue sideband.

Figure 6.4 above shows the results obtained after the application of a bichromatic pulse of $t = 50\,\mu\text{s}$ and $t = 100\,\mu\text{s}$. Both were acting on a single ion with a similar coupling strength to the one used in Figure 6.3 before. The RMS size of the ion's ground state $|0\rangle$ is $x_0 = \hbar/(2m\omega) \approx 10\,\text{nm}$ at the axial trap frequency $\omega_z/(2\pi) = 1.229\,\text{MHz}$ used in the experiment. The distance between the superimposed motional wave packets in the trapping potential is $2|\alpha|x_0$. Clearly showing their separation, this corresponds to 68 nm in the $\langle n\rangle = 11$ case and 132 nm for $\langle n\rangle = 44$, respectively.

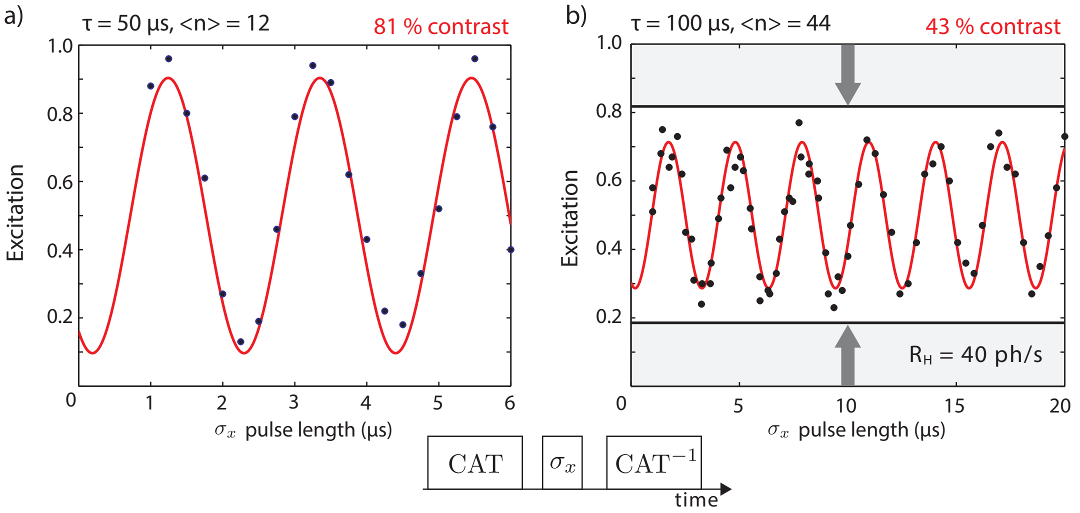

Figure 6.5.: Cat state coherence
Phase coherence of the cat states shown in the corresponding panels of Figure 6.4. In the pulse sequence shown above, a cat state is created (CAT) and interfered (CAT^{-1}) using bichromatic pulses of the same length but with an optical phase difference of π. The relative phase of the cat state's components is varied via a σ_x carrier rotation placed in between. The contrast of the retrieved fringe pattern is indicative of their coherence. The gray shaded area in panel (b) indicates the expected reduction of the fringe contrast from motional heating at rate R_H.

Coherence of motional cat states

Cat states are well known for their sensitivity to perturbation from the environment and exhibit a decoherence rate that scales with $|\alpha|^2$ [176, 177]. In our case, decoherence is mainly caused by two mechanisms: motional heating, that randomly displaces the coherent superposition in phase space (Sections 4.7 and 6.5.2) and drifts of the trap frequency (Section 4.8.3), that rotate both components around the origin in phase space.

Figure 6.5 shows an interference experiment that, akin to the parity signal in Figure 4.13, allows us to directly determine the remaining coherence from the contrast of the observed fringe pattern. Here, a σ_x carrier rotation of variable length placed after the creation of the cat state modifies the state to

$$|\Psi_{\text{cat}}\rangle = \frac{1}{\sqrt{2}}\left(e^{-i\delta}|+\rangle_x|\alpha\rangle - e^{i\delta}|-\rangle_x|-\alpha\rangle\right).$$

The phase factor δ is proportional to the length of the σ_x rotation and causes the signal $p_\uparrow$ to oscillate between $p = 0$ and $p = 1$ after interfering the cat state with a second bichromatic pulse of opposite phase.

6.4. Cat state amplification of a recoil signal

In the same way as the quantum logic spectroscopy introduced in Section 6.1, cat state spectroscopy employs a *logic ion* to implement sympathetic cooling and state detection via electron shelving in the investigation of a co-trapped *spectroscopy ion*.

The procedure used to create the spin-motional cat state of a single ion is readily extended to the two-ion case. Here, the bichromatic light field is tuned in resonance with the sidebands of the two-ion crystal's center of mass mode and a cat state $|\Psi_{\text{cat}}\rangle$ is created in the same way as before. This time, however, only the logic ion's spin state becomes entangled with the motion.

The cat state's two superimposed coherent states oscillate in phase space at the frequency ω of the motional mode that was addressed by the bichromatic pulse. For clarity, Figure 6.6.a depicts a co-rotating frame, such that the displacement in the cat state creation is linear along one direction in phase space (cf. Figure 2.6 in Section 2.3.4). Note that the bichromatic pulse, being the first coherent pulse interacting with the motion of the ions, sets the phase reference for all subsequent interactions.

In the following step, spectroscopy light is sent into the trap. If now a single photon is absorbed by the spectroscopy ion, its recoil causes both vibrational components to be displaced in the same direction in phase space by an amount η_{abs} that corresponds to the Lamb-Dicke factor of the absorbing transition. As a result, the cat state changes to

$$|\Psi'_{\text{cat}}\rangle = \frac{1}{\sqrt{2}}\Big\{\Big(|+\rangle_x|\alpha+\beta\rangle\Big) - \Big(|-\rangle_x|-\alpha+\beta\rangle\Big)\Big\},$$

where $\beta = \eta_{\text{abs}}e^{i\varphi_{\text{sc}}}$ and the *scatter phase* $\varphi_{\text{sc}} = \omega\tau$ relates the time τ of the absorption event to the oscillatory motion at frequency ω of the cat state's components in phase space. Consequently, the displacement vector's direction in phase space is now given by φ_{sc} in the co-rotating frame of Figure 6.6.b.

Finally, a second bichromatic pulse, in which the overall optical phase is shifted by π with respect to the first pulse, recombines both motional parts and disentangles them from the logic ion's internal state. If a photon was absorbed, the complete trajectory in phase space now encloses an area, depicted by the gray shading in Figure 6.6.c, that corresponds to a geometric phase [58]. To see how it affects the electronic states, we calculate the effective unitary evolution associated with the three displacements in each case. State $|+\rangle_x$ is displaced by $D(-\alpha)D(\beta)D(\alpha)$ and $|-\rangle_x$ undergoes $D(\alpha)D(\beta)D(-\alpha)$. In order to show how both states accumulate a phase of opposite sign, it is convenient to

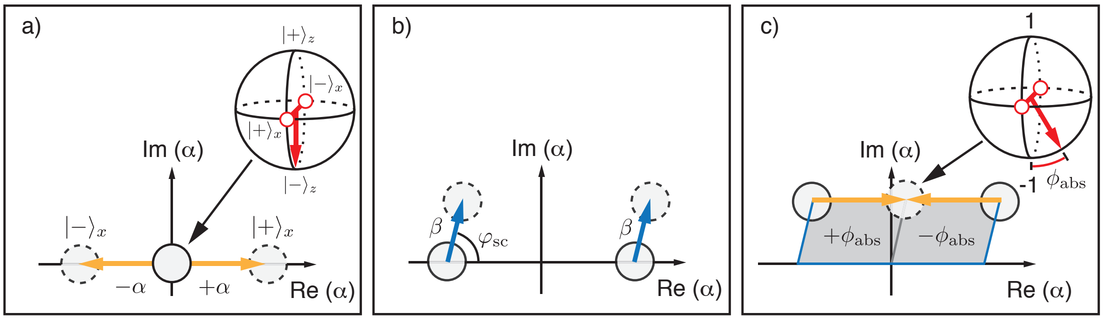

Figure 6.6.: Cat state spectroscopy in phase space
a) Schrödinger cat state preparation. A qubit encoded in a logic ion, initialized in $|{\downarrow}\rangle_z$ (inset Bloch sphere), becomes entangled with a joint vibrational mode of the two-ion crystal formed with the co-trapped spectroscopy ion. **b)** Absorption of a photon by the spectroscopy ion causes a displacement of size η_{abs} (magnified for clarity) in a direction determined by the event's timing φ_{sc} relative to the cat state's oscillation phase. **c)** The cat state is reinterfered, disentangling the internal state from the motion and leaving the geometric phase ϕ_{abs} in the logic ion's internal state, where it can be read out via standard electron shelving.

add a fourth (hypothetical) displacement $D(-\beta)$ to the end of the sequence, such that the motion is completely retuned to its original state and drops out in the calculation. In the case of $|+\rangle_x$ we now have

$$D(-\beta)D(-\alpha)D(\beta)D(\alpha) = D(-\beta-\alpha)e^{i\mathrm{Im}(\alpha^*\beta)}D(\beta+\alpha)e^{i\mathrm{Im}(\alpha^*\beta)} = e^{i2\mathrm{Im}(\alpha^*\beta)},$$

where Eq. (2.25) was used in the calculation, and similarly $e^{-i2\mathrm{Im}(\alpha^*\beta)}$ for state $|-\rangle_x$. Hence, for a real-valued α, the geometric phase

$$\phi_{\mathrm{abs}} = 2\,\mathrm{Im}(\alpha\eta_{\mathrm{abs}}e^{i\varphi_{\mathrm{sc}}}) = 2\alpha\eta_{\mathrm{abs}}\sin\varphi_{\mathrm{sc}} \tag{6.2}$$

ends up in pre-factors associated with the logic ion's electronic states and transforms its state to

$$|-\rangle_z \rightarrow |\Psi_f\rangle = \frac{1}{\sqrt{2}}\left(e^{i\phi_{\mathrm{abs}}}\,|+\rangle_x - e^{-i\phi_{\mathrm{abs}}}\,|-\rangle_x\right) = \cos\phi_{\mathrm{abs}}\,|-\rangle_z + i\sin\phi_{\mathrm{abs}}\,|+\rangle_z\,.$$

The signature of the photon scattering process can now be obtained from a measurement of the logic qubit's spin projection $\langle\Psi_f|\,\sigma_z\,|\Psi_f\rangle = -\cos(2\phi_{\mathrm{abs}})$. If an additional $\sigma_x(\pi/2)$ pulse is carried out prior to detection, a phase factor of $\pi/4$ is added to ϕ_{abs} such that the spin projection $\langle\sigma_y\rangle = \sin(\phi_{\mathrm{abs}})$ is detected instead. As the initial state $|-\rangle_z$ can be represented as an equal superposition of the σ_y basis states $|\pm\rangle_y$, the signal is now centered around 0. However, while its sinusoidal character allows for the highest sensitivity at this point, the $\langle\sigma_y\rangle$-signal vanishes in all cases where the absorption event is not synchronized with the oscillation of the cat state as β has to be averaged over all possible $\varphi_{\mathrm{sc}} = [0, 2\pi]$. The $\langle\sigma_z\rangle$, on the other hand, always yields a non-zero signal that is centered around -1 such that $\varphi_{\mathrm{sc}} =]0, \pi[$ and $\varphi_{\mathrm{sc}} =]\pi, 2\pi[$ do not cancel.

Varying the scatter phase φ_{sc} of the spectroscopy pulse allows us to retrieve a signal in the form of a sinusoidal fringe pattern similar to that seen in Section 4.8. In this respect, cat state spectroscopy can be seen as a Ramsey-like experiment.

6.5. Random geometric phases

The treatment presented so far neglected the fact that a complete scattering event involves two momentum kicks, one in absorption and one in emission. As the spectroscopy light comes from a directed laser beam, it is advantageous to have it pointing in the direction of the motional mode supporting the cat state, such that the Lamb-Dicke factor η_{abs} is maximized. When its application is synchronized with the cat state oscillation, the phase ϕ_{abs} remains constant in every experiment. The direction of the emitted photon associated with the Lamb-Dicke factor η_{em} and phase ϕ_{em}, however, is random and hence needs to be averaged over. The same applies to a third phase ϕ_{H} that is due to fluctuating electric fields heating the ion crystal. Therefore, in total, we detect the the overall phase $\langle\sigma_z\rangle = -\cos(2\phi_{\mathrm{abs}})\overline{\cos(\phi_{\mathrm{em}} + \phi_{\mathrm{h}})}$, where the bar indicates the averaging, whose individual terms will be calculated in the following.

6.5.1. Spontaneous emission

To calculate $\overline{\cos(\phi_{\mathrm{em}})}$ we rely on the isotropic emission of the spontaneous emission from $\mathrm{P}_{1/2} \to \mathrm{S}_{1/2}$, yielding a phase $\phi_{\mathrm{em}} = \tilde{\phi}_{\mathrm{em}} \cos\theta$. Here, θ denotes the angle between the motional mode supporting the cat state and the emission direction of the photon and $\tilde{\phi}_{\mathrm{em}} = 2\alpha\eta_{\mathrm{em}} \sin\varphi_{\mathrm{sc}}$ corresponds to the maximum value possible at $\theta = 0$. Carrying out the averaging in the spherical coordinates θ and $\tilde{\varphi}$, we find

$$\begin{aligned}
\overline{\cos(\phi_{\mathrm{em}})} &= \frac{1}{4\pi}\int_0^{2\pi} \mathrm{d}\tilde{\varphi} \int_0^{\pi} \mathrm{d}\theta \sin\theta \cos\phi_{\mathrm{em}} \\
&= \frac{1}{2}\int_0^{\pi} \mathrm{d}\theta \sin\theta \cos(\tilde{\phi}_{\mathrm{em}} \cos\theta) \\
&= \sin\tilde{\phi}_{\mathrm{em}}/\tilde{\phi}_{\mathrm{em}} = \mathrm{sinc}(\tilde{\phi}_{\mathrm{em}}).
\end{aligned}$$

The last line follows from expanding the cosine of the preceding line into a Taylor series, exchanging summation and integration, evaluating the integrals and finally resumming the resulting Taylor series. As the scatter phase φ_{sc} of the spontaneous emission cannot be controlled, it only contributes to the $\langle\sigma_z\rangle$-signal, while it averages away in $\langle\sigma_y\rangle$ measurements, effectively leaving those to only detect the absorbed photon.

6.5.2. Heating-induced decoherence

Fluctuating electric fields give rise to motional heating during the cat state generation, photon scattering and cat state recombination. The random phase ϕ_{H} accumulated during the time in τ in which a cat state is created is given by

$$\left\langle \phi_{\text{h}}^2 \right\rangle = \frac{16}{3} n_{\text{cat}} R_{\text{h}} \tau, \tag{6.3}$$

where $n_{\text{cat}} = |\alpha|^2$ is the size of the cat state and R_{h} the heating rate associated with the motional mode supporting the cat state (cf. Section 4.7). Expression (6.3) is derived in the following way:

The time interval $T = 2\tau$ corresponding to cat state creation and recombination is divided into N small intervals of length $\mathrm{d}t = T/N$. In each of these intervals, fluctuating electric fields will displace the motional state by an amount $\mathrm{d}\beta_i = \mathrm{d}x_i + \mathrm{d}p_i$, where the two terms corresponding to projections onto the phase space's x- and p-axis are normally distributed independent random variables with variance $\sigma^2 = \frac{1}{2} R_{\text{h}} \mathrm{d}t$. After the total time T, the motional ground state $n = 0$ has become displaced by

$$\beta(T) = \sum_{i=1}^{N} \mathrm{d}\beta_i = \sum_{i=1}^{N} \mathrm{d}x_i + \mathrm{d}p_i$$

such that the average mean phonon number reaches

$$\bar{n} = \left\langle |\beta(T)|^2 \right\rangle = \sum_{i=1}^{N} \left(\left\langle \mathrm{d}x_i^2 \right\rangle + \left\langle \mathrm{d}p_i^2 \right\rangle \right) = R_{\text{h}} \mathrm{d}t N = R_{\text{h}} T,$$

in agreement with the definition of the heating rate.

In a first step, we study the effect of motional heating on a coherent state $|0\rangle$ that is displaced in phase space by some classical well-controlled driving force by an amount $\alpha(t)$. Assuming that the motional excitation by the coherent drive is much bigger than the excitation by the random fluctuating force, we now look at the effect of a heating event at time t_i on the state. Before this event, the state was coherently displaced by an amount $\alpha_1 = \alpha(t_i) - \alpha(t=0)$ where $\alpha(t=0) = 0$. After the event, the coherent displacement is given by $\alpha_2 = \alpha(T) - \alpha(t_i)$. The heating event itself displaces the state by an amount $d\beta_i$. In the absence of heating, the final state at time T is given by

$$|\alpha(T)\rangle = D(\alpha(T))|0\rangle = e^{-i\mathrm{Im}(\alpha_1^*\alpha_2)}D(\alpha_2)D(\alpha_1)|0\rangle$$

where the phase factor cancels the phase arising from the multiplication of the two displacement operations as shown in Eq. (2.25). In the presence of heating at time t_i, the state is modified to

$$\begin{aligned} |\psi\rangle &= e^{-i\mathrm{Im}(\alpha_1^*\alpha_2)}D(\alpha_2)D(d\beta_i)D(\alpha_1)|0\rangle \\ &= e^{i\mathrm{Im}(\alpha_1^* d\beta_i + d\beta_i^*\alpha_2)}D(\alpha_2 + d\beta_i + \alpha_1)|0\rangle \\ &= e^{i\mathrm{Im}(\alpha_1^* d\beta_i + d\beta_i^*\alpha_2)}|\alpha(T) + d\beta_i\rangle, \end{aligned}$$

i.e., the state experiences a small additional displacement and is multiplied by the heating-induced random phase

$$\begin{aligned} \phi_i = \mathrm{Im}(\alpha_1^*\, d\beta_i + d\beta_i^*\, \alpha_2) &= \mathrm{Im}(\alpha_1^*\, d\beta_i) + \mathrm{Im}(d\beta_i^*\, \alpha_2) \\ &= \mathrm{Im}(\alpha_1^*\, d\beta_i) - \mathrm{Im}(d\beta_i\, \alpha_2^*) \\ &= \mathrm{Im}((\alpha_1 - \alpha_2)^*\, d\beta_i). \end{aligned} \tag{6.4}$$

If the coherent displacement $\alpha(t)$ is much bigger than the heating-induced displacement, the final state is to a good approximation equal to $|\alpha(T)\rangle$ multiplied by the product of all heating-induced phase factors occuring in the interval $[0, T]$. Equation (6.4) can be further simplified by splitting $d\beta_i$ into two random variables du_i (dv_i) that are oriented orthogonal (parallel) to $(\alpha_1 - \alpha_2)^*$ and each have variances σ^2 so that

$$\phi_i = |\alpha_1 - \alpha_2| du_i \sin\theta_i$$

where $\theta_i {=} \pm\,\pi/2$ is the angle between the orthogonal component of $d\beta_i$ and $(\alpha_1 - \alpha_2)^*$. After simple substitution, the total heating-induced geometric phase acquired by the coherent state $\alpha(T)$ is given by a sum of N sequential heating-induced random phases

$$\phi_g = \sum_{i=1}^{N} \phi_i = \sum_i |2\alpha(t_i) - \alpha(T_N) - \alpha(0)| du_i \sin\theta_i,$$

which reduces to

$$\phi_g = 2\sum_i |\alpha(t_i)| du_i \sin\theta_i$$

in the case $\alpha(0) = \alpha(T_N) = 0$, where a cat state is created and recombined. Both of its components acquire heating-induced phases $\pm\phi_g$ of opposite sign, resulting in a relative phase of $\phi_h = 2\phi_g$ and its mean-squared value can be calculated to:

$$\langle \phi_h^2 \rangle = 16 \sum_{k=1}^{N} |\alpha(t_k)|^2 \langle du_i^2 \rangle = 8R_h \sum_{k=1}^{N} |\alpha(t_k)|^2 \, dt = 8R_h \int_0^T |\alpha(t)|^2 \, dt. \tag{6.5}$$

In this expression, the heating-induced displacements $\langle du_i^2 \rangle$ were averaged over all random directions θ_i.

For

$$\alpha(t) = \begin{cases} \sqrt{n_{cat}}\; t/\tau & : \; t \le \tau \\ \sqrt{n_{cat}}\; (2\tau - t)/\tau & : \; \tau \le t \le 2\tau \end{cases}$$

the mean squared phase is given by

$$\langle \phi_h^2 \rangle = \frac{16}{3} R_h \tau n_{cat} \tag{6.6}$$

which is the result stated at the beginning in Eq. (6.3). It is easy to include an additional waiting time t_{wait} between cat creation and recombination in the calculation. For

$$\alpha(t) = \begin{cases} \sqrt{n_{cat}}\; t/\tau & : \; t \le \tau \\ \sqrt{n_{cat}} & : \; \tau \le t \le \tau + t_{wait} \\ \sqrt{n_{cat}}\; (2\tau + t_{wait} - t)/\tau & : \; \tau + t_{wait} \le t \le 2\tau + t_{wait} \end{cases}$$

integration of Eq. (6.5) yields the mean-squared phase

$$\langle \phi_h^2 \rangle = 8R_h n_{cat} (\frac{2\tau}{3} + t_{wait}). \tag{6.7}$$

For a random variable X that has a Gaussian distribution with $\langle X \rangle = 0$, the equality

$$\langle \cos X \rangle = \exp(-\frac{\langle X^2 \rangle}{2})$$

holds which enables us to calculate the loss of Ramsey contrast of the cat state spectroscopy from Eqs.(6.6), like in Figure 6.5, or (6.7).

6.6. Experimental demonstration

In the experimental implementation of the cat state spectroscopy protocol, we employ two ions of two different calcium isotopes. With the relevant energy levels illustrated in Figure 6.7, laser cooling and state detection are provided by $^{40}\mathrm{Ca}^+$, which is used as logic ion, while spectroscopy is performed on a co-trapped $^{44}\mathrm{Ca}^+$ ion. The choice of $^{44}\mathrm{Ca}^+$ is merely a practical one as it has the second highest natural abundance ($\sim 2\%$) of all calcium isotopes and can therefore be loaded relatively efficiently from a standard calcium source. However, its isotope shift of 842(3) MHz on the $\mathrm{S}_{1/2} \leftrightarrow \mathrm{P}_{1/2}$ transition at 397 nm and -4.49 GHz on the $\mathrm{D}_{5/2} \leftrightarrow \mathrm{P}_{3/2}$ transition at 866 nm (cf. Section 2.2) necessitates the use of a second set of laser beams for resonant initialization and spectroscopy. To differentiate the beams from those used to address the logic ion, the corresponding wavelengths are marked with an asterisk (*) in the following.

To characterize the sensitivity of the cat state spectroscopy method, we compare both of its signals, $\langle\sigma_z\rangle$ and $\langle\sigma_y\rangle$ as discussed before, with a (direct) detection of the photon recoil that simply probes the red sideband of the two-ion crystal's center-of-mass (COM) mode. In addition, we demonstrate an extension of this direct detection method, which enables the technique to resolve the relative phase of the Fock states involved and thereby provides a significant sensitivity increase even without the use of a cat state. Common to all sequences are the initial preparation and the final read-out. The abbreviations given in brackets are used in the figures on the following pages:

Each experimental cycle starts with Doppler cooling (DC) and resolved sideband cooling (SBC) implemented on $^{40}\mathrm{Ca}^+$ to initialize the two-ion crystal in the ground state $|0\rangle$ of its COM vibrational mode at $\nu = 1.199\,\mathrm{MHz}$. Optical pumping (OP) first initializes the logic ion spin state to $|{\downarrow}\rangle_z$. $^{44}\mathrm{Ca}^+$ is then optically pumped to its metastable $\mathrm{D}_{3/2}$ state by a 397^* nm pulse of appropriate length. The corresponding pulse is enclosed by two carrier π-pulses on $^{40}\mathrm{Ca}^+$, referred to as (hide) and (unhide), that serve to prevent residual, off-resonant light scattering on the logic ion during the $^{44}\mathrm{Ca}^+$ initialization.

In all experiments, independent of the specific method, spectroscopy light is sent into the trap along the axial (z) direction. Absorption of a single infrared photon by the spectroscopy ion populates its $\mathrm{P}_{1/2}$ electronic state that has a lifetime of 7.1 ns [34]. With 96.6% probability [39] it will decay to the $\mathrm{S}_{1/2}$ ground state under emission of a single blue photon at 397 nm wavelength.

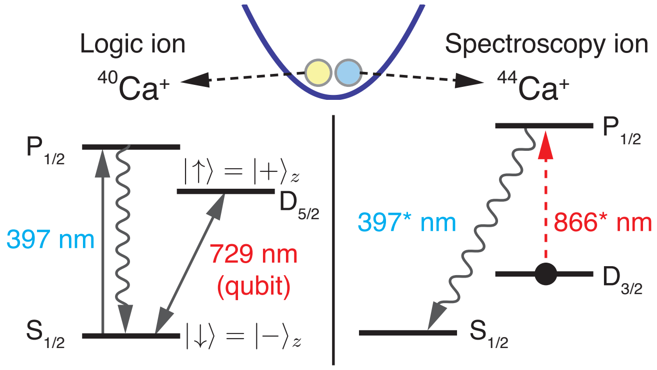

Figure 6.7.: Reduced electronic level schemes relevant in the experiment
A mixed-species ion crystal consisting of the isotopes $^{40}\mathrm{Ca}^+$ and $^{44}\mathrm{Ca}^+$ is confined in the harmonic trapping potential. **(left)** The $\mathrm{S}_{1/2} \leftrightarrow \mathrm{P}_{1/2}$ transition at 397 nm in $^{40}\mathrm{Ca}^+$ is used for Doppler cooling and optical pumping; the quadrupole transition at 729 nm encodes the qubit used in the spectroscopy protocol and provides the means for resolved-sideband cooling. **(right)** Spectroscopy is being performed on the $\mathrm{D}_{3/2} \leftrightarrow \mathrm{P}_{1/2}$ using 866 nm light. The asterisk * indicates isotope shifts between $^{40}\mathrm{Ca}^+$ and $^{44}\mathrm{Ca}^+$.

Each cycle of a measurement sequence produces a binary result $x \in \{0, 1\}$: the logic ion either fluoresces ($s = 1$) or it does not ($s = 0$), which is decided upon thresholded PMT count data as described in Section 3.4. After N measurement cycles, the mean excitation probability is given by

$$\begin{aligned} p_\uparrow &= 1 - \frac{1}{N}\sum_{i=1}^{N} s_i \\ &= \frac{1}{2}\Big(\langle\sigma_z\rangle + 1\Big) \end{aligned}$$

where the second line illustrates the connection to the expectation value of the detected σ_z spin projection. Measurements of $\langle\sigma_y\rangle$ are made by applying a carrier $\sigma_x(\pi/2)$ pulse prior to detection, effectively rotating the y-eigenstates into the z-basis.

As the uncertainty of the mean excitation probability $p_\uparrow$ in N measurement cycles is determined solely by quantum projection noise as defined in Eq. (3.4), the signal-to-noise ratio (SNR) can always be increased by simply taking more measurements. To quantitatively compare the different methods, it is therefore useful to renormalize by the number of measurements made and, instead, consider the measurement sensitivity $\beta = \mathrm{SNR}/\sqrt{N}$ provided by each sequence. The way in which signal S and noise ΔS are determined from the measured excitations depends on the specific experiment and is therefore explicitly given for each of the sequences presented in the following.

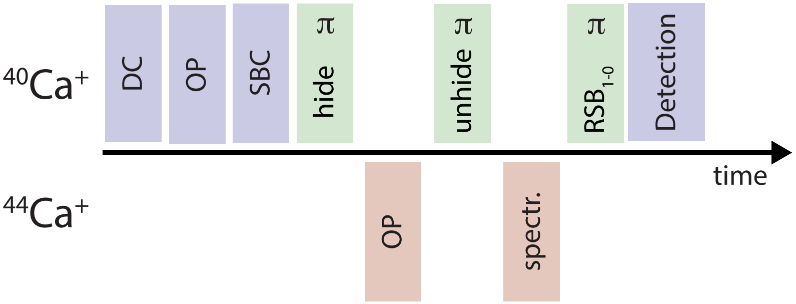

Figure 6.8.: Pulse sequence used in the direct detection experiment
Spectroscopy is performed using a single pulse of 10 µs duration on the $D_{3/2} \rightarrow P_{1/2}$ transition of ^{44}Ca$^+$. The red sideband (RSB) pulse prior to detection is calibrated to be a π pulse on the $|n = 1\rangle \rightarrow |n = 0\rangle$ motional transition of the COM mode.

6.6.1. Direct red sideband detection

The simplest way of detecting a motional energy increase due to a photon scattering event is to probe for excitation of the logic ion with a laser pulse resonant with the COM mode's red sideband. Using all the elements discussed above, the corresponding pulse sequence is shown in Figure 6.8. To exclude contributions from imperfect or fluctuating sideband cooling, the signal is obtained from the difference between the mean excitation detected in N_1 experiments taken with the spectroscopy pulse present and N_2 experiments without it $S = p_\uparrow(N_1^{\mathrm{scatter}}) - p_\uparrow(N_2^{\mathrm{no\,scatter}})$. Data is taken in sets of $N = 50$ experiments at a rate of 50 Hz, alternating between the two configurations. The signal error $\Delta S = \sqrt{\Delta p^2_{\mathrm{scatter}} + \Delta p^2_{\mathrm{no\,scatter}}}$ is taken as the geometric mean of the quantum projection noise of each case. Table 6.1 below lists the obtained results. The total measurement time in this case was 16.7 min to reach a signal-to-noise ratio (SNR) of 2.84, which yields a measurement sensitivity $\beta = \mathrm{SNR}/\sqrt{N} = 0.018(6)$.

Table 6.1.: Results of the direct red sideband detection.

	$p_\uparrow$	Δp	# of cycles	SNR
scatter	0.0551	0.0014	25000	38.17
no scatter	0.0494	0.0014	25050	36.09
signal	0.0057	0.002	$S/\Delta S \rightarrow$	2.84

Direct detection using motional phase information

As shown in Section 6.2 before, photon scattering provides a momentum kick to the ground-state-cooled two-ion crystal associated with a small coherent displacement.

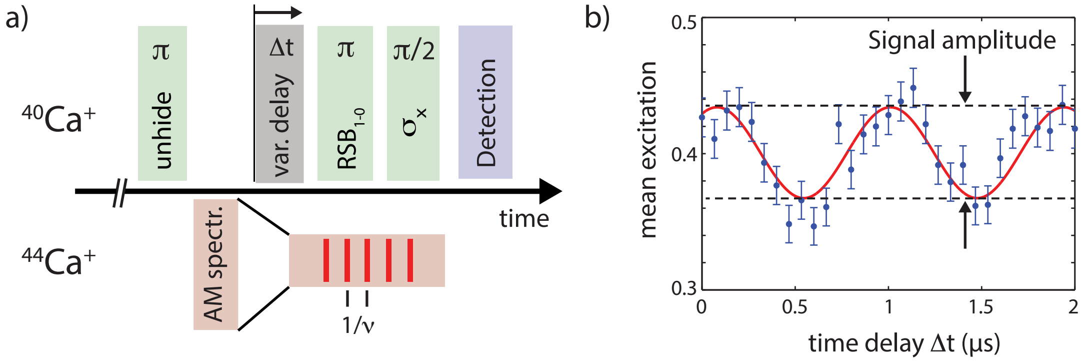

Figure 6.9.: Phase-sensitive direct detection
a) Initially identical to Figure 6.8, the pulse sequence is modified to include amplitude-modulated spectroscopy pulses (see text) that are separated by 800 ns ($= 1/\nu$) within the 10 μs "envelope" as well as a variable time delay and σ_x analysis pulse. **b)** Fringe pattern obtained through a variation of the time delay Δt. The oscillation's mean value is shifted down from 0.5 due to incomplete sideband cooling.

With respect to the oscillation of the ground state at frequency ν, the specific time of the absorption event corresponds to a motional phase ϕ that can be approximated as $|0\rangle + i\eta_{\mathrm{abs}}e^{i\phi}|1\rangle$. A π-pulse on the red sideband maps it from the motion to the logic ion's electronic state, $|{\downarrow}\rangle(|0\rangle + i\eta e^{i\phi}|1\rangle) \longrightarrow (|{\downarrow}\rangle + i\eta e^{i\phi}|{\uparrow}\rangle)|0\rangle$, where a $\sigma_x(\pi/2)$ rotation can be used to extract it via interference in the electronic state population.

So far, however, we have used a single spectroscopy pulse of 10 μs duration in the sequence shown in Figure 6.8 and detected only the population in $|{\uparrow}\rangle$. During the 10 μs pulse time, the ion crystal performs multiple oscillations in the trapping potential completing one full period every $1/\nu \approx 830$ ns. As the scattering event can happen at any time during the oscillations, the motional phase ϕ is randomized over many repeated experiments and thereby lost.

To make the phase available for the detection of a scattering event, a fast RF TTL switch can be used to gate the RF sent to AOM 6 (cf. page 40) in addition to the switching that generates the 10 μs envelope. With this capability, the amplitude of the spectroscopy light is now modulated at frequency ν, which effectively produces a series of short (60 ns) pulses that are separated by $1/\nu$ (cf. Figure 6.9.a). If now the frequency of the amplitude modulation (AM) is identical to the laser frequency difference between the RSB and σ_x pulse, the value of ϕ remains constant in every cycle (to an extend limited by the length of the short AM pulses).

By introducing a variable delay time between the scattering- and the two analysis pulses, the fringe pattern shown in Figure 6.9.b can be recovered that directly reveals

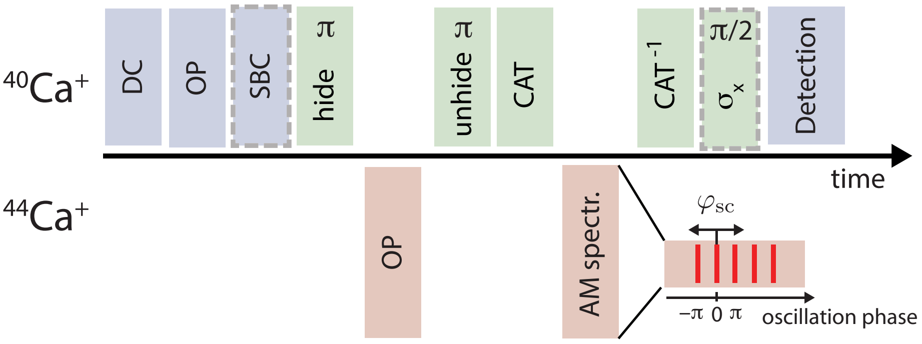

Figure 6.10.: Cat state amplified detection
A bichromatic laser pulse creates (CAT) and reinterferes (CAT^{-1}) a motional Schrödinger cat state $|\Psi\rangle$ before and after the application of amplitude-modulated (AM) spectroscopy light. Consisting of 60 ns pulses separated by 800 ns ($= 1/\nu$), the timing of the photon scattering can be shifted with respect to the oscillation phase of $|\Psi\rangle$ within the 10 µs pulse "envelope" (effectively varying φ_{SC}). An optional $\pi/2$ carrier pulse prior to detection rotates the σ_y-eigenstates into the measurement basis.

the motional phase between the Fock states $|0\rangle$ and $|1\rangle$. In this case, the signal is obtained from the difference of the excitation at a fringe maximum and minimum.

Table 6.2 below details the measurement results. The total measurement time in this case was 6.6 min to reach a signal-to-noise ratio (SNR) of 10.67. The measurement sensitivity $\beta = \mathrm{SNR}/\sqrt{N} = 0.107(10)$ is almost 7 times higher than in the previous direct detection case.

Table 6.2.: Results of the phase sensitive direct red sideband detection.

	$p_\uparrow$	Δp	# of cycles	SNR
fringe maximum	0.4464	0.0050	9850	89.12
fringe minimum	0.3719	0.0049	9900	76.57
signal	0.0745	0.007	$S/\Delta S \rightarrow$	10.67

6.6.2. Cat state amplified detection

As opposed to the direct detection methods outlined above, the cat state spectroscopy method described in Section 6.4 allows for an indirect detection of the photon scattering through amplification of the recoil-induced motional excitation via an adjustable geometric phase. Consequently, here, the sensitivity can be tuned via the size of the cat state and the spin projection chosen for detection.

As before, the measurement sequence illustrated in Figure 6.10 starts with Doppler cooling and optical pumping. This is followed by (optional) sideband cooling and the initialization of the spectroscopy ion. The bichromatic light field (cf. Section 2.5)

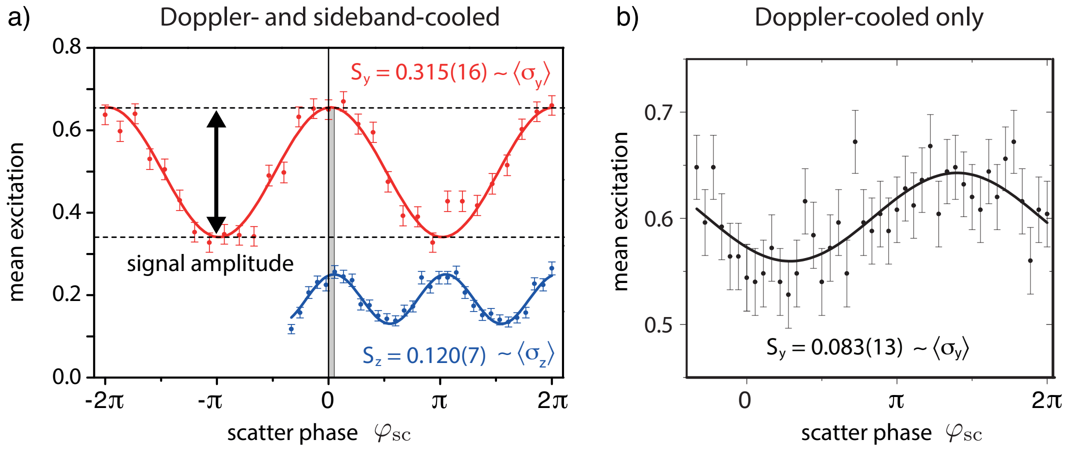

Figure 6.11.: Cat state spectroscopy results
Photon scattering signals on the broad $D_{3/2} \leftrightarrow P_{1/2}$ transition in $^{44}Ca^+$ for a cat state size of $\alpha = 2.9(2)$. **a)** Cat state interference fringes observed by varying φ_{sc} (the relative timing) of a single photon scattering event with respect to the cat state oscillation phase. Weighted sinusoidal fits (solid lines) yield a signal amplitude S in the two detection bases σ_z (blue curve) and σ_y (red curve). To maximize the contrast for the cat state size used, the data is taken at light intensities that ensure a complete pump-out of the $D_{3/2}$ level, such that with 93.6% probability a single photon is scattered and with 6.4% probability ≥ 2 photons are being scattered. The $P_{1/2}$ state's lifetime of ~ 7.1 ns leads to the small phase shift between the two oscillations (marked in gray) as the contribution of the emitted blue photon is delayed from the absorption process. **b)** Detection in the σ_y basis without the application of sideband cooling.

employed next first creates ("CAT") a Schrödinger cat state and then recombines it ("CAT^{-1}") after the spectroscopy laser pulses have been sent into the trap. They are amplitude modulated (AM) in the same way as described in the previous section. However, instead of a delay time between cat state recombination (analysis) and scattering, here, the RF phase offset of the frequency generator responsible for the modulation is varied. Its absolute phase reference is provided by the same 10 MHz clock signal that stabilizes the frequency generators supplying the RF used to create the bichromatic light field. A scan of the AM phase therefore is equivalent to a variation of φ_{sc}. As the spectroscopy pulse train is shifted within its 10 µs envelope, the time of the absorption and emission events shift accordingly with respect to the cat state's components' oscillation at frequency ν.

As described in Section 6.4 before, a variation of φ_{sc} reveals a fringe pattern either in the $\langle\sigma_z\rangle$ eigenbasis or, with a $\sigma_x(\pi/2)$ rotation prior to detection, in the orthogonal $\langle\sigma_y\rangle$ basis. Both signals are shown Figure 6.11 above, where the red signal of larger signal amplitude includes the $\sigma_x(\pi/2)$ rotation and the blue signal does not. Also, the former is sensitive only to the absorption process of a single infrared photon, while the contribution of the emitted blue photon at 397 nm wavelength averages out. In the $\langle\sigma_z\rangle$ detection case, the $\sim 7.1\,\mathrm{ns}$ lifetime of the $\mathrm{P}_{1/2}$ state leads to a small phase shift corresponding to the delay of the 397 nm photon emission after an absorption event. The curve's mean is representative of the contribution by the isotropic emission while the modulation is due to the absorbed photon's momentum kick. Figure 6.11.b shows how even in the absence of sideband cooling with the thermal state reached after the end of Doppler cooling, the absorption of a red photon at 866 nm can be detected in the σ_y basis. As a thermal state can be understood as a distribution of Fock states sampled in each experiment, a sensitivity similar to the phase sensitive direct red sideband detection can be expected and is observed. However, the significant loss of contrast observed in the fringe pattern requires further study, which includes the question as to why the signal in this case is centered around 0.61 instead of the expected value of 0.5.

By alternating between φ_{sc} settings corresponding to a fringe minimum and maximum, the photon scattering signature can be detected reliably, once the fringe pattern has been identified. Tables 6.3 and 6.4 below detail the results of the measurements used in the calibration of the sensitivity. The measurements in the $\langle\sigma_y\rangle$ ($\langle\sigma_z\rangle$) basis have taken 2.8 min and yield sensitivities of $\beta = 0.338(16)$ ($\beta = 0.162(16)$). Without sideband cooling, a 3.4 min measurement yields a sensitivity of $\beta = 0.109(14)$.

Table 6.3.: Results of the cat state amplified detection.

	$p_\uparrow$	Δp	# of cycles	SNR
fringe maximum $\langle\sigma_y\rangle$	0.6083	0.0075	4200	80.77
fringe minimum $\langle\sigma_y\rangle$	0.3757	0.0075	4200	50.28
signal $\langle\sigma_y\rangle$	0.2326	0.0106	$S/\Delta S \rightarrow$	21.92
fringe maximum $\langle\sigma_z\rangle$	0.2664	0.0068	4200	39.06
fringe minimum $\langle\sigma_z\rangle$	0.1721	0.0058	4200	29.55
signal $\langle\sigma_z\rangle$	0.0943	0.009	$S/\Delta S \rightarrow$	10.51

Table 6.4.: Results of the cat state amplified detection without sideband cooling.

	$p_\uparrow$	Δp	# of cycles	SNR
fringe maximum $\langle\sigma_y\rangle$	0.6499	0.0067	5050	96.82
fringe minimum $\langle\sigma_y\rangle$	0.5751	0.007	5050	82.67
signal $\langle\sigma_y\rangle$	0.0749	0.0097	$S/\Delta S \rightarrow$	7.74

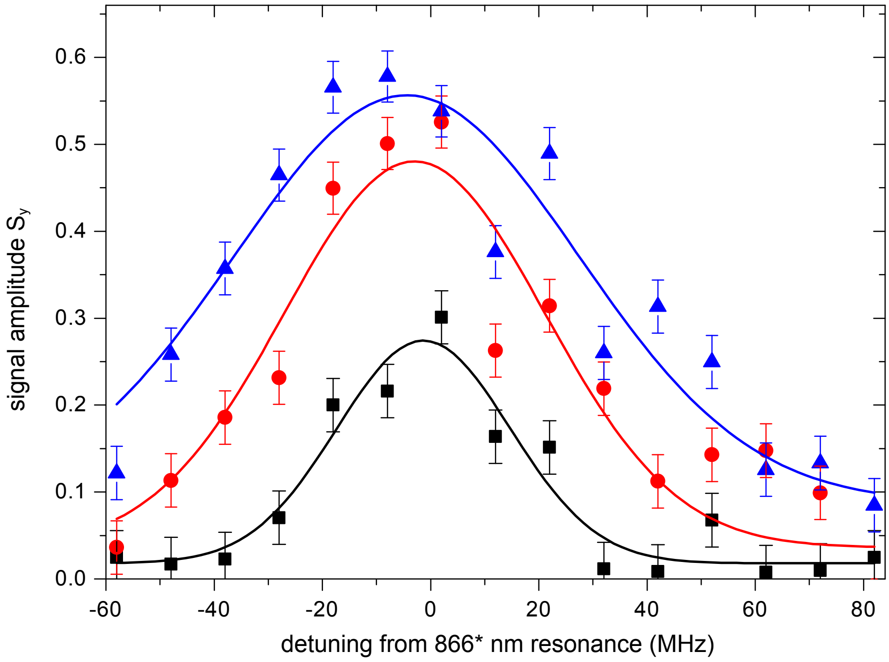

Figure 6.12.: Line profile for different spectroscopy laser powers
The error bars are derived from quantum projection noise and enter the Gaussian fits as weights. The observed linewidths are given as FWHM values: ■ 7 µW : 38(5) MHz; ● 73 µW : 57(6) MHz; ▲ 115 µW : 75(12) MHz

A line profile of the $D_{3/2} \leftrightarrow P_{1/2}$ dipole transition in $^{44}\mathrm{Ca}^+$ can be retrieved by recording the difference between the minimum and maximum of the $\langle\sigma_y\rangle$ fringe pattern. The corresponding measurements for three difference power levels in the spectroscopy beam are shown in Figure 6.12. To prevent power broadening, the light level has to be reduced significantly, yielding a smaller signal amplitude S_y when compared to the fringe pattern in Figure 6.11 as not in all experimental cycles a photon will be scattered. The observed linewidth of $2\pi \times 38(5)$ MHz for the lowest power setting is close to the width expected from a combination of the transition's natural linewidth ($2\pi \times 22.4$ MHz) with the energy splitting between the Zeeman levels of the $S_{1/2}$ and $P_{1/2}$ states induced by the quantization magnetic field of 4 G. It is worth noting that, given the branching ratio of the $P_{1/2} \rightarrow S_{1/2}$ decay channel, this profile is due to the absorption of only a single infrared photon at 866 nm wavelength with 93.6 % probability.

Table 6.5.: Comparison of spectroscopic techniques
The sensitivity of various cat state spectroscopy (CSS) techniques using $\alpha = 2.9(2)$ the direct detection are compared. All errors are calculated from quantum projection noise.

method	sensitivity (β)	measurements for 3σ	measurement time for 3σ @ 50 Hz
Direct detection (single pulse)	0.018(6)	$2.7(1.9)\times10^5$	9.3 min
Direct detection with AM	0.107(10)	$7.8(1.5)\times10^2$	15.6 s
CSS $\langle\sigma_z\rangle$-signal	0.162(16)	$3.4(0.6)\times10^2$	6.8 s
CSS $\langle\sigma_y\rangle$-signal	0.338(16)	$7.9(0.8)\times10^1$	1.6 s
CSS $\langle\sigma_y\rangle$-signal without SBC	0.109(14)	$7.6(2.0)\times10^2$	15.2 s

6.7. Conclusion

Table 6.5 summarizes the results obtained with the different measurement techniques before. Based on the sensitivity determined for each method, the number of measurements that are required to reach a confidence level of 3σ (SNR = 3) is given in the second column. Assuming the same 50 Hz cycle time used in the experiments presented before, the third column calculates the total measurement time needed in each case.

The highest sensitivity of all methods is achieved by cat state spectroscopy detecting the $\langle\sigma_y\rangle$-signal of the absorbed photon. The sensitivity can, in principle, be increased further simply by making the cat state larger. However, the motional heating discussed in Sections 4.7 and 6.5.2 will bound the maximally useful cat state size. The corresponding loss of contrast was illustrated for the single ion case in Section 6.3. A notable sensitivity increase is also observed without the use of a cat state, when phase information is used in the direct detection. However, this detection method could not be applied without ground state cooling, whereas cat state spectroscopy in the $\langle\sigma_y\rangle$-basis still achieves a similar sensitivity for thermal states – even under the observed loss of fringe contrast.

Given the high sensitivity that can be attained using cat state spectroscopy, its application in spectroscopic measurements of very weak transitions, e.g. in molecular ions, can be envisioned. In addition, quantum information processing might benefit from the technique in the transfer of quantum information between ions and photons as the protocol does not obtain any information about the scattered photon or the electronic state of the spectroscopy ion after photon absorption or emission.

7. Summary and outlook

The work presented in this thesis covers both, a large amount of technical work, as well as two selected publications to the fields of quantum simulation and precision spectroscopy.

After the introductory motivation in chapter 1, the foundations in atomic physics and quantum information were briefly discussed before the theoretical framework underlying the light-matter interaction was introduced. In the following Chapter 3, the experimental setup was presented in detail, starting with the new linear ion trap has been designed and optimized in FEM simulations at the start of the work presented in this text. The experimental methods used in the characterization of the new setup as well as the daily operation were detailed in Chapter 4, which is hoped to be a useful reference for experimenters performing similar work in the future. The final two chapters discussed the contributions to the research areas of quantum simulation and precision spectroscopy that were made during the course of this thesis.

In Chapter 5 the well-established theoretical method known as Trotter expansion was implemented experimentally to realize digital quantum simulations of elementary models of magnetism. The focus and motivation was to gain concurrent access to interactions that the system of trapped ions does not provide naturally. Here, the Trotter approximation was used to implement discrete sequences realizing these interactions.

In a first proof-of-principle experiment, the rapid convergence of the “trotterized” simulation approach in a minimal Ising model implemented on two ions was verified. As expected from theoretical simulations of the ideal behavior, higher-order Trotter-Suzuki approximations were found to improve the simulation quality in experiments that naturally incur detrimental effects absent in theoretical models. In addition to the simulation of time-independent Hamiltonians, a time-dependent situation was investigated. This approach one could, for example, use to realize an adiabatic state preparation at the beginning of a simulation, for which the ground state cannot be encoded directly.

The more interesting question from the perspective of quantum simulations reaching beyond what can be realized on classical computers is the scaling behavior (I) in terms of complexity of the simulated interactions and (II) in terms of the number of simulated spins. To investigate these questions, first, the two-ion case was expanded from the Ising to the more complex XY and XYZ models, and second, the number of ions was increased to up to 6 particles.

During the course of the project, variations of the laser-ion coupling strength were found to be a major contribution to the simulation error seen to accumulate in sequences of up to 100 gate operations. Traced back mostly to light intensity fluctuations, these, however, do not constitute a fundamental limitation and provide a direction for future technical improvements to the setup.

A separate contribution that has been made to the field of precision spectroscopy was discussed in Chapter 6. Here, a motional Schrödinger cat state was applied to the amplification of the small displacement caused by the recoil associated with the emission and/or absorption event of a single photon on a broad dipole transition. The experiment made use of the capability to create motional Schrödinger cat states with a single bichromatic laser pulse as opposed to the sequential state generation using Raman beams employed by earlier experiments. First, the effects of heating-rate induced decoherence (Chapter 4) were investigated using only a single ion by creating large cat states of a size up to $\alpha = 6.6$. The implementation of the cat-state amplified spectroscopy was then demonstrated using a two-ion crystal of $^{40}\mathrm{Ca}^+$ and $^{44}\mathrm{Ca}^+$. Here, it was used to obtain a line profile of the $\mathrm{D}_{3/2} \rightarrow \mathrm{P}_{3/2}$ transition using only single-photon scattering events. It was shown that the method can also be used without the need for ground state cooling, which is expected to provide benefits, for example, in the spectroscopy of molecular ions.

At the time of writing, the advanced capabilities offered by the extensions made to the optical setup and computer control have already been used in a number of publications listed in Appendix A. In the most recent example, the newly introduced acousto-optic deflector has been used to realize single-ion addressing in an experiment simulating a 1D spin chain with 15 ions and investigate the propagation of entanglement using the redesigned camera software discussed Section 3.4. After early attempts to stabilize the radial vibrational modes had been able to reach the level of 100 Hz, many additional improvements to the stabilization and optical access were made for this experiment by Petar Jurcevic. They will be detailed in his forthcoming Ph.D. thesis.

Spatial light modulators provide a versatile tool to engineer optical potentials and tailor the light-ion interaction to a higher degree. A high-performance device arrived just as the writing of this thesis concluded and is currently being investigated by Sebastian Schunke. Results will be presented in his forthcoming Master thesis.

With coherent operations now involving longer ion chains on a regular basis, many motional modes need to be cooled to the quantum ground state. Given their large number of 3^n for n ions, the sideband cooling technique discussed in Chapter 4 is no longer efficient in terms of the overall time needed for the laser cooling. A further constraint is given by the motional heating rate discussed in Section 4.7 that tends to heat up previously ground state cooled modes during the sideband cooling of other motional modes. To address this issue, Christine Maier recently set up EIT cooling to replace or complement sideband cooling in future work with long ion strings. The corresponding setup will be described in her forthcoming Ph.D. thesis.

A. List of publications

Publications discussed in this thesis

1. C. Hempel, B. P. Lanyon, P. Jurcevic, R. Gerritsma, R. Blatt, C. F. Roos - ”Entanglement-enhanced detection of single-photon scattering events”,
   Nature Photonics **7**, 630 (2013).

2. B. P. Lanyon, C. Hempel, D. Nigg, M. Müller, R. Gerritsma, F. Zähringer, P. Schindler, J. Barreiro, M. Rambach, G. Kirchmair, M. Hennrich, R. Blatt, C. F. Roos - ”Universal quantum simulation with trapped ions”,
   Science **334**, 57 (2011).

Further publications

3. P. Jurcevic, B. P. Lanyon, P. Hauke, C. Hempel, P. Zoller, R. Blatt, C. F. Roos - ”Observation of entanglement propagation in a quantum many-body system”,
   Nature **510**, 202 (2014).

4. B. P. Lanyon, P. Jurcevic, M. Zwerger, C. Hempel, E. A. Martinez, W. Dür, H. J. Briegel, R. Blatt, C. F. Roos - ”Experimental violation of multipartite Bell inequalities with trapped ions”,
   Phys. Rev. Lett. **112**, 100403 (2014).

5. B. P. Lanyon, P. Jurcevic, M. Zwerger, C. Hempel, E. A. Martinez, W. Dür, H. J. Briegel, R. Blatt, C. F. Roos - ”Measurement-based quantum computation with trapped ions”,
   Phys. Rev. Lett. **111**, 100504 (2013).

6. B. P. Lanyon, P. Jurcevic, C. Hempel, M. Gessner, V. Vedral, R. Blatt, C. F. Roos - ”Experimental generation of quantum discord via noisy processes”,
   Phys. Rev. Lett. **111**, 100504 (2013).

7. R. Gerritsma, B.P. Lanyon, G. Kirchmair, F. Zähringer, C. Hempel, J. Casanova, J.J. Garcia-Ripoll, E. Solano, R. Blatt, C. F. Roos - ”Quantum simulation of the Klein paradox”,
   Phys. Rev. Lett. **106**, 060503 (2011).

B. Useful definitions and relations

The following definitions and relations were used in the derivations of many of the equations given in this text and are meant to provide a quick reference rather than proper derivation and proof.

B.1. Pauli matrices

$$\sigma_x = \begin{pmatrix} 0 & 1 \\ 1 & 0 \end{pmatrix}, \qquad \sigma_y = \begin{pmatrix} 0 & -i \\ i & 0 \end{pmatrix}, \qquad \sigma_z = \begin{pmatrix} 1 & 0 \\ 0 & -1 \end{pmatrix} \tag{B.1}$$

With $\det(\sigma_i) = -1$ and $\mathrm{Tr}(\sigma_i) = 0$, the Pauli matrices have eigenvalues ± 1. The corresponding normalized eigenvectors $|\pm\rangle_i$ (cf. Figure 2.1) are given by:

$$|+\rangle_z = \begin{pmatrix} 1 \\ 0 \end{pmatrix}, \qquad |-\rangle_z = \begin{pmatrix} 0 \\ 1 \end{pmatrix} \tag{B.2}$$

$$|+\rangle_x = \frac{1}{\sqrt{2}} \begin{pmatrix} 1 \\ 1 \end{pmatrix}, \qquad |-\rangle_x = \frac{1}{\sqrt{2}} \begin{pmatrix} 1 \\ -1 \end{pmatrix} \tag{B.3}$$

$$|+\rangle_y = \frac{1}{\sqrt{2}} \begin{pmatrix} 1 \\ i \end{pmatrix}, \qquad |-\rangle_y = \frac{1}{\sqrt{2}} \begin{pmatrix} 1 \\ -i \end{pmatrix} \tag{B.4}$$

Unitary rotations of $\theta = \pi/2$, invoking the Pauli matrices above, transform eigenstates in the following way:

$$U_x(\theta) = \exp\left(-i\frac{\theta}{2}\sigma_x\right) \Longrightarrow |-\rangle_z \to |+\rangle_y \to |+\rangle_z \to |-\rangle_y \to |-\rangle_z$$
$$U_y(\theta) = \exp\left(-i\frac{\theta}{2}\sigma_y\right) \Longrightarrow |-\rangle_z \to |+\rangle_x \to |+\rangle_z \to |-\rangle_x \to |-\rangle_z$$
$$U_z(\theta) = \exp\left(-i\frac{\theta}{2}\sigma_z\right) \Longrightarrow |+\rangle_y \to |-\rangle_x \to |-\rangle_y \to |+\rangle_x \to |+\rangle_y$$

B.2. Transformation to an interaction picture

Pauli matrices and raising/lowering operators

$$e^{i\frac{\theta}{2}\sigma_i}\sigma_j e^{-i\frac{\theta}{2}\sigma_i} = \cos(\theta)\sigma_j + \frac{i}{2}\sin(\theta)[\sigma_i, \sigma_j] \tag{B.5}$$

$$e^{i\frac{\theta}{2}\sigma_z}\sigma_\pm e^{-i\frac{\theta}{2}\sigma_z} = e^{\pm i\theta}\sigma_\pm \tag{B.6}$$

Annihilation and creation operators

$$e^{i\theta a^\dagger a} a e^{-i\theta a^\dagger a} = e^{-i\theta} a \tag{B.7}$$

$$e^{i\theta a^\dagger a} a^\dagger e^{-i\theta a^\dagger a} = e^{i\theta} a^\dagger \tag{B.8}$$

$$e^{i\theta a^\dagger a} e^{i\eta(a+a^\dagger)} e^{-i\theta a^\dagger a} = e^{i\eta(ae^{-i\theta}+a^\dagger e^{i\theta})} \tag{B.9}$$

$$e^{i\eta(a+a^\dagger)} = e^{-\eta^2/2} e^{i\eta a^\dagger} e^{i\eta a} \tag{B.10}$$

B.3. Coherent displacements

$$aD(\alpha)\left|0\right\rangle = D(\alpha)(a+\alpha) \tag{B.11}$$

$$a^\dagger D(\alpha)\left|0\right\rangle = D(\alpha)(a^\dagger+\alpha^*) \tag{B.12}$$

$$D^\dagger(\alpha) = D(-\alpha) \tag{B.13}$$

Using Eq. (B.11) and Eq. (B.12) the average phonon number of coherent state $\left|\alpha\right\rangle$ can be calculated to be:

$$\begin{aligned}\langle\alpha|\hat{n}|\alpha\rangle &= \langle\alpha|a^\dagger a D(\alpha)|0\rangle \\ &= \langle\alpha|D(\alpha)(a^\dagger+\alpha^*)(a+\alpha)|0\rangle \\ &= \langle 0|(a^\dagger+\alpha^*)(a+\alpha)|0\rangle \\ &= |\alpha|^2 \end{aligned} \tag{B.14}$$

B.4. Various

Baker-Campbell-Hausdorff formula

$$e^A e^B = e^{A+B+\frac{1}{2}[A,B]} \tag{B.15}$$

Select trigonometric identities

$$e^{i\theta} = \cos\theta + i\sin\theta \tag{B.16}$$

$$\cos(\theta) = \frac{1}{2}\left(e^{i\theta} + e^{-i\theta}\right) \tag{B.17}$$

$$\sin(\theta) = \frac{1}{2i}\left(e^{i\theta} - e^{-i\theta}\right) \tag{B.18}$$

$$\cos(2\theta) = \cos^2(\theta) - \sin^2(\theta) \tag{B.19}$$

$$\sin(2\theta) = 2\sin(\theta)\cos(\theta) \tag{B.20}$$

C. Vacuum bake of trap II

The following pages give a brief summary of the cleaning and bakeout procedures used in the assembly of trap II. All partial pressures given have been recorded with a residual gas analyzer (RGA)[100] directly attached to the vacuum vessel and a second RGA attached to an external turbo pump station[101] used throughout the baking procedure. To ensure uniform heating of all parts, the bakeout is performed by placing the complete vessel into an industrial oven[102].

The steps marked with an asterisk (*) were taken as a precaution after previous attempts to attain UHV conditions good enough for experiments with long ion strings had failed. The issues encountered were mostly related to collision rates (How often does the ion string get hit by background gas?) and chemical reactions after collisions (Do ions turn into molecular "dark" ions?).

1. **Chemical cleaning of all individual parts**
   With the exception of the pre-cleaned vacuum chamber, all machined parts were first manually cleaned using standard dishwashing detergent. This was followed by a 3-stage chemical cleaning process in an ultrasonic bath[103] using 1st acetone, 2nd isopropanol and 3rd deionized water. The last step helps to remove residue from the organic solvents and was followed by blow-drying using pressurized helium or dry nitrogen. For the safety of their glass-metal transition and coatings, windows and inverted viewports were hand-cleaned using "KimWipes" and deionised water.

2. **Air baking of steel parts**
   This step took place at a temperature of 300 °C (limited by the maximum oven temperature) over about 12 hrs followed by chemical cleaning by hand (methanol) and storage wrapped in clean aluminum foil.

---

[100] SRS RGA 100

[101] TMU071P turbomolecular pump and Duo 2.5 rotary vane pump, both Pfeiffer Vacuum GmbH

[102] ConThermo GmbH & Co. KG

[103] joke Technology GmbH

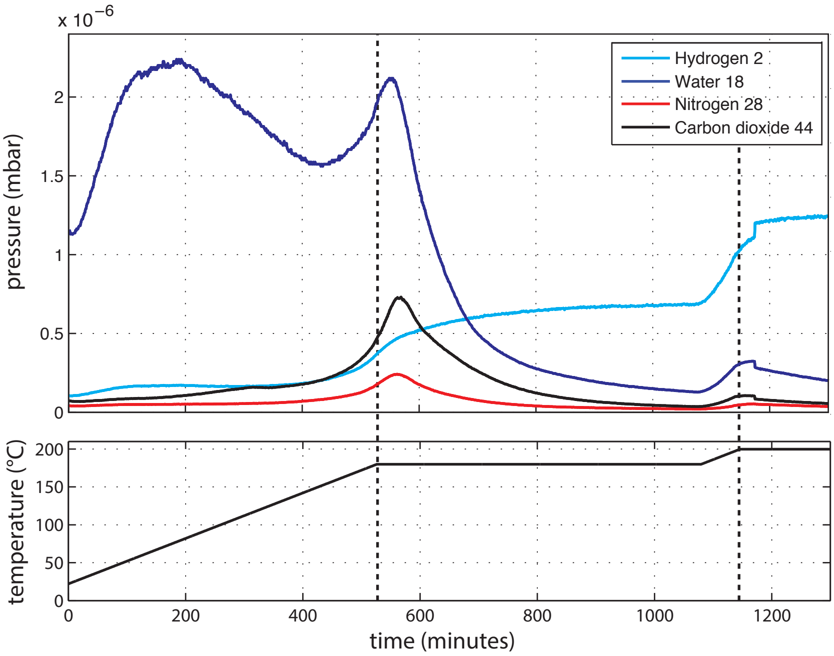

Figure C.1.: Partial pressures vs. time
Partial pressures observed by an RGA (electron multiplier switched off) connected to the external pump station as the temperature of the bakeout-oven was ramped up at a rate of 0.3 °C/min. The rate is chosen such that the vacuum windows of the vessel do not get damaged by large temperature differentials with respect to the surrounding metal. Dashed lines indicate the end of each temperature ramp.

3. **Vacuum baking of sensitive parts**
   Enclosed in a small tube connected to the turbo pump station, parts were were heated to 314 °C for 14 hrs, grouped by material (steel, copper, macor). This was followed by a second round of chemical cleaning and subsequent storage wrapped in clean aluminum foil.

4. (*) **Vacuum bake of the bare chamber without ion trap or calcium oven**
   The entire vacuum vessel was put into the bakeout-oven and heated to 200 °C (to prevent degradation of the window's anti-reflection coatings) while remaining connected to the external turbo pump station via bellows. Figure C.1 shows the importance of heating to high temperatures to effectively remove water and other adsorbates, which is related to the large binding energy of chemisorbed monolayers on a metal surfaces[104]. Note that this has to be repeated every time surfaces are

---

[104] For details see, e.g., the textbook "A User's Guide to Vacuum Technology" by John D. O'Hanlon.

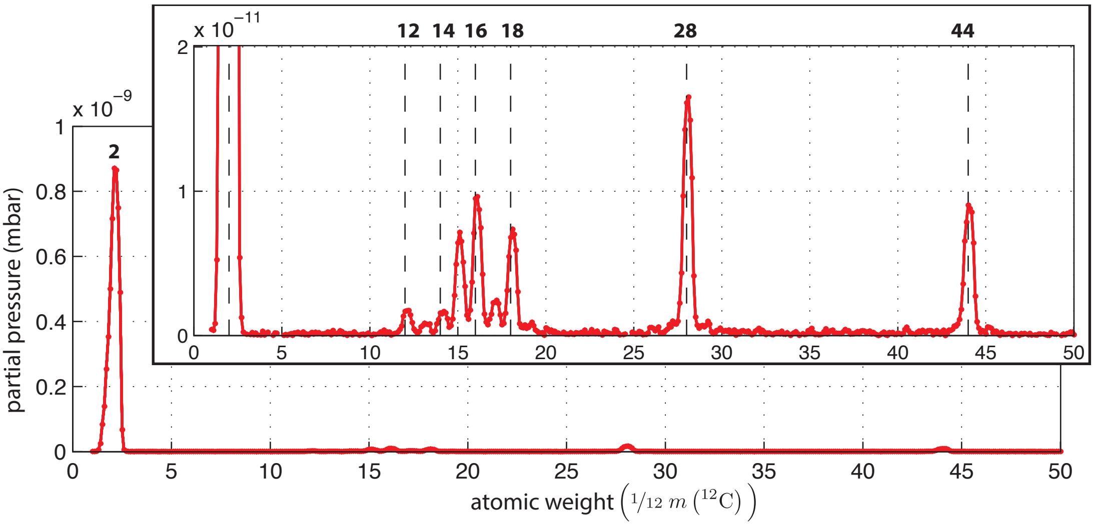

Figure C.2.: Final partial pressures observed after 1 week of baking at 200 °C
The data shown was taken at room temperature using the RGA (electron multiplier switched on) directly attached to the vacuum chamber. While the mass spectrum shown above is for the empty vacuum vessel only, the fully assembled chamber, including the ion trap and calcium oven, showed similar final pressures within at most a factor of two. Table C.1 below provides a useful list to help identify common residual contaminants by their atomic weight.

exposed to air. After a week of baking at 200 °C and subsequent cool-down to room temperature, the partial pressures shown in Figure C.2 were measured using the RGA directly attached to vacuum vessel to have a reference prior to repeating the procedure with ion trap and oven installed.

5. **Vacuum bake of the completely assembled system**

The final assembly of the vacuum system took place in a "clean environment" consisting of a HEPA fan filter unit on top of an enclosed box to create a dust-free work environment. Mouth protection and hair nets were used in addition to gloves and a lab coat. All tools used to assemble in-vacuum parts were chemically pre-cleaned.

To ensure good electrical connectivity, all copper feedthroughs and connectors were cleaned with nitric acid (HNO_3) followed by water rinsing just prior to assembly. The fully assembled system was then baked at 200 °C (0.3 °C/min temperature ramp) for 25 days. At 166 °C oven temperature spikes in the argon and nitrogen pressures indicated the melting of the commercial calcium oven's (Alvatec AS-2-Ca-50-C) indium seal (melting point: 156.6 °C).

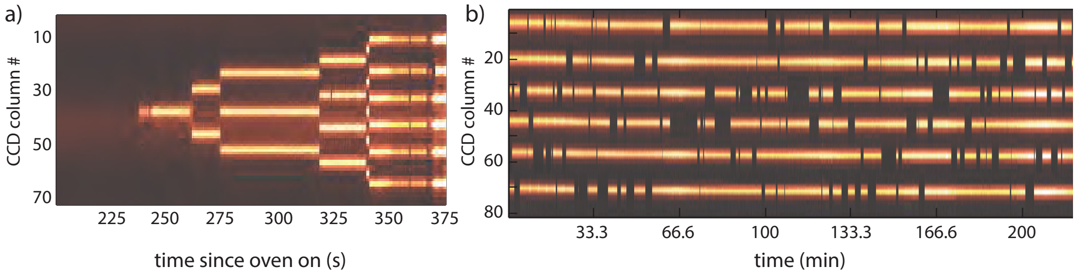

Figure C.3.: Vertically integrated CCD camera images over time
The CCD camera is set to integrate/bin pixels orthogonal to the symmetry axis of the ion trap. The values of all bins (integrated columns) within a region of interest are then read out at a rate between 1-3 Hz yielding a 1D line per time slice. **a)** Example illustrating the time dynamics of loading a string of six ions. The background glow is related to stray light. **b)** Part of a collision rate measurement. The traces monitor configuration changes of the ion crystal, i.e. the positions of non-fluorescing (molecular) ions in the string. The number of changes over time are used to estimate the collision rate. The actual rate is likely to be a bit higher as only changes in the configuration can be detected. In the example shown, the rate was determined to be 0.012 Hz, corresponding to one collision every 86 s.

During the bakeout procedure, the ion getter pump[105] on the chamber vessel was switched on for 30 minutes to 1 hour periodically in order to help clean out contaminants and remained switched on permanently during ramp-down of the oven temperature.

6. **Oven degassing and activation**

   The commercial calcium oven was conditioned *before* the valve to the pump station was closed. This has to be done in order to outgas contaminants as well as "activate" the oven which converts the calcium alloy contained in it, to pure calcium. If possible, it is advisable to insert a loose glass plate into the line of sight between calcium oven and trap during assembly such that contaminants released at this stage hit the glass plate and not the trap electrodes. Depending on the geometry, the loose glass plate might then be removed by simply tilting the vacuum vessel. During the activation process, the hydrogen partial pressure seen by the pump station RGA increased by almost three orders of magnitude (water: two orders of magnitude). We therefore fired the titanium:sublimation pump after activation and baked the system again for 24 hrs at 200 °C.

---

[105] The Curie temperature of the getter pump's magnets (Varian/Agilent Starcell 20 l/s) is high enough for them to remain installed during the bakeout.

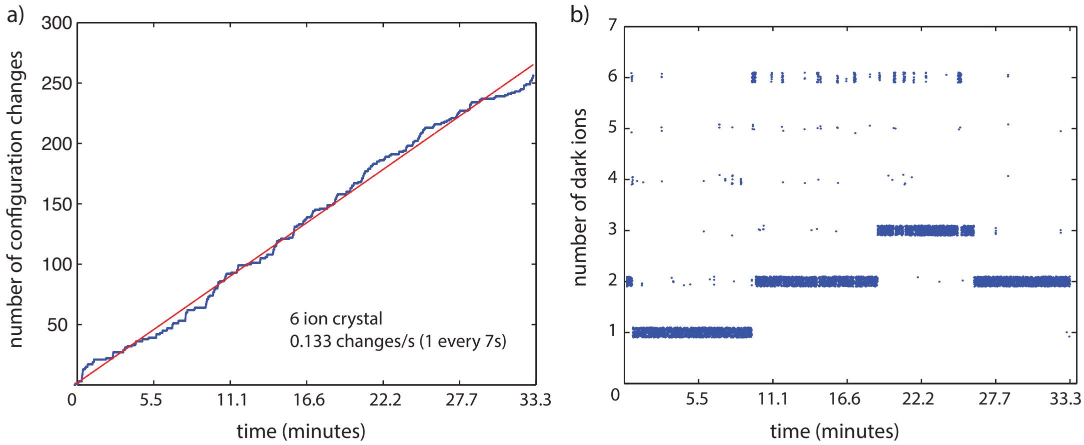

Figure C.4.: Collision rates and "dark" ion numbers after NEG activation
a) Collision rate estimate based on a recording like Figure C.3.b. The red line is a linear fit to the accumulated number of changes in the ion string's configuration. **b)** Number of dark ions occurring in the string considered in a). The cases in which all 6 ions went dark can correspond to laser cooling issues in which the whole crystal briefly melted.

7. **(*) Ion trapping and lifetime check**
   At this point the initial steps described in Section 4.1 were quickly performed to see how many ions could be trapped stably (which was the main limitation of trap I discussed in Section 3.1) and whether chemical reactions producing "dark" (molecular) ions occur.

8. **NEG activation and closed bake**
   Activation of the non evaporative getter (NEG) releases copious quantities of hydrogen into the vacuum system which, combined with the oxygen adsorbed to the getter surface, forms a layer of water on the surfaces inside the vacuum chamber. This was reflected in *very* short ion "lifetimes" post-activation and a fivefold-increased collision rate (cf. Figure C.4). We therefore baked the system for an additional two days at 180 °C just using the attached ion getter pump, i.e. without opening a gate valve to an external turbo pump. This was sufficient to recover the vacuum quality again, bringing the rate at which a single dark changes positions in a linear crystal of six ions back to 12 mHz (once every 86 seconds). In a 20 ion crystal the rate is at 37 mHz (once every 27 seconds). Note, however, that not all of these collisions are energetic enough the heat the ion crystal to an extent where a "refreeze" intervention is necessary. The latter includes a temporary lowering of the radial confinement as well as an additional cooling laser beam with a detuning of about −400 MHz.

Table C.1.: Atomic weights of common residual contaminants and ionization fragments seen in RGA spectra

amu	2	12	13	14	15	16	17	18	28	44
formula	H_2^+	C^+	CH^+	N^+	CH_3^-	O^+, CH_4^+	OH^+	H_2O^+	N_2^+	CO_2^+

Useful in the identification of molecular species is NIST's molecular weight database, available online at `http://webbook.nist.gov/chemistry/mw-ser.html`.

Bibliography

[1] Dehmelt, H. - Experiments with an isolated subatomic particle at rest. *Reviews of Modern Physics* **62**, 525–530 (1990).

[2] Paul, W. - Electromagnetic traps for charged and neutral particles. *Reviews of Modern Physics* **62**, 531–540 (1990).

[3] Schrödinger, E. - Are There Quantum Jumps? Part II. *The British Journal for the Philosophy of Science* **3**, 233–242 (1952).

[4] Wineland, D. J. - Nobel Lecture: Superposition, entanglement, and raising Schrödinger's cat. *Reviews of Modern Physics* **85**, 1103–1114 (2013).

[5] Feynman, R. - Simulating physics with computers. *International Journal Of Theoretical Physics* **21**, 467–488 (1982).

[6] Shor, P. W. - Algorithms for quantum computation: Discrete logarithms and factoring. *Symposium on Foundations of Computer Science* **35**, 124–124 (1994).

[7] Cirac, J. & Zoller, P. - Quantum Computations with Cold Trapped Ions. *Physical Review Letters* **74**, 4091–4094 (1995).

[8] Ladd, T. D. *et al.* - Quantum computers. *Nature* **464**, 45–53 (2010).

[9] Buluta, I., Ashhab, S. & Nori, F. - Natural and artificial atoms for quantum computation. *Reports on Progress in Physics* **74**, 104401 (2011).

[10] Van Meter, R. & Horsman, C. - A blueprint for building a quantum computer. *Communications of the ACM* **56**, 84–93 (2013).

[11] Cirac, J. I. & Zoller, P. - Goals and opportunities in quantum simulation. *Nature Physics* **8**, 264–266 (2012).

[12] Wineland, D. J. *et al.* - Experimental issues in coherent quantum-state manipulation of trapped atomic ions. *Journal of Research of NIST* **103**, 259–328 (1998).

[13] Leibfried, D., Blatt, R., Monroe, C. & Wineland, D. - Quantum dynamics of single trapped ions. *Reviews of Modern Physics* **75**, 281–324 (2003).

[14] Häffner, H., Roos, C. F. & Blatt, R. - Quantum computing with trapped ions. *Physics Reports* **469**, 155–203 (2008).

[15] Roos, C. - Quantum Information Processing with Trapped Ions. In Quint, W. & Vogel, M. (eds.) *Fundamental Physics in Particle Traps*, 253–291 (Springer, 2014).

[16] Oskay, W. *et al.* - Single-Atom Optical Clock with High Accuracy. *Physical Review Letters* **97**, 020801 (2006).

[17] Rosenband, T. *et al.* - Frequency ratio of Al^+ and Hg^+ single-ion optical clocks; Metrology at the 17th decimal place. *Science* **319**, 1808–1812 (2008).

[18] Chou, C., Hume, D., Koelemeij, J., Wineland, D. & Rosenband, T. - Frequency comparison of two high-accuracy Al^+ optical clocks. *Physical Review Letters* **104**, 070802 (2010).

[19] Chou, C., Hume, D., Rosenband, T. & Wineland, D. J. - Optical Clocks and Relativity. *Science* **329**, 1630–1633 (2010).

[20] Schmidt, P. O. *et al.* - Spectroscopy using quantum logic. *Science* **309**, 749–752 (2005).

[21] Giovannetti, V., Lloyd, S. & Maccone, L. - Advances in quantum metrology. *Nature Photonics* **5**, 222–229 (2011).

[22] Itano, W. M. *et al.* - Quantum projection noise: Population fluctuations in two-level systems. *Physical Review A* **47**, 3554–3570 (1993).

[23] Palais, B., Palais, R. & Rodi, S. - A Disorienting Look at Euler's Theorem on the Axis of a Rotation. *American Mathematical Monthly* **116**, 892–909 (2009).

[24] DiVincenzo, D. - Two-bit gates are universal for quantum computation. *Physical Review A* **51**, 1015–1022 (1995).

[25] Nielsen, M. A. & Chung, I. L. - *Quantum Computation and Quantum Information* (Cambridge University Press, Cambridge, U.K., 2000).

[26] Kaye, P., Laflamme, R. & Mosca, M. - *An Introduction to Quantum Computing* (Oxford University Press, 2007).

[27] Barnett, S. M. - *Quantum Information.* Oxford Master Series in Atomic, Optical and Laser Physics (Oxford University Press, 2009).

[28] Schuck, C., Almendros, M., Rohde, F., Hennrich, M. & Eschner, J. - Two-color photoionization of calcium using SHG and LED light. *Applied Physics B* **100**, 765–771 (2010).

[29] de Laeter, J. R. *et al.* - Atomic weights of the elements. Review 2000 (IUPAC Technical Report). *Pure and Applied Chemistry* **75**, 683–799 (2003).

[30] Audi, G., Wapstra, A. & Thibault, C. - The AME2003 atomic mass evaluation (II). Tables, graphs, and references. *Nuclear Physics A* **729** (2003).

[31] Salumbides, E. J. *et al.* - High-precision frequency measurement of the 423-nm Ca I line. *Physical Review A* **83**, 012502 (2011).

[32] Condon, E. U. & Odabasi, H. - *Atomic Structure* (Cambridge University Press, 1980).

[33] Barton, P. *et al.* - Measurement of the lifetime of the 3d $^2D_{5/2}$ state in $^{40}Ca^+$. *Physical Review A* **62**, 032503 (2000).

[34] Jin, J. & Church, D. A. - Precision lifetimes for the Ca^+ 4p ^2P levels: Experiment challenges theory at the 1% level. *Physical Review Letters* **70**, 3213–3216 (1993).

[35] Kramida, A., Yu. Ralchenko, Reader, J. & NIST ASD Team. NIST Atomic Spectra Database (ver. 5.1), [Online]. Available: `http://physics.nist.gov/asd` [2013, November 1]. National Institute of Standards and Technology, Gaithersburg, MD. (2013).

[36] Mårtensson-Pendrill, A.-M. *et al.* - Isotope shifts and nuclear-charge radii in singly ionized $^{40-48}Ca$. *Physical Review A* **45**, 4675–4681 (1992).

[37] Gerritsma, R. *et al.* - Precision measurement of the branching fractions of the 4p $^2P_{3/2}$ decay of Ca II. *The European Physical Journal D* **50**, 13–19 (2008).

[38] Wan, Y. *et al.* - Precision spectroscopy by photon-recoil signal amplification. *Nature Communications* **5**, 3096 (2014).

[39] Ramm, M., Pruttivarasin, T., Kokish, M., Talukdar, I. & Häffner, H. - Precision Measurement Method for Branching Fractions of Excited $P_{1/2}$ States Applied to $^{40}Ca^{+}$. *Physical Review Letters* **111**, 023004 (2013).

[40] Chwalla, M. *et al.* - Absolute Frequency Measurement of the $^{40}Ca^{+}$ 4s $^{2}S_{1/2}$ – 3d $^{2}D_{5/2}$ Clock Transition. *Physical Review Letters* **102**, 023002 (2009).

[41] Nörtershäuser, W. *et al.* - Isotope shifts and hyperfine structure in the 3d $^{2}D_{J} \rightarrow$ 4p $^{2}P_{J}$ transitions in calcium II. *The European Physical Journal D* **2**, 33–39 (1998).

[42] Ozeri, R. - The trapped-ion qubit tool box. *Contemporary Physics* **52**, 531–550 (2011).

[43] Tommaseo, G. *et al.* - The g_j-factor in the ground state of Ca^{+}. *The European Physical Journal D* **25**, 113–121 (2003).

[44] Martin, W. C. & Wiese, W. L. - Atomic Spectroscopy. In Drake, G. W. F. (ed.) *Handbook of Atomic, Molecular, and Optical Physics*, 175–198 (Springer Science+Business Media, 2006).

[45] Loudon, R. - *The Quantum Theory of Light* (Oxford University Press, 2000), 3rd edn.

[46] Foot, C. J. - *Atomic Physics*. Oxford Master Series in Atomic, Optical and Laser Physics (Oxford University Press, 2005).

[47] James, D. F. V. - Quantum Computation with Hot and Cold Ions: An Assessment of Proposed Schemes. *Fortschritte der Physik* **48**, 823–837 (2000).

[48] James, D. - Quantum dynamics of cold trapped ions with application to quantum computation. *Applied Physics B-Lasers And Optics* **66**, 181–190 (1998).

[49] Roos, C. F. - *Controlling the quantum state of trapped ions*. Ph.D. thesis, Universität Innsbruck (2000). Available at http://quantumoptics.at.

[50] Kirchmair, G. - *Quantum non-demolition measurements and quantum simulation*. Ph.D. thesis, Universität Innsbruck (2010). Available at http://quantumoptics.at.

[51] Haroche, S. & Raimond, J.-M. - *Exploring the Quantum* (Oxford University Press, 2006).

[52] Glauber, R. J. - Coherent and incoherent states of the radiation field. *Physical Review* **131**, 2766 (1963).

[53] Sørensen, A. & Mølmer, K. - Quantum Computation with Ions in Thermal Motion. *Physical Review Letters* **82**, 1971–1974 (1999).

[54] Sørensen, A. & Mølmer, K. - Entanglement and quantum computation with ions in thermal motion. *Physical Review A* **62**, 22311 (2000).

[55] Solano, E., de Matos Filho, R. & Zagury, N. - Deterministic Bell states and measurement of the motional state of two trapped ions. *Physical Review A* **59**, R2539–R2543 (1999).

[56] Roos, C. F. - Ion trap quantum gates with amplitude-modulated laser beams. *New Journal of Physics* **10**, 013002 (2008).

[57] Kirchmair, G. *et al.* - Deterministic entanglement of ions in thermal states of motion. *New Journal of Physics* **11**, 023002 (2009).

[58] Chaturvedi, S., Sriram, M. S. & Srinivasan, V. - Berry's phase for coherent states. *Journal of Physics A: Mathematical and General* **20**, L1071–L1075 (1987).

[59] Benhelm, J. - *Precision spectroscopy and quantum information processsing with trapped calcium ions*. Ph.D. thesis, Universität Innsbruck (2008). Available at http://quantumoptics.at.

[60] Kirchmair, G. - *Frequency stabilization of a Titanium-Sapphire laser for precision spectroscopy on Calcium ions*. Master's thesis, Universität Innsbruck (2006). Available at http://quantumoptics.at.

[61] Zähringer, F. - *Quantum walks and relativistic quantum simulations with trapped ions*. Ph.D. thesis, Universität Innsbruck (2012). Available at http://quantumoptics.at.

[62] Gulde, S. - *Experimental Realization of Quantum Gates and the Deutsch-Jozsa Algorithm with Trapped* $^{40}Ca^{+}$ *Ions*. Ph.D. thesis, Universität Innsbruck (2003). Available at http://quantumoptics.at.

[63] Riebe, M. - *Preparation of Entangled States and Quantum Teleportation with Atomic Qubits*. Ph.D. thesis, Universität Innsbruck, Innsbruck (2005). Available at http://quantumoptics.at.

[64] Chwalla, M. - *Precision spectroscopy with* $^{40}Ca^{+}$ *ions in a Paul trap.* Ph.D. thesis, Universität Innsbruck (2009). Available at http://quantumoptics.at.

[65] Monz, T. - *Quantum information processing beyond ten ion-qubits.* Ph.D. thesis, Universität Innsbruck (2011). Available at http://quantumoptics.at.

[66] Schindler, P. - *Quantum computation and simulation with trapped ions using dissipation.* Ph.D. thesis, Universität Innsbruck (2013). Available at http://quantumoptics.at.

[67] Monz, T. *et al.* - 14-Qubit Entanglement: Creation and Coherence. *Physical Review Letters* **106** (2011).

[68] Ghosh, P. K. - *Ion Traps* (Clarendon Press Oxford, 1995).

[69] Home, J. P., Hanneke, D., Jost, J. D., Leibfried, D. & Wineland, D. J. - Normal modes of trapped ions in the presence of anharmonic trap potentials. *New Journal of Physics* **13**, 073026 (2011).

[70] MacAlpine, W. W. & Schildknecht, R. O. - Coaxial Resonators with Helical Inner Conductor. *Proceedings of the IRE* **47**, 2099 – 2105 (1959).

[71] Zverev, A. & Blinchikoff, H. - Realization of a Filter with Helical Components. *IRE Transactions on Component Parts* **8**, 99–110 (1961).

[72] Siverns, J. D., Simkins, L. R., Weidt, S. & Hensinger, W. K. - On the application of radio frequency voltages to ion traps via helical resonators. *Applied Physics B* **107**, 921–934 (2012).

[73] Okada, K. *et al.* - Photodissociation of $CaOH^{+}$ for Regeneration of Ca^{+} in Linear Paul Trap. *Japanese Journal of Applied Physics* **45**, 956–960 (2006).

[74] Hansen, A. K., Sørensen, M. A., Staanum, P. F. & Drewsen, M. - Single-Ion Recycling Reactions. *Angewandte Chemie International Edition* **51**, 7960–7962 (2012).

[75] Drever, R. W. P. *et al.* - Laser phase and frequency stabilization using an optical resonator. *Applied Physics B* **31**, 97–105 (1983).

[76] Black, E. D. - An introduction to Pound–Drever–Hall laser frequency stabilization. *American Journal Of Physics* **69**, 79–87 (2000).

[77] Donley, E. A., Heavner, T. P., Levi, F., Tataw, M. O. & Jefferts, S. R. - Double-pass acousto-optic modulator system. *Review of Scientific Instruments* **76**, 063112 (2005).

[78] Ma, L.-S., Jungner, P., Ye, J. & Hall, J. L. - Delivering the same optical frequency at two places: accurate cancellation of phase noise introduced by an optical fiber or other time-varying path. *Optics Letters* **19**, 1777–1779 (1994).

[79] Schindler, P. - *Frequency synthesis and pulse shaping for quantum information processing with trapped ions.* Master's thesis, Universität Innsbruck (2008). Available at http://quantumoptics.at.

[80] Kessler, T. *et al.* - A sub-40-mHz-linewidth laser based on a silicon single-crystal optical cavity. *Nature Photonics* **6**, 687–692 (2012).

[81] Hagemann, C. *et al.* - Ultra-stable laser with average fractional frequency drift rate below 5×10^{-19}/s. *Optics Letters* **39**, 5102–5105 (2014).

[82] Chen, L. *et al.* - Vibration-induced elastic deformation of Fabry-Perot cavities. *Physical Review A* **74**, 53801 (2006).

[83] Alnis, J., Matveev, A., Kolachevsky, N., Udem, T. & Hänsch, T. - Subhertz linewidth diode lasers by stabilization to vibrationally and thermally compensated ultralow-expansion glass Fabry-Pérot cavities. *Physical Review A* **77**, 53809 (2008).

[84] Dubé, P., Madej, A. A., Bernard, J. E., Marmet, L. & Shiner, A. D. - A narrow linewidth and frequency-stable probe laser source for the $^{88}\mathrm{Sr}^+$ single ion optical frequency standard. *Applied Physics B* **95**, 43–54 (2009).

[85] Oberst, H. - *Resonance fluorescence of single barium ions.* Master's thesis, Universität Innsbruck (1999). Available at http://quantumoptics.at.

[86] Dehmelt, H. G. - Proposed $10^{14}\ \Delta\nu < \nu$ laser fluorescence spectroscopy on Tl^+ mono–ion oscillator II (spontaneous quantum jumps). *Bulletin of the American Physical Society* **20** (1975).

[87] Dehmelt, H. G. - Mono-ion oscillator as potential ultimate laser frequency standard. *IEEE Transactions on Instrumentation and Measurement* **31**, 83–87 (1982).

[88] Myerson, A. *et al.* - High-Fidelity Readout of Trapped-Ion Qubits. *Physical Review Letters* **100**, 200502 (2008).

[89] Burrell, A. H., Szwer, D. J., Webster, S. C. & Lucas, D. M. - Scalable simultaneous multiqubit readout with 99.99% single-shot fidelity. *Physical Review A* **81**, 040302 (2010).

[90] Fox, M. - *Quantum Optics: an introduction.* Oxford Master Series in Atomic, Optical and Laser Physics (Oxford University Press, 2006).

[91] Bollinger, J., Itano, W. M., Wineland, D. J. & Heinzen, D. - Optimal frequency measurements with maximally correlated states. *Physical Review A* **54**, R4649–R4652 (1996).

[92] Sackett, C. *et al.* - Experimental entanglement of four particles. *Nature* **404**, 256–259 (2000).

[93] Häffner, H. *et al.* - Precision Measurement and Compensation of Optical Stark Shifts for an Ion-Trap Quantum Processor. *Physical Review Letters* **90** (2003).

[94] Beiser, L. - *Unified optical scanning technology* (John Wiley & Sons, 2005).

[95] Roos, C. - Viewpoint: Moving traps offer fast delivery of cold ions. *Physics* **5**, 94 (2012).

[96] Schindler, P. *et al.* - A quantum information processor with trapped ions. *New Journal of Physics* **15**, 123012 (2013).

[97] Liu, J.-M. - *Photonic Devices* (Cambridge University Press, 2005).

[98] Chang, I. C. - Acousto-optic devices and applications. In Bass, M. (ed.) *Handbook of Optics*, vol. 2, chap. 12 (McGraw-Hill, 1995), 2 edn.

[99] S. Stellmer and F. Schreck. - Reservoir spectroscopy of 5s5p $^3P_2 - 5snd\ ^3D_{1,2,3}$ transitions in strontium. *Physical Review A* **90**, 022512 (2014).

[100] Pham, P. T. T. - *A general-purpose pulse sequencer for quantum computing.* Master's thesis, Massachusetts Institute of Technology (2005). Available at http://dspace.mit.edu/handle/1721.1/32106.

[101] Bacher, M. - *Sättigungsspektroskopie an Kalziumdampf und Laserstabilisierung für Photoionisationsexperimente*. Master's thesis, Universität Innsbruck (2005). Available at http://quantumoptics.at.

[102] Rotter, D. - *Photoionisation von Kalzium*. Master's thesis, Universität Innsbruck (2003). [in German], available at http://quantumoptics.at.

[103] Diedrich, F., Peik, E., Chen, J., Quint, W. & Walther, H. - Observation of a Phase Transition of Stored Laser-Cooled Ions. *Physical Review Letters* **59**, 2931–2934 (1987).

[104] Blümel, R. *et al.* - Phase transitions of stored laser-cooled ions. *Nature* **334**, 309–313 (1988).

[105] Sawamura, H., Kitamura, H., Toyoda, K. & Urabe, S. - Observation of motional sidebands in single $^{40}\mathrm{Ca}^{+}$ ions with improved detection efficiency. *Applied Physics B* **80**, 1011–1014 (2005).

[106] Linke, N. M. *et al.* - Background-free detection of trapped ions. *Applied Physics B* **107**, 1175–1180 (2012).

[107] Pruttivarasin, T., Ramm, M. & Haeffner, H. - Direct spectroscopy of the $^2\mathrm{S}_{1/2}$–$^2\mathrm{P}_{1/2}$ and $^2\mathrm{D}_{3/2}$–$^2\mathrm{P}_{1/2}$ transitions and observation of micromotion modulated spectra in trapped Ca^{+}. *Journal of Physics B: Atomic, Molecular and Optical Physics* **47**, 135002 (2014).

[108] Wineland, D. J. & Itano, W. M. - Laser cooling of atoms. *Physical Review A* **20**, 1521–1540 (1979).

[109] Berkeland, D., Miller, J., Bergquist, J., Itano, W. M. & Wineland, D. J. - Minimization of ion micromotion in a Paul trap. *Journal of Applied Physics* **83**, 5025–5033 (1998).

[110] Diedrich, F., Bergquist, J., Itano, W. M. & Wineland, D. J. - Laser Cooling to the Zero-Point Energy of Motion. *Physical Review Letters* **62**, 403–406 (1989).

[111] Roos, C. *et al.* - Quantum State Engineering on an Optical Transition and Decoherence in a Paul Trap. *Physical Review Letters* **83**, 4713–4716 (1999).

[112] Marzoli, I., Cirac, J. I., Blatt, R. & Zoller, P. - Laser cooling of trapped three-level ions: Designing two-level systems for sideband cooling. *Physical Review A* **49**, 2771–2779 (1994).

[113] Turchette, Q. A. *et al.* - Heating of trapped ions from the quantum ground state. *Physical Review A* **61**, 063418 (2000).

[114] Deslauriers, L. *et al.* - Scaling and Suppression of Anomalous Heating in Ion Traps. *Physical Review Letters* **97**, 103007 (2006).

[115] Hite, D. A. *et al.* - 100-Fold Reduction of Electric-Field Noise in an Ion Trap Cleaned with In Situ Argon-Ion-Beam Bombardment. *Physical Review Letters* **109**, 103001 (2012).

[116] Hite, D. A. *et al.* - Surface science for improved ion traps. *MRS Bulletin* **38**, 826–833 (2013).

[117] Daniilidis, N. *et al.* - Surface noise analysis using a single-ion sensor. *Physical Review B* **89**, 245435 (2014).

[118] Ramsey, N. F. - Experiments with separated oscillatory fields and hydrogen masers. *Reviews of Modern Physics* **62**, 541–552 (1990).

[119] Hahn, E. - Spin Echoes. *Physical Review* **80**, 580–594 (1950).

[120] Biercuk, M. J. *et al.* - Optimized dynamical decoupling in a model quantum memory. *Nature* **458**, 996–1000 (2009).

[121] Kotler, S., Akerman, N., Glickman, Y., Keselman, A. & Ozeri, R. - Single-ion quantum lock-in amplifier. *Nature* **473**, 61–65 (2011).

[122] Kotler, S., Akerman, N., Glickman, Y. & Ozeri, R. - Nonlinear Single-Spin Spectrum Analyzer. *Physical Review Letters* **110**, 110503 (2013).

[123] Ott, H. W. - *Electromagnetic Compatibility Engineering* (Wiley, 2009).

[124] - Insight – Quantum Simulation. *Nature Physics* **8**, 263–299 (2012).

[125] Georgescu, I. M., Ashhab, S. & Nori, F. - Quantum simulation. *Reviews Of Modern Physics* **86**, 153–185 (2014).

[126] Johnson, T. H., Clark, S. R. & Jaksch, D. - What is a quantum simulator? *EPJ Quantum Technology* **1**, 10 (2014).

[127] Ball, P. - Physics of life: The dawn of quantum biology. *Nature* **474**, 272–274 (2011).

[128] Lambert, N. *et al.* - Quantum biology. *Nature Physics* **9**, 10–18 (2012).

[129] Gerlach, W. & Stern, O. - Das magnetische Moment des Silberatoms. *Zeitschrift für Physik* **9**, 353–355 (1922).

[130] Gerritsma, R. *et al.* - Quantum Simulation of the Klein Paradox with Trapped Ions. *Physical Review Letters* **106**, 060503 (2011).

[131] De Raedt, K. *et al.* - Massively parallel quantum computer simulator. *Computer Physics Communications* **176**, 121–136 (2007).

[132] Hilbert, M. & Lopez, P. - The World's Technological Capacity to Store, Communicate, and Compute Information. *Science* **332**, 60–65 (2011).

[133] Buluta, I. & Nori, F. - Quantum Simulators. *Science* **326**, 108 (2009).

[134] Leibfried, D. *et al.* - Trapped-ion quantum simulator: Experimental application to nonlinear interferometers. *Physical Review Letters* **89**, 247901 (2002).

[135] Friedenauer, A., Schmitz, H., Glueckert, J. T., Porras, D. & Schaetz, T. - Simulating a quantum magnet with trapped ions. *Nature Physics* **4**, 757–761 (2008).

[136] Britton, J. W. *et al.* - Engineered two-dimensional Ising interactions in a trapped-ion quantum simulator with hundreds of spins. *Nature* **484**, 489–492 (2012).

[137] Kim, K. *et al.* - Quantum simulation of frustrated Ising spins with trapped ions. *Nature* **465**, 590 (2010).

[138] Edwards, E. E. *et al.* - Quantum simulation and phase diagram of the transverse-field Ising model with three atomic spins. *Physical Review B* **82**, 060412 (2010).

[139] Islam, R. *et al.* - Onset of a quantum phase transition with a trapped ion quantum simulator. *Nature Communications* **2**, 377 (2011).

[140] Islam, R. *et al.* - Emergence and Frustration of Magnetism with Variable-Range Interactions in a Quantum Simulator. *Science* **340**, 583–587 (2013).

[141] Richerme, P. *et al.* - Quantum Catalysis of Magnetic Phase Transitions in a Quantum Simulator. *Physical Review Letters* **111**, 100506 (2013).

[142] Toyoda, K., Matsuno, Y., Noguchi, A., Haze, S. & Urabe, S. - Experimental Realization of a Quantum Phase Transition of Polaritonic Excitations. *Physical Review Letters* **111**, 160501 (2013).

[143] Gerritsma, R. *et al.* - Quantum simulation of the Dirac equation. *Nature* **463**, 68–71 (2010).

[144] Barreiro, J. T. *et al.* - An open-system quantum simulator with trapped ions. *Nature* **470**, 486–491 (2011).

[145] Lloyd, S. - Universal quantum simulators. *Science* **273**, 1073–1078 (1996).

[146] Trotter, H. F. - On the product of semi-groups of operators. *Proceedings of the American Mathematical Society* **10**, 545–551 (1959).

[147] Berry, D., Ahokas, G., Cleve, R. & Sanders, B. - Efficient quantum algorithms for simulating sparse hamiltonians. *Communications in Mathematical Physics* **270**, 359–371 (2007).

[148] Jozsa, R. - Fidelity for mixed quantum states. *Journal of Modern Optics* **41**, 2315–2323 (1994).

[149] Efron, B. & Tibshirani, R. - Bootstrap Methods for Standard Errors, Confidence Intervals, and Other Measures of Statistical Accuracy. *Statistical Science* **1**, 54–75 (1986).

[150] Poyatos, J. F., Cirac, J. I. & Zoller, P. - Complete characterization of a quantum process: the two-bit quantum gate. *Physical Review Letters* **78**, 390 (1997).

[151] Chuang, I. L. & Nielsen, M. A. - Prescription for experimental determination of the dynamics of a quantum black box. *Journal Of Modern Optics* **44**, 2455–2467 (1997).

[152] Riebe, M. *et al.* - Process tomography of ion trap quantum gates. *Physical Review Letters* **97**, 220407 (2006).

[153] Ježek, M., Fiurášek, J. & Hradil, Z. - Quantum inference of states and processes. *Physical Review A* **68**, 012305 (2003).

[154] Suzuki, M. - Improved Trotter-like formula. *Physics Letters A* **180**, 232–234 (1993).

[155] Leonhardt, U. - Quantum-State Tomography and Discrete Wigner Function. *Physical Review Letters* **74**, 4101–4105 (1995).

[156] Leibfried, D. *et al.* - Experimental Determination of the Motional Quantum State of a Trapped Atom. *Physical Review Letters* **77**, 4281–4285 (1996).

[157] White, A. G. *et al.* - Measuring two-qubit gates. *Journal of the Optical Society of America B* **24**, 172–183 (2007).

[158] Hofmann, H. F. - Complementary Classical Fidelities as an Efficient Criterion for the Evaluation of Experimentally Realized Quantum Operations. *Physical Review Letters* **94**, 160504 (2005).

[159] Brown, K., Clark, R. & Chuang, I. - Limitations of Quantum Simulation Examined by Simulating a Pairing Hamiltonian Using Nuclear Magnetic Resonance. *Physical Review Letters* **97**, 050504 (2006).

[160] Schindler, P. *et al.* - Experimental repetitive quantum error correction. *Science* **332**, 1059–1061 (2011).

[161] Schindler, P. *et al.* - Quantum simulation of dynamical maps with trapped ions. *Nature Physics* **9**, 361–367 (2013).

[162] Wieman, C., Pritchard, D. & Wineland, D. J. - Atom cooling, trapping, and quantum manipulation. *Reviews of Modern Physics* **71**, S253–S262 (1999).

[163] Shu, G., Chou, C. K., Kurz, N., Dietrich, M. R. & Blinov, B. B. - Efficient fluorescence collection and ion imaging with the “tack” ion trap. *Journal Of The Optical Society Of America B-Optical Physics* **28**, 2865–2870 (2011).

[164] Streed, E. W., Jechow, A., Norton, B. G. & Kielpinski, D. - Absorption imaging of a single atom. *Nature Communications* **3**, 933 (2012).

[165] Schrödinger, E. - Are there quantum jumps? Part I. *The British Journal for the Philosophy of Science* **3**, 109–123 (1952).

[166] Nagourney, W., Sandberg, J. & Dehmelt, H. - Shelved optical electron amplifier: Observation of quantum jumps. *Physical Review Letters* **56**, 2797–2799 (1986).

[167] Sauter, T., Neuhauser, W., Blatt, R. & Toschek, P. - Observation of Quantum Jumps. *Physical Review Letters* **57**, 1696–1698 (1986).

[168] Bergquist, J., Hulet, R., Itano, W. & Wineland, D. - Observation of Quantum Jumps in a Single Atom. *Physical Review Letters* **57**, 1699–1702 (1986).

[169] Larson, D., Bergquist, J., Bollinger, J., Itano, W. M. & Wineland, D. J. - Sympathetic cooling of trapped ions: A laser-cooled two-species nonneutral ion plasma. *Physical Review Letters* **57**, 70–73 (1986).

[170] Clark, C. R., Goeders, J. E., Dodia, Y. K., Viteri, C. R. & Brown, K. R. - Detection of single-ion spectra by Coulomb-crystal heating. *Physical Review A* **81**, 043428 (2010).

[171] Schrödinger, E. - Die gegenwärtige Situation in der Quantenmechanik. *Die Naturwissenschaften* **23**, 807–812 (1935).

[172] Cirac, J., Blatt, R., Parkins, A. & Zoller, P. - Preparation of Fock states by observation of quantum jumps in an ion trap. *Physical Review Letters* **70**, 762–765 (1993).

[173] Cirac, J., Blatt, R., Parkins, A. & Zoller, P. - Quantum collapse and revival in the motion of a single trapped ion. *Physical Review A* **49**, 1202–1207 (1994).

[174] Blatt, R., Cirac, J. I., Parkins, A. S. & Zoller, P. - Quantum motion of trapped ions. *Physica Scripta* **T59**, 294 (1995).

[175] Monroe, C. R., Meekhof, D. M., King, B. E. & Wineland, D. J. - A “Schrödinger Cat” Superposition State of an Atom. *Science* **272**, 1131–1136 (1996).

[176] Myatt, C. J. *et al.* - Decoherence of quantum superpositions through coupling to engineered reservoirs. *Nature* **403**, 269–273 (2000).

[177] Turchette, Q. A. *et al.* - Decoherence and decay of motional quantum states of a trapped atom coupled to engineered reservoirs. *Physical Review A* **62** (2000).

[178] Zheng, S.-B. - Preparation of motional macroscopic quantum-interference states of a trapped ion. *Physical Review A* **58**, 761–763 (1998).

Index